

2017

Development and Clinical Application of a New Two-Dimensional in vivo Dosimetry by Electronic Portal Imaging

Peca, Stefano

Peca, S. (2017). Development and Clinical Application of a New Two-Dimensional in vivo Dosimetry by Electronic Portal Imaging (Doctoral thesis, University of Calgary, Calgary, Canada). Retrieved from <https://prism.ucalgary.ca>. doi:10.11575/PRISM/25639
<http://hdl.handle.net/11023/3648>

Downloaded from PRISM Repository, University of Calgary

UNIVERSITY OF CALGARY

Development and Clinical Application of a New Two-Dimensional *in vivo* Dosimetry by
Electronic Portal Imaging

by

Stefano Peca

A THESIS

SUBMITTED TO THE FACULTY OF GRADUATE STUDIES
IN PARTIAL FULFILMENT OF THE REQUIREMENTS FOR THE
DEGREE OF DOCTOR OF PHILOSOPHY

GRADUATE PROGRAM IN PHYSICS AND ASTRONOMY

CALGARY, ALBERTA

JANUARY, 2017

© Stefano Peca 2017

Abstract

In vivo dosimetry (IVD) in radiotherapy refers to direct measurement of dose deposited in the patient during treatment. IVD can be of great use in early detection of harmful errors, for assessment of patient setup and anatomy changes, and to guide adaptive radiotherapy. Routine IVD is hindered by the costs and complexities associated with most systems, and thus has not obtained widespread application.

In this thesis I describe a novel method of using the electronic portal imaging device (EPID) for IVD. Images are measured through phantoms/patients making use of treatment beams. From these, 2D dose maps at isocentre depth are calculated from signal-to-dose correlation ratios. Convolution by optimized multi-Gaussian kernels, specific to direction (cross-plane, in-plane), field size, and attenuator thickness, allows dose modelling in the whole plane. The EPID-calculated dose map is compared to that predicted by the treatment planning system (TPS) by pixel-wise comparison, gamma analysis, and a novel approach of morphological connected component analysis. Tests with off-reference values of phantom thickness, field size, and monitor units showed good agreement, with the great majority of points within $\pm 3\%$ of TPS dose.

The method was evaluated on 20 patients, spanning multiple body sites and treatment techniques (334 fields). Excluding lung treatments, the mean dose difference at isocentre had good accuracy at $1.5 \pm 6.6\%$. The large standard deviation is due to both algorithm limitations and true differences, mainly anatomical changes and setup variability. In the isocentre plane, the median area that passed 10% / 3 mm gamma analysis was 96.1%. In three of ten rectal cancer patients, soft tissue differences resulting from suboptimal setup and immobilization devices

caused up to 2% overdose to the small bowel. Results suggest that connected component analysis may be as good or superior to gamma analysis for detection of specific dose differences. Further work is necessary before clinical implementation, but EPID IVD by correlation ratios has enormous potential for error detection, process quality assurance, and adaptive treatment guidance, thus increasing safety and quality of radiotherapy.

Acknowledgements

The cliché phrase “this thesis would not have been possible if not for the help of...” has never been truer than in reference to Dr. Wendy Smith. She provided the guidance and support that I needed, was always persistent and direct, while also caring, and always set the bar higher than my comfort zone. As well, I am grateful to Dr. Derek Brown, for taking me on this research project and for his guidance and assistance, and to Dr. Elizabeth Kurien and Dr. Nicolas Ploquin for their guidance as my supervisory committee. Thank you also to Dr. Peter Dunscombe for accepting me in the program, Dr. Eduardo Villareal and Dr. David Spencer for the many enlightening chats, and all the physicists at the Tom Baker for their teaching and example.

My fellow students and the physics assistants have always been a huge help and great company. Thank you for sharing knowledge, supporting QC work, and much more. In particular I'm very grateful to (in order of appearance): Philip, Sarah, Yannick, Gosia, Leigh, Brandon, Jared, Casey, Elizabeth, Parisa, David Sinn, Emily, Michael: thank you for the chats, laughs, and coffee. Much coffee.

Finally, the deepest support and motivation for this research has come from my wife, Alethea, whose constant love and trust encourage me, every day, to become a ‘better version of myself’ (M. Kelly). She also gave me three wonderful gifts, Kolbe, Giorgio, and Aurelia, all born while this research work was in the making. Which suggests she is at least three times more efficient than I am.

To my father

Table of Contents

Abstract.....	ii
Acknowledgements.....	iv
Dedication.....	v
Table of Contents.....	vi
List of Tables.....	ix
List of Figures and Illustrations.....	x
List of Symbols, Abbreviations and Nomenclature.....	xviii
Chapter One: Radiation therapy and <i>in vivo</i> dosimetry.....	1
1.1 Radiation therapy and errors.....	2
1.1.1 The radiation therapy process.....	2
1.1.2 Error classifications.....	7
1.1.3 Documented errors in RT.....	9
1.2 Methods for <i>in vivo</i> dosimetry.....	16
1.2.1 Thermoluminescent and optically stimulated luminescent dosimeters.....	16
1.2.2 Diodes and MOSFETs.....	17
1.2.3 Film.....	19
1.2.4 Head-mounted devices.....	20
1.2.5 Summary.....	22
Chapter Two: The electronic portal imaging device and its use.....	24
2.1 EPID components and operation.....	24
2.1.1 Correction Images.....	27
2.1.2 Limitations of MV imaging.....	30
2.2 <i>In vivo</i> Dosimetry by EPID.....	35
2.2.1 The Winnipeg-Newcastle collaboration.....	37
2.2.2 The NKI Model.....	38
2.2.3 The Rome Model.....	40
2.2.4 Scope of this thesis.....	43
Chapter Three: Two-dimensional <i>in vivo</i> dose verification using portal imaging and correlation ratios.....	45
3.1 Introduction.....	47

3.2 Methods.....	51
3.2.1 EPID signal to dose correlation ratios	52
3.2.2 2D dose calculation in solid water phantoms	55
3.2.3 2D dose calculation in anthropomorphic phantom	56
3.3 Results and Discussion	58
3.3.1 Correlation ratios and dose calculation in solid water phantoms	58
3.3.2 Dose calculation in anthropomorphic phantom	61
3.3.3 Limitations	63
3.4 Conclusions.....	64

Chapter Four: Dose modelling by multi-Gaussian convolution of transit portal images.....67

4.1 Introduction.....	70
4.2 Methods.....	71
4.2.1 Theory	71
4.2.2 Materials and measurements.....	75
4.3 Results.....	76
4.4 Discussion.....	81
4.4.1 Application to in vivo dosimetry	83
4.5 Conclusion	84

Chapter Five: Improved two-dimensional EPID dosimetry by correlation ratios86

5.1 Introduction.....	89
5.2 Methods.....	91
5.2.1 EPID imaging	91
5.2.2 Commissioning procedure	91
5.2.3 Testing	98
5.3 Results.....	100
5.3.1 EPID dose vs. MU, field size, and thickness	100
5.3.2 Accuracy in the presence of thickness errors.....	103
5.4 Discussion.....	106
5.4.1 Accuracy in the presence of thickness errors.....	107
5.4.2 Limitations	109
5.5 Conclusion	110

5.6 Appendix: Derivation of dose calculation error expressions in cases of thickness changes between CT and treatment	111
---	-----

Chapter Six: *In vivo* portal imaging dosimetry in rectal cancer radiotherapy on the belly board device116

6.1 <i>In vivo</i> EPID dosimetry detects interfraction errors in 3D-CRT of rectal cancer: a relative dosimetry study	118
6.1.1 Introduction.....	119
6.1.2 Methods	120
6.1.3 Results.....	124
6.1.4 Discussion.....	127
6.1.5 Conclusion	129
6.2 <i>In vivo</i> portal imaging dosimetry identifies delivery errors in rectal cancer radiotherapy on the belly board device	130
6.2.1 Introduction.....	131
6.2.2 Methods	132
6.2.3 Results and discussion	134
6.2.4 Conclusions.....	144

Chapter Seven: Morphological dose difference analysis for a novel *in vivo* portal dosimetry147

7.1 Introduction.....	149
7.2 Methods.....	151
7.2.1 Patients and <i>in vivo</i> imaging.....	151
7.2.2 EPID vs planned dose evaluation	152
7.2.3 ROC analysis	153
7.3 Results and Discussion	154
7.3.1 SBRT case study: lung-liver border.....	155
7.3.2 Dose difference and gamma analyses	156
7.3.3 ROC analysis of dose difference, gamma, and CC metrics.....	156
7.4 Conclusion	162
7.5 Appendix: Further results in lung	163

Chapter Eight: Conclusions and future work167

References.....	172
Appendix: Copyright permissions	185

List of Tables

Table 1-1: Radiation therapy delivery errors which have allegedly caused death of patients, directly or indirectly.....	11
Table 1-2: Some relevant characteristics of the most widely used <i>in vivo</i> dosimetry systems. ...	23
Table 6-1: Quality assurance summary from <i>in vivo</i> EPID dosimetry on 10 rectal cancer patients. In brackets are the imaged fields and fractions in which the dose discrepancy was visible. S-I: superior-inferior, L-R: left-right, AP:antero-posterior, PA:postero-anterior, LAT:lateral, fx:fraction(s).	136
Table 7-1: Dose difference statistics (pixel-by-pixel and gamma) for 15 patient treatments.....	156
Table 7-2: Qualitative sensitivity, to various types of errors, of our EPID <i>in vivo</i> dosimetry (IVD), evaluating results by dose difference (DD) only, by gamma analysis, and by morphological connected component (CC) analysis. (References: ^{104, 130} and Chapter 6.2)	160
Table 7-3: Dose difference statistics (pixel-by-pixel and gamma) for all fields.	163

List of Figures and Illustrations

Figure 1-1: Simplified RT workflow with possible errors that would affect delivery (S=systematic, R=random). Operational categories taken from *Safety is no Accident*.⁷ 3

Figure 1-2: An error (divergence between action and protocol) can be either an incident (dose delivered differs from dose planned) or a near miss (potential incident caught before delivery). An incident, in turn, may be classified as an adverse event if harm results to the patient. The percentage estimates are based on multiple publications.^{17, 22, 25, 26} 8

Figure 1-3: Percentage of total errors (top) and incidents (bottom) reported at the Ottawa Hospital in 2007-2011, divided into four operational categories. The majority of errors take place in treatment preparation, but the majority of those that lead to patient harm occur in treatment delivery. Reprinted from Clark *et al.*²⁶ with permission by Elsevier..... 15

Figure 1-4: Schematic of a diode dosimeter. Any hole (h) – electron (e) pair produced by radiation inside or in proximity of the depletion layer will migrate due to electrostatic potential. This will cause a current in the circuit, proportional to the dose. 18

Figure 1-5: Head-mounted devices are of practical clinical use, as they require no staff intervention. On the other hand, they attenuate the beam and provide no information at the level of the patient. 21

Figure 2-1: Schematic cross-section of four pixels of an EPID imager. Incident radiation sets electrons in motion in the Cu. These in turn may enter and interact with the scintillator, which produces optical photons. The light-sensitive detectors accumulate a charge which is read out when the TFT switch is activated. (Scale is approximate and based on the Varian aS500/aS1000). 25

Figure 2-2: A 2×2 section of the pixel array. The photodiode acts like a capacitor and integrates charge. When the appropriate voltage is applied to a gate line, all connected TFT switches become transparent and the charge is read out via the data lines..... 26

Figure 2-3: Flood field correction images (left) and central profiles (right; blue=cross-plane, green=in-plane) taken through a solid water slab phantom with thickness 0, 10, 20 cm. For an unperturbed beam, intensity increases off axis due to the combined effect of the beam’s ‘horns’ and the increased EPID sensitivity to lower energy photons.^{71, 72} Increasing depth reverses the horn effect. (Note: wider scale for 0 cm). 28

Figure 2-4: Relative probability of photon interaction modalities in matter. The curves represent equal probability of two neighbouring effects. Adapted from Attix⁶⁶ with data from Evans *et al.*⁷⁵ 29

Figure 2-5: When imaging a small object inside an x-ray field, the finite dimension of the focal spot causes a geometric penumbra of width proportional to the spot size itself. In

kV imaging, the smaller spot size (a) allows a better spatial resolution than MV imaging (b).....	33
Figure 2-6: If the phantom is centered at isocentre, then clearly $D_m=D_{iso}$ (a). However, if the phantom has a vertical shift of d , one may make use of TMRs to shift the calculation point from a depth of $w/2$ (b) to $w/2-d$, which is isocentre (c).....	42
Figure 3-1: Dose calculation pipeline. Gray: commissioning procedure which has to be run only once. White: dose calculation steps per each patient/field. Dashed frame identifies calculations performed in MATLAB environment. (s.w.=solid water; ‘patient’ also refers to anthropomorphic phantom.)	51
Figure 3-2: Solid water phantom setup for measurement of correlation factors F_{CAX} (a) and f (a and b) (see ¹⁰² for details). Measurements were performed for five thicknesses w , seven field sizes l , and nine displacements d . (c) Schematic for off-axis $F_{i,j}$ measurements.....	53
Figure 3-3: (a) 2D map of the signal-to-dose correlation factor $F_{i,j}$. For every pixel i,j of the EPID, $F_{i,j}=S_{i,j}/D_{i,j}$ where S is the signal intensity and D is the dose determined by the TPS in the point where the ray line from the source to the pixel intersects the isocentre plane (Figure 3-2.c). This matrix was calculated for three field sizes (shown: $l=10$ cm) and for five phantom thicknesses (shown: $w=12$ cm). The black rectangle contains the cross-plane profile which was averaged and normalized by $F_{CAX}(w,l)$ to compute the mean 10×10 edge correction curve. (b) Edge correction curves for three field sizes from the 12 cm thick phantom.....	59
Figure 3-4: The fundamental steps of our dose map calculation and evaluation. (a) EPID image of 16 cm solid water with 15×15 cm ² field, continuous acquisition mode. (b) Calculated dose using signal-to-dose correlation factor from the central axis F_{CAX} as previously described. ¹⁰² (c) Field edge correction to F_{CAX} obtained using the 15×15 curve from Figure 3-2.b and a binary mask of the EPID image. (d) Edge-corrected dose map obtained by pixel-by-pixel division of (b) by (c). (e) Dose map predicted by the TPS. (f) Gamma evaluation (3% / 3mm) of the dose maps. Passing values ($\gamma < 1$ for >95% of in-field pixels) were obtained for all solid water thicknesses and field sizes. Dose maps are masked to field size.	60
Figure 3-5: Validation of our dose calculation algorithm on the anthropomorphic phantom. Top to bottom: whole brain with gantry 270°, brain primary with gantry 40°, lung tumour with gantry 0°. Left-to-right: EPID-calculated dose, TPS-predicted dose, and their gamma evaluation (3% / 3mm). Edge correction from the curves of Figure 3-2.b. Maps are masked to field size. *Note: to provide a meaningful analysis for the lung tumour the calculated dose has been scaled <i>ad hoc</i> by -6.8% because our calculation overestimated dose in proximity of low density tissue.....	62
Figure 4-1: Pixel-by-pixel dose difference map, between TPS and EPID-based calculation (colour bar is $\pm 5\%$). The off-axis correction is based on the central profiles only (described in Ch.3), and thus does not adequately describe dose away from central	

profiles. (Dose map estimated in mid-depth of a 20 cm phantom irradiated with 6X, 20 cm square field)..... 67

Figure 4-2. Theoretical framework of the multi-Gaussian approach. (a) Dose profile at isocentre depth in phantom (red) may be modelled as a boxcar function (black) convolved (\otimes) with a Gaussian (SD ~ 3.2 mm).⁹ (b) Similarly, the EPID signal (blue dotted) from an unperturbed beam can be modelled by convolution of the boxcar with a thin (SD ~ 1 mm) Gaussian to account for imager glare and geometric penumbra. This profile is offset by a small and semi-uniform scatter component (green dash-dot) due to photons scattered from the gantry head. (c) To model a transit image (black dash) one must consider also the photons scattered in the phantom that reach the imager (green dash-dot). This can be modelled by convolution with a wide Gaussian (SD ~ 10 cm). (d) We propose *in vivo* dose modelling from the transit EPID signal by convolution with a linear combination of Gaussians, G_i . (e) Schematic of experimental setup, illustrating transit EPID images obtained through slab phantoms of thickness w vertically centered about the isocentre. (f) Zooming in on the left edge of the dose (red) and EPID signals (blue dotted, black dashed) illustrates differences in the profiles. Data from: 6 MV, 10×10 cm² field, $w=25$ cm. All plots are normalized to unity. X-axis is distance (cm) from CAX. Scatter from phantom (green dash-dot) is an estimate, for illustrative purposes. 73

Figure 4-3: Representative results for the multi-Gaussian optimization algorithm. (a,b) The optimal coefficients differed between cross-plane and in-plane central profiles, producing different multi-Gaussian kernels (black dashed). (c,d) Convolution of the normalized EPID transit image by the corresponding kernel approximates TPS dose. (e) Pixel-by-pixel comparison of TPS dose map to map calculated from the EPID image with no off-axis correction, highlighting the differences in the shoulder region. (f) Conversely, applying the multi-Gaussian convolutions for every row and column of the EPID image gives a map which better approximates the dose map. (Data: 6 MV, 10×10 cm² field, 20 cm phantom, 10 cm depth. Values $< 50\%$ of CAX not plotted.) 77

Figure 4-4: Coefficients (weights) resulting from the optimization. Black box plots include the 28 data sets, each panel is different energy and profile orientation. For 6 MV (a, b), the Gaussian of SD 3.2 mm is the most important in describing dose profiles, while for 15 MV (c, d) the second Gaussian becomes more relevant. Data is also separated by field size (colours). There is dependence of some coefficients with field size: smaller fields have more heavily weighted G_4 . (Box is 25th–75th percentile, inscribed line is median, whiskers include all non-outlier data, no whiskers on field size (colour) boxes for clarity). 78

Figure 4-5: Multi-Gaussian curves resulting from the coefficients in Figure 4-4. In almost all cases, the smallest fields need the widest Gaussians to model dose from EPID transit images. (All curves are normalized to area=1. Vertical axis is a.u. Tails are not shown.)... 79

Figure 4-6: Global percent difference between planned dose and portal image multi-Gaussian convolution for all 28 phantom thicknesses and field size combinations. Excluding the high dose gradient field edges, the difference is generally within 1% for 6 MV (a, b).

For 6 MV through 5 cm (blue dashed) and for most 15 MV profiles the difference is larger due to the dip between the horns, which is not modelled.	80
Figure 5-1: Commissioning procedure of EPID IVD by correlation ratios. Green rounded boxes represent suggested EPID measurements and TPS calculations. Blue boxes are output data, used for subsequent dose calculations, specific to machine, energy, dose rate, and imaging parameters. (w =phantom thickness on CAX, l =square field size, d =vertical displacement off-centre, see Figure 5-2.)	92
Figure 5-2: <i>In vivo</i> isocentre dose measurement by EPID, as proposed by Piermattei et al. ¹⁰² (a) Measurement of correlation ratio F (Equation 25). (a,b) Measurement of f (Equation 26). (c) Use of F , f , and TMRs to measure dose at isocentre in a patient. In our approach, we account for inhomogeneities by water equivalent thicknesses (bowel gas and vertebral body shown).....	93
Figure 5-3: Correction for beam-off image loss. In <i>cine</i> imaging, the last frames which are too few to form an image (i.e. are $<$ the f/i value) are discarded. This was accounted for by multiplying the image sum by the corrected (non-integer) number of images (red) for its MU value over the physical number of images (blue), found by fitting the data points characterized by the lowest number of MU per image.	94
Figure 5-4: Horn correction matrix (HCM) for phantom thickness 10 cm, $15 \times 15 \text{ cm}^2$ field. An <i>in vivo</i> dose calculation must be divided by the appropriate HCM to account beam horns. The correlation ratio F between EPID transit signal and dose in the mid-depth of the phantom was established on the CAX, hence the HCM is equal to one in the centre of the image. (Axes are pixel numbers).	97
Figure 5-5: Two-dimensional EPID dose calculation from patient/phantom images.....	98
Figure 5-6: F correlation ratio for 6 MV.	100
Figure 5-7: (a) Half-resolution and (b) full resolution CAX $S^{(raw)}$, for both energies, $l=10$, $w=20$. Higher $S^{(raw)}$ corresponds to lower dose. In all cases, the first images are susceptible to linear accelerator ramp-up artifacts ⁷⁴ and were therefore removed. For 6 MV half-resolution, a correction factor was introduced to account for the systematic offset. Note that the scale of (b) is 10 times smaller, so no other correction factors were necessary. *Acquired 9 months before all other images, before imager upgrade.	101
Figure 5-8: Boxplot of pixel-by-pixel dose differences between EPID and TPS dose maps, varying MU. Box edges are the 25 th and 75 th percentiles; red line is median. Dose maps passed a 3% / 3mm gamma analysis in all but two of the lowest MU tests (top row). In all but three cases, the CAX EPID dose (black diamond) was within $\pm 2\%$ of the TPS. (Whiskers are set at $q_3+1.5(q_3-q_1)$ and $q_1-1.5(q_3-q_1)$, where q_1 and q_3 are the 25th and 75th percentiles, respectively. This corresponds to approximately $\pm 2.7\sigma$ and 99.3% coverage if the data are normally distributed. Outliers not plotted. *Out of scale, +8%.) .	102

Figure 5-9: Boxplot of pixel-by-pixel dose differences shows good agreement between EPID and TPS dose maps, varying square field size (l) and absorber thickness (w). In all but two cases, the CAX EPID dose (black diamond) was within $\pm 2\%$ of the TPS. 103

Figure 5-10: In phantoms of thickness $w \pm \Delta w$, the ratio of dose measured with CT-calculated thickness w to dose measured with CT-calculated thickness $w \pm \Delta w$. In the case of patient tissue gain/swelling ($\Delta w = +1$, top), planning CT thickness causes EPID to underestimate dose. The dose calculation error is largest for thickness changes downstream of the isocentre (dashed), and is larger for 6 MV (left) than 15 MV (right). 104

Figure 5-11: Screenshot of *in vivo* EPID dose calculation showing good agreement with planned dose (prone cervical cancer patient, lateral field). (a) Beam's eye view of water equivalent depth, obtained by projection of planning CT along ray lines from source to each EPID pixel. (b) One of the *in vivo cine* EPID images (a.u.). (c) Value of the central pixels for each of the 5 *cines* (x axis). The first three *cines* were discarded as they usually suffer from beam-on artifacts. (d) EPID-reconstructed dose at isocentre depth. (e) Planned dose. (Dose scales relative to TPS maximum.) (f) In-field pixel-by-pixel dose difference map. (g,h) Cross-plane and in-plane central profiles of: planned dose (blue), dose reconstruction steps (green, cyan), and final EPID dose (dashed red). (i) 5% / 3 mm gamma evaluation. (Unlabeled axes are pixel number.) 105

Figure 5-12: When the measurement conditions match the CT used for back projecting dose from EPID signal to the isocentre plane, as in (a), EPID dose D' calculated at isocentre depth (red dashed line) is in agreement with true dose D . However, the EPID signal cannot detect the location of added attenuation. For this reason, back-projected dose to the isocentre plane is a flag of changes in e.g. patient set up but does not always accurately measure the change in delivered dose at isocentre. When (b) $\Delta w = +1$ cm is introduced upstream of isocentre in the measurement, but not in CT, the EPID dose calculation slightly exaggerates the dose difference. For example, when the extra attenuator is distributed equally upstream and downstream (c), the true dose is greater than in (b), but the EPID signal is practically unchanged, and the EPID dose calculation is further overestimated. (d) When the extra attenuator is placed downstream, isocentre dose is the same as (a), but EPID signal is very close to that of (b) and (c). In this situation EPID underestimates dose by 4%/cm. (see Figure 5-10.a for exact values) 108

Figure 5-13: Overestimation of EPID dose from attenuator thickness reduction of 1 cm. In the case of attenuator loss upstream of isocentre, EPID dose overestimates by up to 1.5%. This error increases to approx. 4.5% if thickness loss is entirely downstream of isocentre. Measured values (points) are in good agreement with calculated values (lines). 114

Figure 6-1: Patient F, PA field ($GA=0^\circ$). (a) Raw EPID images. (b) Lateral view from the TPS showing the imaging plane (red) and the body adapting to the belly board opening. (c) Dose difference (cGy) between the first imaged fraction (Im.Fx.) and five later treatment days. The large mismatch is located at the edge of the belly board opening (red arrows), indicating inconsistent setup of the patient with respect to the board in the S-I direction. This was verified by visual inspection of the raw images (blue arrows). As

well, all dose difference maps are affected by the gas bubble present during the Ref fraction (white arrow).	123
Figure 6-2: Patient E, PA field (GA=0°). (a) Raw EPID images. (b) Lateral view from the TPS showing the imaging plane (red) and the body adapting to the belly board opening. (c) Dose difference maps between the first imaged fraction (Im.Fx.) and five later treatment days. Dose maps display inconsistent setup, especially at the opening of the belly board (red arrows). Most likely there is inconsistency in the amount of abdomen compressed in the corner of the belly board-couch interface (b, red arrow). In addition, this patient is prone to frequent gas bubbles (black arrows), warranting for adaptive radiotherapy (i.e. replanning including gas).	125
Figure 6-3: Patient B, RL field (GA=90°). (a) EPID images show frequent gas bubbles, but provide no information on their impact on dose. (b) Lateral view from the TPS showing the imaging plane (red). (c) Dose difference maps between the first imaged fraction (Im.Fx.) and five later treatment days. Dose maps confirm correct setup, but display large variations due to gas bubbles, warranting for adaptive radiotherapy.	126
Figure 6-4: Cumulative dose difference maps, summed over all imaged fractions. Belly board-couch interface setup errors sum in Patients F and E, indicating a systematic error which warrants intervention (red arrows). In Patients E and B dose differences due to presence/absence of gas bubbles accumulate (black arrows). In Patient B setup appears to be reliable.....	128
Figure 6-5: Example of <i>in vivo</i> EPID dose calculation showing good agreement with planned dose at isocentre depth (patient 1, PA field, fraction 2). (a,b) Frontal, sagittal views of CT and field with the small bowel contoured in cyan. (c) Single <i>cine</i> frame. (d) Planned dose map. (e) EPID-reconstructed dose at isocentre depth. (f) Point-to-point dose difference map. (g,h) Cross-plane and in-plane dose profiles (blue: TPS; dashed red: EPID dose). (i) 5%, 3 mm gamma evaluation, showing good agreement.	135
Figure 6-6: Variability in the amount of abdomen that fills the belly board opening affects dose in patient 3, AP field. The filling of the opening is ‘sharp’ at planning (a, d: white arrow). The EPID-calculated dose map at isocentre depth, averaged over 6 fractions, displays a more gradual dose gradient (b). This is due to both different patient positioning and to the softer belly board cushion at the treatment unit (due to greater wear and tear), which in effect makes the hole in the board shallower. The dose discrepancy is especially clear in a point-to-point dose difference map (c). As a result, some of the small bowel (d, e: cyan) was likely overdosed by ~8%. (Dose percentages with respect to AP field.)	138
Figure 6-7: Belly board positioning error (patient 8). Dose difference maps for four non-consecutive fractions show that on fx 3, the belly board was placed about 1.5 cm inferior with respect to planning CT (arrows). As a result, an extra ~6 cm of attenuator are in the superior region of the field, causing dose reduction to the target and more small bowel to be in the field. ¹⁶⁸	140

Figure 6-8: Persistent bowel gas affects dose (patient 2). Dose difference maps (left) and 5%, 3mm gamma analysis (right) over six non-consecutive treatment fractions for the left lateral field. The average dose difference map (bottom) indicates consistently more gas at treatment than simulation. There was likely some overdose to the small bowel (cyan contour on the planning CT). For patients like this, *in vivo* dosimetry may warrant adaptive treatment by repeating CT to account for consistent gas. (Percentages with respect to the lateral field’s dose.) 141

Figure 6-9: Systematic dose discrepancy indicative of muscle relaxation and/or anatomy rotation at treatment with respect to planning (patient 4). Dose difference maps (first row) and 5%, 3 mm gamma evaluation (second row). 143

Figure 7-1: Illustration of the morphological approach proposed to evaluate dose difference maps. (a) Initial dose difference with multiple pixel values. (b) Thresholding produces a binary image, with 4 connected components (CC). (c) Small components are ignored. (d) Dilation and (e) erosion by the same radius produce final image, with 2 CCs. The area of the largest CC was chosen as metric for dose difference detection. 150

Figure 7-2: Example output of our EPID *in vivo* dosimetry; prone cervix patient, AP field. (a) Projection of water equivalent depth (WED) along ray lines from source to each EPID pixel, from planning CT. (b) One of the *cine* EPID images (a.u.). (c) Value of the central 5×5 pixels for each of the 5 *cines* (x axis). The first two *cines* are discarded as they suffer from beam-on artifacts.⁸⁰ (d) Planar dose at isocentre depth, reconstructed from EPID and WEDs. (e) Planned dose. (f) In-field pixel-by-pixel dose difference map. (g,h) Cross-plane and in-plane central profiles of: planned dose (blue), dose reconstruction steps (green, cyan), and final EPID dose (dashed red). (i) Gamma evaluation (5% / 3mm). 154

Figure 7-3: Left: Results from EPID IVD from the liver SBRT case treated with exhale breath hold monitored by RPM. Percent difference (top) and gamma analysis (bottom) maps between EPID-measured and TPS dose display a region of disagreement across the centre of the field, more so in fraction 1 (left). Inspection of the breath-held planning CT (right) showed that the region of discrepancy is in the lung-liver border. IVD indicates that at time of treatment the liver was 4-7 mm inferior with respect to planning..... 155

Figure 7-4: Illustration of the connected component (CC) analysis. (a) Planned vs EPID-calculated dose difference map. (b) Binary dose difference map, thresholded at 10%. (c) Binary map after removal of small CCs, dilation, erosion, overlaid on field mask. Two CCs result, the largest having area 21 cm². (Data: single fraction of an Ant-Post field.) .. 157

Figure 7-5: ROC curves for various metrics suggest that connected component (CC) analysis performs best in detection of specific dose discrepancies. The larger the area under the curve (AUC, in parenthesis in the legend), the greater the ability of the metric to discriminate relevant dose differences between plan and delivery. At multiple dose difference (DD) levels, including 5% (a) and 10% (b), the largest AUC comes from CC analysis. (TPF: true positive fraction; FPF: false positive fraction; *:p<0.05)..... 158

Figure 7-6: Connected component (CC) analysis (bottom) performs equal or better than gamma analysis (middle) and dose difference (DD) alone (top). Crosses: fields manually flagged for relevant dose discrepancy (positives); circles: other fields (negatives). CC better discriminates positive dose deviations due to soft tissue variations caused the belly board immobilization device (a) and setup differences (b). CC also produced some false positives (c). The dashed lines represent choices between sensitivity and specificity..... 159

Figure 7-7: Pixel-by-pixel dose difference between dose calculations from EPID images and TPS, 21 treatments. Solid coloured points are median values for a single patient; dashed black is median over all patients. For fields which do not go through lung (top), a median value of 96.1% of the field has dose difference less or equal to 10%. For fields through lung (bottom) there is more variability across patients and worse agreement with TPS..... 165

List of Symbols, Abbreviations and Nomenclature

<i>Symbol</i>	<i>Definition</i>
\otimes	Convolution operator
AAA	Analytical Anisotropic Algorithm
AAPM	American Association of Physicists in Medicine
AIC	Akaike information criterion
ART	Adaptive radiation therapy
a-Si	Amorphous Silicon
CAX	Central axis
CT, CBCT	Computed tomography, Cone-beam computed tomography
DF	Dark field
EPID	Electronic portal imaging device
FF	Flood field
Fx	Fraction
GTV, CTV, PTV	Gross, clinical, and planning target volume
HCM	Horn correction matrix
IGRT	Image-guided radiation therapy
IMRT	Intensity modulated radiation therapy
IVD	<i>In vivo</i> dosimetry
MLC	Multi-leaf collimator
MOSFET	Metal oxide semiconductor field effect transistor
MU	Monitor unit
MV, kV	Megavoltage, kilovoltage
OAR	Organ at risk
OSL	Optically stimulated luminescence (dosimeter)
RT	Radiation therapy, radiotherapy
SBRT	Stereotactic body radiation therapy
SRS	Stereotactic radiosurgery
TFT	Thin-film-transistor
TLD	Thermoluminescent dosimeter
TMR	Tissue maximum ratio
TPS	Treatment planning system
TX	Treatment
VMAT	Volumetric modulated arc therapy

Chapter One: **Radiation therapy and *in vivo* dosimetry**

Close to half of all Canadians develop cancer during their lifetime, and more than a quarter of Canadians are expected to die from it, making cancer the leading cause of death in the country.¹ Radiation therapy (RT), chemotherapy, and surgery are the three major tools to cure or control cancer. RT today predominantly makes use of a linear accelerator to generate high energy x-rays in what is called external beam RT. The geometry of the RT plan is chosen to most effectively deliver the prescribed dose to the target, while minimizing dose to surrounding healthy tissues. To this aim, multiple beams are directed to the target, each with optimal gantry and collimator angles, energy, and multi-leaf collimator (MLC) settings.

Although the history of modern RT goes back many decades, it is still a developing field; new techniques that allow faster and more precise treatment delivery are still emerging. As is often the case, with every innovation comes also a potential for error.² Thus, alongside developments in therapy, the scientific community also focuses on patient safety. The first part of this chapter gives an overview of the RT process, with a special emphasis on treatment errors which may occur. A summary of recent RT errors is also provided. Motivated by such errors, the second part of this chapter is an overview of methods to measure the dose delivered to the patient (i.e. *in vivo* dosimetry), which is the focus of this research work.

1.1 Radiation therapy and errors

1.1.1 *The radiation therapy process*

Modern external beam RT is a complex process which is comprised of a number of steps that differ for treatment modality and across centres. A simplified workflow which applies to almost all cases is presented in Figure 1-1. After the patient is prescribed radiation, the *treatment preparation* process begins. A computed tomography (CT) dataset is acquired with the patient in a pre-determined position (e.g. prone or supine) and, if prescribed, with use of immobilization devices. This step is referred to as *simulation*, since the patient setup up simulates that which will be used at treatment. Subsequently, contours of the target and possible organs at risk (OARs) are drawn on the patient's CT data. Based on these, and making use of prior knowledge from previous patients, a RT *plan* is created. If required by protocol, the plan will be delivered to a phantom, a step of the quality control known as credentialing. One or more dosimeters placed inside or downstream of the phantom measure dose, which must differ less than a specified tolerance (site- and treatment-dependent) from the planned dose. At *treatment delivery*, the patient is set up on the treatment couch, and the planned fields are delivered. Normally, dose delivered is not measured during delivery. During the treatment cycle and at its end, management and care is provided. For all of these steps, there are a number of variables to be considered (e.g. body changes with time, human judgement in contouring and in patient setup, machine output fluctuations, etc.) and an equal number of errors which may occur. To prevent such errors, thorough quality assurance of the entire workflow is of the utmost importance.³⁻⁶

Radiation Therapy Process

	Operational category	Major actions	Possible errors
	1. Patient Evaluation	ROs evaluate patient history and findings, recommend TX.	
	2. Preparing for Treatment	a. Clinical Treatment Planning TX modality is chosen. Dose to target, energy, fractionation are determined. Toxicities to OARs are considered.	
		b. Therapeutic Simulation Radiographic images acquired in treatment position in CT-sim.	<ul style="list-style-type: none"> •Simulation of TX position inaccurate (S). •Immobilization device failure (S). •Tattoo placement error (S). •CT-sim laser misalignment (S).
		c. Dosimetric Treatment Planning RO contours target and OARs. Dosimetrist produces TX plan.	<ul style="list-style-type: none"> •Contours incorrect (S). •TPS commissioned improperly (S). •TPS used improperly (S).
		d. Pre-TX QA and Plan Verification Independent calculation or measurement of the patient's plan is done.	<ul style="list-style-type: none"> •Machine output miscalibrated (S). •Measurement device miscalibrated or misaligned (S).
	3. Radiation Treatment Delivery <i>(Repeat for number of fractions)</i>	a. Patient setup Patient is set up on TX couch using tattoo markings.	<ul style="list-style-type: none"> •Human error during setup (R). •Patient anatomy changed (S/R). •TX vault laser misalignment (S). •Immobilization device failures (S/R).
		b. Setup is verified by imaging (optional) MV, kV, or CBCT imaging is performed. Image is compared to reference. Couch is shifted if needed.	<ul style="list-style-type: none"> •Imaging system miscalibration (S). •Patient motion after imaging (R). •Mechanical couch shifts inaccurate (S).
		c. Patient is treated with radiation Radiation field is turned on manually. It is shut off automatically when the set number of MUs are counted.	<ul style="list-style-type: none"> •Machine output miscalibrated (S). •Machine mechanics error (e.g. jaws, MLC, filter position) (S). •MU counter defective (S). •Patient plan file corrupt (S/R).
	4. Radiation Treatment Management <i>(Simultaneous to step 3)</i>	Review of portal images, dose delivery parameters, TX setup. Periodic patient visits.	
	5. Follow-up Evaluation and Care	Morbidity from TX is managed. Possible unexpected morbidities are investigated.	

Figure 1-1: Simplified RT workflow with possible errors that would affect delivery (S=systematic, R=random). Operational categories taken from *Safety is no Accident*.⁷

For the purpose of error prevention, the most relevant classification of errors is likely in terms of where along the RT process the error originates. In Figure 1-1 some possible errors at different steps of a patient's flow through the treatment are shown. It is apparent that the majority of errors in the treatment preparation step would result in systematic errors, affecting all fractions, leading to potentially more severe outcomes. On the other hand, errors in the delivery phase are more likely to be random, affecting a single fraction. In conventional fractionation schemes (25-30 fractions) this would minimize the adverse effect. In treatments with fewer fractions, such as SBRT (stereotactic body RT) and SRS (stereotactic radiosurgery), which typically are administered in 1-5 fractions, a random delivery error can produce adverse effects similar to a systematic treatment preparation error.

There is another vital component of the RT process which is not displayed in Figure 1-1: commissioning of the linear accelerator and treatment planning system. Any error in this phase may produce adverse effects on a large number of patients treated. As well, a commissioning error may be more problematic to detect, as it would require a measurement with an independent system

1.1.1.1 Treatment delivery and patient setup

As this work is concerned mainly with treatment delivery (Figure 1-1, step 3), it is worthwhile to provide some detail on setup and delivery. Patient setup, steps 3.a and 3.b in Figure 1-1, is a user-dependent process with measurement uncertainty and a possibility of human error. Typically, the patient lies on the treatment couch in the same position and with the same immobilization devices as at time of the planning CT. Initial positioning of the patient with respect to isocentre is attained by aligning tattoos or markers on the skin with wall-mounted lasers, and then shifting by a preset amount in the three cardinal directions. Depending on the

protocol, the therapists may image the patient with a set of 2D MV or kV images, or with a 3D cone beam CT. Generally, such imaging will detect that the isocentre of the plan is non-coincident with that of the linear accelerator, and another shift is applied to correct for that. Typically, every measurement and shift has millimetre resolution.

Appropriate setup of the patient is crucial, but subject to variability. The patient's body is deformable and subject to day-by-day variations: swelling, gas, weight changes, etc. The setup process involves a series of judgement calls by the therapist, for example whether to repeat imaging or apply shift. Even with a setup procedure performed according to protocol, soft tissues further from the skin markers may be positioned differently on different days. Finally, a human error in either transcription of a shift, tattoo marking, or calibration of lasers or imaging apparatus will result in a systematic setup error, repeated at every fraction. The AAPM's Task Group 58 identified a large number of papers published between 1985 and 1998 and found reports of random and systematic setup errors of up to 6 mm.⁸ In this context, the commonly used term 'setup error' refers to the bony anatomy misalignment between initial and desired patient positioning, as detected by pre-treatment imaging. This differs from the general definition of 'error' adopted in this thesis, which is defined in section 1.1.2.

In conclusion, the setup process has an uncertainty and a probability for error. A widely adopted method to account for these is by expanding the clinical target volume (CTV) artificially of a certain margin to produce a planning target volume (PTV). The initial CTV is determined by the contoured gross tumour volume (GTV) plus a margin to account for microscopic invasion of surrounding tissues. The CTV-to-PTV margins have size based on probabilistic formulas to ensure full target coverage for organ motion and most errors.⁹

1.1.1.2 Adaptive radiotherapy

In 1995 Yan *et al.* defined adaptive radiation therapy (ART) as a process where the treatment plan can be modified using a systematic feedback of measurements.¹⁰ The authors envisioned plan re-optimization through modification of field margins and prescription dose, based on monitoring treatment variations. This action would take place between treatment fractions (i.e. off-line) and particularly early on during treatment. Twenty years later, ART is still a topic of research, but has not found wide implementation in the clinic, due to both clinical and logistic challenges.¹¹

ART may be warranted by a bias in the planning CT, temporal changes in anatomy, or changes in tumour biology (e.g. hypoxia). An example of planning CT bias was quantified by Frank *et al.*¹² who performed CT scans thrice per week on 15 prostate carcinoma patients. Comparing bladder volumes from the planning CT to subsequent CTs showed that in 90% of fractions, the bladder volume is less than at simulation. Frequent imaging like CT and cone beam CT (CBCT) can provide useful information in guiding ART, but the challenge lies in identifying those differences which warrant plan re-optimization. For example, Nijkamp *et al.*¹³ reported on the use of CBCT to guide ART in prostate cancer. The initial plan made use of 10 mm isotropic margins to define the planning target volume starting from the clinical target volume. CBCT scans acquired during the first six fractions were used to create an average prostate clinical target volume and average rectum. Making use of these new structures, a new plan was created with a 7 mm margin, reducing the dose received by the rectum and anal wall.

The main drawback in using CBCT image guidance for ART is the added treatment time, extra dose to the patient, and limited availability of the imaging system. Further in this thesis I

propose the use of a low resource *in vivo* dosimetry which makes use of the treatment beam (i.e. no extra time, dose, or resources) as an effective marker for ART.

1.1.2 Error classifications

1.1.2.1 Definitions

Across publications there is ambiguity over the terminology commonly used in the field of radiotherapy safety.^{6, 7, 14–23} In this thesis, we shall adopt the definitions proposed by the British Institute of Radiology¹⁴ and the World Health Organization^{17, 24} as follows.

- A radiotherapy *error* is an “unintended divergence between a radiotherapy treatment delivered or a radiotherapy process followed and that defined as correct by local protocol.”¹⁴
- Some errors can lead to radiotherapy *incidents*, defined as an “error where the delivery of radiation during a course of radiotherapy is other than that which was intended ... and which therefore could have resulted, or did result, in unnecessary harm to the patient.”¹⁴ This term is almost synonymous to *accident*, with the difference that the latter form is usually used to describe incidents of greater clinical consequence and of an unpredictable nature.
- An *adverse event* is an incident which results in harm to the patient, sometimes further classified into *minor* and *non-minor*.
- Finally, a *near miss* is “A potential radiation incident that was detected and prevented before treatment delivery. However, mistakes in plans, calculations, etc., do not constitute near misses if they were detected and corrected as part of the checking procedure before authorising for clinical use.”¹⁴

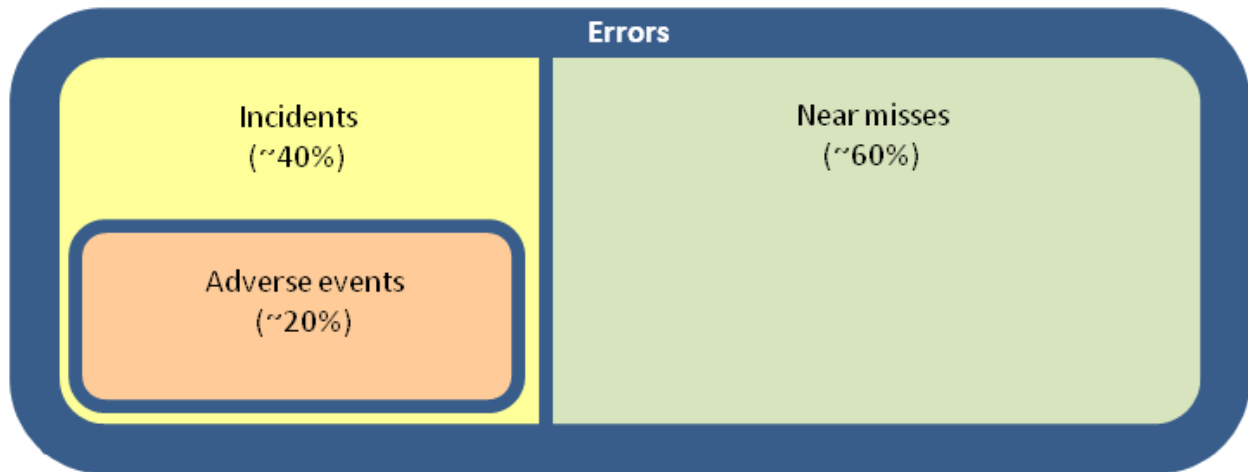


Figure 1-2: An error (divergence between action and protocol) can be either an incident (dose delivered differs from dose planned) or a near miss (potential incident caught before delivery). An incident, in turn, may be classified as an adverse event if harm results to the patient. The percentage estimates are based on multiple publications.^{17, 22, 25, 26}

1.1.2.2 Classification by severity

In 1993 the American Association of Physicists in Medicine Task Group 35 proposed some definitions to quantify the risk associated with RT errors.²⁷ The Task Group lamented the vagueness of the existing FDA classification of hazards: Class I (risk of death or serious injury is high) and Class II (risk is small). To fill this gap, it proposed to separate Class I hazards into two types based on the severity of their consequence to patients. *Type A hazards* can likely be directly responsible for life-threatening complications to the patient. The most immediate example would be an overdose of 25% or more of the prescribed dose. The threshold was set at 25% in consideration that for many treatments such an overdose would place the patient in the LD50/5 dose range, that is 50% probability of lethal complications in the following five years. This type of event can be caused by incorrect calibration of the linear accelerator (either of its output or of its beam-shaping mechanics) or by incorrect plan files. Other examples of type A

hazards are treatment-level doses delivered outside the target, or incorrect beam energy or modality. *Type B hazards* are defined as “errors that increase the probability of unacceptable outcome (complication or lack of tumour control), but usually do not pose a [direct] threat to life”. These may have the same cause as a type A error, but will be smaller in magnitude or in duration, for example an overdose >5% and <25%. An example specific to type B would be underdosage, in which the probability of tumour control is compromised, but no direct damage results from it.

The challenge with classification by severity resides in the placement of boundaries within adverse effects. Huang *et al.* for instance, classified the errors they tracked as having the following degrees of harm, by judgement of the radiation oncologist: none, minor, moderate, severe.²² The Ottawa Hospital incident learning system, on the other hand, classifies errors as: minor, serious, major, critical.²⁶ At least two publications made use of a more standardized severity assessment score developed outside the context of radiation oncology.^{17, 25} It is apparent that classification by severity is marginally useful in error management, since the same type of error can have very different adverse effects based on its magnitude or repetition. On the other hand, it is useful as a comparison tool against other areas of potential harm to the public, as illustrated in the section below.

1.1.3 Documented errors in RT

In the past few years, there has been a decisive push, by many governments,^{14, 28, 29} the public,^{18, 19, 21} and the scientific community⁷ to document RT delivery errors. As a result, a number of publications have been released^{17, 20, 22, 28, 30–36} and there are web-based tools to report

errors such as SAFRON (Safety in Radiation Oncology) developed by the IAEA, and ROSIS (Radiation Oncology Safety Information System) supported by the ESTRO.³⁷

1.1.3.1 Lethal and critical errors

Table 1-1 summarizes the eight incidents which have been reported in the last 11 years, which allegedly caused the death of patients, either directly or indirectly. In the case of the two New York City incidents, details were released to the public after five years²¹ suggesting there may other, more recent, incidents of which details are not released at the time of writing. To add perspective, the number of fatalities is very small with respect to the number of treatments which are about 10^5 per year in Canada alone.¹ As well, the rate of lethal errors has decreased compared to the 1980's and 1990's.²⁰ To further support this statement, a comprehensive report by the World Health Organization stated that of the 3125 patients that suffered adverse events from RT in 1976-2007, 38 died as a result of radiation toxicity.^{17, 25} Although the numbers are too small to allow conclusive statements, one may extrapolate that the approximate fatalities/year dropped from 1.3 to 0.7, while the number of patients treated increased (the number of cancer diagnoses increased by 20% over the last ten years^{38, 39}). Nonetheless, arguably all these incidents were preventable or at least detectable earlier in time, supporting the need for improved error detection.

Table 1-1: Radiation therapy delivery errors which have allegedly caused death of patients, directly or indirectly.

Year	Body site	Location	Num. affected	Num. deaths	Patient or machine error?	Random or systematic error?	Step in RT process	Description
2009	Brain	Evanston, IL, USA	3	2	Machine	Systematic	Delivery	Communication error at treatment caused field wider than SRS cone.
2008	Lung	Hawaii, HI, USA	1	1	Machine	Systematic	Planning	Incorrect manual input of MU after fields split.
2006	Brain	Glasgow, UK	1	1	Machine	Systematic	Planning	Incorrect manual input of MU after TPS upgrade.
2005	Head & neck	New York, USA	1	1	Machine	Systematic	Delivery	MLC parked open due to corrupt data transfer.
2005	Breast	New York, USA	1	1	Machine	Systematic	Planning	Missing wedge in beam in patient plan.
2005	Prostate	Epinal, France	23	1-5*	Machine	Systematic	Planning	After upgrade from static to dynamic wedges, wrong wedge factor.
2004	Brain	N/A, France	1	1	Machine	Systematic	Delivery	Field too wide, leaked outside SRS cone.

*Differing reports.

Returning to the concept of class I errors, we may now compare RT risks against that of other activities. Summarizing the literature review presented above, the risk of a class I error (causing death or very severe injury) in RT is of the order of 10^{-6} . Conversely, the class I hazard in flight industry, a comparison used by the American Association of Physicists in Medicine, is of the order of 10^{-6} - 10^{-8} per hour of flight.²⁷ Unlike the airline passenger, the patient likely has a life threatening disease, so a higher hazard may be acceptable to achieve the benefit of cure or control. A more fair comparison would be against risk levels for surgery, general anaesthesia, and drugs where the hazard is of the order of 10^{-4} - 10^{-6} per procedure.²⁷ Class I hazard in RT is typically smaller than these other medical interventions.

1.1.3.2 Discrepancies due to setup and anatomical variability

A separate category of differences between planned and delivered dose are those due to anatomical and setup variability. As to some degree these differences are expected, they do not fit the definition of ‘errors’ adopted in this thesis. Intuitively, a difference in dose delivery due to setup or anatomical change may be considered an error if it is greater than a certain tolerance, but establishing such tolerances is arduous.

As mentioned in the previous section, the setup process of alignment of treatment setup images (acquired immediately before radiation delivery) to simulator images (typically acquired weeks prior) is subject to uncertainty. First, the bony anatomy and the patient’s soft tissues are both prone to variability. An example of the former are small differences in patient position on the couch which do not allow perfect bony match with the simulation images. Soft tissue variations include changes size and shape of bowel gas, internal organs, fat, and the tumour itself. In addition, for all image matches, there is the user’s (i.e. therapist) subjective evaluation of the shift that would produce the best match between images.

Pre-treatment CBCT is a powerful tool to quantify anatomical variations, but determining dosimetric variations from imaging alone is usually not possible. Recently, Rozendaal *et al.*⁴⁰ quantified the dosimetric effect of anatomical changes in 633 fractions for 20 head and neck cancer patients by recalculating the treatment planning dose on daily CBCT data. The maximum change in tumour volume over all fractions ranged between 1% and 11%, across patients (mean: 6%). Yet, the largest changes in D2, D50, and D98 of the planning target volume^a were only of

^a D2 is defined¹⁸⁶ as the dose value on the dose-volume histogram above which lies 2% of the contoured volume. D2 is the near-maximum dose, D50 the median dose, and D98 the near-minimum dose.

approximately 1%. Thus, to detect significant dose delivery differences, imaging alone is not sufficient, but a dosimetry method is needed.

Another method to detect anatomical and setup variability which will be described in detail in the following sections is *in vivo* dosimetry, i.e. the measurement of dose during delivery to the patient. An example is the work by Cilla *et al.*⁴¹ who performed *in vivo* dosimetry in the isocentre plane on 50 IMRT fields for 10 pelvic cancer patients. They found that 13-14% of tested fractions displayed significant^b differences attributed to anatomical changes and setup variations. Replanning was carried out with new CT scans in two cases (one had unacceptable gas, the other had weight loss between first CT and treatment). This thesis focuses on the potential of *in vivo* dosimetry for error detection and quantification of delivery variability.

1.1.3.3 General error analysis

A number of publications are available that describe the total error rates in radiotherapy. Huang *et al.*²² published an account of all delivery errors documented in Canada's largest cancer hospital, the Princess Margaret Cancer Center. The error rate depended largely on disease site and ranged between 0.35%-5.54% per patient. Summing all sites together, one finds a total of 555 errors for 27,907 patients, or an error rate of 2.0%. These errors were also classified per severity of consequence to the patient: none (44.1%), minor (50.3%), moderate (5.2%), severe (0.4%). In summary, 2% of patient treatments had an error and over 5% of these (or 0.1% of the total) suffered moderate to severe complications as a result of the error.

Derreumax *et al.*²⁸ published an analysis of the clinically significant RT errors in France, which affected a total of 881 patients between 1987 and 2007. In the same year, the French

^b In this context, 'significant' changes meant that less than 90% of points passed a 5% / 3mm gamma evaluation of the two portal images being compared

government passed a legal directive requiring hospitals to use *in vivo* methods to verify dose delivery.²⁸ Two more recent publications found error rates per fraction of 0.06%⁴² and 0.09%⁴³. In the approximation of an average of 25 fractions per patient, these correspond to rates of 1.5% and 2.3%, in close agreement to the Canadian 2% figure cited above.

Further insight is provided by a study of all RT errors which occurred at the Ottawa Hospital.²⁶ Over the years 2007-2011 a total of 345,792 individual treatments were delivered and 2506 errors were reported, yielding an error rate of 0.7%.^c Furthermore, errors and incidents were classified in four categories: treatment preparation, treatment delivery, prescription, booking. The dominant source of total errors was treatment preparation, but the majority of incidents and adverse events took place in treatment, (Figure 1-3). This is a noticeable difference compared to recorded errors from the mid-1970's to the mid-2000's, in which most adverse events originated from treatment planning.¹⁷

In agreement with this recent trend is a report on RT errors in New York State.³³ The authors counted 244 non-minor adverse events in the years 2001-2009, for an event rate per patient of 0.07%, in close agreement with the 0.1% reported by Huang *et al.*²² Furthermore, the events were categorized based on the staff involved: radiation oncologists (10% of total errors), physicists and dosimetrists (22%), and therapists (68%).

^c This error rate is per treatment volume. A number of patients are treated in more than one volume, accounting at least in part for this error rate to be smaller than the ones reported previously.

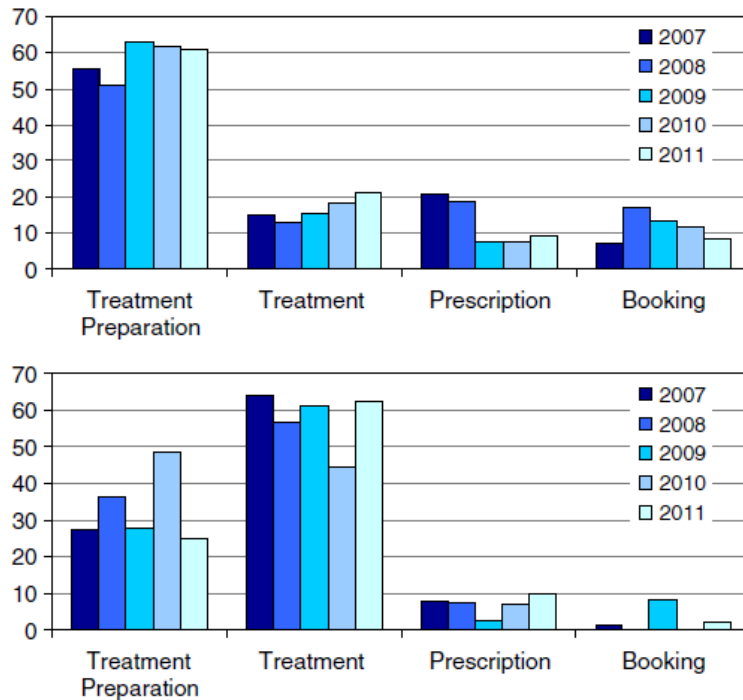


Figure 1-3: Percentage of total errors (top) and incidents (bottom) reported at the Ottawa Hospital in 2007-2011, divided into four operational categories. The majority of errors take place in treatment preparation, but the majority of those that lead to patient harm occur in treatment delivery. Reprinted from Clark *et al.*²⁶ with permission by Elsevier.

1.1.3.4 Summary

From the literature search outlined above, the following conclusions may be drawn.

- The probability of an error during radiation therapy is of the order of 2%.
- The probability of a non-minor adverse event is of the order of 0.1%.
- The probability of a lethal or critical error during radiation therapy is of the order of 10^{-6} .
- The majority of total errors arise during the treatment preparation stage.
- The majority of non-minor adverse events arise during the treatment delivery stage.

Further case-by-case analysis of the adverse events suggests that a dose monitoring system during treatment would have been effective in minimizing patient harm.^{20, 28, 36, 44} This is a strong motivation to develop routine *in vivo* dosimetry, *i.e.* the goal of this research project.

1.2 Methods for *in vivo* dosimetry

In vivo dosimetry (IVD) refers to the measurement and monitoring of dose delivered to a patient to ensure that the treatment is carried out as planned. This measurement takes place during treatment (i.e. it differs from a calculated or predicted dose). According to the most recent review paper on IVD in external beam radiotherapy, IVD has been used extensively in specific applications of RT, but in few centres in the world it is routine for the majority of treatments.²⁹ This is because although multiple bodies have recommended^{3, 14, 45} and even mandated²⁸ its use, the practical challenges described below have limited its application. In this section, an overview of the most common methods for IVD are presented, with the exception of the Electronic Portal Imaging Device, which is the topic of Chapter 2.

1.2.1 Thermoluminescent and optically stimulated luminescent dosimeters

Two types of dosimeters commonly used in the clinic are thermoluminescent dosimeters (TLDs) and optically stimulated luminescent dosimeters (OSLs).⁴⁶⁻⁴⁸ These are *integrating dosimeters*, meaning the effect of radiation exposure accumulates and is read out at a later time. This makes them of practical use in the clinic, where they can be placed on a patient prior to treatment, or may be worn by staff in the context of radiation protection (the full dosimeter is typically smaller than 1 cm²).

Phosphorescence is a phenomenon displayed by numerous crystalline materials. As the crystal is irradiated, a small fraction of the energy is absorbed by the crystal lattice, causing electrons to be excited to a higher energy state. Some of these enter a metastable electron ‘trap’, characteristic of the crystalline lattice. In phosphorescent materials, return to ground state is only possible by the addition of energy. In materials that exhibit *thermoluminescence* (the most

widely used being Lithium Fluoride) the probability of de-excitation is greatly increased by adding heat. In other materials, energy may be provided by selective absorption of radiation of specific wavelengths, a phenomenon known as *optically stimulated luminescence*. In both cases, as the electron returns to ground state, energy is emitted in the form of visible light. The emission wavelength depends on the energy gap between ground state and the particular trap. A fraction of these photons enter a photomultiplier tube, producing a current proportional to the number of incident photons. The plot of the thermoluminescence signal as a function of temperature is a *glow curve*. Similarly, an *OSL curve* is a plot of luminescence as a function of time of optical excitation. In both cases, the area under the curve is proportional to the radiation dose absorbed.

In the clinic, TLDs and OSLs provide valuable information on patient dose, but also have a number of disadvantages which hinders their use for *in vivo* monitoring of the majority of treatment fractions. Their use is very labour intensive, as they require manual placement on the patient and subsequent manual readout and annealing. The readout process in general is not immediate; especially in the case of TLDs, to have a stable signal the readout must be performed hours after irradiation. The centre must also purchase a complete readout system, in addition to the single dosimeters. Dose can be measured only in the point where the dosimeter was placed, providing no information on the remainder of the field. For these reasons, their use is generally limited to special cases, such as monitoring dose to a pacemaker or a particularly sensitive organ.

1.2.2 Diodes and MOSFETs

Of approximately the same size or smaller than TLDs and OSLs, diodes and MOSFETS have been used successfully as *in vivo* dosimeters.^{45, 49-51} A Silicon semiconductor diode

dosimeter, or diode, is an asymmetrical p-n junction, as illustrated in Figure 1-4. A single Silicon crystal is doped with an electron donor (e.g. Phosphorus) on one side (n-type Si), and with an electron acceptor (e.g. Boron) on the other (p-type Si). P-type diodes have predominant p-type doping, so the majority of charge carriers are holes; the opposite is true for n-type diodes, with electrons as majority carriers. Diffusion of charges across the junction creates a thin region with no charge carriers known as the depletion layer. Across the depletion layer, a potential difference of little under 1 V exists at equilibrium.⁵² Radiation creates electron-hole pairs in the diode, which migrate subject to the electric field and cause a current, proportional to the dose absorbed by the diode itself. Due to its high density and small 1.1 eV energy gap between valence and conductive bands, the sensitivity (charge collected per unit of dose to the diode) of a Silicon diode is about 18,000 times that of an ion chamber.⁴⁵

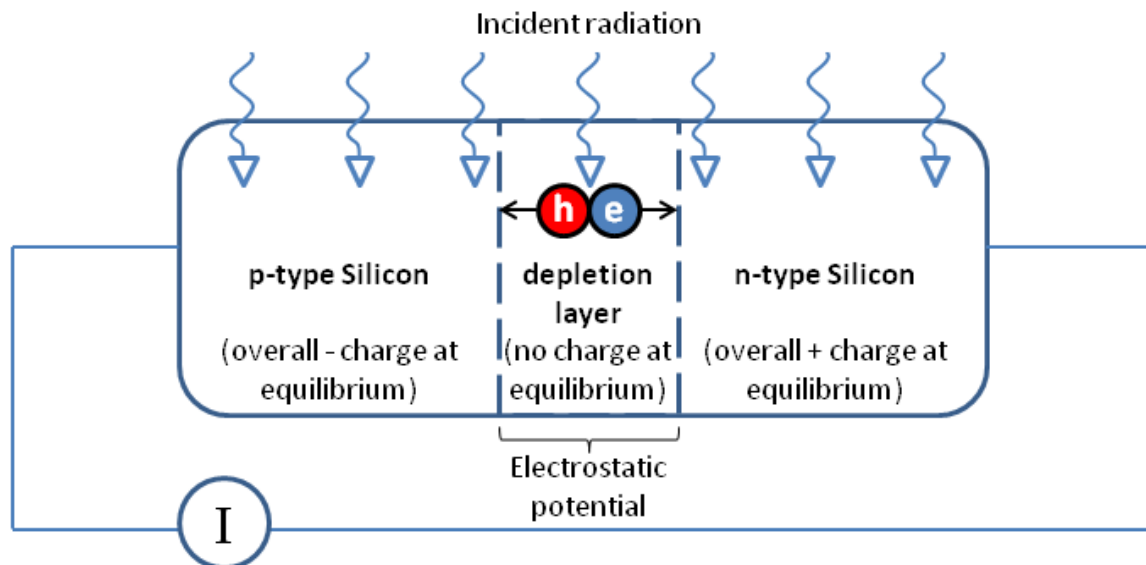


Figure 1-4: Schematic of a diode dosimeter. Any hole (h) – electron (e) pair produced by radiation inside or in proximity of the depletion layer will migrate due to electrostatic potential. This will cause a current in the circuit, proportional to the dose.

A more recent development for IVD is the MOSFET (metal oxide semiconductor field effect transistor). Originally developed for other applications, the MOSFET is a very small (200 microns) transistor which requires a threshold voltage for switching. This threshold voltage is a linear function of absorbed dose, since radiation generates charges which remain permanently trapped and alter electrical conductivity. The change in threshold voltage can be measured on-line, with a connecting cable, in similar fashion to a diode, or post-irradiation, in the same way a TLD is used.

Diodes and MOSFETs are of practical use in special situations in the clinic, but are not ideal candidates for routine IVD. Although they can be read out in real time, like TLDs and OSLs they require additional staff time to apply, and provide point dose information on the surface of the patient only. In addition, most diodes exhibit large directional dependence, so diode setup would have to be adjusted manually for every different gantry angle of the treatment, or need introduction of correction factors.

1.2.3 Film

The use of radiographic film in radiation dosimetry goes back to the 1950s⁵³ and is still clinically relevant today, especially in Intensity Modulated Radiotherapy.⁵⁴ The immediate advantage of film with respect to the IVD methods above, is that it provides 2D, rather than single point, dose information. A detailed explanation of film dosimetry can be found in textbooks (e.g. Mayles *et al.*⁵⁵, chapter 17.2). In brief, film contains a gelatin emulsion that suspends silver halide crystals that are sensitive to radiation. A latent image is recorded by generation of free electrons, inside the film's 'grain' (0.1 μm to 3 μm in diameter), proportionally to dose. These electrons interact with the crystals producing 'specks' of negative

charge which attract the silver ions. The film processing step renders the latent image visible by supplying electrons which enter the grain and darken the silver ions. As a result, regions irradiated by a larger dose become more opaque, i.e. have increased optical density. Each combination of film type, energy, and angle of incidence will be characterized by its own calibration curve of optical density versus dose.

Historically, films have been used *in vivo* in two methods: localization and verification.⁵⁶ *Localization films* provide images using a small amount of radiation (4-6 MU, MV energy) and are irradiated and developed prior to beam on, to verify appropriate portal geometry and patient setup. A limitation of this procedure is that by the time the film has been developed, the patient on the treatment couch may have moved. *Verification films* have lower sensitivity and in fact make an image using the entire treatment beam. Their use is again to verify the treatment geometry and setup, and if necessary provide guidance for the following treatment fraction.

As in the case of TLDs, radiographic film has the disadvantage of requiring handling at setup and for processing. A more recent development which eliminates the need for processing is radiochromic (or Gafchromic) film, which exhibits colour change immediately following exposure to radiation.⁵⁷ Nonetheless, any film must be set up with the patient and scanned after treatment, rendering film impractical for routine use *in vivo*.

1.2.4 Head-mounted devices

A new category of IVD products that install onto the head of the linear accelerator has been commercialized in the last few years. Currently, three products are available: *Delta4 Discover* by ScandiDos (Uppsala, Sweden), *Dolphin* by IBA (Schwarzenbruck, Germany), *IQM* by iRT (Koblenz, Germany). All three of these solutions are transmission detectors, i.e. they are

mounted upstream of the patient, in the same way as the MU counter internal to the linear accelerator (Figure 1-5).

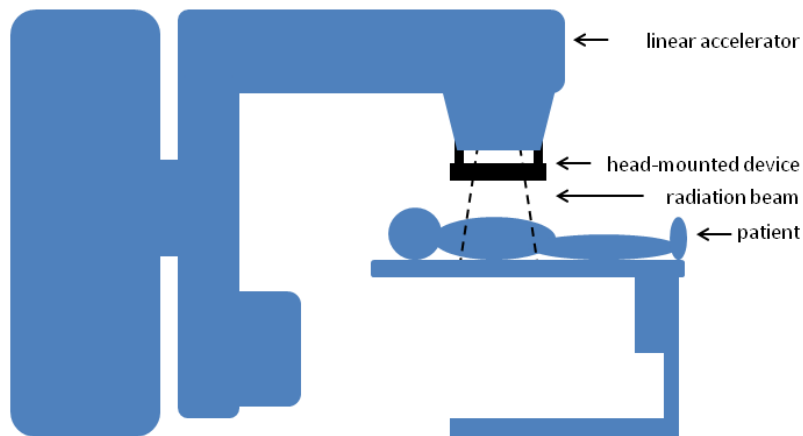


Figure 1-5: Head-mounted devices are of practical clinical use, as they require no staff intervention. On the other hand, they attenuate the beam and provide no information at the level of the patient.

The Delta4 Discover consists in an array of 4040 diodes, attenuates the beam by ~1%, and over consecutive readings demonstrates a SD of 0.1% of the mean signal, as reported by the company.^d The Dolphin consists in 1513 ion chambers, which generally are more stable and require fewer corrections than diodes.⁵⁸ The two systems provide ample spatial resolution to verify correct beam shape. The IQM (Integral Quality Monitor), on the other hand, consists in a single, large (26.5 x 26.5 cm²) asymmetrical ion chamber with a gradient in the direction of MLC motion.⁵⁹ Its output is not an array of measurements, rather a single time-resolved signal integrated over the entire chamber's sensitive volume. This characteristic limits its use to an

^d “Initial clinical evaluation of a ScandiDos transmission detector” presentation by A. Gutierrez at the 2014 American Society for Radiation Oncology ASM. Available at <http://www.scandidos.com/home/solutions/at-treatment-qa/discover-presentations>.

inter-fractional reproducibility test. Repeated measurements had SD of 1% of mean signal,⁶⁰ while attenuation is of the order of 5%.⁶¹

Head mounted devices are very convenient for routine IVD: battery powered, wireless data transfer, and designed to be left on the gantry for all treatments. They are able to detect gantry-related deviations in delivery such as: total output (including MU), portal shape, beam modulation (e.g. dynamic wedges and MLC motion), and possibly gantry/collimator angles (making use of an internal inclinometer). On the other hand, they are completely insensitive to errors at the level of the patient (i.e. couch placement, patient setup, motion, and anatomy), and are generally very expensive (~100,000 USD).

1.2.5 Summary

The methods for IVD outlined above have each their advantages and limitations. For the majority of these, corrections are required for energy, setup geometry, angle of incidence, dose rate, temperature. Table 1-2 summarizes some of the characteristics of the IVD methods outlined above. The choice will depend on, among other factors, treatment modality, fractionation, body site, and financial and personnel resources. For example, TLDs are suited for additional dose measurements in proximity of critical structures or equipment (i.e. pacemaker). Diodes are the gold standard for real-time measurements in total body irradiation.⁴⁵ Newly introduced head-mounted device are excellent for routine IVD of the linear accelerator for centres with financial resources. Thus said, if the goal is a convenient, low-resource intensive system for routine IVD, sensitive to both machine and patient errors, the best option will in most cases be the EPID (Electronic Portal Imaging Device).

In this work, we propose a novel method to use the EPID for routine IVD for most treatments.

Table 1-2: Some relevant characteristics of the most widely used *in vivo* dosimetry systems.

	TLD, OSL	MOSFET, Diode	Film	Head-mounted devices	EPID
2D	No	No	Yes	Yes	Yes
Sensitive to patient errors	Yes (depends on placement)	Yes (depends on placement)	Yes (depends on placement)	No	Yes
Capital cost	High	Medium	Medium	High	Low*
Operational cost	High	High	High	Low	Low
Real-time	No	Yes	No	Yes	Yes
Typical accuracy	~5%	~5%	~5%	~1%	~5%

Green: desirable, red: less desirable.

*Although its cost is not low, the EPID has been a standard feature for the majority of linear accelerators since the 1990's, and thus is readily available in the great majority of treatment vaults.

Chapter Two: **The electronic portal imaging device and its use**

Portal imaging, which refers to imaging of the treatment beam (which emanates from the *portal*, or beam-shaping opening, of a radiotherapy apparatus) has played a major role for four decades.⁶² In 1976, Marks *et al.* showed a link between frequency of imaging and reduced localization errors. As the number of verification films per course increased from 9 to 24, localization and field design error dropped from 36% to 15%.⁶³ Film began to be increasingly used to verify the placement of the treatment portal with respect to the patient's body. On the other hand, film exposure and development are time-consuming, and subsequent analysis of non-digital information is tedious and thus unlikely to attain widespread use in the clinic.⁶⁴ Approximately fifteen years later, the replacement of film with Electronic Portal Imaging Devices (EPIDs) started to become available.⁶⁵ The EPID is mounted on the gantry, downstream of the isocentre, making it suited for *transit imaging*, i.e. acquiring images of the treatment beam through the patient, in the same way film is commonly used. The EPID image is still today made to appear as a film: it is inverted such that regions of higher dose appear darker.

2.1 EPID components and operation

The current generation of EPIDs are indirect detection active matrix flat panel imagers, known also as amorphous Silicon (a-Si) EPIDs. The imager itself consists in a pixelated array of a-Si light sensitive elements, each connected to a thin-film-transistor (TFT) switching element, mounted on a glass substrate. Upstream are a Terbium-doped Gadolinium oxysulfide ($Gd_2O_2S:Tb$) scintillator and a copper plate (Figure 2-1). The imager is sandwiched in low

density plastic, connected to controlling electronics, and mounted on the linear accelerator via a robotic arm.

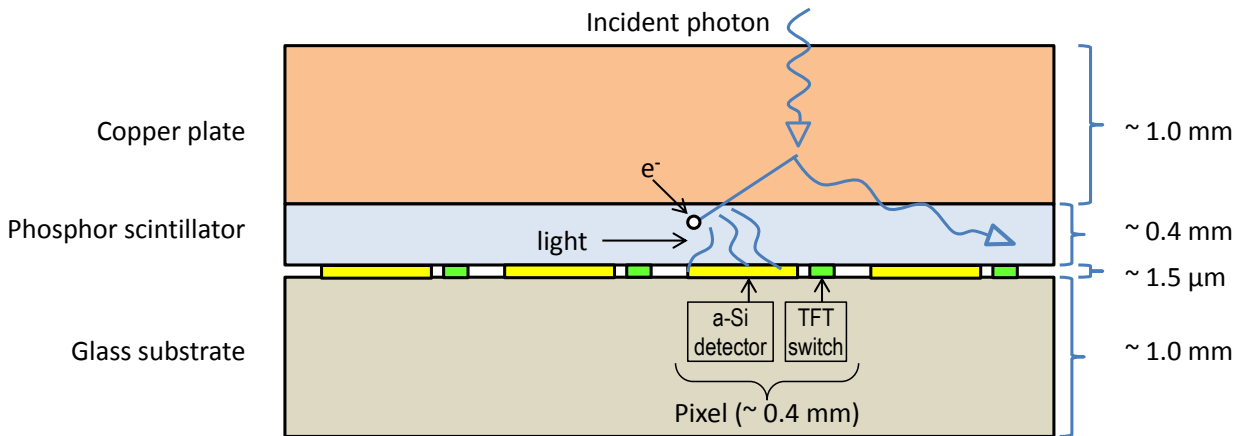


Figure 2-1: Schematic cross-section of four pixels of an EPID imager. Incident radiation sets electrons in motion in the Cu. These in turn may enter and interact with the scintillator, which produces optical photons. The light-sensitive detectors accumulate a charge which is read out when the TFT switch is activated. (Scale is approximate and based on the Varian aS500/aS1000).

The copper plate serves a double function. In Cu, in the 0.2 MeV to 10 MeV range the Compton effect is dominant,⁶⁶ so the plate increases the signal by providing Compton x-rays and electrons that reach the scintillator. At the same time, the Cu shields from some low-energy scattered photons and electrons which would deteriorate image quality. The incoming electrons in the phosphor produce a shower of optical photons. A single x-ray interaction can produce thousands of optical photons.⁶⁷ Many of these photons reach the a-Si detector, producing a large signal.⁶⁸ The term *indirect detection* used to describe this system refers to the presence of this intermediate step: it is not the primary radiation that is detected, rather, secondary particles produced in the scintillator. During this multi-step process, the particles that eventually generate

signal migrate laterally, causing a signal spread known as *glare*. This was modelled by McCurdy *et al.*⁶⁹ with a symmetrical double-exponential kernel that drops to ~1% at a radius of 1mm.

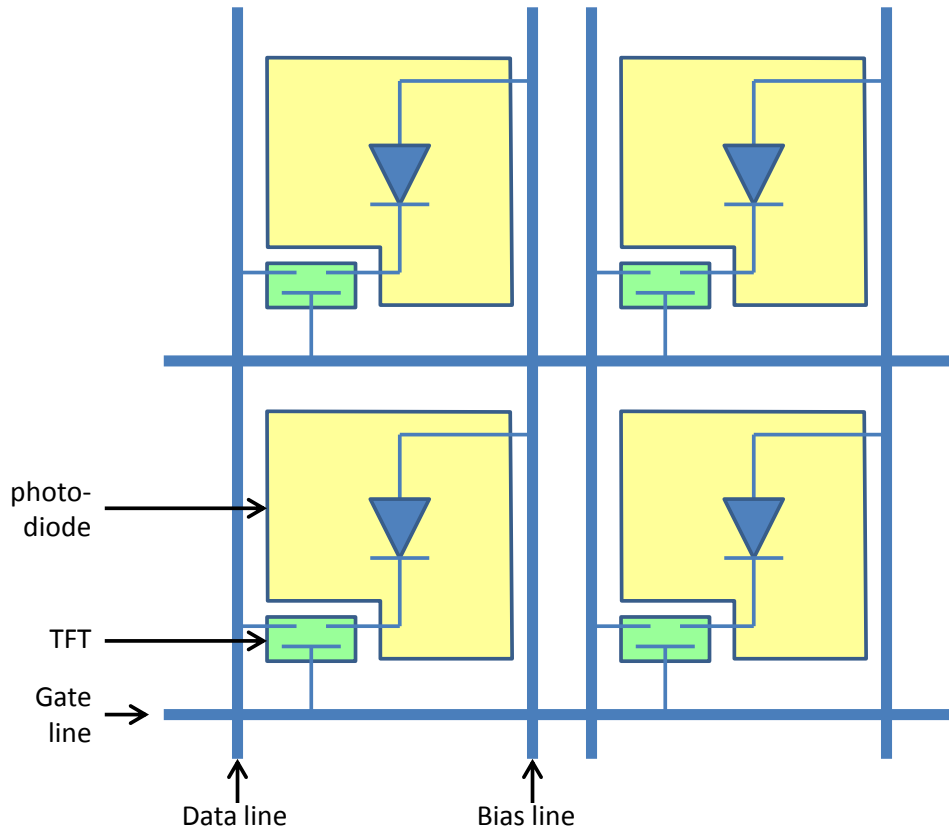


Figure 2-2: A 2×2 section of the pixel array. The photodiode acts like a capacitor and integrates charge. When the appropriate voltage is applied to a gate line, all connected TFT switches become transparent and the charge is read out via the data lines.

An EPID pixel consists in a hydrogenated amorphous Silicon photodiode which liberates electrons via the photovoltaic effect, and a TFT switch used in reading the charge (Figure 2-2). Each pixel's charge is read out in an active fashion (*active matrix*). Voltage applied to the gate line determines whether the switch is conductive or not. When the switch is open (not conductive), the photodiode acts like a capacitor. Initially, it is charged by means of a bias voltage. The incoming photons create electron-hole pairs which migrate to the opposite contacts

and gradually discharge it.⁷⁰ To acquire an image, the gate driver electronics enable the first row, opening all the TFT switches connected to it. All the charge readings are collected along the data lines, and each line is connected to its own amplifier. The process is repeated for all rows.

Commercially available imaging panels are typically 40×30 cm² or 40×40 cm² with resolutions ranging from 512×384 to 1024×1024 pixels. The data coming from a single scan of all rows is called a *frame*. In integrated mode, all frames are averaged into an *image*. In continuous acquisition or *cine* mode, the user can choose the number of frames to be averaged into each *cine image*, or simply *cine*.

2.1.1 Correction Images

The signal from each EPID pixel i,j must be corrected for offset and gain. Offset is caused by electronic noise which produces a dark current, i.e. a collection of charge when no radiation is present. This is achieved by recording an image with the beam off, that is, a dark field (DF). Gain is caused by the fact that each photodiode has, in general, a different sensitivity. To account for this, a ‘weight’ is given to each pixel based on its response to the identical dose. This is achieved by means of a flood field (FF) image which irradiates the whole panel at once. The corrected signal is calculated automatically by the EPID as follows, where $\langle \dots \rangle$ denotes an average over all the pixels.

$$S_{i,j}^{corr} = \frac{S_{i,j}^{raw} - DF_{i,j}}{FF_{i,j} - DF_{i,j}} \langle FF_{i,j} - DF_{i,j} \rangle \quad \text{Equation 1}$$

The gain correction presupposes that the FF delivers approximately the same dose to all pixels. In practice, FF images are taken with an unperturbed (‘open’) beam because it is less resource intensive and of equal value for patient setup purposes. As a result, FF images are

characterized by ‘horns’ produced by the flattening filter (Figure 2-3, top). When these are used to correct future images in the denominator of Equation 1 the result is an image with inverted horn effect. For quantitative imaging, the best FF correction image would be that taken through the same thickness which one wants to image, although this is not feasible in clinical practice.

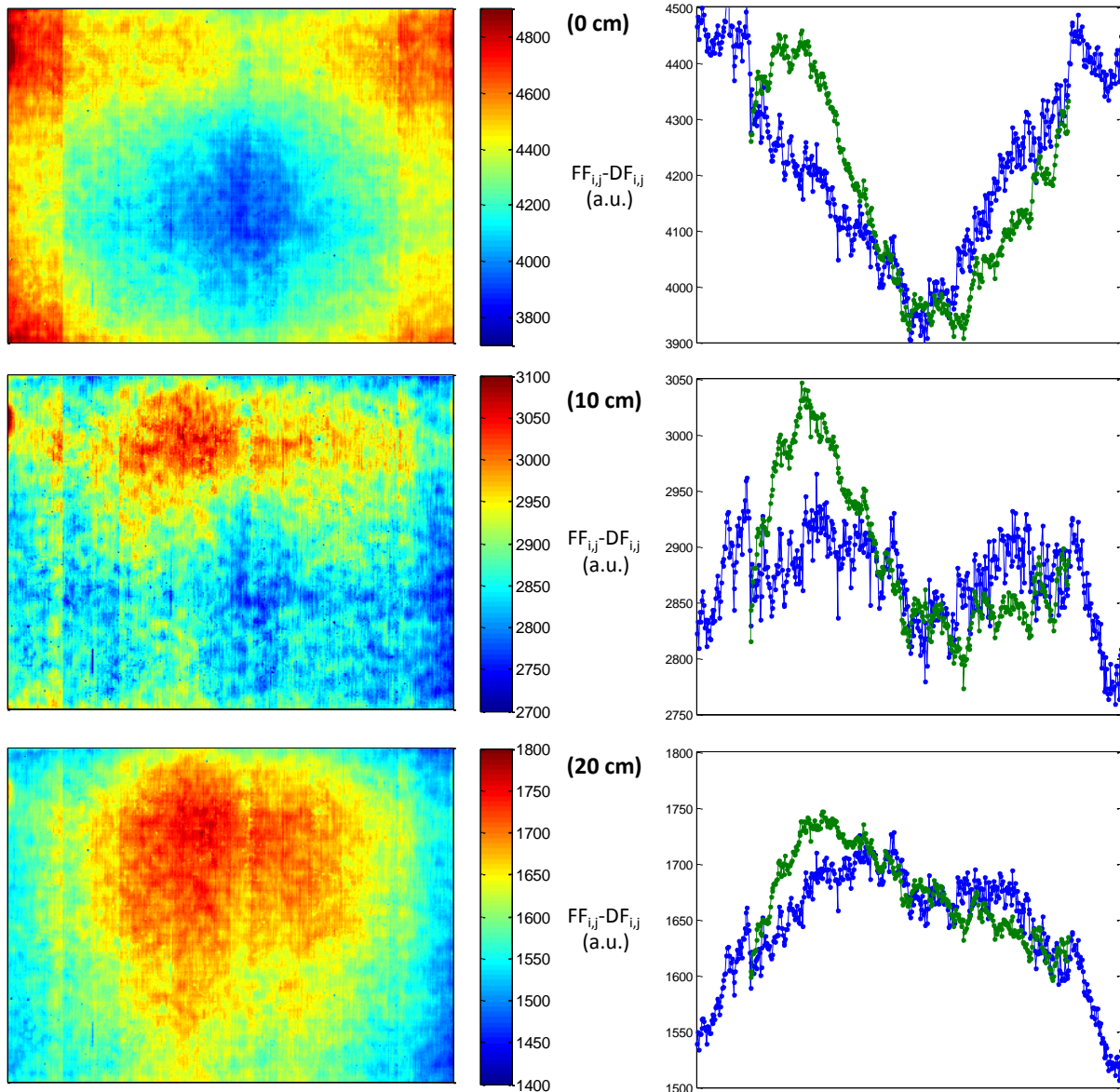


Figure 2-3: Flood field correction images (left) and central profiles (right; blue=cross-plane, green=in-plane) taken through a solid water slab phantom with thickness 0, 10, 20 cm. For an unperturbed beam, intensity increases off axis due to the combined effect of

the beam's 'horns' and the increased EPID sensitivity to lower energy photons.^{71, 72}

Increasing depth reverses the horn effect. (Note: wider scale for 0 cm).

In addition, the EPID tends to over-respond for lower energy photons due to increased photoelectric effect in the Gadolinium contained in the scintillator⁷² (see Figure 2-4 and further detail in section 2.1.2.1). Larger fields produce increased lower energy scatter, so that any clinical field smaller than the 30×40 cm² FF, has fewer lower energy photons, in proportion, than the FF. As a result, an offset is expected, dependent on field size.^{73, 74}

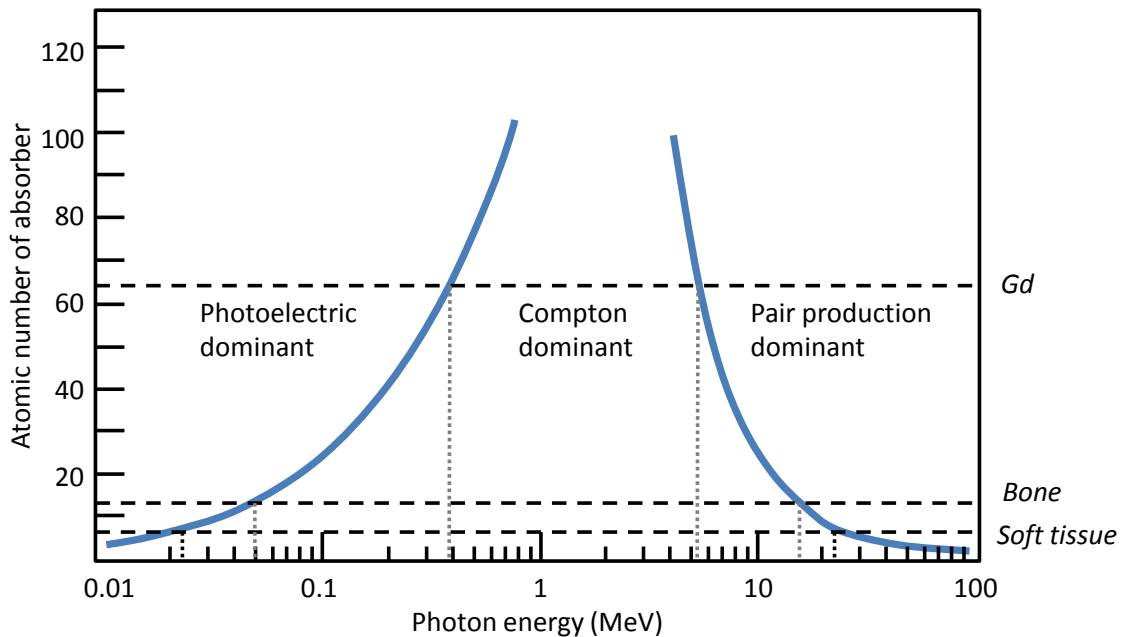


Figure 2-4: Relative probability of photon interaction modalities in matter. The curves represent equal probability of two neighbouring effects. Adapted from Attix⁶⁶ with data from Evans *et al.*⁷⁵

2.1.2 Limitations of MV imaging

An intrinsic challenge on EPIDs is due to the fact that portal imaging necessarily takes place with a megavoltage (MV) radiation source that is optimized for treating patients, not producing images. Conversely, diagnostic imaging is optimized to produce high quality images by means of a kilovoltage (kV) source. This constraint gives rise to: low contrast (discussed in 2.1.2.1), low spatial resolution (discussed in 2.1.2.2), low signal and the presence of artifacts (discussed in 2.1.2.3).

2.1.2.1 Contrast

An important characteristic of imaging is contrast, which is the ability to detect small objects of different composition, such as the presence of bone inside tissue. Imaging by MV treatment energies does not easily distinguish differences in atomic number (Z) and thus has lower contrast than kV imaging. An example of detection of 1 cm of bone inside tissue is presented below. Although more detailed descriptions of contrast have been developed, this simple calculation is in good agreement with more thorough calculations.⁸

Photon transport in matter is well described by the model in which a photon crossing a medium can, at any given time, undergo one of three main interactions: photoelectric effect, Compton scattering, pair production. The relative probability of each interaction is determined by, among other factors, the photon's energy and the atomic number of the medium. Referring again to Figure 2-4 it is evident that, for tissue, at kV energies the photoelectric effect is most probable, while at MV energies the Compton scattering is dominant. Now, the probability of photoelectric effect (τ) per unit mass (normalized by density ρ) is largely dependent on atomic number, as expressed by Attix,⁶⁶

$$\frac{\tau}{\rho} \cong \left(\frac{Z}{h\nu}\right)^3 \quad \text{Equation 2}$$

where Z is the atomic number and $h\nu$ is the incoming photon energy. The effective atomic number (Z_{eff}) is noticeably different for soft tissue and bone (approximately 7 and 14 respectively^{55, 76}). Assuming that a photon that interacts does not reach the imager (i.e. neglecting scatter), radiation intensity downstream of the attenuator (I) is inversely proportional to the probability of interaction (τ for photoelectric, σ for Compton). Therefore the ratio of intensity downstream of tissue (I_1) to that downstream of an equal thickness of bone (I_2) is then (with density values ρ_{bone} and ρ_{water} from Mayles *et al.*⁵⁵)

$$\left(\frac{I_1}{I_2}\right)_{kV} \approx \left(\frac{Z_{bone}}{Z_{tissue}}\right)^3 \frac{\rho_{bone}}{\rho_{water}} \cong \left(\frac{14}{7}\right)^3 \frac{1.5}{1} = 12. \quad \text{Equation 3}$$

On the other hand, Compton scattering has a probability of occurrence which is almost independent on Z ,

$$\frac{\sigma}{\rho} = \frac{N_A Z}{A} \sigma_e \quad \text{Equation 4}$$

where N_A is Avogadro's constant, A is number of grams per mole, and σ_e is the cross-section per electron. With the exception of Hydrogen, Z/A ranges between 0.4 and 0.5, and σ_e has no dependence on Z since the scattering electron has been assumed to have zero binding energy.⁶⁶ As a result, probability of Compton interaction depends almost exclusively on electron density, which is approximately proportional to physical density. Continuing with the same example, the ratio of intensity downstream of the attenuator is now

$$\left(\frac{I_1}{I_2}\right)_{MV} \approx \frac{\rho_{bone}}{\rho_{water}} = 1.5 \quad \text{Equation 5}$$

which is approximately an order of magnitude smaller than in the case of photoelectric effect. In conclusion, contrast is greatly inferior in MV imaging with respect to kV.

2.1.2.2 Spatial resolution

Another intrinsic difference between diagnostic and therapeutic x-ray generators that affects imaging quality is the *focal spot* size. To produce x-rays via bremsstrahlung, electrons are accelerated towards a target normally made of Tungsten. The focal spot is the area on the target in which x-rays are generated, including the broadening caused by scattered radiation and beam filtering. In diagnostic x-ray tubes, which make use reflection targets with small target angles⁷⁷, the spot size can be as small as $0.1 \times 0.1 \text{ mm}^2$. In MV linear accelerators, the higher dose deposited in the target, along with the need for transmission target geometry, causes for a larger focal spot. In addition, the flattening filter acts as a source of secondary photons, thus broadening the effective focal spot.⁵⁵ Measurements on a Varian Clinac 21EX found an elliptical focal spot with a primary axis between 1.7 and 2.2 mm.⁷⁸ More recently, studies on a Clinac iX estimated a circular spot size of size 1.0 mm.⁷⁹

The larger focal spot causes *geometric penumbra*, as illustrated in Figure 2-5. A wider penumbra, as is the case with MV energies, limits the spatial resolution of the imager. For this reason, the resolution of MV detectors has remained constant at 0.392 mm since their first commercial introduction in 2000.⁵⁶

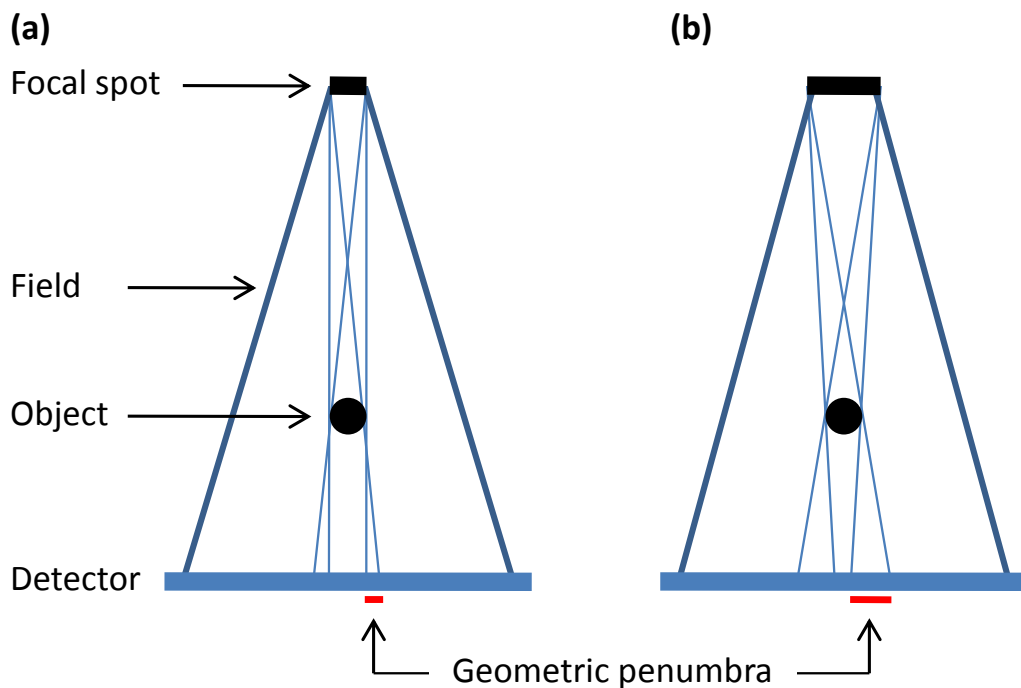


Figure 2-5: When imaging a small object inside an x-ray field, the finite dimension of the focal spot causes a geometric penumbra of width proportional to the spot size itself. In kV imaging, the smaller spot size (a) allows a better spatial resolution than MV imaging (b).

2.1.2.3 Other potential limitations: probability of interaction, SNR, ghosting

There are further limitations of MV with respect to kV imaging. Although these have little impact to EPID dosimetry, for completeness they are summarized below.

High energy treatment radiation has a much smaller probability of interaction than diagnostic radiation. To produce the same signal, then, more MV than kV photons are needed, resulting in increased dose to the patient. Fortunately, in *in vivo* transit dosimetry, which is the focus of this thesis, this is not a limitation, as the treatment beam has a sufficiently large fluence and more than enough monitor units to produce the necessary signal.

A second limitation of MV imaging is its signal-to-noise ratio, or SNR. In a review paper⁵⁶, Antonuk defines two classes of this quantity, for input (SNR_{in}) and output (SNR_{out}).

SNR_{in} describes the radiation fluence which produces the desired signal (i.e. the primary beam) to that which adds undesired noise (i.e. the scattered beam). In kV imaging, unwanted scatter is reduced by means of a grid placed over the detector, which attenuates those photons which, having scattered, are not directed along the rayline from the source to the detector. In addition, any detection system will add noise to the signal, in the case of the EPID, this is mainly electronic noise (eddy currents from photodiodes). The system's SNR_{out} will generally be worse than its input, and the ratio SNR_{in}/SNR_{out} is the detective quantum efficiency (DQE). DQE for kV systems ranges in 20-80%, while for EPIDs it is generally below 5%.⁵⁶

While low DQE does not greatly impact EPID dosimetry (the treatment beam has sufficient intensity to compensate this), low SNR_{in} must be taken into account. In particular, scattered radiation (i.e. 'noise') from the patient will irradiate the imager almost uniformly,⁷³ and will thus offset the signal. When using the signal to reconstruct dose, this offset must be accounted for.

A further complication specific to a-Si EPIDs is due to the effects of *image lag* and *gain ghosting*.⁸⁰ Both these are due to charges that remain trapped in the photodiode layer. Image lag is the release of these trapped charges in subsequent frames, adding a signal offset. Image lag can be measured by recording the dark field after the beam is switched off. However, lag by itself cannot account for the under-response of the EPID in the first ~40 s of operation.⁸¹ This additional signal loss is due to gain ghosting, which is the effect by which the trapped charge alters the electric field associated with the photodiode and thus its sensitivity. For the purposes of EPID dosimetry, these effects cause a non-linearity between MU and EPID response, which can be accounted for. The effect of trapped charges on subsequent irradiations can be avoided by waiting ~30 s between beam deliveries.

Finally, in MV imaging one must consider the effect of glare (p.26), the need for increased shielding (EPIDs are located in the shielded treatment vault), and radiation damage to the imaging panel which can shorten the imager's life.

2.2 *In vivo* Dosimetry by EPID

The earlier work on EPID dosimetry, which still comprises the great majority of the total publications on the topic, focuses on *patient specific pre-treatment QA*. With the advent of intensity modulated radiation therapy (IMRT) in the early 2000's, in which spatial modulation of dose is obtained by motion of the multi-leaf collimator (MLC) leaves, there came a need to verify that the linear accelerator could deliver the planned fluence correctly. This verification is performed before the patient begins treatment (i.e. 'pre-treatment') and of course requires a 2D detector, such as the EPID. This push came especially to ensure patient safety, as IMRT treatments have up to eight times the MUs compared to previous RT methods. To this aim, the treatment fields are delivered without the patient in the beam path and are delivered to the EPID. An integrated image is recorded which is compared to the one predicted by the TPS. It should be noted that pre-treatment QA is normally not a dosimetry method: it verifies fluence without the patient perturbing the beam, but says nothing about dose absorbed in the patient him/herself. The amount of literature on EPID pre-treatment QA is staggering; an excellent review is that by Van Elmpt *et al.*⁸² This thesis focuses, on the other hand, on EPID dosimetry *in vivo*, that is, during treatment. Furthermore, this thesis focuses not on general treatment verification, which can be based on transit (i.e. recorded through the patient) fluence images, but on dosimetry inside the patient, in which from the fluence one calculates dose inside the body. In the following sections (2.2.1-2.2.3), the work of the three major contributors to *in vivo* EPID dosimetry the field is

summarized: these groups stand out by the number of publications in the field and by the application of their research to clinical practice. Other groups have also investigated the use of the EPID to calculate 2D/3D dose inside the patient *in vivo*, and the key references are presented below. Studies which are not true 2D or 3D (i.e. that estimate dose in a few points only) or that verify treatment without estimating dose are not considered.

The first attempt of EPID *in vivo* dosimetry which made use of transit images dates back to 1996 and reported that relative dose distribution was within 2% to that of the treatment planning system and that measured by TLDs.⁸³ Although this was a relative dosimetry study (i.e. there was no report of the absolute dose delivered), it was a promising first result. That study made use of a prototype scintillation crystal-photodiode detector which was never commercialized, but concurrently the a-Si EPID was being developed and in the following years multiple groups proposed various methods of EPID transit dosimetry with the new detector. As outlined in Table 3 of the review by Van Elmpt *et al.*⁸², a number of groups explored a-Si EPID treatment verification. However, the body of work relating specifically to 2D and 3D patient dosimetry is much smaller. McNutt *et al.*⁸⁴ reconstructed 3D dose inside the patient using EPID transit images, the patient's simulation CT, and the treatment planning system's own convolution/superposition method. Jarry *et al.*⁸⁵ reported on a similar work in which dose calculation was obtained by means of a novel Monte Carlo reconstruction method. Partridge *et al.*⁸⁶ also obtained 3D dose in patient, but making use of megavoltage CT data obtained immediately before treatment delivery, thus avoiding errors due to anatomy and setup differences between simulation and treatment. More recently, Kavuma *et al.* estimated patient exit dose in 3D conformal treatments⁸⁷ and with dynamic wedges⁸⁸ from monitor unit and source-to-surface distance values by relating pixel intensity to attenuator thickness.

2.2.1 The Winnipeg-Newcastle collaboration

There are two general approaches to EPID IVD: verification at the level of the imager or at the level of the patient. In the first approach, a model that makes use of the patient's CT data is used to predict the EPID image, and the prediction is compared to the recorded image. An example is the model-based EPID image prediction method developed by the research group led by B. McCurdy of the University of Winnipeg, Canada, in collaboration with that led by P. Greer of the University of Newcastle, Australia. The method⁸⁹ consists in modeling the fluence to the imager as the sum of that transmitted through the patient and that scattered from the patient onto the imager. To this aim, four models are needed: linear accelerator fluence model, patient transmission fluence model, patient scatter fluence model, EPID dose model. The first of these is based on Monte Carlo simulations, manufacturer specifications, and *ad hoc* optimization of select parameters. The primary transmitted fluence is calculated from attenuation ray-tracing through the patient's CT data. The fluence of scattered radiation from the patient was approximated again with Monte Carlo, using a range of slab phantom thicknesses and air gaps between the imager and phantom. Dose to the EPID is calculated by convolution of the total incident fluence by EPID-specific Monte Carlo-calculated dose kernels. The method was applied clinically and showed promising results for pre-treatment volumetric arc therapy and for *in vivo* error detection during IMRT deliveries.⁹⁰

The intrinsic limitation of verification at the level of the EPID (i.e. by comparing predicted and measure images) is that it is unclear how possible image differences correspond to differences in dose to the patient.²⁹ Multiple groups have therefore explored backprojection methods to reconstruct dose in the patient from the EPID image, and compared that to the dose predicted by the TPS or measured with other devices. The two approaches described below

belong to this second category. Recently, the Winnipeg-Newcastle group have also moved from discrepancy detection to dose calculation.⁹¹ For this, they implemented a detailed dose calculation model which uses the backprojected fluence upstream of the patient as input.

2.2.2 The NKI Model

The Netherlands Cancer Institute (NKI) has produced the greatest impact in the field of EPID IVD, both in terms of number of publications and number of patients treated. In 2007 the NKI group published their first results on EPID IVD of 75 prostate IMRT plans.⁹² The method is based on previous work⁹³ from 1998 on a liquid-filled EPID (a technology which was replaced by the a-Si detectors), and is summarised below.

First, an EPID image is taken through the patient/phantom, with an energy-dependent build-up placed over the imager to ensure the detector is at depth of maximum dose. This image is converted to a dose map ('EPID dose') by means of a signal-to-dose factor calculated in advance through deliveries to an ion chamber. From the EPID dose, the dose from photon scatter to the imager is subtracted to yield the primary radiation dose. This dose from scatter is estimated from previous measurements, and is dependent on the measured transmission, patient-detector distance, and field size. The primary dose is then backprojected to the exit side of the patient (in the plane perpendicular to the central axis, or CAX, at a distance of dose maximum upstream from the exit surface) using the inverse square law. To calculate the scattered dose in the same plane, the primary exit dose is convolved by a kernel calculated as described elsewhere.^{94, 95} The authors then present multiple methods to obtain the dose at isocentre plane from the exit dose. The final results are point dose agreements between calculated and planned doses of 2.5% in homogeneous phantoms.

Applying this method to prostate IMRT treatments *in vivo*, the ratio of EPID-calculated dose to TPS-predicted dose at isocentre ranged between 0.96 and 1.02, indicating that the method calculates within accuracy required for clinical use.⁹² In 2D, measured and planned dose maps were compared using 3% 3mm gamma analysis, as defined by Low *et al.*⁹⁶ The authors investigated various gamma metrics that would provide sensitivity to dose discrepancies while minimizing false positives or clinically irrelevant discrepancies. These were: the percentage of field with value less than 1 ($P_{\gamma<1}$), the average in-field value (γ_{avg}), and the maximum in-field value (γ_{max}). They found that the alert criteria which best matched the sensitivity of their current clinical pre-treatment verification was: $\gamma_{avg}<0.67$, $\gamma_{max}<2.00$, $P_{\gamma>1}>95\%$ for three fractions. Whenever a gamma comparison arising from one of the first three treatment fractions failed one or more of these criteria, an alert was raised, and a measurement in phantom was performed. Based on these results, the NKI abandoned pre-treatment patient specific QA for IMRT prostate patients, and adopted clinical IVD.

The NKI method has proven very effective not only in prostate IMRT, but also in other applications: 3D conventional RT⁹⁷, wedged beams⁹⁸, volumetric modulated arc therapy.⁹⁹ More recently, the workflow has been automated, reducing time required for treatment verification.⁹⁷ Nonetheless, due to its numerous levels of complexity presented through multiple publications, it requires great effort to translate to other clinics. In addition it calls for a lengthy commissioning procedure, including ion chamber measurements. Furthermore, it needs EPID images of each treatment field without the patient in the beam, adding significant time for calculation, and it does not account for inhomogeneities, although further work has addressed these two limitations.^{100, 101}

2.2.3 The Rome Model

In 2006 the physics group based at the *Universita' Cattolica del Sacro Cuore*, Rome, Italy, published a method of calculating dose at isocentre from EPID images using correlation ratios.¹⁰² The so-called 'correlation ratio' is a simple proportion between EPID signal through the phantom and dose at the isocentre, making this method unique in its simplicity. Unlike others, it does not require extensive modelling of the linear accelerator, nor does it require independent ion chamber measurements. Most importantly, it is straightforward to understand, and thus lends itself well to further development. The research work presented in this thesis is in fact based upon this approach, and thus these methods are described in greater detail below.

The general principle of this approach is to record the transit CAX EPID signals which result from irradiations of known doses to phantoms, and derive signal to dose correlations. The authors irradiated PMMA phantoms of water equivalent thicknesses ranging between $w=18$ cm and $w=58$ cm with square fields of side $l=5,10,15,20$ cm. For each, EPID images were recorded and the transit signal from the central 25 pixels^e, corresponding to a 3.7×3.7 mm² area, was averaged, here referred to as S_{CAX25} . Simultaneously, an ion chamber placed at phantom mid-depth (coincident with isocentre) measured dose, D_m . The presence of the ion chamber affected the signal by approximately 1%, and this perturbation was taken into account by offsetting the S_{CAX25} value. Signal-to-dose correlation ratios were then calculated as

$$F(w, l) = \frac{S_{CAX25}(w, l)}{D_m(w, l)}. \quad \text{Equation 6}$$

A second correlation ratio f is defined as

^e "Central 25 pixels" is a misnomer, as the photodiode array has an even number of lines and columns. Nonetheless, due to the small size of the pixels and flatness of the beam, this longitudinal-lateral misalignment by 1 pixel is negligible.

$$f(l, d) = \frac{S_{CAX25}(w, l)}{S_{CAX25}(w, l, d)} \quad \text{Equation 7}$$

Where $S_{CAX25}(w, l, d)$ is the EPID signal with the phantom shifted downstream by d . This takes into account the change in secondary scatter which reaches the detector (the primary beam is unaffected). The ratio $f(l, d)$ is empirically independent of w to within $\pm 0.3\%$.¹⁰²

The dose in the mid-depth ($w/2$) of the phantom, in the general case of non-coincidence with the isocentre, can then be approximated as

$$D_m(w, l) = \frac{f(l, d) \cdot S_{CAX25}(w, l, d)}{F(w, l)} \cdot ISQL(d) \quad \text{Equation 8}$$

Where $ISQL(d)$ represents the effect from the inverse square law associated with moving the calculation point downstream by d . To move from the dose at mid-depth ($w/2$) to the dose at isocentre ($w/2-d$), the authors use the ratio of TMR (tissue maximum ratio) values from the literature¹⁰³ and the inverse square law. This last statement can be understood by considering the following steps which refer to Figure 2-6. In the manuscript, these steps are implicit, but are here made explicit for clarity, making use of the formalism and notation coherent with the rest of the thesis. In equations 10-13, the dependency on field size is omitted, and the same field size l is assumed for all expressions. As well, the notation $D(w)$ states that dose depends on total phantom thickness, w , while $D(depth=x)$ refers to a dose calculation at depth x .

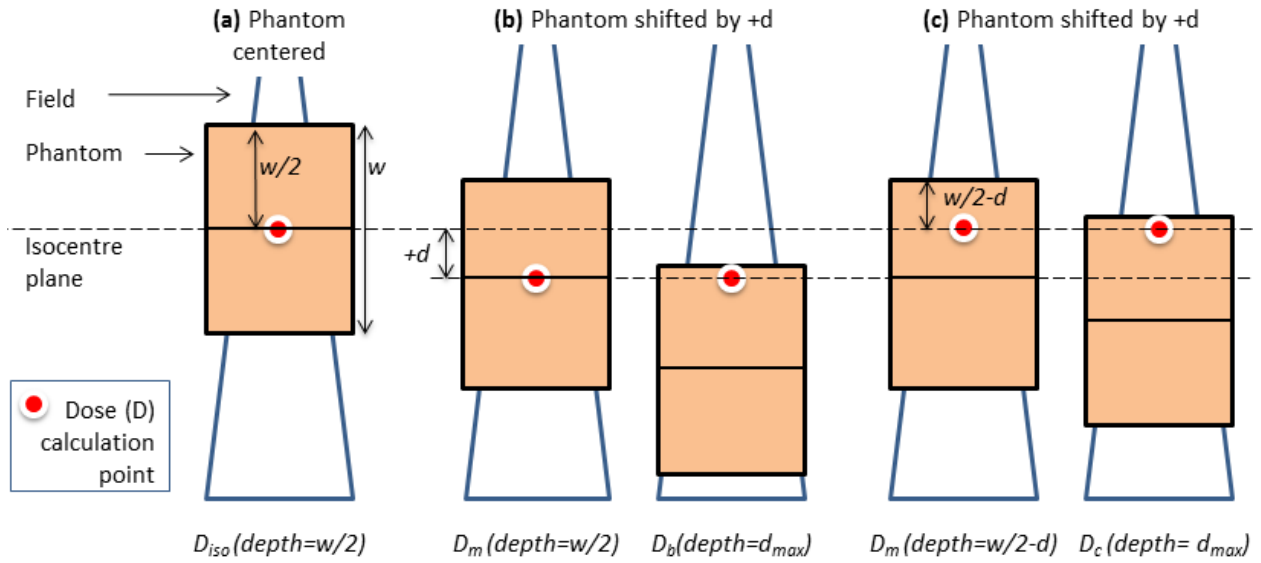


Figure 2-6: If the phantom is centered at isocentre, then clearly $D_m = D_{iso}$ (a). However, if the phantom has a vertical shift of d , one may make use of TMRs to shift the calculation point from a depth of $w/2$ (b) to $w/2-d$, which is isocentre (c).

The definition of TMR applied to Figure 2-6.b is

$$TMR(\text{depth} = \frac{w}{2}) = \frac{D_m(\text{depth} = \frac{w}{2})}{D_b(\text{depth} = d_{max})} \quad \text{Equation 9}$$

where $D_m(w/2)$ is the dose at mid-depth and $D_b(d_{max})$ is the dose at the same point in space, but at depth of dose maximum. Similarly, for Figure 2-6.c one may write

$$TMR(\text{depth} = \frac{w}{2} - d) = \frac{D_{iso}(\text{depth} = \frac{w}{2} - d)}{D_c(\text{depth} = d_{max})} \quad \text{Equation 10}$$

where $D_{iso}(w/2-d)$ is the dose at isocentre depth, and $D_c(d_{max})$ is the dose in the same point in space at depth of dose maximum. Now, noting that

$$D_b(\text{depth} = d_{max}) = D_c(\text{depth} = d_{max}) \cdot ISQL(d) \quad \text{Equation 11}$$

by substitution we have

$$\frac{D_{iso} \left(\text{depth} = \frac{w}{2} - d \right)}{D_m \left(\text{depth} = \frac{w}{2} \right)} = \frac{TMR \left(\text{depth} = \frac{w}{2} - d \right)}{TMR \left(\text{depth} = \frac{w}{2} \right)} \cdot ISQL(-d) \quad \text{Equation 12}$$

We can substitute this expression in Equation 8 and the *ISQL* contributions cancel out.

The final expression, re-introducing the field size dependency, is

$$D_{iso}(w, l) = \frac{f(l, d) \cdot S_{CAX25}(w, l, d)}{F(w, l)} \cdot \frac{TMR(\text{depth} = \frac{w}{2} - d, l)}{TMR(\text{depth} = \frac{w}{2}, l)} \quad \text{Equation 13}$$

The authors then tested the accuracy of the D_{iso} calculation by acquiring images *in vivo* during ten pelvic treatments, six fractions per patient. Per field results agreed to within $\pm 5\%$ with the TPS dose, with a mean error of 1%. Summing all fractions per patient some fluctuations canceled out yielding an agreement to within $\pm 3\%$.

A few limitations of this work are to be pointed out. Firstly, dose is calculated in one point only (the isocentre), not making full use of the 2D nature of the EPID. The dose calculation was not tested in phantoms, but directly in patient data, making the task of pinpointing inaccuracies more difficult. The calibration (i.e. determination of $F(w, l)$ values) is performed with an ionization chamber, but D_{iso} values are compared to planned values introducing the inaccuracy of the TPS as a confounding factor. Finally, the thinnest calibration water equivalent thickness of 18 cm is too large to allow application in most non-pelvic treatments.

2.2.4 Scope of this thesis

In my research work, I built upon the method proposed by Piermattei *et al.*¹⁰². The greatest challenge was extending this method in 2D, as the calibration ratios F and f acquired on the CAX are not constant off axis. In Chapter 3, preliminary results on an anthropomorphic phantom using an empirical off-axis correction are presented. In chapter 4, I propose a novel

method for off-axis dose modelling based on convolution of the EPID image by a multi-Gaussian. In Chapter 5, said method is applied to EPID dosimetry and investigated in phantoms. The entire method is presented, for others to apply and adapt it to their environments and needs. As well, some simple tests in solid water slab phantoms are run to quantify its accuracy and sensitivity. In chapter 6, the first *in vivo* results are reported, on ten rectal cancer patients. This work highlights, among other results, the impact of soft tissue changes to dose delivery. Finally, in chapter 7, results on 20 patients (including the ten from the previous studies) are presented. In this chapter we also propose the use of morphological analysis as a metric to flag possible dose discrepancies. The last chapter is dedicated to drawing conclusions and proposing future work.

Chapter Three: **Two-dimensional *in vivo* dose verification using portal imaging and correlation ratios**

General introduction

In 2006, Piermattei *et al.* published on an approach to calculate dose at isocentre by means of *in vivo* EPID images.¹⁰² The work included in this chapter presents a method to extend that approach to obtain dose in the whole plane at isocentre depth. This is attained by means of empirical off-axis correction factors. The work presented has been published in the peer reviewed *Journal of Applied Clinical Medical Physics*¹⁰⁴ and is reproduced with permission. The notation has been slightly modified for coherency with the rest of the thesis.

This chapter represents an initial proof of concept of 2D *in vivo* dosimetry by correlation ratios, and is the first work that was published on the topic. I was the first author on this work, with Dr. Derek Brown as senior author. I designed the study, collected and analyzed data, and wrote the first draft of the manuscript. Dr. Brown proposed the study idea, provided guidance throughout, and reviewed the final manuscript.

Two-dimensional *in vivo* dose verification using portal imaging and correlation ratios

Stefano Peca & Derek Brown

Abstract

PURPOSE: The electronic portal imaging device (EPID) has the potential to be used for *in vivo* dosimetry during radiation therapy as an additional dose delivery check. In this study we have extended a method developed by Piermattei *et al.*¹⁰² that made use of EPID transit images (acquired during treatment) to calculate dose in the isocentre point. The extension allows calculation of two-dimensional dose maps of the entire radiation field at the depth of isocentre.

METHODS: We quantified the variability of the ratio of EPID signal to dose in the isocentre plane in solid water phantoms of various thicknesses and with various field sizes, and designed a field edge dose calculation correction. To validate the method we designed three realistic conventional radiation therapy treatment plans on a thorax and head anthropomorphic phantom (whole brain, brain primary, lung tumour). Using CT data, EPID transit images, EPID signal-to-dose correlation, and our edge correction, we calculated dose in the isocentre plane and compared it with the treatment planning system's prediction.

RESULTS: Gamma evaluation (3% / 3 mm) showed good agreement ($P_{\gamma < 1} \geq 96.5\%$) for all fields of the whole brain and brain primary plans. In the presence of lung, however, our algorithm overestimated dose by 7-9%.

CONCLUSION: This 2D EPID-based *in vivo* dosimetry method can be used for post treatment dose verification, thereby improving the safety and quality of patient treatments. With

future work it may be extended to measure dose in real time and to prevent harmful delivery errors.

3.1 Introduction

The goal of radiation therapy (RT) is to deliver the prescribed dose to the target while sparing surrounding tissues. To this aim, the great majority of cancer centres rely on pre-treatment quality assurance of the plan calculation by the treatment planning system (TPS) and of the dose distribution in homogeneous phantoms. Nonetheless, there are many arguments in favor of *in vivo* dosimetry (IVD), that is, a method to measure the dose deposited in the patient during treatment, as an auxiliary optimization and safety procedure. IVD can identify errors in dose calculation, data transfer, patient setup, dose delivery, and may be used as a trigger for adaptive radiotherapy in cases of changing patient anatomy.^{29, 44, 105} More importantly, most RT errors which have led to serious patient injury or death^{28, 31, 106} could have been avoided or reduced with IVD.

Currently, the two most common methods of *in vivo* dosimetry available are thermoluminescent dosimeters and diodes; however, both have a number of limitations. The placement of the device on the patient and the readout procedure are time consuming, prone to error, and require additional resources. The acquired measurement represents only one point in space and provides only surface dose (or at depth 1-2 cm using buildup). In addition, the presence of any device on the patient's skin may modify the surrounding dose distribution.

Another tool for *in vivo* dosimetry which has been largely investigated but used clinically only in few select sites⁴⁴ is the electronic portal imaging device, or EPID. The intensity of the transit portal image (acquired through the patient during treatment) can be related to the dose

absorbed by the patient. Amorphous-silicon (a-Si) EPIDs in particular have desirable dosimetric properties, including linearity with dose, non-dependency with dose rate, and good reproducibility.^{69, 71, 74, 82} Additional strengths of the EPID as a dosimeter are: it is readily available, easy to operate, and can produce two-dimensional maps. Finally, the EPID can be run in continuous acquisition or *cine* mode and thus has potential to provide dose measurement in real-time.⁶⁹

Possibly the major contributions to clinical EPID-based dosimetry come from Netherlands Cancer Institute group, that was able to produce 2D dose maps inside a phantom¹⁰⁷ and translate the method into routine clinical practice.⁴⁴ In its first 4.5 years since implementation (2005-2009), treatment plans of 4337 patients have been verified and 17 serious errors that led to intervention were detected, of which nine would not have been caught by pre-treatment verification.⁴⁴ Although the clinical results are very good, the method also has some drawbacks. Firstly, it requires extensive commissioning, including ion chamber profile measurements for various field sizes. As well, it does not account for effects which may produce artefacts in the final dose maps: beam flatness variation with depth (see Figure 2-3), ghosting (described in section 2.1.2.3 and in greater detail by McDermott *et al.*⁸¹) and signal dependence on energy spectrum.⁷² Regarding the latter, the energy spectrum which reaches the imager is different for each pixel due to differential beam hardening from the flattening filter and from the patient. The Gd₂O₂S phosphor scintillator of the detector is not water-equivalent due to the large atomic mass of Gadolinium. As a result, at lower energies its higher equivalent Z increases the probability of photoelectric events, causing a larger response. Lastly, the method does not account for tissue inhomogeneities, although a variation was later proposed to circumvent this limitation.¹⁰¹

On another front, a number of groups have modeled the response of the EPID for dosimetric purposes using Monte Carlo techniques.^{108, 109} One group in particular was able to calculate accurate 2D dose maps inside a phantom by means of sophisticated EPID modeling.^{81, 104} Pure simulation and mixed simulation/empirical methods can provide very accurate results but require highly specific mathematical models for both the accelerator and the EPID. As well, the long calculation times can render them inapplicable to clinical routine, (up to 336 hours for a single volumetric modulated arc therapy plan in which both the MLC moves and the gantry rotates around the patient during delivery)¹¹¹.

Another group has investigated IVD using the EPID modified to direct detection with promising results, but presently not applicable with ease to clinical routine as it requires replacement of the phosphor screen with solid water.¹¹² Kavuma *et al.* developed a promising method for IVD using EPID images and depth-dose data.⁸⁸ *Cine* mode EPID imaging has found application in the realm of gantry motion verification for dynamic RT techniques^{113, 114} and as a pre-treatment dose verification tool,^{74, 115} but real-time EPID IVD is not current clinical practice. For further applications of portal imaging IVD the reader is referred to comprehensive review papers available in literature.^{29, 82}

Although much research has been done in the field of EPID IVD, the methods described above are not easily implementable in the clinic. In regards to commercial applications, there are the only available option is *Dosimetry Check*^{116, 117} with the *exit-transit dose option* (available through Oncology Systems Limited, Shrewsbury, UK, and through Math Resolutions, Columbia, MD). Unfortunately the calculation method is proprietary and the *in vivo* option lacks peer-reviewed publications. More recently, *EPIgray* by DOSIsoft (Cachan, France) has been developed in France, where *in vivo* dosimetry has been mandated²⁸ but it calculates dose in select

points in the body only, and thus is not a complete 2D dosimetry method. For these reasons we decided to develop a fast, easy-to-implement, and clinically reliable method of two-dimensional EPID IVD.

The *in vivo* dosimetry method we propose is a two-dimensional extension of previous work by Piermattei *et al.* that have successfully implemented transit EPID dosimetry to calculate absorbed dose at the isocentre to within 3% of the value predicted by the TPS.¹⁰² Their method relies on a set of correlation ratios which must be determined in advance, and takes into account the impact of tissue inhomogeneities on the primary component of the radiation beam by use of computed tomography (CT) data. Further work has enabled this group to implement their *in vivo* dose-at-isocentre verification in various centres in Italy¹¹⁸ and to apply it in multiple equipment and treatment situations^{118–122}

We expanded the work by Piermattei *et al.* to calculate 2D dose maps in an anthropomorphic phantom during three-dimensional conformal RT (3D-CRT). To this aim, we had to characterize the off-axis variability of the correlation ratios F , here defined as the ratios of the EPID signals and the TPS doses in equivalent water phantom mid-planes.¹⁰² The variability of the F factor is due to multiple effects. Most importantly, moving from the central axis (CAX) to the field edge, the dose decreases more rapidly than the signal due to a major loss of lateral electronic equilibrium in the phantom, thus causing F to increase^{107, 123} A lesser effect is due to the flattening filter which causes beam hardening closer to the CAX. The detector, being non water-equivalent, has a response which is oversensitive to photons of lower energy,^{124, 125} producing a higher response for the same dose when farther from the CAX. This effect is actually overcompensated by the flood field correction (acquired with an empty beam), which does not account for the variation in beam attenuation caused by in-patient hardening.¹⁰⁷ Because

these two effects are most likely accelerator- and EPID-dependent, we chose to account for them by an empirical rather than model-based approach. This was done by measuring the values of F in the whole isocentre plane for various thicknesses and field sizes to determine the appropriate correction factors.

The goal of this work is to provide proof of principle for a 2D *in vivo* dose verification method which is simple to implement and to use routinely, and that is sensitive to clinically relevant dose delivery errors.

3.2 Methods

A number of measurements and calculations must be performed in order to obtain dose maps from EPID images. Figure 3-1 provides an overview of the calculation process, separated into commissioning and beam-specific measurements. A detailed procedure is provided below.

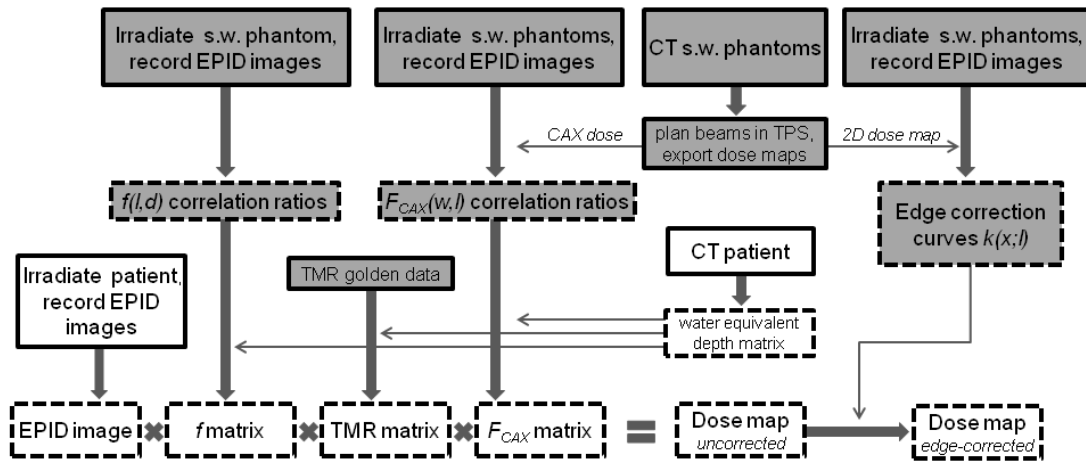


Figure 3-1: Dose calculation pipeline. Gray: commissioning procedure which has to be run only once. White: dose calculation steps per each patient/field. Dashed frame identifies calculations performed in MATLAB environment. (s.w.=solid water; ‘patient’ also refers to anthropomorphic phantom.)

3.2.1 EPID signal to dose correlation ratios

The correlation ratios F_{CAX} and the displacement factors f were measured by irradiating solid water phantoms (Gammex, Middleton, WI) while acquiring transit EPID images as described by Piermattei *et al.* (see ¹⁰² for more details). In this work, F_{CAX} values relate central-axis EPID signal to the dose in the midpoint of the phantom when centered at isocentre (Figure 3-2.a), and were determined as the ratio of the signal from the EPID's central 20×20 pixels (S_{CAX}) to the dose at isocentre (D_{CAX}) given by the TPS (Eclipse 8.9, Varian Medical Systems, Palo Alto, CA), for five solid water phantom thicknesses ($w = 6, 12, 16, 20, 26$ cm) and seven square fields ($l = 5, 7.5, 10, 12.5, 15, 17.5, 20$ cm). The thickness values were chosen to approximate most clinically realistic situations, and the thinnest phantom was set at 6 cm to ensure dose at mid-depth was calculated beyond the depth of maximum dose. The field sizes were set so that full lateral electronic equilibrium was achieved (>4 cm approx) and limited by the dimensions of the imager (20 cm in the sup-inf direction). Similarly, f values account for different scatter photon contributions on the EPID due to displacement of the phantom from isocentre (Figure 3-2.b), and were measured as the ratio of the EPID signal with the phantom centered on isocentre to that with the phantom displaced by d , for four field sizes ($l = 5, 10, 15, 20$ cm) and eight displacements ($d = -10$ to $+10$ cm in steps of 2.5 cm), on a phantom of thickness 26 cm (because f was seen to be independent of w to within 0.3%¹⁰²). In this work the field edge is defined as those points where the portal image has signal equal to half of the sum of S_{CAX} and of an average pixel value well outside the field.

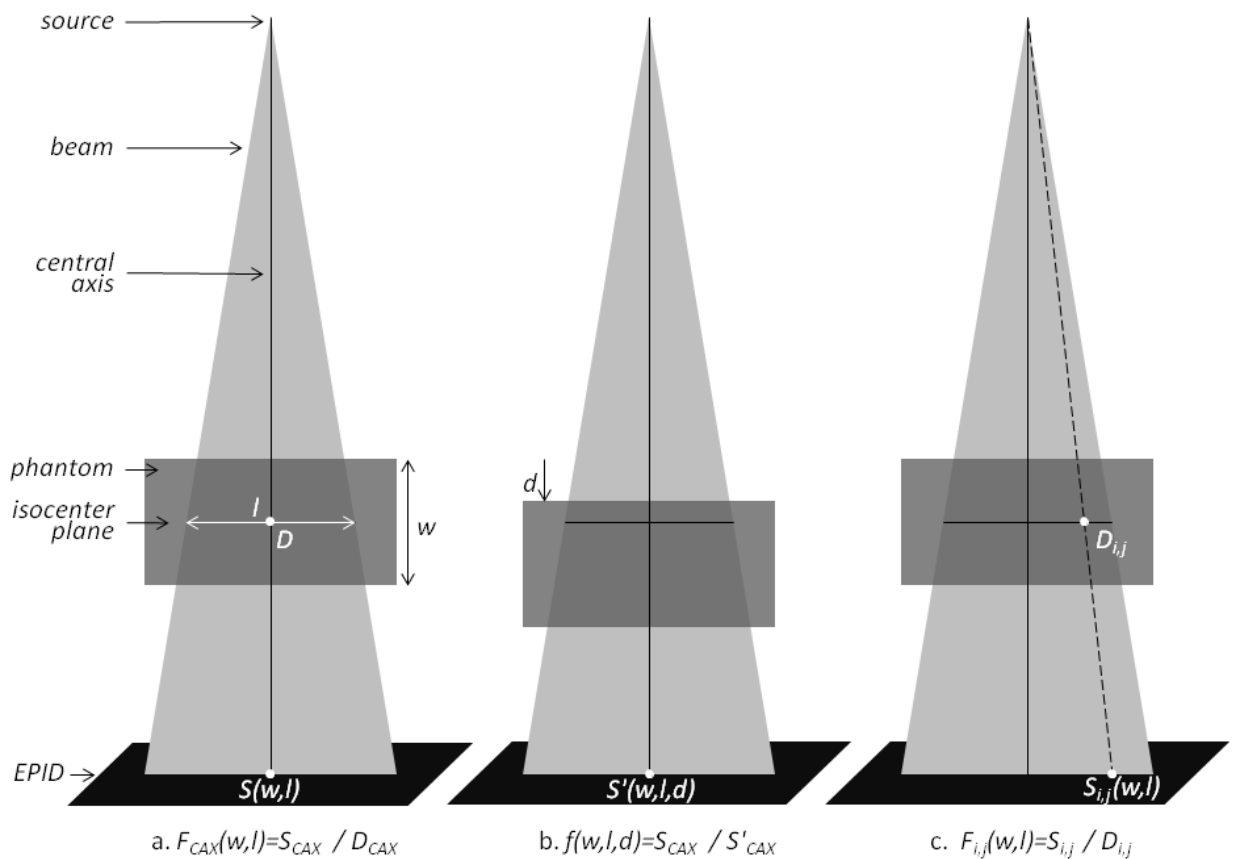


Figure 3-2: Solid water phantom setup for measurement of correlation factors F_{CAX} (a) and f (a and b) (see ¹⁰² for details). Measurements were performed for five thicknesses w , seven field sizes l , and nine displacements d . (c) Schematic for off-axis $F_{i,j}$ measurements.

All beams were delivered on a Varian Clinac 21 EX in service mode (6 MV, 100 MU, 300 MU/minute), with the EPID acquiring images in *cine* mode using the AM (Acquisition Module) Maintenance software (Varian Medical Systems). The EPID was a Varian aSi 1000 with resolution set at 384×512 pixels which produces an image field size of 20.1×26.8 cm² and was placed at a source-to-detector distance of 150 cm. The EPID frame rate was set to 10 fps, with 8 consecutive frames averaged into a single image, resulting in 1.25 images/sec. The detector was read out synchronously to the beam pulse pattern, and as this is generally different for different dose rates, the calibration is dose rate dependent. All “raw” EPID images are flood

field and dark field corrected. For each field, images were exported separately and summed in MATLAB (The MathWorks Inc., Natick, MA).

To investigate the variability of the F factors in 2D we made use of the EPID images described above, determining the ratios

$$F_{i,j}(w,l) = \frac{S_{i,j}(w,l)}{D_{i,j}(w,l)} \quad [\text{a.u./cGy}] \quad \text{Equation 14}$$

for every ray line from the source through the phantom to each detector pixel i,j (Figure 3-2.c). Here $S_{i,j}$ are the detector pixel values and $D_{i,j}$ are point doses inside the phantom in the isocentre plane. The dose calculation was performed with the AAA algorithm with heterogeneity correction. The 3D dose calculation grid was set at 0.25 cm but to obtain $D_{i,j}$ values a dose map was exported from the TPS with the same number of points as the detector pixels. Subsequently, we defined unitless $K_{i,j}$ values as $F_{i,j}$ normalized to F_{CAX} ,

$$K_{i,j}(w,l) = \frac{F_{i,j}(w,l)}{F_{CAX}(w,l)}. \quad \text{Equation 15}$$

From this 2D matrix we determined one-dimensional correction curves by taking the cross-plane profiles averaged over 20 rows of pixels (to account for pixel variability). From this profile, only the 53 pixels (2.76 cm projected on the isocentre plane) closest to the central-right field edge were kept. This was done for all values of w and for three values of l (5, 10, 15 cm). The result is an edge correction factor $k(x;w,l)$ which describes the spatial variation of F . Here, x refers to the distance from the point i,j to the field edge in the cross-plane direction. We chose the length of 53 pixels because we found that in all cases this region contained >99% of the variability of F . Mathematically, this step may be written as:

$$\langle K_{i,j}(w,l) \rangle_{53\text{columns},20\text{rows}} = k(x;w,l). \quad \text{Equation 16}$$

This same procedure was repeated in the in-plane direction for the superior-most field edge to yield $k(y;w,l)$.

For clarity, the major dependence of F on position in the plane is with the distance to field edge (and only indirectly with distance from central axis). For this reason it is more appropriate to refer to it as an *edge correction factor* rather than an *off-axis factor*. The purpose of the $k(x;w,l)$ and $k(y;w,l)$ curves is precisely to approximate the behavior of the pixel-to-dose ratio at a distance x and y from the field edges.

3.2.2 2D dose calculation in solid water phantoms

We obtained 2D dose maps in phantoms using the F_{CAX} correlation ratios and then corrected these maps by multiplying by $k(x;w,l)$ and $k(y;w,l)$ where x and y are the distances from the point i,j to the closest field edges in the cross-plane and in-plane directions. Here we are approximating that for any given point of the isocentre plane i,j the edge proximity effect is due to two field edges only, i.e. the closest edges in the cross-plane and in-plane directions.

A simple example serves to illustrate this step. Suppose one wishes to know the correct F factor for a point in the top-right corner of a square field of side l incident on a homogenous phantom of thickness w . Said point is x cm from the right edge (cross-plane direction) and y cm away from the top edge (in-plane direction). The corrected factor $F_{i,j}$ is then the product of F_{CAX} by $k(x;w,l)$ and $k(y;w,l)$, or

$$\frac{F_{i,j}(w,l)}{F_{CAX}(w,l)} = k(x;w,l) \cdot k(y;w,l). \quad \text{Equation 17}$$

Empirically, we found that for the same field size, using the correction curve obtained from solid water of thickness $w=12$ cm gave good results for all other thicknesses. For any given field l , then, $k(x;w,l)$ can be approximated as $k(x;12cm,l)$ which for simplicity from here onwards we will write as $k(x;l)$. The same consideration applies to k calculated in the in-plane direction, y . Consequently, for any point i,j we can write the following approximation:

$$\frac{F_{i,j}(w,l)}{F_{CAX}(w,l)} \approx k(x;l) \cdot k(y;l) \quad \text{Equation 18}$$

where the k curve is derived from the $w=12$ cm phantom measurements.

In conclusion, in the case of homogeneous phantoms centered at isocentre, dose in the isocentre plane can be calculated using the relation

$$D_{i,j}^{EPID}(w,l) = \frac{S_{i,j}}{F_{i,j}(w,l)} \approx \frac{S_{i,j}}{F_{CAX}(w,l) \cdot k(x;l) \cdot k(y;l)}. \quad \text{Equation 19}$$

The variability of the f displacement factors in the isocentre plane was also investigated.

3.2.3 2D dose calculation in anthropomorphic phantom

Three realistic 3D-CRT treatment plans were designed on a thorax and head anthropomorphic phantom (The Phantom Laboratory, Salem, NY): (1) whole brain (WB) irradiation with gantry angles (GA) 90° and 270° ; (2) brain primary (BP) with GA 40° , 90° , 140° ; (3) lung tumour (LT) with GA 0° , 40° , 180° . Beams were shaped with a multi-leaf collimator (Varian Millennium 120 leaf MLC) and by setting the most appropriate collimator angle. Couch angle was 0° for all beams.

The anthropomorphic phantom was imaged by means of a clinical CT scanner (Varian Big Bore) with standard imaging parameters (2 mm contiguous slices, 512×512 pixels,

1.1 pixels/mm). CT data was fed into an in-house algorithm developed in MATLAB environment which calculates the water equivalent depths (i.e. radiological depths) along every ray line from the source to the isocentre plane and from the isocentre plane to the corresponding EPID pixel. The sum of these two depths is equal to the phantom thickness along the ray line, $w_{i,j}$, and their difference is $d_{i,j}$. With knowledge of these values for every ray line, one may calculate dose in every point of the isocentre plane by extending the central axis calculation proposed by Piermattei et al.¹⁰² to the whole plane at isocentre depth as follows:

$$D_{i,j}^{EPID}(w_{i,j},l) \approx \frac{TMR(\text{depth} = \frac{w_{i,j}}{2} - d_{i,j},l)}{TMR(\text{depth} = \frac{w_{i,j}}{2},l)} \cdot \frac{f(d_{i,j},l)}{F_{i,j}(w_{i,j},l)} \cdot S_{i,j} \quad \text{Equation 20}$$

where l is now the equivalent square field size for the conformal beam.

The use of tissue maximum ratio (TMR) values in the above equation requires clarification. The ratio of TMRs was previously introduced to compensate for the different water equivalent depths upstream and downstream with respect to the isocentre plane.¹⁰² In other words, along the CAX, the TMR ratio shifts the point of dose calculation from the half-depth in the phantom ($w/2$) to the level of the isocentre plane ($w/2-d$). It can be easily verified that the ratio of TMRs calculated in such two points is equal to the ratio of dose values in the same two points, and the inverse square law dependence cancels out.¹⁰² In writing Equation 20 we are now approximating the dose off-axis by using the TMR ratio corresponding not to the phantom's half depth ($w/2$) but the phantom's half-depth *along the ray line* ($w_{i,j}/2$). We are therefore shifting the point of calculation from half-depth in the phantom along the ray line ($w_{i,j}/2$) to the depth of the isocentre plane ($w_{i,j}/2-d_{i,j}$), for the purpose of reconstructing a 2D dose map at isocentre depth.

The actual TMR values are those calculated along the CAX and provided by Varian. Using our clinic's off-axis factors (OAR) for 6X beams we verified that the TMR values would not change by more than about 1-2% off-axis, thus supporting the approximation.

Making use of Equation 18, we can rewrite this relation as:

$$D_{i,j}^{calc}(w_{i,j}, l) \approx \frac{TMR(\text{depth} = \frac{w_{i,j}}{2} - d_{i,j}, l)}{TMR(\text{depth} = \frac{w_{i,j}}{2}, l)} \cdot \frac{f(d_{i,j}, l)}{F_{CAX}(w_{i,j}, l) \cdot k(x; l) \cdot k(y; l)} \cdot S_{i,j} \quad \text{Equation 21}$$

Note that the equation above is written for the general case in which the radiological thickness is specific for each ray line (i.e. $w_{i,j}$ and $d_{i,j}$ are different for each pixel). Agreement between calculated dose maps using Equation 21 and TPS maps for the anthropomorphic phantom was tested with 3% / 3mm gamma evaluation. The gamma criteria was chosen taking into account the approximations above, and to allow comparison with other publications.¹²⁶ The complete methods are summarized in Figure 3-1.

3.3 Results and Discussion

3.3.1 Correlation ratios and dose calculation in solid water phantoms

The F_{CAX} and f curves as functions of w and l resemble those reported by Piermattei *et al.*¹⁰² with the exception that values of f were contained within 0.6%, a much smaller variability than the 5% previously reported (data not shown). This is due to the definition of S_{CAX} : in our work we used the raw pixel value, while Piermattei *et al.* subtracted an offset to create a proportionality between S_{CAX} and dose. The f factors for the whole field were always well within 1% of the CAX value; for all practical purposes, from here onwards we approximated f to be constant off-axis, causing an error in dose estimation well within 1%. F_{CAX} and f curves were

obtained by cubic interpolation of the data points, as it provided the best agreement to measurements. It is important to emphasize that in general every setup (the specific accelerator, EPID, energy, etc.) will have its characteristic correlation ratios and values obtained in one situation may not be easily applied to another. The specific dose penumbra, in particular, will greatly impact the edge correction curves.

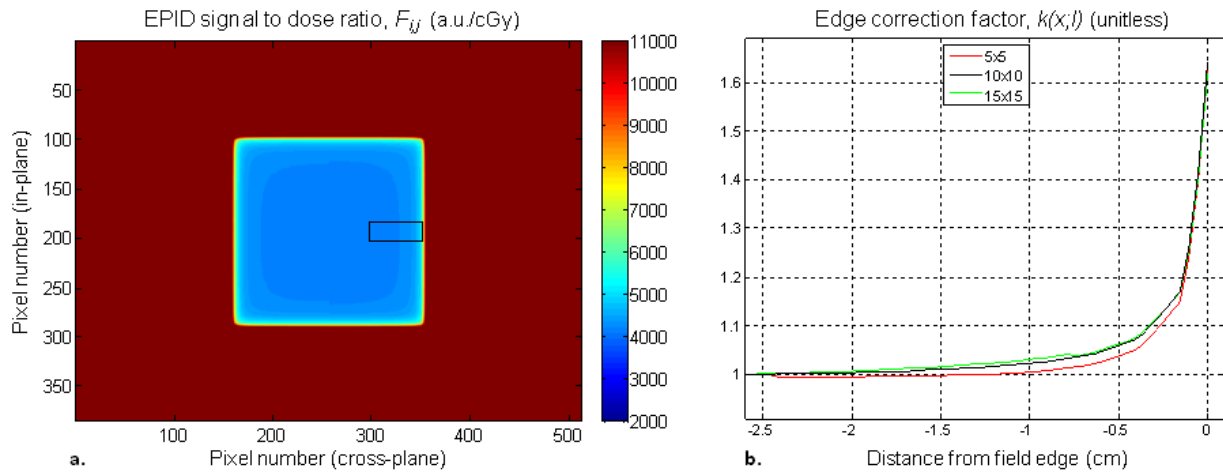


Figure 3-3: (a) 2D map of the signal-to-dose correlation factor $F_{i,j}$. For every pixel i,j of the EPID, $F_{i,j}=S_{i,j}/D_{i,j}$ where S is the signal intensity and D is the dose determined by the TPS in the point where the ray line from the source to the pixel intersects the isocentre plane (Figure 3-2.c). This matrix was calculated for three field sizes (shown: $l=10$ cm) and for five phantom thicknesses (shown: $w=12$ cm). The black rectangle contains the cross-plane profile which was averaged and normalized by $F_{CAx}(w,l)$ to compute the mean 10×10 edge correction curve. (b) Edge correction curves for three field sizes from the 12 cm thick phantom.

Values of $F_{i,j}$ increased as expected in proximity of field edges (Figure 3-3.b). This off-axis trend was similar for all water equivalent depths and square field sizes. When applying the edge corrections $k(x;w,l)$ we found the best overall agreement ($\gamma < 1$ for $>95\%$ of points inside field) for all thicknesses (irradiated by the same field size) by using the correction curves derived

from the 12 cm phantoms. In other words, for our setup, the field edge behavior of $F_{i,j}$ displayed in 12 cm phantoms well approximated that of both thinner and thicker phantoms, supporting the use of Equation 21 to calculate dose in the anthropomorphic phantom. On the other hand, the field size dependence could not be neglected, as there was no single field size which produced good overall agreement for all other field sizes. Rather, we found that using the curves derived from the closest field sizes gave good agreement. The three curves displayed in Figure 3-3.b were then all that we needed to correct the edges of the dose maps from all water equivalent depths and square field sizes, including the anthropomorphic phantom calculations.

As an example, the dose calculation and correction steps for the $15 \times 15 \text{ cm}^2$ field of the 16 cm thick phantom are shown in Figure 3-4.

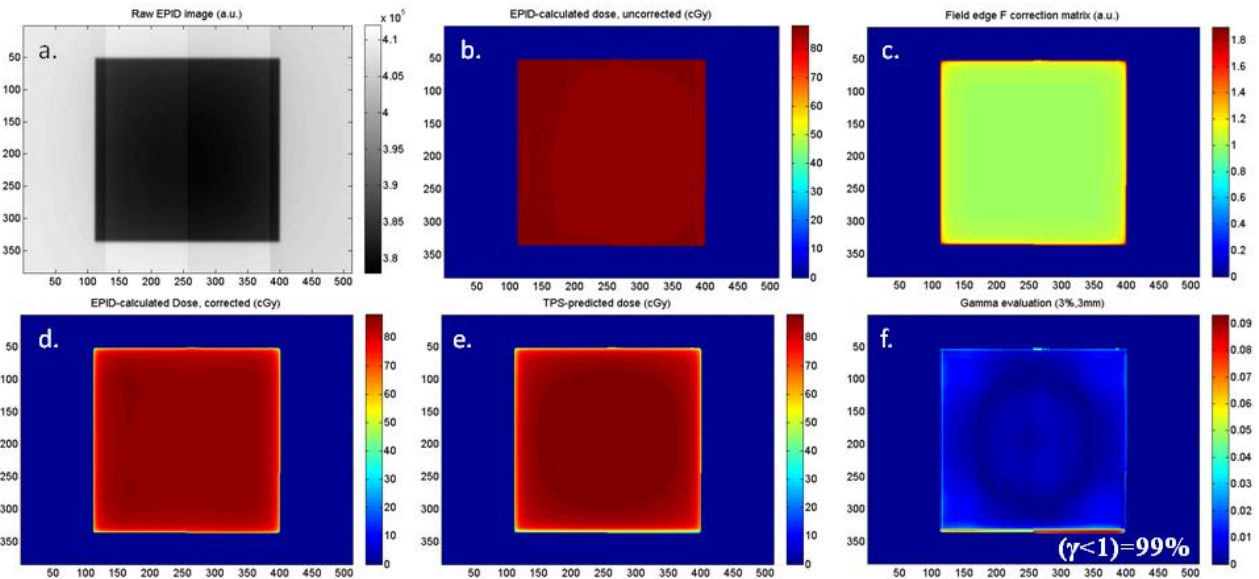


Figure 3-4: The fundamental steps of our dose map calculation and evaluation. (a) EPID image of 16 cm solid water with $15 \times 15 \text{ cm}^2$ field, continuous acquisition mode. (b) Calculated dose using signal-to-dose correlation factor from the central axis F_{CAX} as previously described.¹⁰² (c) Field edge correction to F_{CAX} obtained using the 15×15 curve from Figure 3-2.b and a binary mask of the EPID image. (d) Edge-corrected dose map obtained by pixel-by-pixel division of (b) by (c). (e) Dose map predicted by the TPS. (f)

Gamma evaluation (3% / 3mm) of the dose maps. Passing values ($\gamma < 1$ for >95% of in-field pixels) were obtained for all solid water thicknesses and field sizes. Dose maps are masked to field size.

3.3.2 Dose calculation in anthropomorphic phantom

Our algorithm calculated dose for the nine beams we delivered to the anthropomorphic phantom. Figure 3-5 reports dose calculation results from one field of each of the treatment plans. The left column displays dose maps calculated from EPID images recorded during beam delivery, while the central column reports dose maps exported from the TPS using the same settings as in the clinic. For the WB and BP plans, all calculated dose maps passed gamma analysis (98.3% and 99.3% for WB, 99.1%, 96.5%, 97.2% for BP). For the LT beams, on the other hand, our calculation consistently overestimated dose by about 7-9%.

The dose overestimation in lung is likely due to two major effects: tissue inhomogeneity and field shape. Regarding the former, although our model takes into account photon phantom scatter differences due to displacement of the phantom along the beam direction, it does not consider scatter differences due to tissue inhomogeneities. Specifically, much of the target suffers loss of electronic equilibrium due to the lower density tissue surrounding it, resulting in an effectively lower dose as compared to our calculation. Additional correction factors could be introduced to account for this, with the drawback that it would make the calculation process more cumbersome to implement in the clinic.

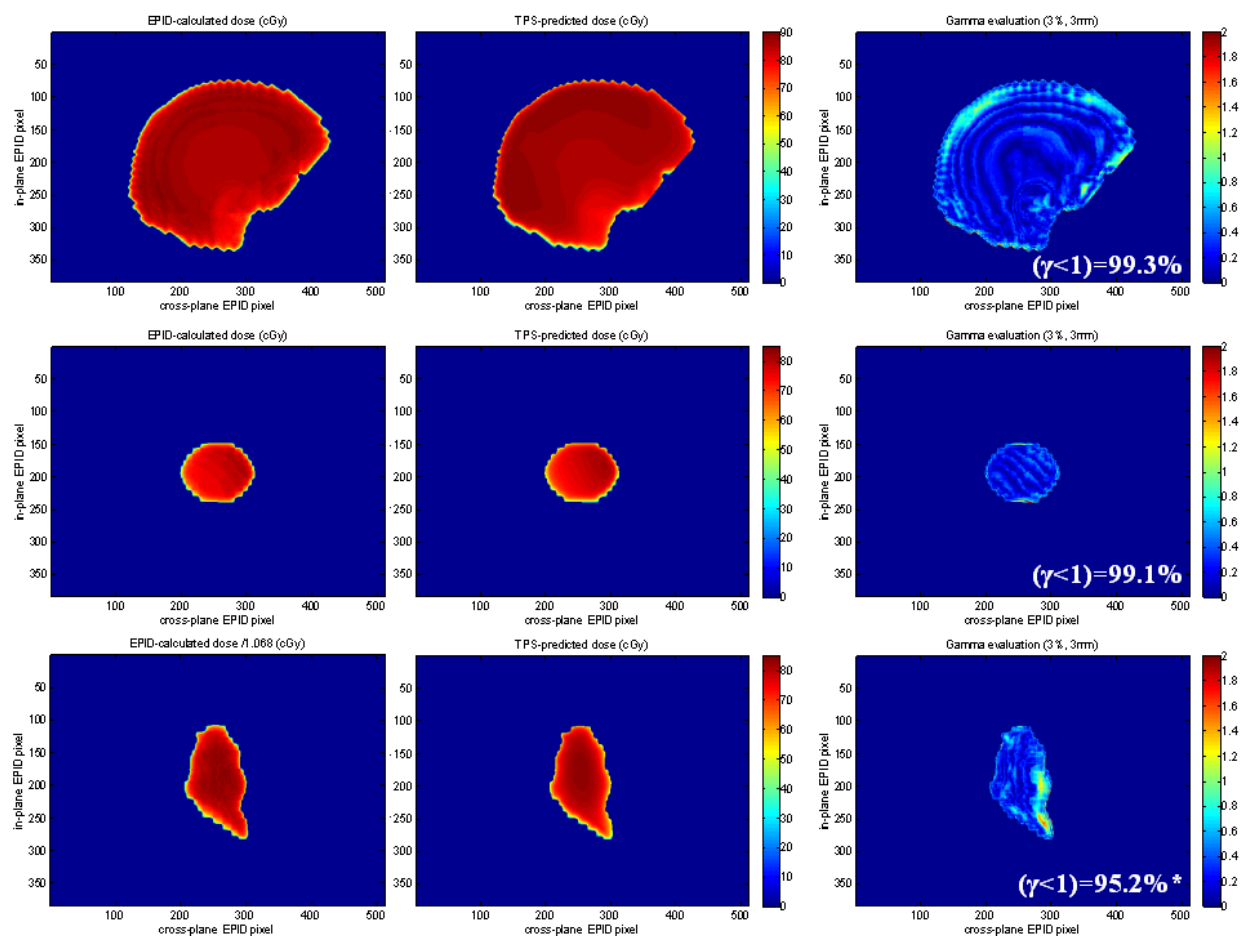


Figure 3-5: Validation of our dose calculation algorithm on the anthropomorphic phantom. Top to bottom: whole brain with gantry 270°, brain primary with gantry 40°, lung tumour with gantry 0°. Left-to-right: EPID-calculated dose, TPS-predicted dose, and their gamma evaluation (3% / 3mm). Edge correction from the curves of Figure 3-2.b. Maps are masked to field size. *Note: to provide a meaningful analysis for the lung tumour the calculated dose has been scaled *ad hoc* by -6.8% because our calculation overestimated dose in proximity of low density tissue.

A further variable that may account for dose overestimation in lung is the irregular shape of the lung fields. Our edge-correction method is built to account for proximity of field edges in the cross-plane and in-plane directions. In smaller and irregular fields, on the other hand, many points may be in proximity (<2cm) of field edges in a diagonal direction. These edges would

likely not be well-accounted for, and thus an incorrect signal-to-dose ratio $F_{i,j}$ of these points may lead to dose overestimation.

3.3.3 Limitations

A number of factors may be identified that limit the accuracy of this dose calculation method. Firstly, the edge correction curve has a non-negligible dependency on thickness and field size and shape. Our approximation of using just three curves to correct maps from all water equivalent thicknesses and field sizes will lose some accuracy in very thin or thick regions of tissue, or for more complex field shapes. As well, the approximation of using TMRs (by definition measured along the CAX) to obtain dose at the isocentre depth in points off-axis may lose validity in presence of large inhomogeneities such as lung. These considerations, along with the poor results in lung, suggest that our dose calculation may not be accurate in tumour sites which have high inhomogeneities or require complex field shapes.

It should be pointed out that in the present work we did not verify the TPS calculation, but rather validated our dose calculation against it. The TPS dose calculation (including the inhomogeneity correction and CT density table) should be verified independently. In the future we plan to also use Monte Carlo simulations to produce reference dose maps against which we may compare our calculations. As well, there is uncertainty associated with the Varian TMR data.

It must be noted that all our beams delivered 100 MUs, and it is documented that the dose-response relationship of EPID tends to lose linearity at low (≤ 30) MUs.⁷⁴ In subsequent work (described in chapter 5) we found that tests at 40 MU were more prone to error, while those of 80 MU and above showed better agreement. Regarding our *cine* imaging modality, we are

aware of a source of loss of linearity which we did not correct for. At the end of each acquisition, there are ‘leftover’ frames which, being fewer than the set frames/image rate, are discarded. This loss of signal becomes more relevant at lower MUs and may become particularly important as we extend the method to intensity modulated (IM) RT in which subfields may receive small numbers of MU. A simple strategy to limit this signal loss would be to set the averaging rate to 1 frame/image, with the drawback that it would increase multi-fold the number of images to work with. We found that this setting caused an unacceptable slowing down of the image acquisition software and hindered the data transfer, so we retained the multiple frame averaging.

Lastly, some unavoidable hardware limitations of any type of EPID-based IVD should also be stated. Not all beam geometries will allow use of the EPID during treatment, as it may be in collision with the couch, and some very large fields may irradiate the electronics of the detector. In addition, backscatter from the EPID arm can impact pixel signal by up to 6% in the periphery of the detector array¹²⁷ and bias results. In subsequent work (chapter 5) we accounted for this effect, and found that the error it caused was generally $< 2\%$ with our equipment. Finally, increasing many-fold the use of the EPID may shorten the detector's life span.

3.4 Conclusions

We have shown that transit EPID dosimetry based on correlation factors (as defined in ¹⁰²) can be adapted to two dimensions and used to estimate dose in the whole isocentre plane for 3D-CRT treatment fields.

The main strengths of the method are ease of implementation and speed. Commissioning requires 59 solid water irradiations with EPID transit image acquisitions for a total beam-on time of just below 20 minutes (excluding time required for setup adjustments). No ion chamber

measurements are needed. Once implemented, the beam-specific dose calculation is performed in a few seconds, which, combined with the *cine* imaging, is promising for future real-time dose verification applications.

This IVD method has potential to be useful in clinical settings, especially when treating regions not in close proximity to large tissue inhomogeneities. The accuracy of the dose calculation is comparable to that used in the clinic for at least some tumour sites. We propose this IVD method not as a substitute to pre-treatment QA, but as an adjuvant dose verification to track dose delivery and to catch serious errors which may be harmful or fatal for patients.

With further work, this method may also be used to evaluate dose distribution variations throughout treatment fractions due to inter-fractional variability (weight loss, swelling, positioning) and help guide adaptive radiotherapy. We are currently working to improve accuracy and to extend it to real-time applications and to IMRT. All the MATLAB code is freely available to anyone who will request it by contacting the authors.

General conclusion

This paper proved the feasibility of 2D *in vivo* dosimetry by EPID using correlation ratios. The method used to extend dose calculation from the isocentre to the plane at isocentre depth was empirical and made use of measurements in phantoms. Results were encouraging both in slab and anthropomorphic phantoms, although artefacts were present in the slab phantom dose maps. The next step was to create a model that would better describe the data. Improvement of these preliminary results is the goal of the following chapters.

Chapter Four: Dose modelling by multi-Gaussian convolution of transit portal images

General Introduction

The work presented in the previous chapter extended the isocentre point dose calculation to the plane at isocentre depth by an empirical correction curve calculated on the central cross- and in-plane profiles. As a result, dose estimation was adequate close to the central profiles, but inadequate further away. This is particularly evident in larger fields, as illustrated in Figure 4-1.

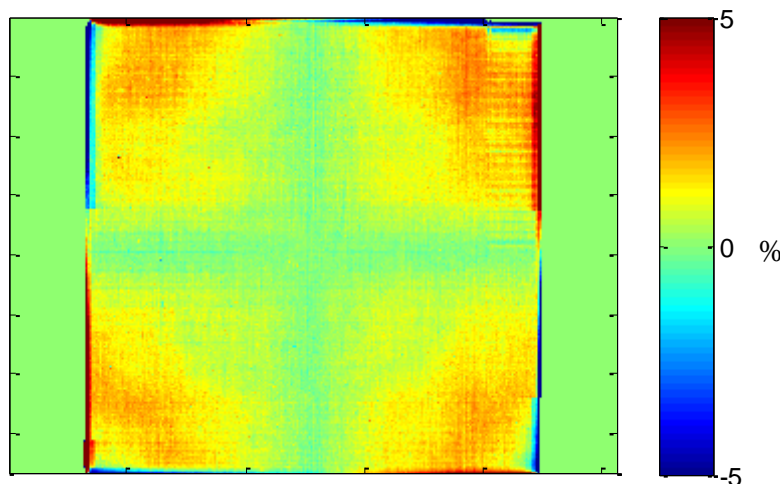


Figure 4-1: Pixel-by-pixel dose difference map, between TPS and EPID-based calculation (colour bar is $\pm 5\%$). The off-axis correction is based on the central profiles only (described in Ch.3), and thus does not adequately describe dose away from central profiles. (Dose map estimated in mid-depth of a 20 cm phantom irradiated with 6X, 20 cm square field).

In this chapter a more comprehensive method for 2D dose calculation from EPID images is presented, based on a combined theoretical-empirical approach. The result is a noticeable improvement in producing dose maps which more closely resemble those of the TPS: better modelling of loss of lateral scatter and horns, and accounting for phantom scatter to the EPID.

The work presented in this chapter has been submitted to peer review for publication. I designed the methods and wrote the manuscript. Dr. Wendy Smith motivated the project and provided feedback and guidance. Dr. Smith and Dr. Derek Brown reviewed the manuscript. Leigh Conroy provided essential insight both at the onset and throughout the work, and performed the final revision and submission of the manuscript.

Dose modelling by multi-Gaussian convolution of transit portal images

S. Peca, L. Conroy, D. Brown, and W.L. Smith

Abstract

PURPOSE: *In vivo* electronic portal imaging device (EPID) dosimetry requires modelling of dose inside the patient from transit images; however in-patient dose and EPID signal have different penumbral widths, due to differences in dose deposition and scatter contribution. We propose a method to derive 2D dose maps on the isocentre plane from transit images, based on convolution by optimized multi-Gaussians.

METHODS: Slab phantoms of thickness 5 – 35 cm were irradiated with 6 MV and 15 MV square fields (5 – 20 cm) while continuous EPID images were collected. Isocentre planar dose maps were calculated in the treatment planning system. An analytical optimizer minimized the difference between the planned dose profile and the convolution of the EPID profile with a linear combination of four Gaussian distributions by varying the relative weights of the distributions. EPID images were then convolved in 2D by the optimal multi-Gaussian, normalized to the same CAX value, and central profiles compared pixel-by-pixel with planned dose profiles.

RESULTS: For 6 MV, agreement between planned and EPID-derived dose profiles was within $\pm 2\%$ for 96% of points, with the exception of the thinnest (5 cm) phantom. For 15 MV, this agreement dropped to 79% due to the dip between the profile horns which is not modelled.

CONCLUSIONS: We demonstrate reconstruction of a 2D dose distribution inside a phantom from transit EPID images by convolution of images with optimized multi-Gaussians. The results are being implemented in a novel EPID *in vivo* dosimetry method.

4.1 Introduction

The electronic portal imaging device (EPID) is primarily used for verification imaging and pre-treatment quality assurance (QA); and is increasingly being used for patient dosimetry.^{29,}⁸² For pre-treatment QA, images are formed from an unperturbed beam, and the fluence or dose to the EPID detector is calculated.⁸² In contrast, EPID *in vivo* dosimetry uses images taken with the patient between the source and the detector (hereafter referred to as transit images), to calculate dose within the patient.^{92, 102, 104} Unlike pre-treatment QA approaches with an unperturbed beam,¹²⁸ in transit images the signal at the EPID detector is dependent on beam characteristics as well as attenuator composition and geometry. Dose reconstruction within the phantom/patient is thus hindered by the different scatter contributions and penumbral effects in the attenuator versus the imager, resulting in increased calculation complexity.

Multiple groups have reported on various solutions to attain *in vivo* dosimetry by transit images. The Netherlands Cancer Institute implemented EPID *in vivo* dosimetry based on backprojected transit images, unperturbed images, and commissioning ion chamber measurements.¹⁰⁷ More recently, a collaboration between CancerCare Manitoba and the University of Newcastle generated *in vivo* dose calculation¹²⁹ based on a detailed Monte Carlo model¹¹⁰ and image prediction algorithm.⁸⁹ Zwan *et al.* calculated dose from transit images by means of the commercial treatment planning system. Lastly, Camilleri *et al.*¹²⁸ estimated dose

maps by convolving images taken through a phantom with an empirical kernel, although their work was geared exclusively towards pre-treatment verification.

Our group has recently proposed a simple method for 2D transit EPID dosimetry¹⁰⁴. As our dose prediction had limited accuracy away from the central profiles, we implemented a convolution-based approach which gave encouraging preliminary results *in vivo*.¹³⁰ In this paper we describe this model and the procedure we followed to determine the multi-Gaussian kernels required to model dose from transit images. While the results presented here apply to specific equipment, this method can be reapplied with ease for other equipment such as diode arrays.

4.2 Methods

4.2.1 Theory

Profiles and penumbrae of in-phantom dose and transit images

The profiles of dose inside a phantom and of its transit image differ for multiple reasons. The width of the 20-80% dose penumbra (20% to 80% of the maximum value, along the dose profile) within a phantom is primarily due to loss of lateral electronic equilibrium and varies with depth, density, field size, and energy. For example, a 6 MV beam in water has a dose penumbra between 5 – 10 mm at depths of 1.5 – 20 cm for a 10x10 cm² field.^{131, 132} The profile of a transit image (i.e. produced by the same radiation field which delivers the dose) is determined primarily by finite source size, transmission through collimators, and glare,⁶⁹ and by the photons scattered in the phantom that reach the imager. The distribution of these scattered photons is geometrically magnified at the imager location (20 – 40 cm downstream of the phantom) compared to where dose is calculated (inside the phantom). The net effect of scatter from the phantom to the transit

image is a wide signal of standard deviation 8 – 30 cm (Figure 4-2, green dash-dot) that sums to the primary signal ⁷³. The overall combination of these effects results in transit images that have much smaller 20-80% penumbra than the corresponding in-phantom dose penumbra. As a result, to go from a portal image to a dose map, the profile must be widened: convolution of the image by a smoothing kernel is an efficient way to achieve this goal. ^{9, 133}

In this paper we use EPID transit images to model the in-field dose in phantoms, at the depth of the isocentre. To this aim, we define two quantities similar to penumbra. The *50%-to-max dose* is the region of the dose profile from the field edge to the point of maximum dose, or to the first local maximum in the case of horns. The *50%-to-max signal* are the corresponding projected points of the EPID transit image, i.e. the section of the image ‘in the shadow’ of the 50%-to-max dose profile. Note that the first and last point of the 50%-to-max signal may not coincide with 50% and maximum of pixel intensity. Both these quantities are defined along the central *x* and *y* profiles, and much of the above considerations on 20-80% penumbra apply to the 50%-to-max profiles.

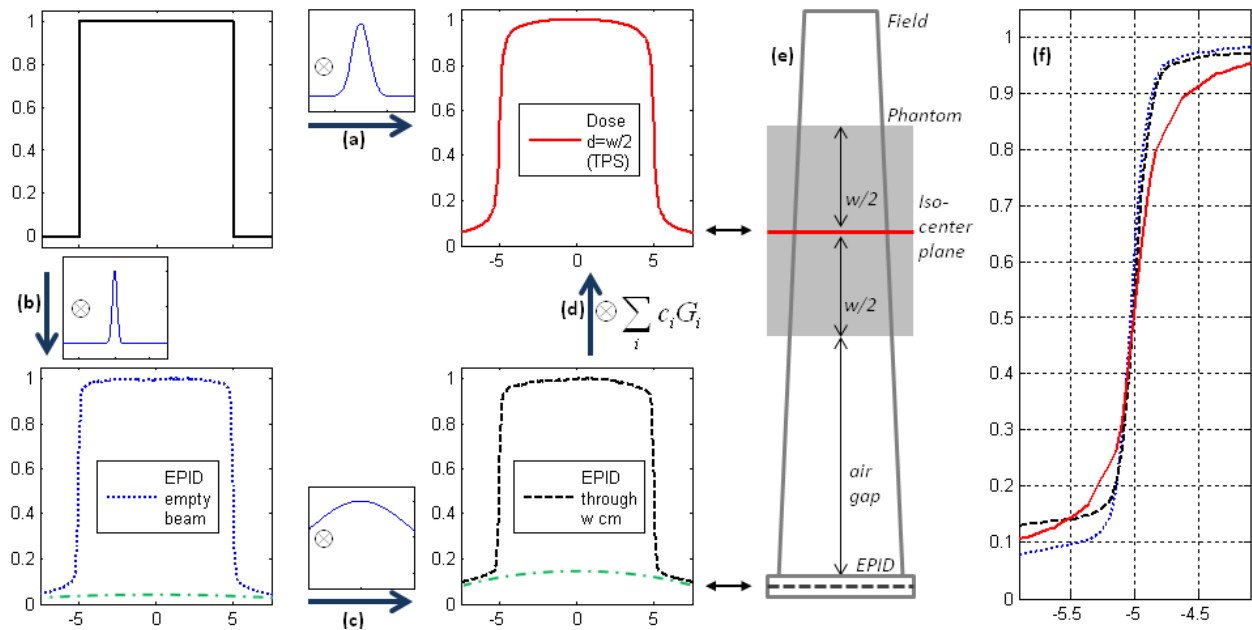


Figure 4-2. Theoretical framework of the multi-Gaussian approach. (a) Dose profile at isocentre depth in phantom (red) may be modelled as a boxcar function (black) convolved (\otimes) with a Gaussian (SD ~ 3.2 mm).⁹ (b) Similarly, the EPID signal (blue dotted) from an unperturbed beam can be modelled by convolution of the boxcar with a thin (SD ~ 1 mm) Gaussian to account for imager glare and geometric penumbra. This profile is offset by a small and semi-uniform scatter component (green dash-dot) due to photons scattered from the gantry head. (c) To model a transit image (black dash) one must consider also the photons scattered in the phantom that reach the imager (green dash-dot). This can be modelled by convolution with a wide Gaussian (SD ~ 10 cm). (d) We propose *in vivo* dose modelling from the transit EPID signal by convolution with a linear combination of Gaussians, G_i . (e) Schematic of experimental setup, illustrating transit EPID images obtained through slab phantoms of thickness w vertically centered about the isocentre. (f) Zooming in on the left edge of the dose (red) and EPID signals (blue dotted, black dashed) illustrates differences in the profiles. Data from: 6 MV, 10×10 cm² field, $w=25$ cm. All plots are normalized to unity. X-axis is distance (cm) from CAX. Scatter from phantom (green dash-dot) is an estimate, for illustrative purposes.

Multi-Gaussian optimization

For the purpose of modelling in-phantom dose profiles from EPID transit image profiles we built a four-Gaussian optimizer in MATLAB. Previously, Witte *et al.*¹²⁹ used a bi-Gaussian convolution to describe penumbra in heterogeneous media, building upon the penumbra model by Van Herk *et al.*⁹ Here, the use of four Gaussians (G_1 - G_4) may be related to physical phenomena: (i) dosimetric penumbra (present in the dose profile but not in the image profile) for small fields (<10 cm squares) and shallow depths (<10 cm); (ii) dosimetric penumbra for larger fields and greater depths; (iii) the dose profile's shoulder region (>80% of CAX value), mainly due to loss of lateral scatter. The optimizer minimized the quantity shown below, by iteratively searching for the optimal values of the coefficients c_{1X} - c_{4X} .

$$\sum_x |D^{TPS}(x) - [c_{1X}G_1 + c_{2X}G_2 + c_{3X}G_3 + c_{4X}G_4] \otimes S^{EPID}(x)| \quad \text{Equation 22}$$

D^{TPS} and S^{EPID} are the treatment planning system (TPS) 50%-to-max dose and 50%-to-max EPID signal along the central cross-plane axis x . We did not model the dip between the 'horns', present in some shallower dose profiles, to allow better modelling of the peripheral region of the field.

The optimization made use of the built-in MATLAB function *fminsearch*, an unconstrained non-linear derivative-free method, with the maximum number of iterations set at 10,000. The starting points for c_{1X} - c_{4X} were four random numbers between 0 and 1, and multiple iterations pointed to the same solutions, indicating that the optimizer did not get stuck in local minima. Similarly, along the in-plane central axis y , we found coefficients c_{1Y} - c_{4Y} that minimized Equation 23.

$$\sum_y |D^{TPS}(y) - [c_{1Y}G_1 + c_{2Y}G_2 + c_{3Y}G_3 + c_{4Y}G_4] \otimes S^{EPID}(y)| \quad \text{Equation 23}$$

In preliminary work we found that the following values provided best results: $\sigma_1=3.2$ mm (in agreement with Van Herk *et al.*⁹), $\sigma_2=2*\sigma_1$, $\sigma_3=10*\sigma_1$, and $\sigma_4=30*\sigma_1$ (in agreement with Jaffray *et al.*⁷³)

To determine whether the model could be simplified to fewer variables (Gaussians), minimum Akaike information criterion (AIC) estimate calculations^{134–136} were run. For each model X (bi-Gaussian, tri-Gaussian, quad-Gaussian) and each set of data (phantom thickness and field size) we calculated:

$$AIC_X = N \ln(SS_X) + 2P_X \quad \text{Equation 24}$$

where N is the number of points in the 50-100% section of the profile, SS_X is the sum of squares of the difference between the model (convolution of EPID profile and multi-Gaussian) and the reference (TPS dose profile), and P_X is the number of parameters (Gaussians) in the model. The equation with minimum AIC is regarded as the best representation of the data. In 11 of the 56 geometries (28 per energy), the 4-Gaussian model represented the data better than the 3-Gaussian, and in all cases the bi-Gaussian model was sub-optimal. To provide a framework of wider applicability, we chose to retain the 4-Gaussian model.

4.2.2 Materials and measurements

Planned dose was calculated using Eclipse treatment planning system (TPS, Varian Medical Systems, Palo Alto, CA) AAA version 11.0.31 with a 2.5 mm calculation grid.

EPID images were taken with aS-1000 mounted on a Clinac 21 EX (Varian Medical Systems) operating in *cine* (continuous acquisition) mode located at source-detector distance of 150 cm. Images were taken with 100 MU (6 MV and 15 MV) for square fields of size 5, 10, 15, 20 cm through solid water slab phantoms (Gammex, Middleton, WI) of thickness $w=5-35$ cm in

steps of 5 cm, vertically centered about the isocentre (Figure 4-2.e). The resultant air gap between the bottom of the phantoms and the imager ranged from 47.5 cm to 32.5 cm. Images were corrected for pixel offset and gain by means of dark field (DF) and flood field (FF) images. The flood field was acquired through 20 cm of solid water, approximating patient thickness, to allow closer match between transit image profile and in-phantom dose profile. A standard empty beam FF would cause the transit image to lose the characteristic ‘horns’ of the dose profile. Each image was then inverted to the negative image and offset by 2^{14} (the EPID is a 14-bit system) to make pixel value proportional to dose.¹¹⁸ Finally, all cine images in one set were summed into one image. To account for imager sag, the image profile was re-aligned to the dose profile. This was achieved by measuring the width of each profile, between the two 50% values, and translating the image accordingly. Analysis was performed in MATLAB (The MathWorks Inc. Natick, MA).

For each combination of field size and phantom thickness, $c_{IX} - c_{4X}$ and $c_{IX} - c_{4X}$ were calculated by minimizing Equation 22 and Equation 23. Each transit image was then convolved by its corresponding multi-Gaussian to produce an EPID-calculated map, normalized to planned dose. To quantify results, we performed a point-to-point dose difference between the central profiles of the TPS dose and the EPID-calculated dose.

4.3 Results

A representative result for a single energy / phantom thickness / field size combination is given in Figure 4-3.

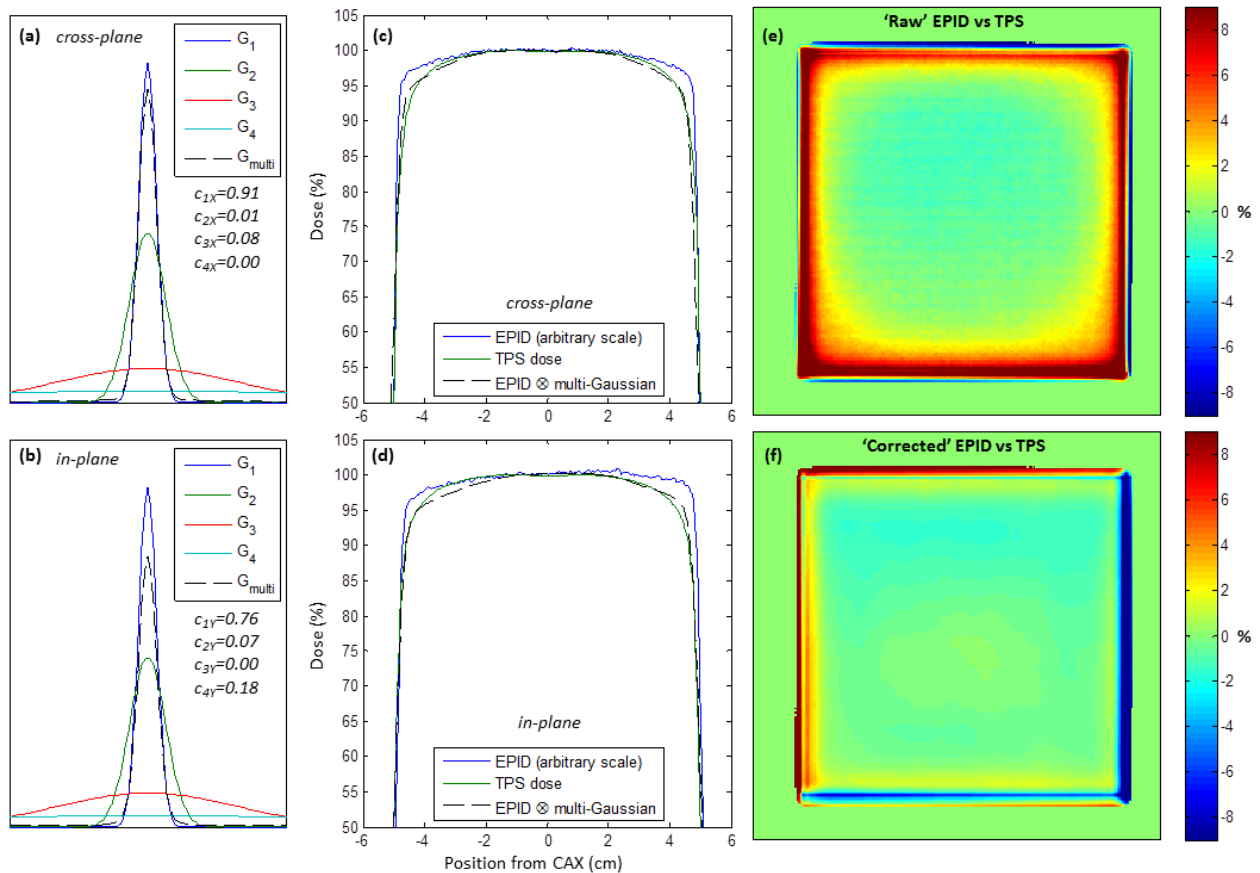


Figure 4-3: Representative results for the multi-Gaussian optimization algorithm. (a,b) The optimal coefficients differed between cross-plane and in-plane central profiles, producing different multi-Gaussian kernels (black dashed). (c,d) Convolution of the normalized EPID transit image by the corresponding kernel approximates TPS dose. (e) Pixel-by-pixel comparison of TPS dose map to map calculated from the EPID image with no off-axis correction, highlighting the differences in the shoulder region. (f) Conversely, applying the multi-Gaussian convolutions for every row and column of the EPID image gives a map which better approximates the dose map. (Data: 6 MV, 10x10 cm² field, 20 cm phantom, 10 cm depth. Values < 50% of CAX not plotted.)

The distribution of weights grouped by field size is given in overlaid box plot form in Figure 4-4. For 6 MV, the Gaussian of 3.2 mm SD is the most relevant, in agreement with Van

Herk *et al.*⁹ For 15 MV, on the other hand, the 6.4 mm Gaussian is of equal or greater importance in describing the data.

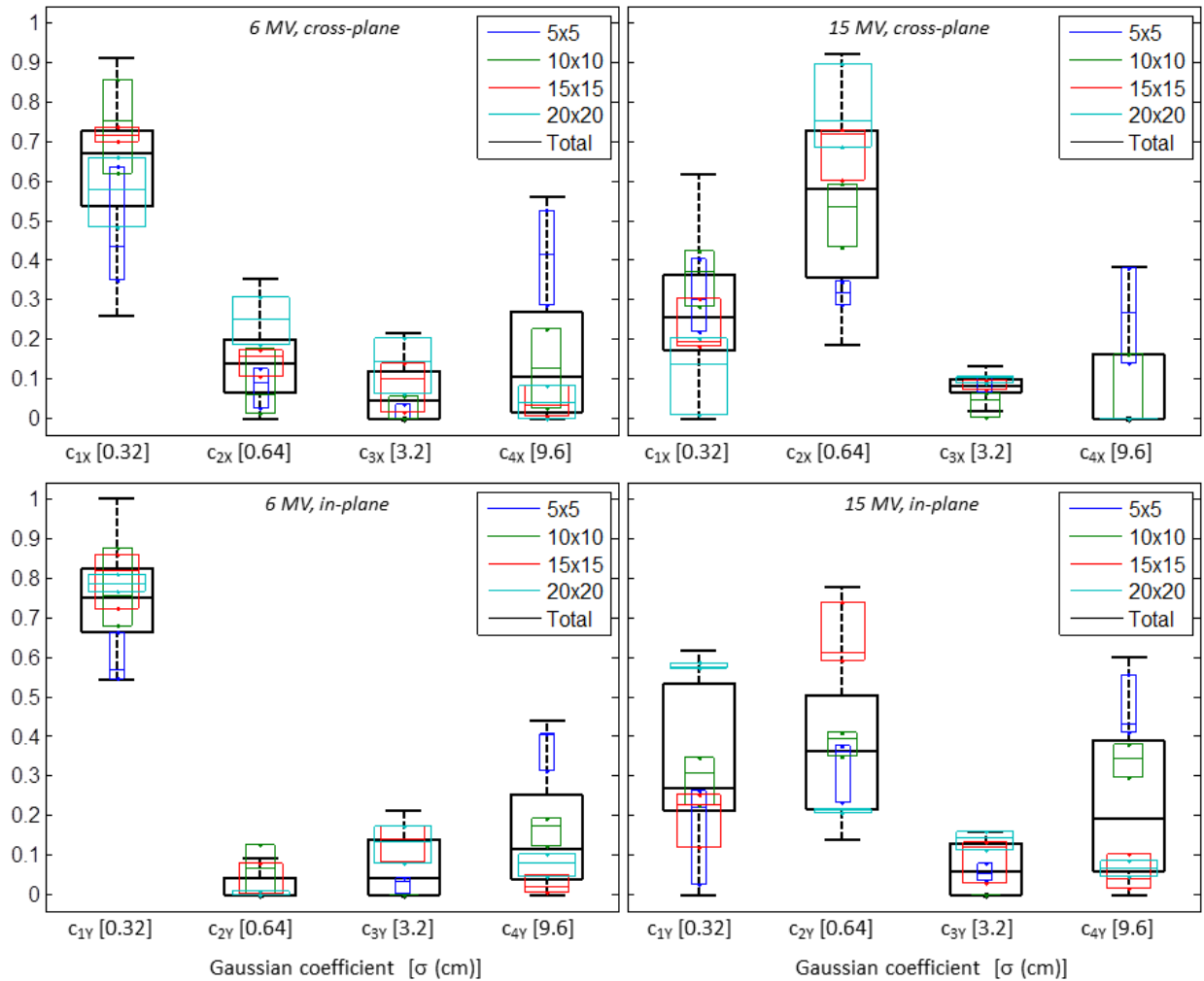


Figure 4-4: Coefficients (weights) resulting from the optimization. Black box plots include the 28 data sets, each panel is different energy and profile orientation. For 6 MV (a, b), the Gaussian of SD 3.2 mm is the most important in describing dose profiles, while for 15 MV (c, d) the second Gaussian becomes more relevant. Data is also separated by field size (colours). There is dependence of some coefficients with field size: smaller fields have more heavily weighted G₄. (Box is 25th–75th percentile, inscribed line is median, whiskers include all non-outlier data, no whiskers on field size (colour) boxes for clarity).

Multiplying the weights in Figure 4-4 by the corresponding Gaussians, we constructed the multi-Gaussian kernels reported in Figure 4-5 (normalized by area). Grouping the multi-Gaussians by phantom thickness rather than field size showed no dependence (data not shown).

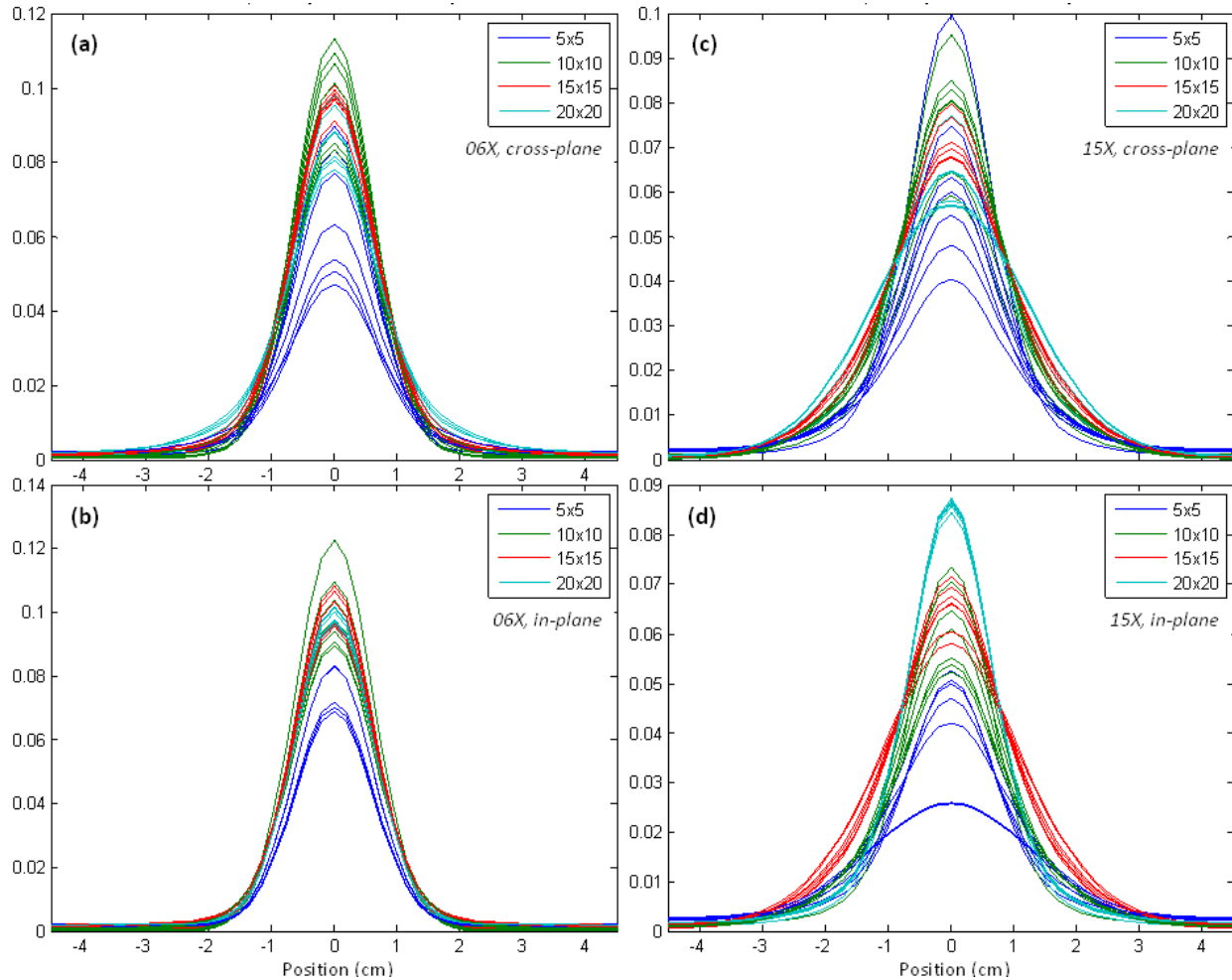


Figure 4-5: Multi-Gaussian curves resulting from the coefficients in Figure 4-4. In almost all cases, the smallest fields need the widest Gaussians to model dose from EPID transit images. (All curves are normalized to area=1. Vertical axis is a.u. Tails are not shown.)

Figure 4-6 displays the percent difference between TPS dose and the convolution of the corresponding EPID image profile by the associated multi-Gaussian, normalized to have the same maximum value. For 6 MV, excluding the 5 cm phantom, the mean percentage of points

inside the field (>50% of CAX dose) that differ by <2% with respect to the planned dose was 95% for cross-plane and 97% for in-plane profiles (Figure 4-6, a and b). For 15 MV, 83% (cross-plane profiles) and 77% (in-plane profiles) of points, on average, had a dose difference of < 2%, resulting in overestimation of up to 5% (Figure 4-6 c and d).

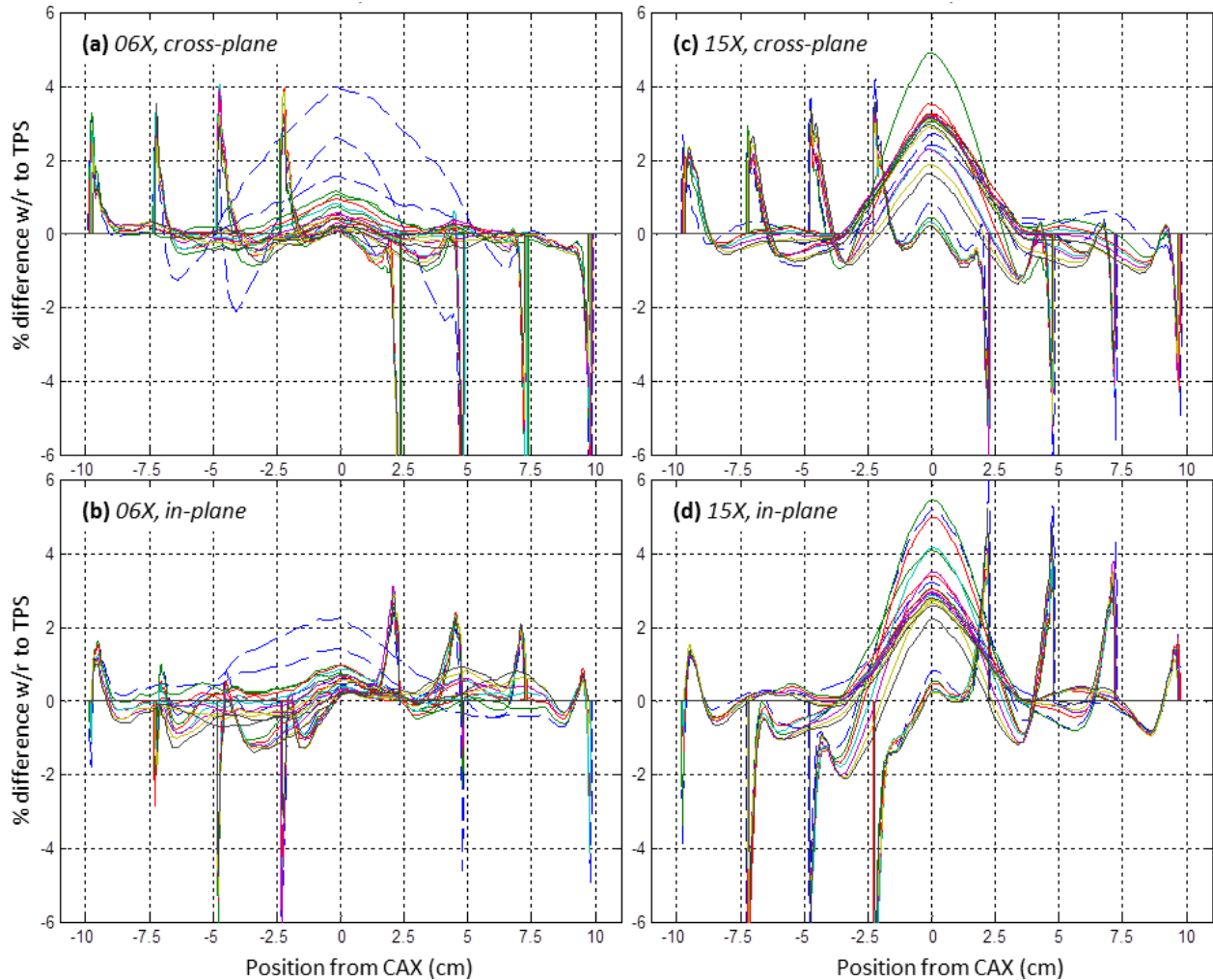


Figure 4-6: Global percent difference between planned dose and portal image multi-Gaussian convolution for all 28 phantom thicknesses and field size combinations. Excluding the high dose gradient field edges, the difference is generally within 1% for 6 MV (a, b). For 6 MV through 5 cm (blue dashed) and for most 15 MV profiles the difference is larger due to the dip between the horns, which is not modelled.

4.4 Discussion

The proposed EPID-based dose estimation approach is accurate for all 6 MV deliveries excluding the 5 cm phantom (Figure 4-6). For most 15 MV fields, on the other hand, accuracy is up to 5%. This is because the algorithm does not model the dose dip between the horns, which is greater for 15 MV and for shallower depths. In our EPID *in vivo* dosimetry, we developed a separate empirical 2D correction to account for this, based on a ratio of planned to EPID-calculated dose.¹³⁰

The weights in Figure 4-4 and kernels in Figure 4-5 show dependency with field size (colours). In particular, the dose profiles of the smallest fields are best modeled with heavier weighting of the widest Gaussian. This may seem counter-intuitive, because smaller fields generally have narrower penumbra (mainly due to reduced in-phantom scatter) and thus would require narrower convolution kernels for the same input function. In our model, on the other hand, the input function for the convolution is the profile of the transit image, which also changes with field size. In particular, the dose profile widening at isocentre depth is mainly due to photons scattered upstream, from the top half of the phantom (which is vertically centered about the isocentre), while the image profile widening is due to scatter from the entire phantom thickness. Moreover, the distribution of the latter is magnified by the increased distance and field divergence. As the field size is reduced, so are these scatter contributions. As a result, for small fields, convolution of the transit image profile by a wider kernel is needed to model the dose profile

There are three more confounding factors that may affect the field size dependency of the kernels. First, the 50%-to-max profiles on which the optimization was performed were of different lengths: shorter for smaller fields and thinner phantoms, longer for larger fields and

thicker phantoms. Second, the $5 \times 5 \text{ cm}^2$ field edge may be falling inside the horns. Third, changing field size there may be differences in the head scatter that reaches the isocentre plane with respect to that reaching the imager plane.

Finally, although the field size dependency of the kernels in Figure 4-5 is apparent, the coefficients in Figure 4-4 display large variability. This is likely due to the redundancy of the model, i.e. similar kernels can be obtained with different combinations of the four starting Gaussians. While reducing the number of Gaussians would simplify the model and likely reduce variability in the weighting factors, AIC calculations showed that for some field size and phantom thickness combinations that would result in suboptimal modeling.

Interestingly, there is no apparent dependency of the kernels with attenuator thickness. This too is counter-intuitive, as penumbra is known to increase with depth. Once again, the solution is likely in the fact that both the input function (the 50%-to-max signal of the image profile) and the product of the convolution (the 50%-to-max of the dose profile at isocentre depth) change with phantom thickness, but in this case the relative change between the two is negligible.

The process of two subsequent 1D convolutions (with two different kernels) is advantageous compared to a single 2D convolution by a symmetrical kernel. While TPS dose profiles are symmetric, cross- and in-plane EPID profiles have different shapes for multiple reasons. One factor is that the focal spot is not circular, but rather an ellipse oriented along the x and y axis.^{55, 137} As a result, geometrical penumbra is different in the two profiles. As well, penumbra may be different due to differences between collimators. In jaw-defined fields, for example, the two sets of jaws are at different distances from the source. In some recent linear accelerators, the multi leaf collimator replaces a set of jaws, likely causing differences in

transmission and geometric penumbras in the two directions.¹³² Finally there may be differences linked to backscatter artifacts from the robotic arm behind the imaging panel.¹³⁸

There is also asymmetry within profiles, attributable to differences in response of the imager segments¹³⁹ in the cross-plane direction, and the superior-inferior backscatter gradient^{127, 138} in the in-plane direction. The result of the optimization is thus a compromise, a multi-Gaussian kernel which produces two profile edges which approximate the TPS profile as much as possible.

4.4.1 Application to in vivo dosimetry

The multi-Gaussian kernels obtained in this work may be applied to calculate dose in the plane at isocentre depth, extending to 2D the isocentre-only calculation proposed by Piermattei *et al.*¹⁰² In our method, the patient water-equivalent thickness along the CAX (from CT data) and the equivalent square size of the field are input to determine the ‘closest’ multi-Gaussian kernels (example: if patient equivalent thickness is 22 cm and equivalent square 13 cm, apply the kernels from phantom thickness 20 cm, field size 15x15 cm²). The transit image is then convolved in 1D by the two kernels, in-plane and cross-plane. The absolute dose value is then obtained by correlation ratios determined on the CAX as described previously.¹⁰² Although this is an approximation, preliminary results in ten rectal cancer patients are promising, suggesting the method is suitable for clinical application.¹³⁰

For further application of this method to dynamic deliveries such as IMRT or VMAT, the same procedure may be applied to each subfield. This is made possible by the choice of operating the EPID in continuous acquisition mode. It remains to be verified, though, if the

convolution kernels obtained from simple square fields will adequately model dose in irregularly shaped subfields present in highly modulated IMRT deliveries.

4.5 Conclusion

We have developed a simple method to derive dose distribution in phantoms from transit EPID images via multi-Gaussian convolution. In this semi-empirical approach the number and widths of the Gaussians are set in advance and the weight of each Gaussian is calculated with an analytical optimizer. This method can be applied in multiple settings (e.g. pre-treatment, *in vivo*) to any type of 2D detector. The results of this study have been successfully applied to patient *in vivo* dosimetry¹³⁰ by means of correlation ratios.¹⁰²

General Conclusion

In this chapter I presented a mixed theoretical-empirical method to derive 2D dose maps inside a phantom from transmission images through the phantom itself. Among other factors, this required understanding of the effect on EPID signal due to variation in phantom thickness and phantom distance from imager. The purpose of this work was to calculate 2D delivered dose at isocentre depth inside the patient during treatment, in the context of *in vivo* dosimetry. The remainder of the thesis will thus describe the application of this work inside the larger scope of 2D *in vivo* dosimetry method by correlation ratios.

Chapter Five: Improved two-dimensional EPID dosimetry by correlation ratios

General Introduction

In this chapter the general method for 2D dose reconstruction at isocentre depth from *in vivo* EPID images and correlation ratios is presented. Improvements from the first proof of concept (Chapter 3) are incorporated into the dose calculation algorithm. The primary improvement consists in planar dose modelling by 2D multi-Gaussian convolution, as described in Chapter 4. Further improvements are: pre-processing of the EPID images and backscatter correction. Appropriate information is presented to allow the reader to implement the method for any linear accelerator with a mounted flat panel EPID. Where further detail is required, the reader is referred to the relevant sources. As well, some basic tests are presented to quantify the accuracy and precision of the dose calculation. This chapter is a complete review of the dose calculation method, illustrating its benefits and acknowledging some limitations.

The notation in this chapter follows that introduced in section 2.2.3, with two exceptions. $S_{CAX25}(w,l)$ of Equation 6 (page 40) is now referred to as $S(w,l)$, since it is understood that this EPID signal is always collected on the CAX, and since the choice of number of pixels around the CAX is arbitrary. Secondly, the original notation for dose calculated at the isocentre point used by Piermattei et al.,¹⁰² D_{iso} , is replaced by the array D^{EPID}_{2D} to make it explicit that dose calculation is in the whole plane at isocentre depth. In case of dose calculation in a single point, D^{EPID}_{iso} refers to the isocentre point and $D^{EPID}_{i,j}$ to the point i,j on the isocentre plane.

This work is the product of a research project first proposed by Dr. Derek Brown, who provided guidance and assistance. Dr. Wendy Smith also provided close guidance throughout the

process. Both co-authors reviewed the manuscript and provided feedback and support. I performed the measurements, analyzed the data, and wrote the manuscript. At the time of writing, the manuscript has been submitted for publication and is undergoing peer review.

A simple method for 2D *in vivo* dosimetry by transit portal imaging

S. Peca, D. Brown, and W.L. Smith

Abstract

PURPOSE: To improve patient safety and treatment quality, verification of dose delivery in radiotherapy is desirable. We present a simple, easy to implement, open source method for *in vivo* planar dosimetry of conformal radiotherapy by electronic portal imaging device (EPID).

METHODS: Correlation ratios which relate dose in the mid-depth of slab phantoms to transit EPID signal were determined for multiple phantom thicknesses and field sizes. Off-axis dose is corrected for by means of model-based convolution. We tested efficacy of dose reconstruction through measurements with off-reference values of thickness, field size, and MU. We quantified the dose calculation error in the presence of thickness changes, to simulate anatomical or setup variations. An example of dose calculation on patient data is provided.

RESULTS: Varying phantom thickness, field size, and MU, dose reconstruction was almost always within 3% of planned dose. In the presence of thickness changes with respect to planning CT, the dose discrepancy is exaggerated for every cm of added/removed attenuator, by up to approximately 1.5% for thickness changes upstream of the reconstructed dose plane and 4% for thickness changes downstream.

CONCLUSION: Our novel EPID *in vivo* dosimetry allows clinically accurate reconstruction of dose inside a patient at isocentre depth. Due to its simplicity, commissioning can be performed in a few hours per energy, and may be modified to the user's needs. It may

provide useful dose delivery information to detect harmful errors, guide adaptive radiotherapy, and assure quality of treatment.

5.1 Introduction

The Electronic Portal Imaging Device (EPID), originally developed for patient positioning prior to treatment, may also be used for verification of radiation therapy treatment delivery. While EPID for pre-treatment verification has been investigated extensively and is common practice in many clinics, its use for *in vivo* dosimetry (IVD) is still growing.^{29, 82} EPID IVD has the potential to identify errors in dose calculation, data transfer, patient setup and motion, and dose delivery. It may also provide a valuable trigger for adaptive radiotherapy.¹⁰⁵ Most importantly, EPID IVD could have detected recent catastrophic errors which led to major injury or death.^{19, 28, 31}

The Netherlands Cancer Institute implemented an in-house EPID IVD solution⁹² and reported to have caught 17 serious errors out of 4337 verified patient plans.⁴⁴ The method backprojects dose inside the patient making use of transit (i.e. through the patient) EPID images and ion chamber commissioning measurements.¹⁰⁷ Over time, the model was improved to calculate dose in 3D,¹⁴⁰ be used in rotational deliveries,⁹⁹ and account for inhomogeneities.¹⁰¹ Others, making use of transit images and a complex image prediction algorithm,⁸⁹ achieved 3D dose reconstruction in the patient⁹¹ and 2D real-time treatment verification,¹⁴¹ both at the cost of laborious implementation and heavy computational requirements. A third group has focused on calculating the dose at the isocentre point by means of correlation ratios.^{102, 142, 143} This method has the advantage of being of simple implementation, but also has the drawback of providing

only point dose. In addition to the in-house methods above, there are currently two commercial solutions: Dosimetry Check¹⁴⁴ (by Math Resolutions) and EPIgray¹⁴⁵ (by DOSIsoft).

As the 2D and 3D EPID *in vivo* dose estimation solutions currently available are either proprietary or complex in-house methods, the need for an easy-to-implement and freely available method is apparent. We built upon the 1D model initially proposed by Piermattei *et al.*¹⁰² and further developed by the same group^{119–121} aiming to develop a solution with the following characteristics: is sensitive to gross errors and most setup errors, does not require additional instrumentation, has fast and simple commissioning, and provides 2D dose maps in the isocentre plane. Previously, we presented preliminary results in anthropomorphic phantoms for a simple method for 2D dose calculation using correlation ratios and an empirical off-axis correction.¹⁰⁴ In this paper, we describe details of our improved model and test its ability to accurately calculate dose. The purpose of this manuscript is to allow other centres to adopt this method of EPID *in vivo* dosimetry. Preliminary clinical results showed power to detect inter-fractional variations,¹³⁰ and more detailed clinical results on 10 patients are available (see Chapter 6.2). Flow charts that describe commissioning and measurement procedures are provided. As well, we investigate how changes in attenuator thickness between simulation and treatment (as in the case of most anatomy or setup variations) affect results. Our method is entirely open source, so it can be modified according to the user's needs. It is based on *cine* imaging, to allow possible extension to real-time dose verification and dynamic treatments.

5.2 Methods

5.2.1 EPID imaging

All *cine* images were obtained with a-Si 1000 EPID on a Varian Clinac 21 EX linear accelerator (Varian Medical Systems), 6 MV and 15 MV at 600 MU/min. The imager panel was placed 50 cm beyond isocentre, covering a field size of 26.8 x 20.1 cm² at isocentre. Both half-resolution (348×512, 0.4 MB per image) and full-resolution (768×1024, 1.6 MB) were investigated. Dark and flood field (FF) correction images were applied for all 4 image types: 6 MV half-res (12.86 frames/sec or f/s, 8 frames/image or f/i), 6 MV full-res (7.5 f/s, 8 f/i), 15 MV half-res (15 f/s, 4 f/i), 15 MV full-res (7.827 f/s, 4 f/i). To quantify the EPID's constancy in time, repeat *cine* images (6 MV half-res, 10×10 cm² field, 100 MU, 300 MU/min) through a 22 cm phantom were acquired at weeks 1-8, 14, and 18. Phantoms consisted in slabs of solid water (Gammex, Middleton, WI). The specific measurements presented herein apply to this particular equipment and settings, but the method is applicable to any system.

5.2.2 Commissioning procedure

Commissioning of our transit EPID IVD requires two sets of calibration images acquired with multiple field sizes through various thicknesses of phantom, and treatment planning system (TPS, here AAA Eclipse version 11.0.31, Varian Medical Systems, Palo Alto, CA) dose maps at corresponding mid-depths inside the phantom. A commissioning flow chart is displayed in Figure 5-1.

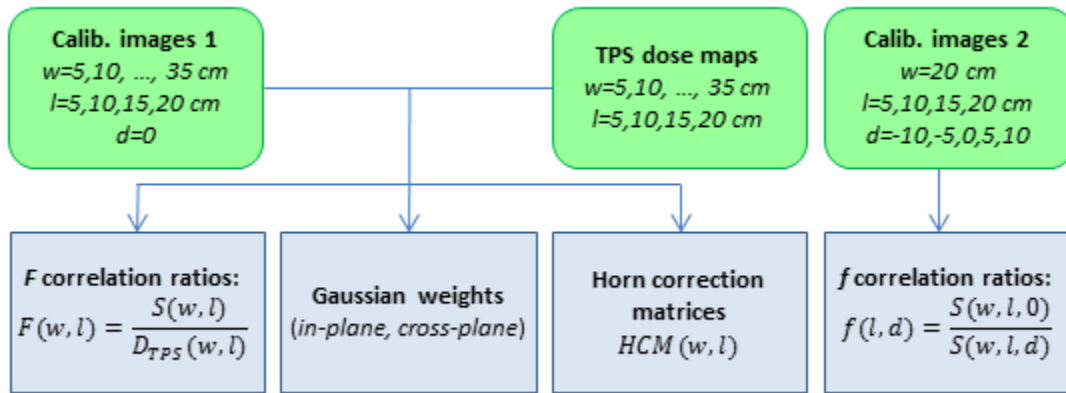


Figure 5-1: Commissioning procedure of EPID IVD by correlation ratios. Green rounded boxes represent suggested EPID measurements and TPS calculations. Blue boxes are output data, used for subsequent dose calculations, specific to machine, energy, dose rate, and imaging parameters. (w =phantom thickness on CAX, l =square field size, d =vertical displacement off-centre, see Figure 5-2.)

5.2.2.1 Dose at isocentre

The isocentre point dose estimation is based on the work of Piermattei *et al.*¹⁰² and is summarized here for completeness. We use correlation ratios, $F(w,l)$, between the EPID CAX signal through a phantom of thickness w , centered at isocentre, and the dose at mid-depth ($w/2$) from the TPS, for square fields of size l . In the case of phantom vertical off-centering by d , another correlation ratio is introduced, $f(l,d)$.

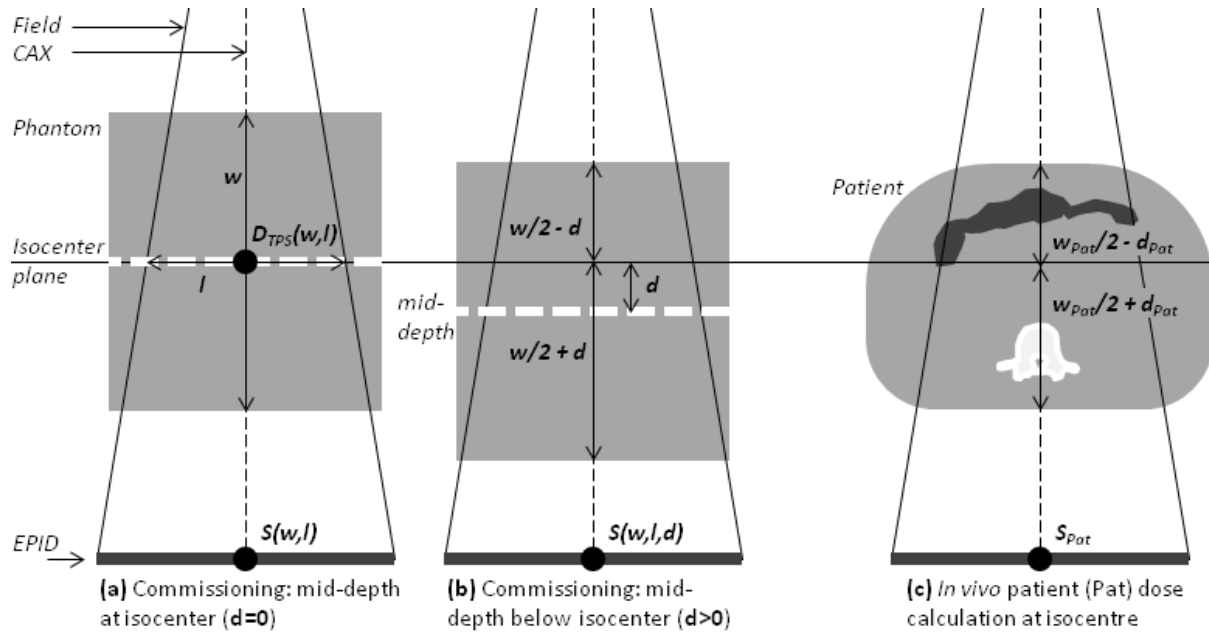


Figure 5-2: *In vivo* isocentre dose measurement by EPID, as proposed by Piermattei et al.¹⁰²

(a) Measurement of correlation ratio F (Equation 25). (a,b) Measurement of f (Equation 26). (c) Use of F , f , and TMRs to measure dose at isocentre in a patient. In our approach, we account for inhomogeneities by water equivalent thicknesses (bowel gas and vertebral body shown).

For each energy, 28 sets of EPID *cine* calibration images were collected, corresponding to seven thicknesses of solid water phantoms (5, 10, 15, 20, 25, 30, 35 cm) and four square field sizes ($l = 5, 10, 15, 20$ cm), as in Figure 5-2.a. Each *cine* set was produced by 100 MU. The total water equivalent thickness along the CAX, w , is equal to that of the phantom plus that of the couch, and was vertically centered about the isocentre. Each *cine* image set was pre-processed to determine the signal $S(w, l)$ of Figure 5-2 as follows.

1. To invert and offset the *cine* produced by the EPID, each ‘raw’ pixel value $S^{(raw)}_{i,j}$ was replaced by $2^{14} - S^{(raw)}_{i,j}$. While the original (‘raw’) 14-bit image is designed to resemble film (with lower pixel values representing greater dose), this step produced an image in which intensity is proportional to dose.

2. An FF correction image was taken through 20 cm of solid water, a ‘typical’ patient thickness.
3. Resolution was set to half-resolution, to reduce computational time.
4. *Cines* whose CAX value differed from the mean CAX value of the whole *cine* set by more than one standard deviation were replaced with the average frame from the remaining ones. This removes beam-on artifacts due to dose rate ramp up and ghosting⁸¹ while maintaining the correct number of frames.
5. All *cines* in the set were summed to produce a single image.
6. The sum image is corrected for backscatter following the method by Berry *et al.*¹⁴⁶
7. The sum image was corrected for beam-off image loss (Figure 5-3).

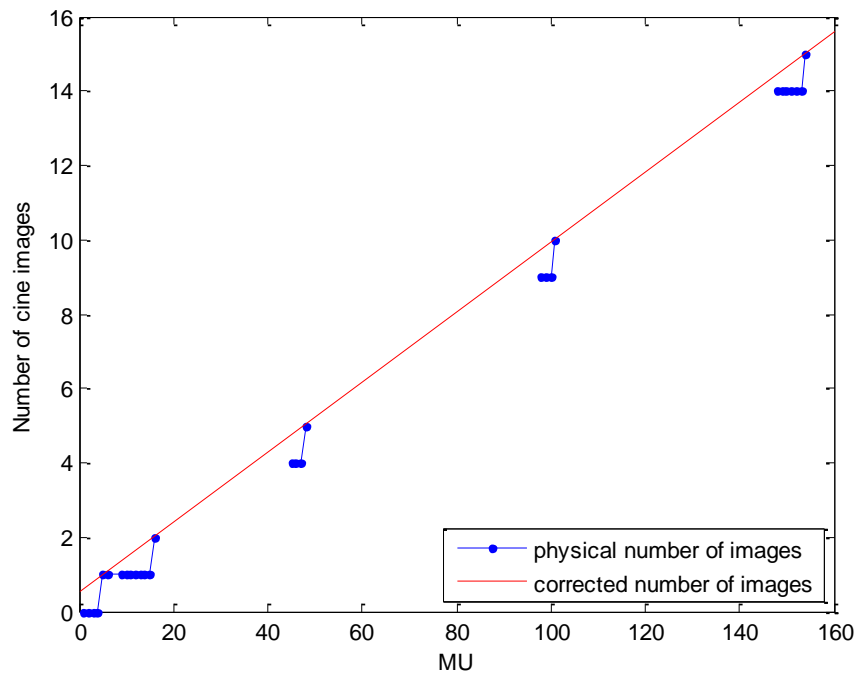


Figure 5-3: Correction for beam-off image loss. In *cine* imaging, the last frames which are too few to form an image (i.e. are < the f/i value) are discarded. This was accounted for by multiplying the image sum by the corrected (non-integer) number of images (red) for its MU value over the physical number of images (blue), found by fitting the data points characterized by the lowest number of MU per image.

For each $S(w,l)$ the corresponding TPS dose at isocentre was $D_{TPS}(w,l)$, (referring to dose at mid-depth $w/2$). $S(w,l)$ and $D_{TPS}(w,l)$, were interpolated and extrapolated to $w=45$ cm.

Correlation ratios were given (Figure 5-2.a) by:

$$F(w,l) = \frac{S(w,l)}{D_{TPS}(w,l)} \quad \text{Equation 25}$$

To account for the general case of the patient/phantom not vertically centered about the isocentre, the second correlation ratio is:

$$f(l,d) = \frac{S(w,l)}{S(w,l,d)} \quad \text{Equation 26}$$

Here $S(w,l,d)$ is the CAX signal with the attenuator shifted by d (>0 if shifted downstream, Figure 5-2.b). $f(l,d)$ ratios were measured for $l = 5, 10, 15, 20$ cm, and $d = -10, -5, 0, 5, 10$ cm (each image 50 MU, w fixed at 26 cm because dependence of F with phantom thickness is $<0.3\%$ ¹⁰²).

Making use of F and f correlation ratios, and TPS tissue maximum ratios (TMR), dose at isocentre in a patient (Figure 5-2.c) is, as per Piermattei *et al.*¹⁰²

$$D_{iso}^{EPID} = S(w_{pat}, l_{eq}) \frac{f(l_{eq}, d_{pat})}{F(w_{pat}, l_{eq})} \frac{TMR(depth = \frac{w_{pat}}{2} - d_{pat}, l_{eq})}{TMR(depth = \frac{w_{pat}}{2}, l_{eq})} \quad \text{Equation 27}$$

Here, w_{pat} and d_{pat} are the total water equivalent thickness through the patient along the CAX, and l_{eq} is the equivalent square field size of the treatment field.

5.2.2.2 From isocentre dose to 2D dose at isocentre depth

To calculate dose in the plane at isocentre depth, we applied Equation 27 for every ray line from the source to each EPID pixel i,j , with w_{pat} and d_{pat} becoming $w_{i,j}$ and $d_{i,j}$.

$$D_{i,j}^{EPID\ uncorr} = S_{i,j}(w_{i,j}, l_{eq}) \frac{f(l_{eq}, d_{i,j})}{F(w_{i,j}, l_{eq})} \frac{TMR\left(\text{depth} = \frac{w_{i,j}}{2} - d_{i,j}, l_{eq}\right)}{TMR\left(\text{depth} = \frac{w_{i,j}}{2}, l_{eq}\right)} \quad \text{Equation 28}$$

This 2D dose map is accurate at isocentre but off-axis accuracy suffers from loss of lateral electronic equilibrium in the phantom/patient. In our previous work, we proposed an empirical method to correct for this, based on the shape of F profiles for various field sizes and absorber thicknesses.¹⁰⁴ While results were good along the central in-plane and cross-plane profiles, this solution was inadequate in the corners of larger ($>10 \times 10$ cm²) fields.

Here, we modeled dose profile at phantom mid-depth by the convolution of the corresponding transit EPID image profile with an optimized linear combination of four Gaussian functions, G_1 - G_4 , standard deviations: 0.32, 0.64, 3.20, 9.60 cm. The widths of the four Gaussians were set to best model the physical phenomena involved (dosimetric penumbra dependence with phantom thickness, field size, and phantom-to-imager distance, and scatter from phantom to imager⁷³), and were appropriate according to minimum Akaike information criteria.^{135, 136} Relative weights of the four curves were determined by an in-house optimizer in MATLAB that minimized the quantity

$$\sum_x |D_{TPS}(x) - [c_{1X}G_1 + c_{2X}G_2 + c_{3X}G_3 + c_{4X}G_4] \otimes S(x)| \quad \text{Equation 29}$$

for the central cross-plane (x) and in-plane (y) profiles, resulting in two sets of four coefficients each, for every one of the 28 phantom commissioning measurements. Performing two 1D convolutions in each direction rather than a single 2D convolution allows for different kernels in each, since the imager responds slightly differently in the two directions due to differences in backscatter (e.g. from the imager arm)¹³⁸ and geometric penumbra (e.g. elliptical shape of the focal spot^{55, 137} and distances of jaws from said focal spot). The Gaussian convolution is not

capable of modeling the dose profile horns at shallow depths, especially for 15 MV. So a horn correction matrix, $HCM(w,l)$, is determined by point-by-point division of the convolved image by the TPS dose map (Figure 5-4).

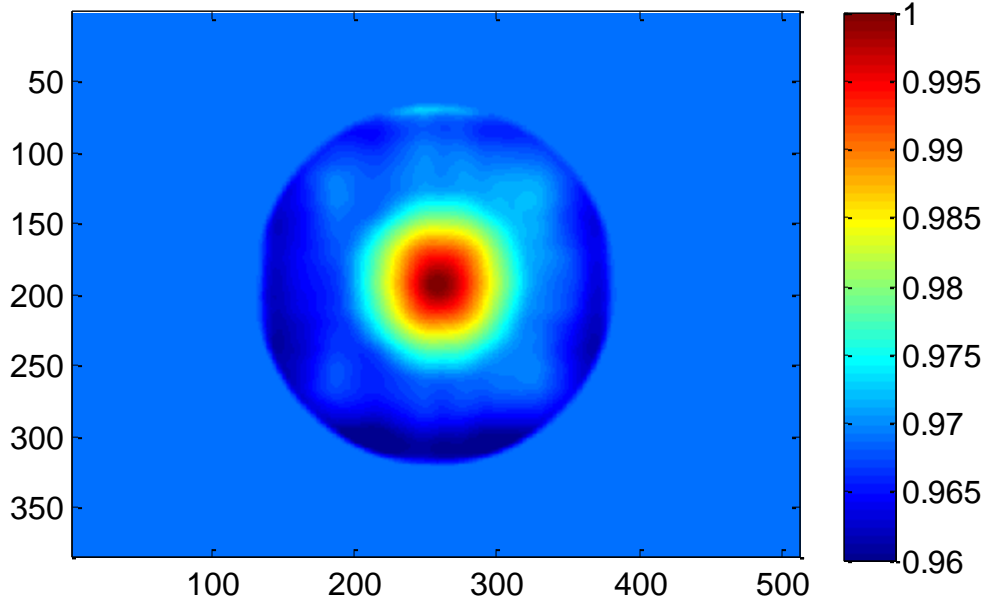


Figure 5-4: Horn correction matrix (HCM) for phantom thickness 10 cm, 15×15 cm² field. An *in vivo* dose calculation must be divided by the appropriate HCM to account beam horns. The correlation ratio F between EPID transit signal and dose in the mid-depth of the phantom was established on the CAX, hence the HCM is equal to one in the centre of the image. (Axes are pixel numbers).

The 2D dose in the isocentre plane is then (Figure 5-5):

$$\begin{aligned}
 D_{2D}^{EPID} = & D_{2D}^{EPID\ uncorr} \otimes_X [c_{1X}G_1 + c_{2X}G_2 + c_{3X}G_3 + c_{4X}G_4] \\
 & \otimes_Y [c_{1Y}G_1 + c_{2Y}G_2 + c_{3Y}G_3 + c_{4Y}G_4] \quad \text{Equation 30} \\
 & \div HCM(w_{pat}, l_{eq})
 \end{aligned}$$

where \otimes_X and \otimes_Y are 1D convolutions in the cross- and in-plane directions.

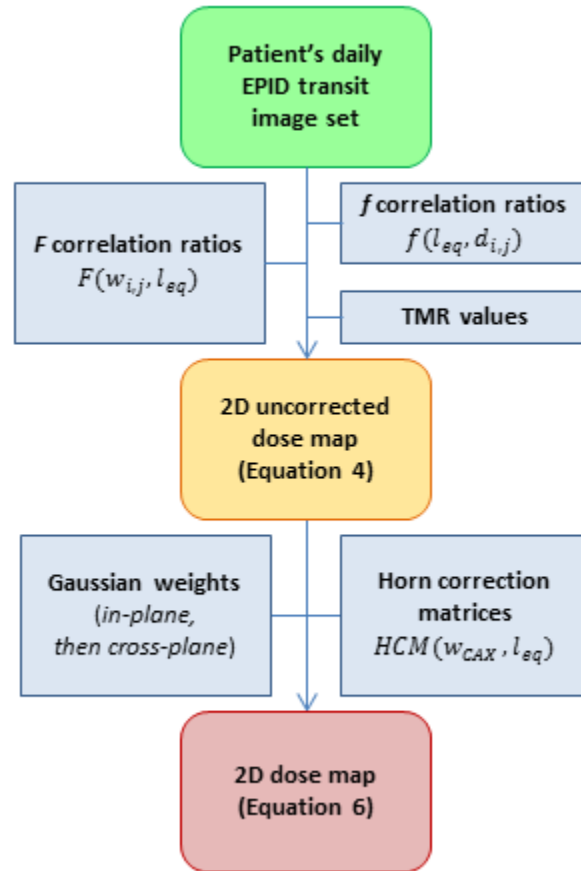


Figure 5-5: Two-dimensional EPID dose calculation from patient/phantom images.

5.2.3 Testing

5.2.3.1 EPID dose vs MU, field size, and thickness

To test dose calculation, images were taken with both 6 MV and 15 MV energies through slab phantoms:

1. Versus MU: 40, 80, 120, 160, and 200 MU ($w=20$ cm, $l=10$ cm, half-res & full-res).
2. Versus l and w : For half-res, $l = 7, 12, 17$ cm and $w = 12, 22, 32$ cm. For full-res: $l = 8, 16$ cm and $w = 6, 28$ cm.

Measured and planned dose maps were compared: on the CAX, pixel-by-pixel, and by means of 3% / 3mm gamma evaluations. This gamma criteria was chosen because it is the most prevalent¹⁴⁷ and useful for comparison with other techniques.

5.2.3.2 Accuracy in the presence of thickness errors

A characteristic limitation of using planning CT data (*i.e.* thickness w) to calculate dose delivered at treatment is that the CT may not accurately reflect the patient at time of treatment (actual thickness $w + \Delta w$). If this occurs, the calculated EPID dose will have a systematic error, quantified here as the ratio between D'_{EPID} , calculated with w values obtained from planning CT, and D_{EPID} , calculated with the actual patient thickness $w + \Delta w$. If the thickness changes by Δw (>0 for thickness increase and vice versa) upstream, downstream, and symmetrically with respect to the isocentre, the ratios of apparent to true EPID doses are (making use of Equation 27, see 5.6: Appendix for derivation) respectively:

$$\frac{D'_{EPID,up}}{D_{EPID,up}} = \frac{TMR\left(\frac{w}{2} + \frac{\Delta w}{2}, l\right)}{TMR\left(\frac{w}{2} + \Delta w, l\right)} \frac{1}{f\left(l, -\frac{\Delta w}{2}\right)} \frac{F(w + \Delta w, l)}{F(w, l)} \quad \text{Equation 31}$$

$$\frac{D'_{EPID,down}}{D_{EPID,down}} = \frac{TMR\left(\frac{w}{2} + \frac{\Delta w}{2}, l\right)}{TMR\left(\frac{w}{2}, l\right)} \frac{1}{f\left(l, \frac{\Delta w}{2}\right)} \frac{F(w + \Delta w, l)}{F(w, l)} \quad \text{Equation 32}$$

$$\frac{D'_{EPID,symm}}{D_{EPID,symm}} = \frac{F(w + \Delta w, l)}{F(w, l)} \quad \text{Equation 33}$$

Analytical calculations of Equation 31 to Equation 33 were performed on the CAX for $\Delta w = +1$ cm, for the commissioning ranges of w (5-45 cm) and l (5-20 cm).

5.2.3.3 *In vivo* calculation

Proof of concept was tested with analysis of patient *cine* images, obtained as part of a trial approved by the Conjoint Health Research Ethics Board of the University of Calgary. The *in vivo* gamma analysis criteria was loosened to 5% / 3mm to account for acceptable setup and anatomical differences, as employed by previous reports.^{119, 120}

5.3 Results

The CAX EPID signal range over 18 weeks was 0.9% of the median signal. This variability did not follow any discernible trend. F and f correlations ratios were in agreement with previous reports^{102, 104} (example: F for 6 MV in Figure 5-6).

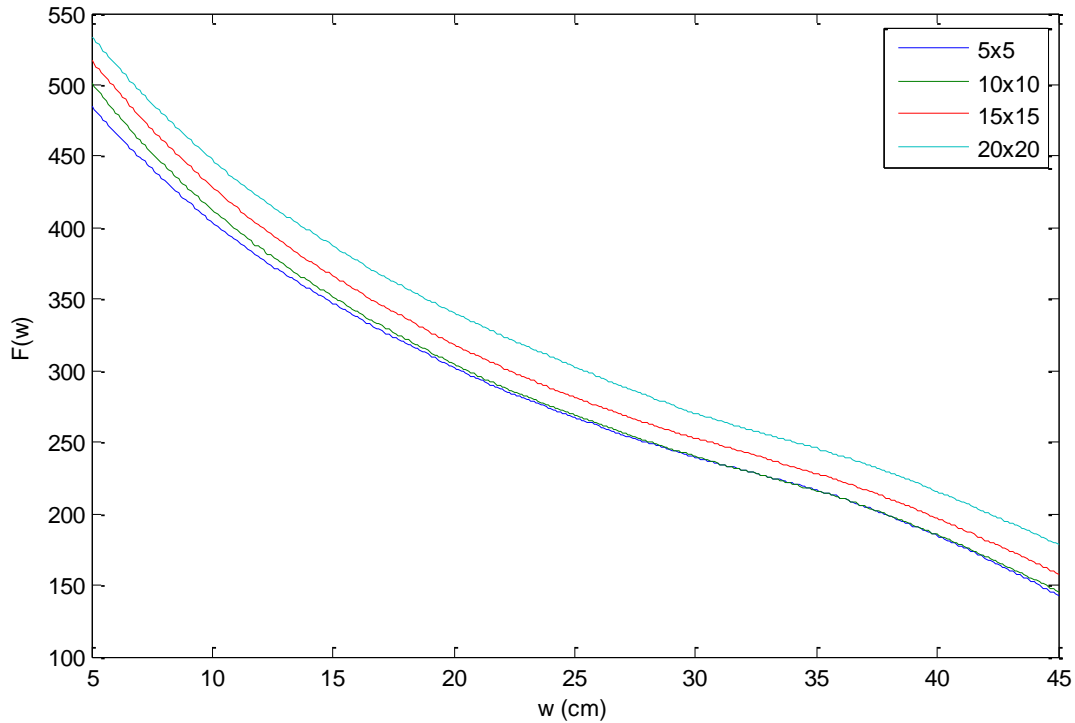


Figure 5-6: F correlation ratio for 6 MV.

5.3.1 EPID dose vs. MU, field size, and thickness

The number of frames required to achieve a stable signal depended on imaging parameters (Figure 5-7), and was approximately 1.2 sec and 2.4 sec for the 6 MV and 15 MV beams respectively. The magnitude of the effect did not depend on total MU.

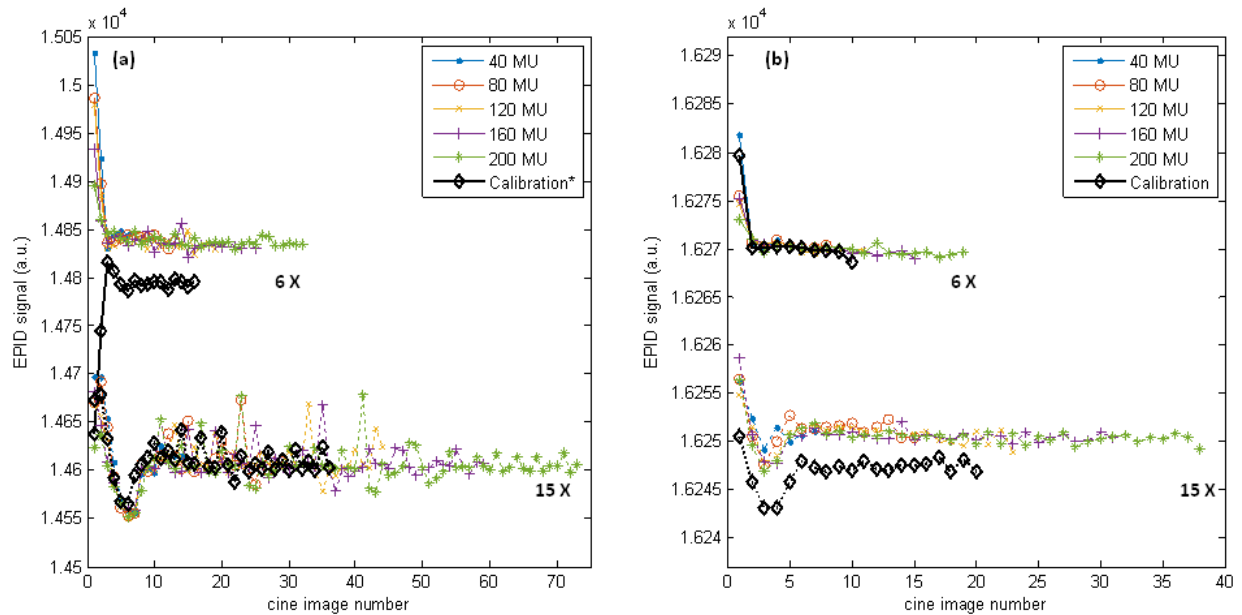


Figure 5-7: (a) Half-resolution and (b) full resolution CAX $S^{(raw)}$, for both energies, $l=10$, $w=20$. Higher $S^{(raw)}$ corresponds to lower dose. In all cases, the first images are susceptible to linear accelerator ramp-up artifacts⁷⁴ and were therefore removed. For 6 MV half-resolution, a correction factor was introduced to account for the systematic offset. Note that the scale of (b) is 10 times smaller, so no other correction factors were necessary.
***Acquired 9 months before all other images, before imager upgrade.**

Agreement between planned and measured dose for different MU values was generally within 3% (Figure 5-8). On the CAX, mean deviation was $(0.26 \pm 2.23) \%$. Two of the 20 tests, both at the lowest MU value, failed a 3% / 3mm gamma evaluation and had the largest CAX deviations, -3% and +8%. These are due to the beam loss correction, which is limited by the impossibility to deliver fractions of a MU, and whose relative uncertainty is larger with fewer images (i.e. low MU). The best agreement is at 100 MU where the F factors were measured: calibration dose should be close to delivered field dose to optimize accuracy.

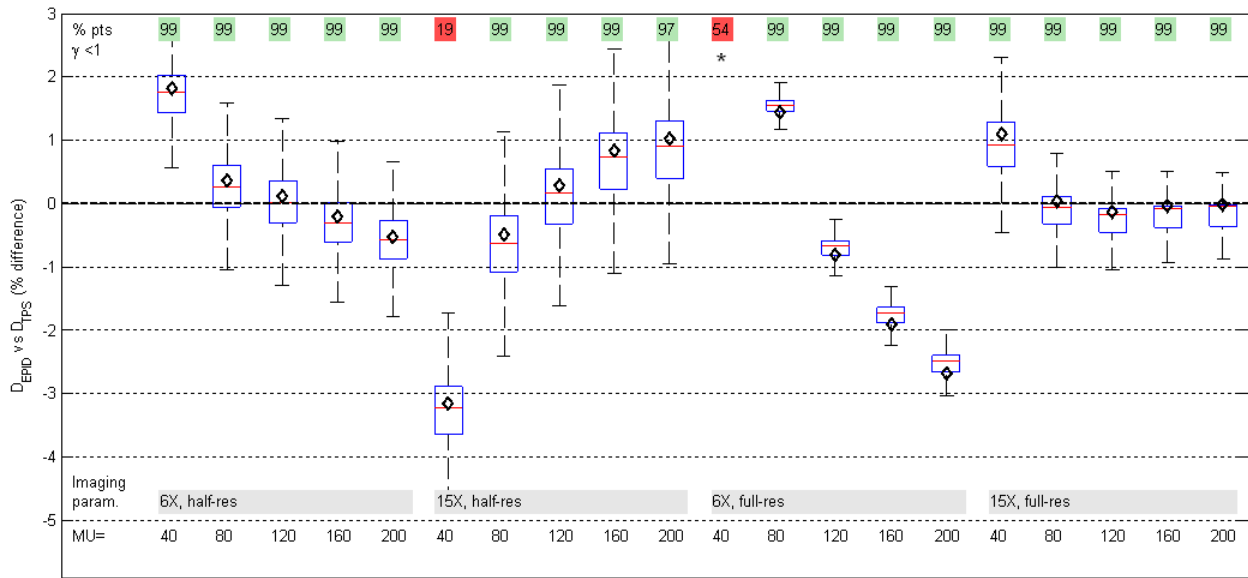


Figure 5-8: Boxplot of pixel-by-pixel dose differences between EPID and TPS dose maps, varying MU. Box edges are the 25th and 75th percentiles; red line is median. Dose maps passed a 3% / 3mm gamma analysis in all but two of the lowest MU tests (top row). In all but three cases, the CAX EPID dose (black diamond) was within $\pm 2\%$ of the TPS. (Whiskers are set at $q_3 + 1.5(q_3 - q_1)$ and $q_1 - 1.5(q_3 - q_1)$, where q_1 and q_3 are the 25th and 75th percentiles, respectively. This corresponds to approximately $\pm 2.7\sigma$ and 99.3% coverage if the data are normally distributed. Outliers not plotted. *Out of scale, +8%.)

The EPID dose calculation showed good agreement with the TPS for non-reference field sizes and solid water thicknesses (Figure 5-9). On the CAX, mean deviation from TPS value was $(-0.23 \pm 0.97) \%$. In 24 out of the 26 fields, $>97\%$ of points passed the gamma 3% / 3mm evaluation.

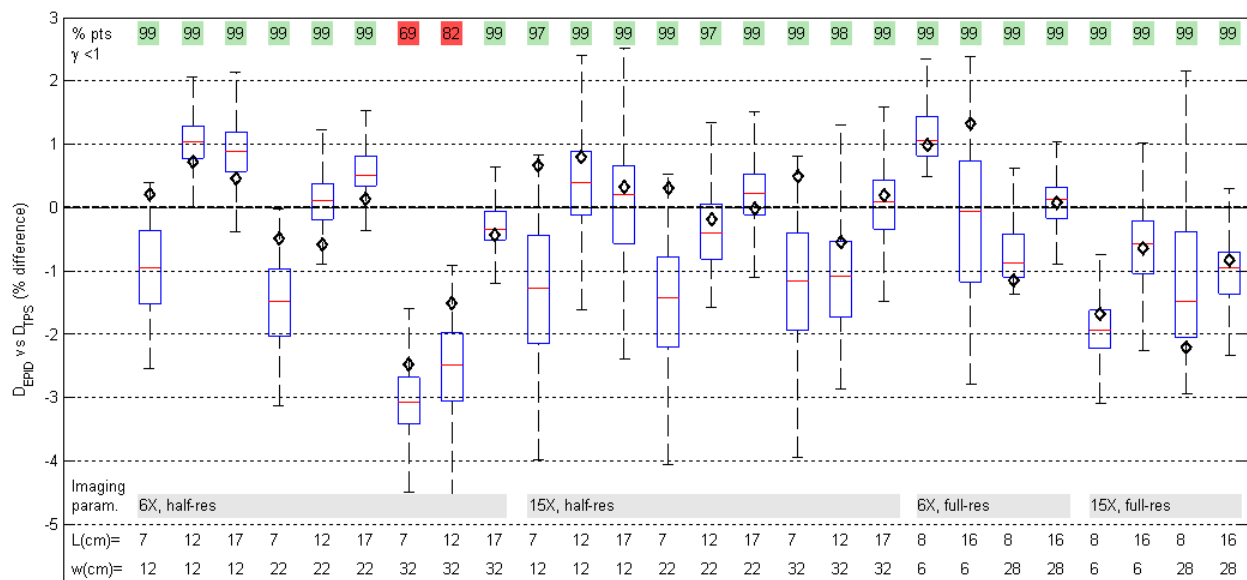


Figure 5-9: Boxplot of pixel-by-pixel dose differences shows good agreement between EPID and TPS dose maps, varying square field size (l) and absorber thickness (w). In all but two cases, the CAX EPID dose (black diamond) was within $\pm 2\%$ of the TPS.

5.3.2 Accuracy in the presence of thickness errors

Changes in patient characteristics from the planning CT have a complex impact on the accuracy of dose estimation at the isocentre plane from the EPID cine images (Figure 5-10). If the water equivalent thickness changes by 1 cm upstream of the isocentre, the estimated dose is generally within $\pm 1.5\%$ of the actual dose for 6 MV and $\pm 0.5\%$ for 15 MV. On the other hand, changes downstream of the isocentre result in poorer estimates: within $\pm 4.5\%$ for 6 MV and $\pm 3.0\%$ for 15 MV. The shape of the Figure 5-10 curves is due to F factor characteristics. With increasing thickness, the air gap between the phantom and the imager shortens, increasing the CAX EPID signal, S . For even larger thickness ($w > 30$ cm), more photons scattered in the phantom are absorbed by the phantom itself, decreasing S and causing an inflection point at 30-35 cm in Figure 5-6. This causes a maxima when calculating the ratio $F(w)/F(w+1)$ (Figure 5-10

a and c) and a minima when calculating $F(w)/F(w-1)$ (Figure 5-10 b and d). Lastly, the behavior of D'_{EPID}/D_{EPID} at shallow depths for 15 MV is due to proximity to the depth of maximum dose (dose is calculated at mid-depth, $w/2$).

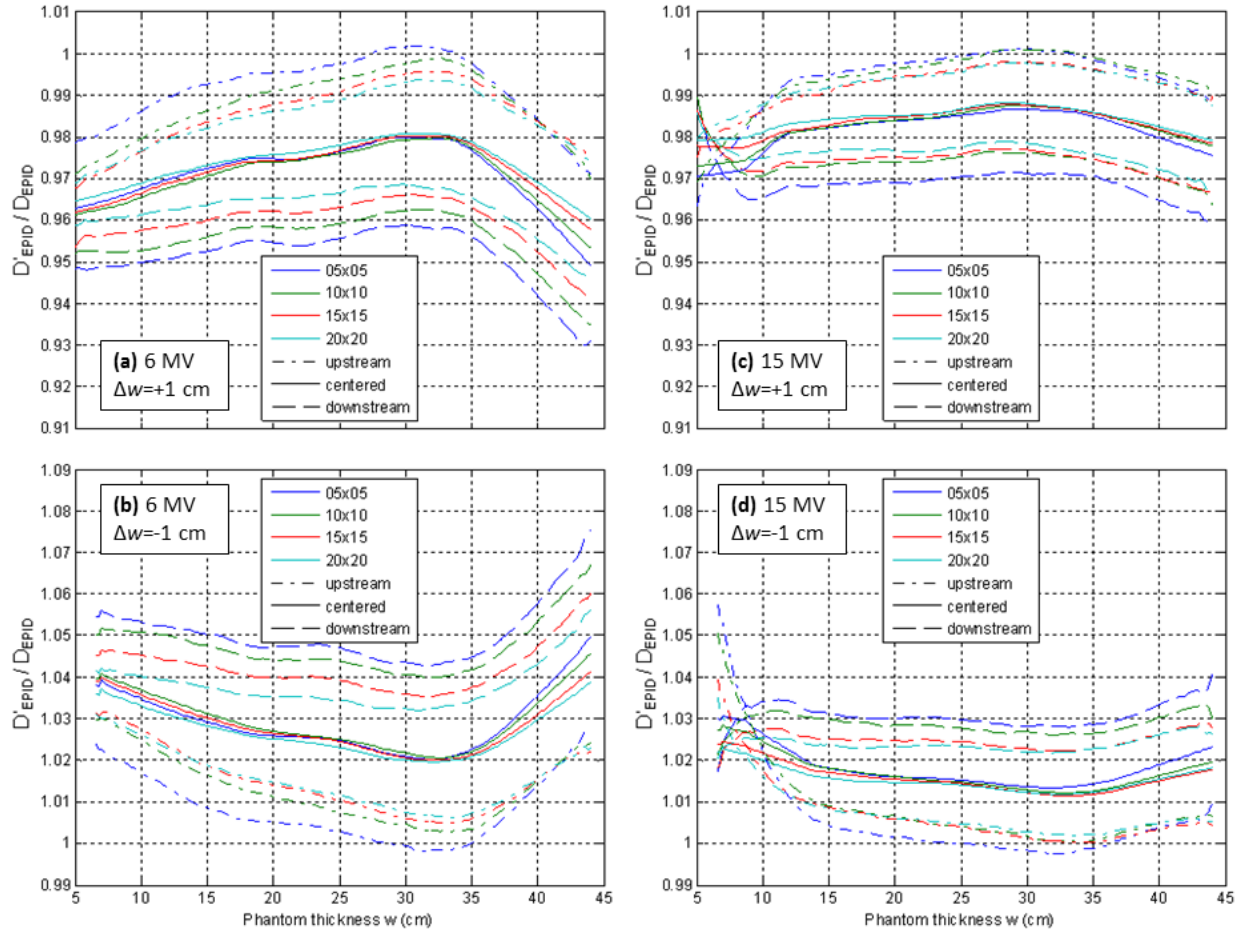


Figure 5-10: In phantoms of thickness $w \pm \Delta w$, the ratio of dose measured with CT-calculated thickness w to dose measured with CT-calculated thickness $w \pm \Delta w$. In the case of patient tissue gain/swelling ($\Delta w = +1$, top), planning CT thickness causes EPID to underestimate dose. The dose calculation error is largest for thickness changes downstream of the isocentre (dashed), and is larger for 6 MV (left) than 15 MV (right).

5.3.2.1 *In vivo* calculation

EPID dose calculation with real patient data (CT and *in vivo* transit portal images) is shown (Figure 6-5), with 98% of the field passing gamma evaluation.

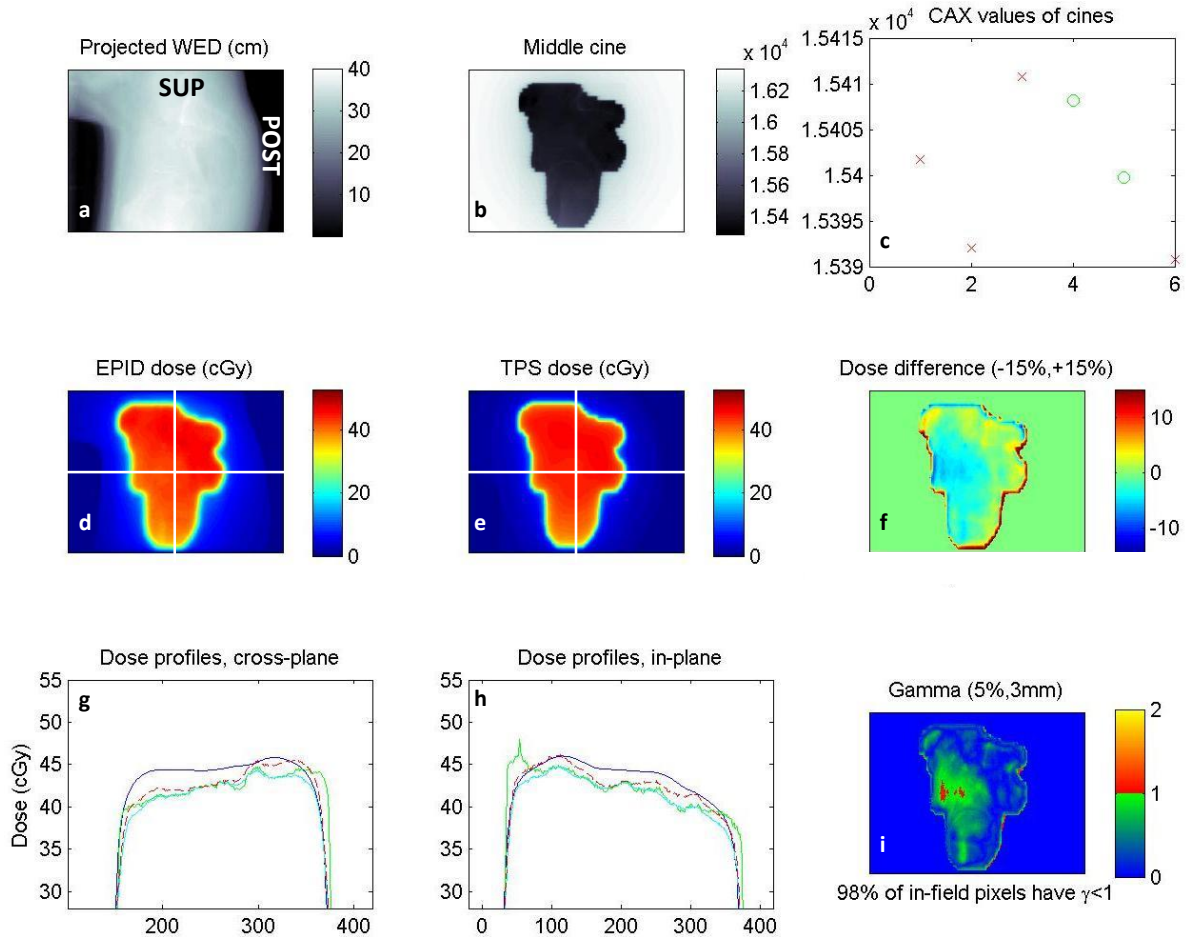


Figure 5-11: Screenshot of *in vivo* EPID dose calculation showing good agreement with planned dose (prone cervical cancer patient, lateral field). (a) Beam's eye view of water equivalent depth, obtained by projection of planning CT along ray lines from source to each EPID pixel. (b) One of the *in vivo* cine EPID images (a.u.). (c) Value of the central pixels for each of the 5 cines (x axis). The first three cines were discarded as they usually suffer from beam-on artifacts. (d) EPID-reconstructed dose at isocentre depth. (e) Planned dose. (Dose scales relative to TPS maximum.) (f) In-field pixel-by-pixel dose difference map. (g,h) Cross-plane and in-plane central profiles of: planned dose (blue), dose

reconstruction steps (green, cyan), and final EPID dose (dashed red). (i) 5% / 3 mm gamma evaluation. (Unlabeled axes are pixel number.)

5.4 Discussion

The ramping up effect observable in the CAX value of the first cine images is in agreement with previous observations by McCurdy and Greer⁷⁴ who found the same trend in both *cine* images and ion chamber measurements, leading to the conclusion that this effect is due to the linear accelerator. For the 6 MV beam only, the beam-on effect switched from an abnormal ‘ramping down’ (Figure 5-7.a, 6 MV, black) to ramping up (Figure 5-7.b, 6 MV, black) over the nine months between calibration and measurement, during which the upgrade from half-res to full-res was carried out. This upgrade also caused a one-time systematic deviation in signal of about 3% which was accounted for by means of a correction factor. It is unclear why the 6 MV beam produced these results, and further investigation was not possible due to the non-reversible upgrade. We speculate it may relate to imaging system defects, including sensitivity changes due to accumulated dose, which is why the upgrade was performed.

Agreement between planned and EPID-calculated dose was within 3% for deliveries of 80 MU and above. Some 40 MU deliveries had poor agreement for two reasons. First, the beam-off image loss correction is limited. Data used to derive the linear fit in Figure 5-3 is discretized because only whole MU values are deliverable, resulting in a fit uncertainty equal to a horizontal offset of 1MU. This error is more important for images with fewer MU, reaching 2.5% for a 40 MU image. Second, the EPID signal is unstable at beam-on. Discarding the first *cines* is necessary (Figure 5-7) but for 40 MU deliveries that may leave as little as two *cines* in the set, increasing susceptibility to noise. This is in agreement with previous findings⁷⁴ which showed

that *cine* images pixel values only stabilize after about 30 MU. We suggest reducing the number of frames per image to less than 4 to accurately verify fields of ≤ 40 MU, although this would increase computational requirements, and matching the MU for calibration to anticipated field doses.

The other two cases of gamma analysis failure were small fields through thick attenuator ($w=32$ cm, $l=7, 12$ cm). These two tests were the first to be delivered in the run of nine tests for that set of imaging parameters, and both calculations resulted in an underdosage of approximately 3%, suggesting that ghosting artifacts may have affected the commissioning data used to determine the F calibration factor. To prevent this, we suggest waiting an adequate time (e.g. 1 minute) between commissioning fields.

5.4.1 Accuracy in the presence of thickness errors

For IVD using planning CT data, the magnitude of detected dose discrepancies may not be accurate because the CT data used to backproject the EPID signal to isocentre dose no longer accurately reflects the measurement conditions.⁴⁰ The dose measured by our algorithm will be less than the actual dose when the attenuator increases (by swelling or setup errors), and greater than actual dose when attenuator decreases (weight loss, setup errors). The amount depends on energy, field size, thickness, and location (upstream versus downstream of isocentre) of thickness change, but is almost always within 4% per cm of water equivalent thickness change (Figure 5-10). Therefore, *dose discrepancies should be interpreted primarily as flags which warrant further investigation, rather than an accurate measure of delivered dose* (Figure 5-12).

For *in vivo* data, it is likely that uncertainties may increase, and tolerances of 5% / 3mm as adopted by Cilla *et al.*⁴¹ may be more appropriate, although tolerances depend on the desired objective (e.g. gross error detection vs detection of small setup/anatomical changes).

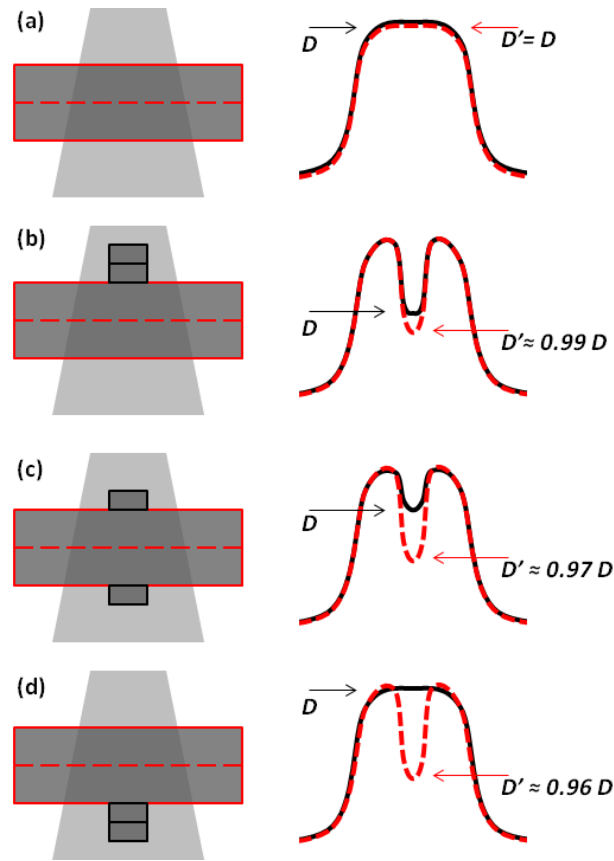


Figure 5-12: When the measurement conditions match the CT used for back projecting dose from EPID signal to the isocentre plane, as in (a), EPID dose D' calculated at isocentre depth (red dashed line) is in agreement with true dose D . However, the EPID signal cannot detect the location of added attenuation. For this reason, back-projected dose to the isocentre plane is a flag of changes in e.g. patient set up but does not always accurately measure the change in delivered dose at isocentre. When (b) $\Delta w = +1$ cm is introduced upstream of isocentre in the measurement, but not in CT, the EPID dose calculation slightly exaggerates the dose difference. For example, when the extra attenuator is distributed equally upstream and downstream (c), the true dose is greater than in (b), but the EPID signal is practically unchanged, and the EPID dose calculation is further

overestimated. (d) When the extra attenuator is placed downstream, isocentre dose is the same as (a), but EPID signal is very close to that of (b) and (c). In this situation EPID underestimates dose by 4%/cm. (see Figure 5-10.a for exact values).

5.4.2 Limitations

Because the correlation ratios between EPID signal and dose in phantom are acquired with square fields, the immediate application is to 3D-CRT. In lower resource settings, such as middle and lower income countries, conformal radiotherapy is likely to retain a leading role, making our *in vivo* dosimetry readily applicable. Extension of our IVD to IMRT is straightforward, by summation of all cine images into an integrated image, although the modulated beam will produce slightly different scatter to the imager, affecting dose reconstruction accuracy. Extension to VMAT, on the other hand, requires considerable work. To produce true in-patient dose data, 2D dose maps are needed at every gantry angle (an integrated image over all the arc is less sensitive to dosimetric variations¹⁴⁸). This would require CT-based calculation of water equivalent thicknesses, from the source to each pixel, at every gantry angle. This calculation is currently time consuming (~1 hr per gantry angle), and would require further optimization. The resulting 2D dose maps would then have to be summed appropriately in 3D, to provide patient dose. In addition, small and/or irregularly shaped subfields of a VMAT arc cause different photon scatter to the imager compared to the square fields used at commissioning, and would likely cause errors in dose estimation.

This method uses only water equivalent thickness for calibration and calculation. While this does account for changes in attenuation of the primary beam due to inhomogeneities, it does not account for changes in scatter dose. For this reason, its utility in regions of large inhomogeneities such as lung, is limited.¹⁰⁴

We used the TPS as reference for commissioning rather than measured data (e.g. ion chamber) in order to develop an easy-to-implement method. The AAA algorithm calculates dose to within 0.5% in equilibrium conditions in homogeneous media, and the penumbra is modelled with an accuracy of 1%, 1mm, which is sufficiently accurate for F correlation ratios and planar measurements.¹⁴⁹

5.5 Conclusion

We propose a simple, open-source, two-dimensional EPID *in vivo* dosimetry by correlation ratios, with a fast commissioning procedure. Varying MU, thickness, and field size within clinical ranges, agreement between EPID-calculated and TPS dose was in almost all cases better than 3%, suggesting that our EPID IVD method is sufficiently robust. Dose reconstruction makes use of planning CT data, so its accuracy is related to anatomical and setup reproducibility. In case of anatomy and setup differences with respect to planning, EPID dose may overestimate the error by up to about 4% per cm of attenuator change. Results on a patient provide proof of concept; further *in vivo* testing is warranted for clinical implementation. The *in vivo* dose information may be used as a flag for delivery errors, and to guide adaptive radiotherapy. All MATLAB code is freely available by contacting the authors.

5.6 Appendix: Derivation of dose calculation error expressions in cases of thickness changes between CT and treatment

In the case of a phantom vertically centered about the isocentre of known water equivalent thickness w , D_{EPID} is:

$$D_{EPID} = \frac{1}{F(w)} S$$

When a discrepancy between the CT and measurement conditions is introduced, Δw (>0) upstream of isocentre (Figure 5-12.b), the (incorrect) dose calculated from the measured EPID signal is:

$$D'_{EPID,up} = \frac{1}{F(w)} S_{up}$$

The prime symbol (') clarifies that this calculation is inaccurate because the water equivalent thickness value is incorrect.

Conversely, applying Equation 27 with $d = -\Delta w/2$ (i.e. correctly applying the larger water equivalent thickness $w+\Delta w$ and vertical displacement d of the phantom mid-depth from isocentre, as in Figure 5-2.b), the true expression for dose calculation is

$$D_{EPID,up} = S_{up} f\left(-\frac{\Delta w}{2}\right) \frac{1}{F(w+\Delta w)} \frac{TMR\left(\frac{w+\Delta w}{2} + \frac{\Delta w}{2}\right)}{TMR\left(\frac{w+\Delta w}{2}\right)}$$

which by substitution becomes

$$D_{EPID,up} = D'_{EPID,up} f\left(-\frac{\Delta w}{2}\right) \frac{F(w)}{F(w+\Delta w)} \frac{TMR\left(\frac{w}{2} + \Delta w\right)}{TMR\left(\frac{w}{2} + \frac{\Delta w}{2}\right)}$$

In conclusion, when calculating dose using an incorrect thickness which is Δw greater than the physical length upstream of isocentre, our calculation method overestimates dose by a factor of:

$$\frac{D'_{EPID,up}}{D_{EPID,up}} = \frac{1}{f\left(-\frac{\Delta w}{2}\right)} \frac{F(w + \Delta w)}{F(w)} \frac{TMR\left(\frac{w}{2} + \frac{\Delta w}{2}\right)}{TMR\left(\frac{w}{2} + \Delta w\right)}$$

which is Equation 31.

Similarly, in the case of thickness loss downstream (Figure 5-12.d) the accurate EPID-calculated dose is

$$D_{EPID,down} = S_{down} f\left(\frac{\Delta w}{2}\right) \frac{1}{F(w + \Delta w)} \frac{TMR\left(\frac{w+\Delta w}{2} - \frac{\Delta w}{2}\right)}{TMR\left(\frac{w-\Delta w}{2}\right)}$$

and the overestimation in this case becomes

$$\frac{D'_{EPID,down}}{D_{EPID,down}} = \frac{1}{f\left(\frac{\Delta w}{2}\right)} \frac{F(w + \Delta w)}{F(w)} \frac{TMR\left(\frac{w}{2} - \frac{\Delta w}{2}\right)}{TMR\left(\frac{w}{2}\right)}$$

i.e. Equation 32.

The third case to consider is that of equal loss of tissue above and below isocentre (Figure 5-12.c). In this case in which the mid-depth of the phantom is still coincident with the isocentre, the correct dose calculation is simply

$$D_{EPID,symm} = \frac{1}{F(w + \Delta w)} S_d$$

which leads to a dose calculation error of

$$\frac{D'_{EPID,symm}}{D_{EPID,symm}} = \frac{F(w - \Delta w)}{F(w)}$$

which is Equation 33.

It is apparent that in all three cases (Figure 5-12.b-d) the same ratio of F correlation ratios appears. In the cases of asymmetrical thickness change two extra terms appear: the ratio of TMRs and the scatter factor f .

Using the F and f correlation ratios specific of the 6 MV and 15 MV energies of our linear accelerator, we calculated the effect of tissue gain and loss of 1 cm ($\Delta w = +1$ cm and -1 cm respectively) and plotted the results in Figure 5-10. In addition, for the case 6 MV, $\Delta w = -1$ cm, we also simulated thickness errors by processing the commissioning images, but manually inputting CT data 1 cm thinner (example: EPID images taken through 20 cm of attenuator were used to calculate EPID dose in the assumption that attenuator was 19 cm). Theoretical and measured data are both plotted in Figure 5-13.

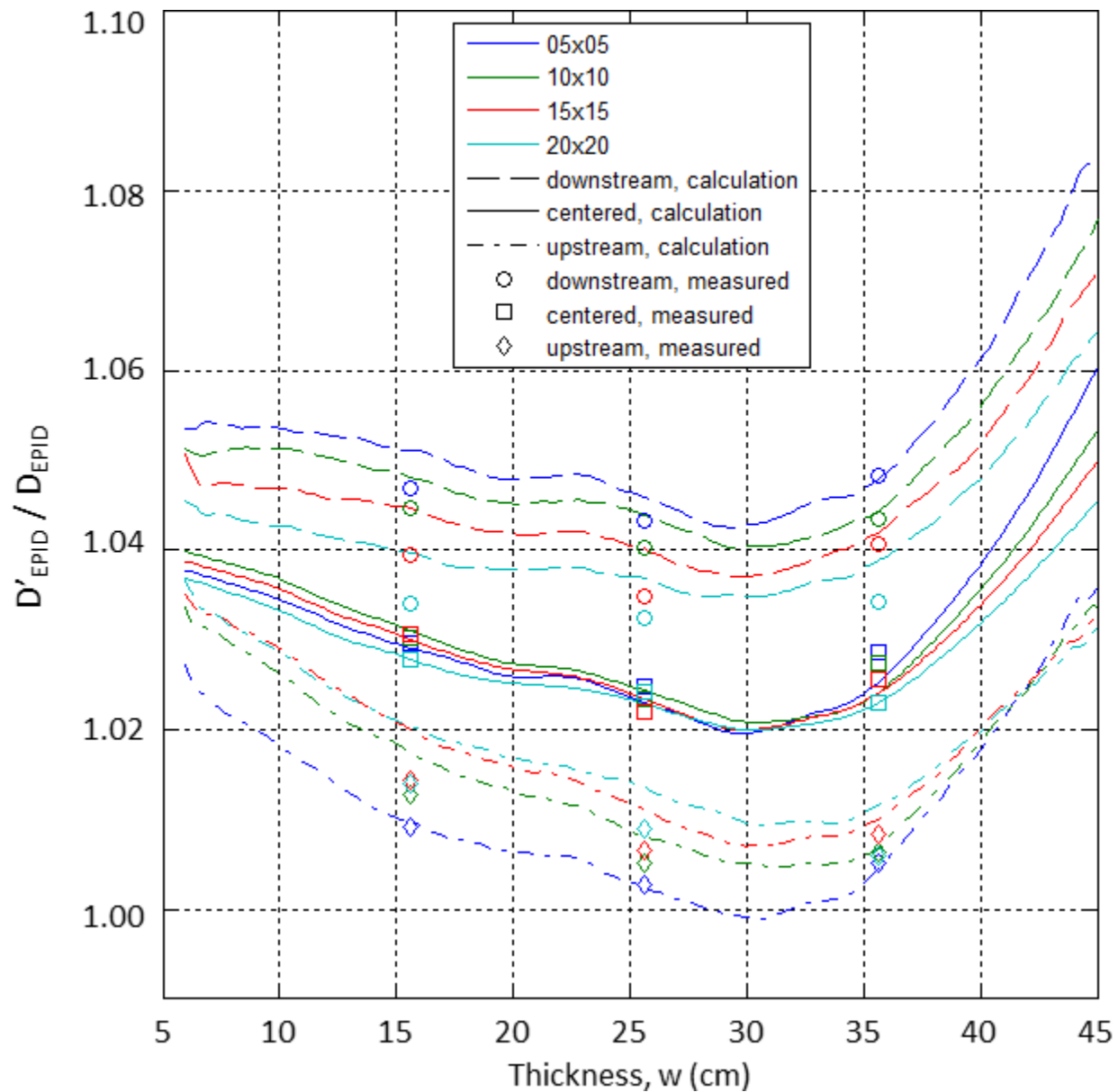


Figure 5-13: Overestimation of EPID dose from attenuator thickness reduction of 1 cm. In the case of attenuator loss upstream of isocentre, EPID dose overestimates by up to 1.5%. This error increases to approx. 4.5% if thickness loss is entirely downstream of isocentre. Measured values (points) are in good agreement with calculated values (lines).

General Conclusion

In this chapter, the improved 2D EPID *in vivo* dosimetry by correlation ratios has been described. The measurements and steps necessary to implement it have been illustrated, and it is expected that dose reconstruction for each energy/dose rate combination can be implemented in a matter of hours. The algorithm proved adequate in modelling planar dose for a variety of slab phantom thicknesses, field sizes, and MU values. For patient data, we expect further challenges related to realistic field shapes and the patients anatomy. It remains to be verified if the method retains its utility in the presence of these effects. To this aim, the remainder of this thesis presents and discusses *in vivo* data.

Chapter Six: *In vivo* portal imaging dosimetry in rectal cancer radiotherapy on the belly board device

General Introduction

The previous chapters describe the method for 2D *in vivo* dosimetry by correlation ratios; in this chapter we present true *in vivo* results, i.e. in patients. The patients we recruited were all treated for rectal cancer at the Tom Baker Cancer Centre, and all were setup prone on the belly board device, described below. This immobilization device is effective in displacing the small bowel away from the treatment fields, thus reducing acute toxicity. At the same time, the combination of the prone position and the use of the soft cushions of the device, increase setup error and soft tissue variability. For this reason, this patient population is appropriate to detect interfractional setup differences.

In the first section of this chapter (6.1), results on six patients from a simplified (relative dosimetry) adaptation of the method introduced in the previous chapters is presented. All EPID-calculated dose maps are compared to the first of the series (i.e. not to the planned dose), resulting in an elimination of absolute dose error detection, but also of dose calculation inaccuracy. Thus, this mode is ideal for error *detection*, but not for error *quantification*. This brief manuscript was selected for the Young Investigators Competition at the 2015 World Congress on Medical Physics and Biomedical Engineering (Toronto, June 7-12) and was published in the conference proceedings.¹³⁰ It is reproduced here with permission. The notation was updated to be coherent with the remainder of the thesis, and details were added as footnotes.

The second section (6.2) is a full analysis on all 10 rectal cancer patients enrolled in the study. Here, absolute dose is calculated from EPID images and compared to the planned dose,

exported from the treatment planning system. This manuscript follows the dose calculation method presented in detail in chapters 4 and 5, and is currently under peer review for publication in a scientific journal.

For both these manuscripts, I collected and analyzed the data and wrote the manuscript. Dr. Wendy Smith and Dr. Derek Brown provided guidance and feedback. For the second manuscript, Dr. Richie Sinha provided invaluable clinical insight in data interpretation. All co-authors reviewed each manuscript.

6.1 *In vivo* EPID dosimetry detects interfraction errors in 3D-CRT of rectal cancer: a relative dosimetry study

S. Peca, D. Brown, and W.L. Smith

Abstract

BACKGROUND: *In vivo* dosimetry can record the delivered dose during radiotherapy, which may be used to trigger adaptive radiotherapy or other user intervention. We demonstrate the use of our in-house *in vivo* electronic portal imaging dosimetry in quantifying interfraction dose variability in rectal cancer.

METHODS: We recorded MV images from nine treatment beams for six patients prone on the belly board, during 4-7 fractions, for a total of 50 measurements. Images were processed with our dosimetry system to produce dose maps. The dose map from the reference fraction was compared to all subsequent ones to determine interfraction delivery variation, yielding 41 dose difference maps.

RESULTS: We identified a number of dose discrepancies. In several patients, persistent gas bubbles may result in cumulative dose deviations large enough to warrant adaptive radiotherapy. In three patients, discrepancies in dose resulted from variability of patient positioning on the belly board. These issues were not readily identified by standard imaging procedures.

CONCLUSION: We are developing an open-source *in vivo* portal dosimetry method to automatically track delivered dose at every fraction. Results can be used to flag unexpected discrepancies, guide adaptive radiotherapy, or warrant image guidance. Further data is needed to test applicability with other treatment sites and setups.

6.1.1 Introduction

6.1.1.1 Challenges in the treatment of rectal cancers with RT

Dose to the small bowel often limits the treatment of rectal malignancies with radiotherapy (RT). To displace this organ away from the fields, the ‘belly board’ (a cushion on which the patient is prone, with an opening for the abdomen) has been used successfully for about 25 years.¹⁵⁰ Even with the advent of intensity modulated RT, the belly board retains its small bowel sparing value.¹⁵¹ However, the prone position has larger setup and motion uncertainties, and systematic setup errors are larger, especially in the antero-posterior direction.¹⁵² In the clinic, these uncertainties are in part accounted for by image-guided (IG) RT protocols, such as kV-kV matching to bony anatomy or cone-beam CT to guide couch shifts. Even errors associated with sacrum rotation¹⁵³ may, in theory, be compensated by newer treatment couches with six degrees of freedom.

Unfortunately these imaging based solutions have limitations. Firstly, they provide no dosimetric information; the user does not know the effect on delivered dose of applying a couch shift or ignoring the presence of gas bubbles. Especially when using the belly board, shifting the patient to the correct position may cause shifting the belly board away from the reference position, affecting delivered dose. In addition, frequent imaging gives extra dose to the patient, is resource intensive, and not always available. For these reasons, a convenient method of quantifying the impact of said uncertainties on absorbed dose to identify set-up issues and/or trigger adaptive radiotherapy is desirable.

6.1.1.2 *In vivo* dosimetry by means of EPID

Arguably, the most effective method for ensuring correct delivery and for catching errors is to measure dose *in vivo* during treatment, and the electronic portal imaging device, (EPID) is an ideal tool for this purpose.⁴⁴ Inspired by previous work,¹⁰² we have recently developed a simple method for 2D *in vivo* dosimetry by EPID during 3D conformal RT.¹⁰⁴ Its versatility makes it an ideal tool to investigate delivery errors due to setup, inter- and intra-fraction motion, anatomy changes, and machine uncertainties.

The purpose of this study is to determine whether our 2D EPID *in vivo* dosimetry method can identify which patients are not receiving the prescribed daily dose. Further, we aim to determine the cause for such error (setup, anatomical changes, etc.). Ultimately, this will provide the user with a marker for adaptive radiotherapy, warranting corrective action such as introducing a patient-specific setup procedure or re-planning the treatment.

6.1.2 *Methods*

6.1.2.1 In-house 2D EPID *in vivo* dosimetry

The working principle of our MATLAB-based EPID dosimetry has been described elsewhere¹⁰⁴ and is here outlined in brief. To commission the system we calculate correlation ratios between dose at the midpoint of a solid water phantom (D_{CAX}) and EPID pixel intensity (S_{CAX}), for various field sizes and thicknesses of water, along the CAX. Then, during patient treatment, we acquire *cine* EPID images using the treatment beam. Separately, we use the patient's CT data to calculate the total attenuation for every ray line from the source to each EPID pixel (ray tracing). This allows calculation of the dose deposited in the midpoint of the ray. Multiplying this by the appropriate ratio of TMRs (tissue maximum ratios), we estimate the dose

deposited at the point of intersection between the ray and the plane perpendicular to the CAX containing the isocentre. Repeating for all pixels, we have an estimate dose map at isocentre depth.

This map must be corrected for off-axis effects. In particular, the S_{CAX}/D_{CAX} ratios change in proximity of the field edge. This is because the dose penumbra inside a phantom (caused mainly by the lack of lateral electronic equilibrium) is very different from the ‘signal penumbra’ recorded by the EPID (caused by short range electron scatter and optical photon glare,¹⁵⁴ as well as geometrical magnification of the penumbra exiting the patient). We modeled this change by means of convolution. For every cross-plane and in-plane profile, we searched for the coefficients c_1 - c_4 that best matched the treatment planning system (TPS) dose profile (D) as a 1D convolution of the EPID signal profile (S) and a linear combination of four Gaussian curves,

$$S \otimes \{c_1 G_1 + c_2 G_2 + c_3 G_3 + c_4 G_4\} \approx D \quad \textbf{Equation 34}$$

where G_i is a 1D Gaussian of width σ_i . We used two Gaussians with $\sigma_2=10\sigma_1$ to model different components of the of the 2%-98% penumbra.¹⁵⁵ As well, we found that at larger depths we needed to use wider Gaussians ($\sigma_3=2\sigma_1$, $\sigma_4=15\sigma_3$) to approximate the greater scatter^f. To this aim we wrote an optimization algorithm in MATLAB to weigh four different Gaussians.

Cine images were taken by two Varian aSi-1000 EPIDs mounted on a Clinac 21EX and Trilogy (Varian Medical Systems, Palo Alto California, USA). Dose calculation is from Varian Eclipse TPS, using AAA with a 2.5mm grid.

^f At greater depths with constant source-to-axis distance (SAD), phantom scatter increases, broadening the penumbra. Geometric and transmission penumbra, on the other hand, are, for all practical purposes, constant.

6.1.2.2 Patients and analysis

Six rectal cancer patients (A-F) were planned and treated prone on our clinic's belly board with a four field box (45 Gy in 25 fractions where all the PTV must receive at least 95% of the prescribed dose). EPID *cine* images were acquired approximately once/week on all four fields (independently of kV/MV setup verification images). Only the fields at gantry 0° (postero-anterior, or PA, field) and 90° (right-lateral, or RL, field) without dynamic wedges were analyzed in this study, for a total of nine fields (5 PA, 4 RL) which produced 50 image sets. All fields had energy 15 MV, except for one (Pat.E, PA field) which had energy 6 MV.

For each field, the *cine* images of the set were added together and the image sum was processed with our in-house processing pipeline to produce the EPID-calculated dose, D_{EPID} . Since we are focusing on inter-fractional delivery variability, the calculated dose maps were scaled to match the TPS dose at the CAX (i.e. relative dosimetry mode) to eliminate absolute dose uncertainties^g. The D_{EPID} map from the first imaging day (taken as reference) was subtracted from each subsequent one, yielding dose difference (DD) maps^h. The DD maps were analyzed qualitatively. When hot/cold spots were found, the raw EPID *cine* images were analyzed to determine its cause.

^g For clarity, each image sum was rescaled so that the value of the central 8x8 pixels matched the TPS dose at isocentre. While this makes it impossible to detect absolute differences, such as those produced by accelerator miscalibration or MU errors, it singles out 2D variations such as those due to anatomical or setup differences.

^h The DD maps have units of cGy. The value of each pixel expresses the absolute dose difference between corresponding pixels of the two rescaled dose maps. For the purpose of relative dosimetry DD maps were found to be more suitable than gamma maps. Gamma maps would 'hide' all differences smaller than the thresholds set for distance-to-agreement and dose-difference, which may be of interest. As well, the units of a gamma map necessarily indicate that the pixel either 'passes' or 'fails', while DD values are continuous and more appropriate for further analysis.

The study is approved by the local Ethics Board and conforms to the ethical standards of the responsible committee on human experimentation and the Helsinki Declaration of 1975 (revisions: 2000, 2008). Patients gave written consent.

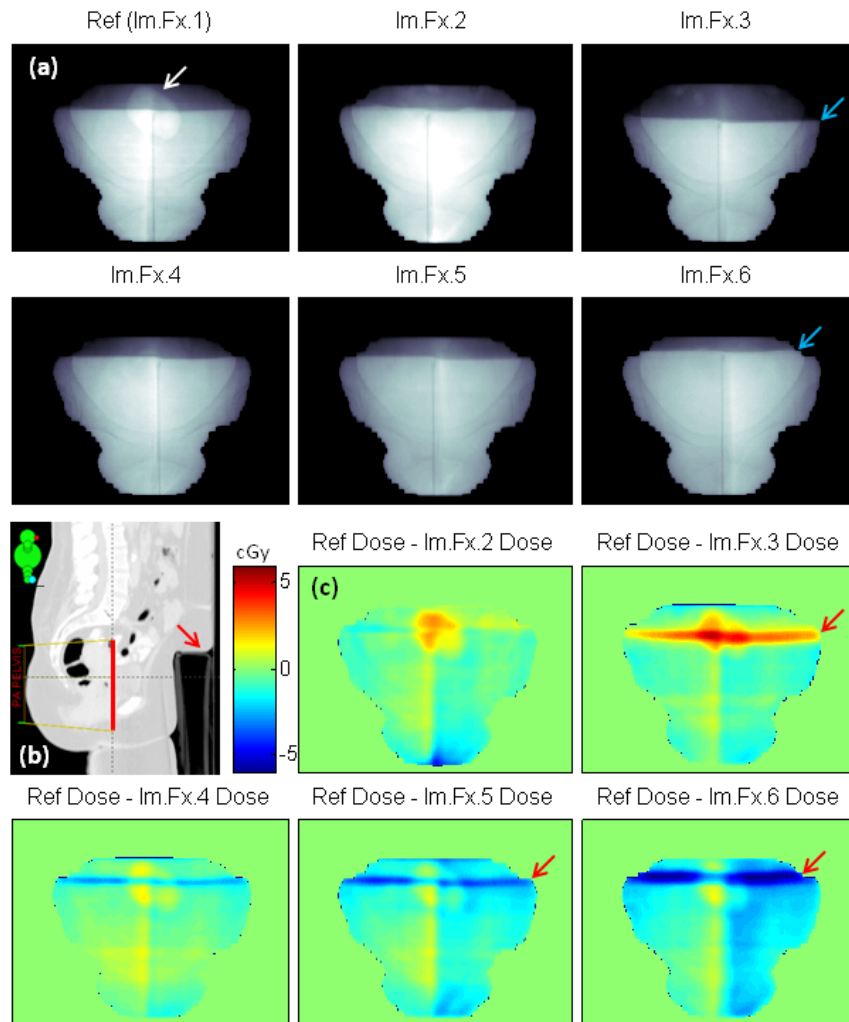


Figure 6-1: Patient F, PA field ($GA=0^\circ$). (a) Raw EPID images. (b) Lateral view from the TPS showing the imaging plane (red) and the body adapting to the belly board opening. (c) Dose difference (cGy) between the first imaged fraction (Im.Fx.) and five later treatment days. The large mismatch is located at the edge of the belly board opening (red arrows), indicating inconsistent setup of the patient with respect to the board in the S-I direction. This was verified by visual inspection of the raw images (blue arrows). As well, all dose

difference maps are affected by the gas bubble present during the Ref fraction (white arrow).

6.1.3 Results

Our method was able to identify a variety of dose discrepancies in our limited patient population. In patient F, the positioning of the belly board varied by 2.3cm in the S-I direction over the 6 fractions observed (Figure 6-1.a). This random setup error was readily observable in the DD maps (Figure 6-1.c), and resulted in accumulation of dose difference (Figure 6-4, Pat.F).

In Patients E (Figure 6-2) and C (not shown) the DD maps displayed a similar discrepancy in correspondence of the belly board opening. However, analysis of the EPID and CT images suggests that in this case it was due to variability in the amount of abdomen compressed in the edge of the belly board-couch interface (compare for instance the CT images in Figure 6-1.b and Figure 6-2.b, red arrows). Again, this error accumulated significantly over all imaged fractions (Figure 6-4, Pat.E).

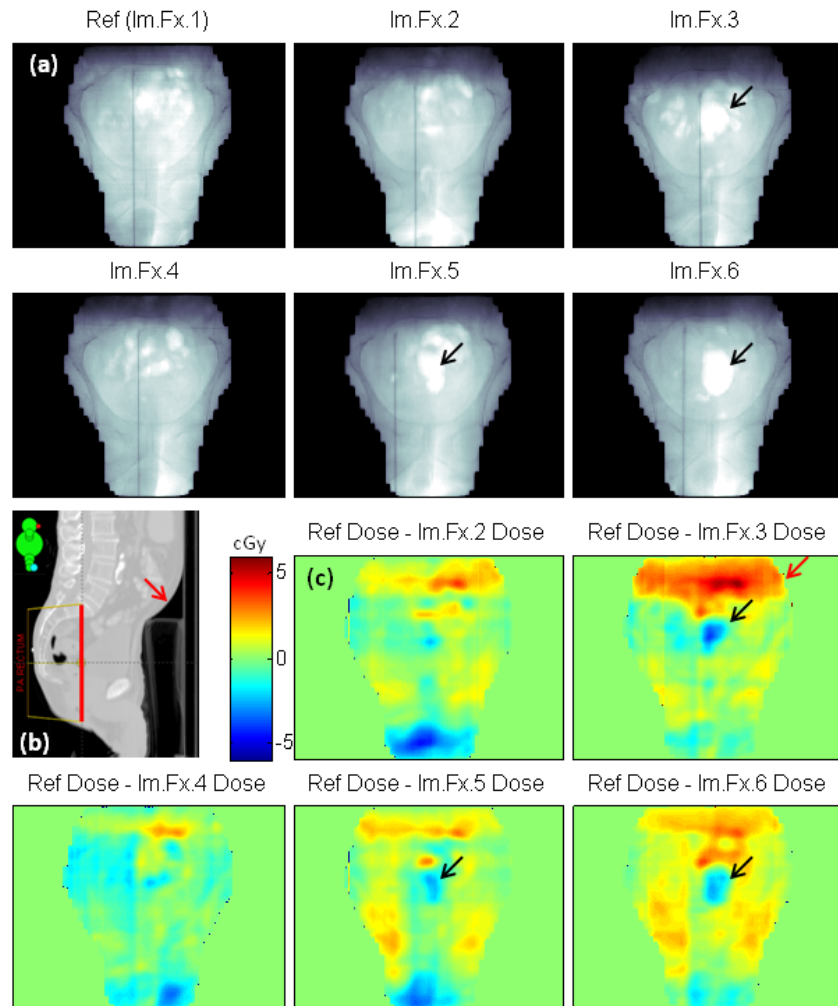


Figure 6-2: Patient E, PA field ($GA=0^\circ$). (a) Raw EPID images. (b) Lateral view from the TPS showing the imaging plane (red) and the body adapting to the belly board opening. (c) Dose difference maps between the first imaged fraction (Im.Fx.) and five later treatment days. Dose maps display inconsistent setup, especially at the opening of the belly board (red arrows). Most likely there is inconsistency in the amount of abdomen compressed in the corner of the belly board-couch interface (b, red arrow). In addition, this patient is prone to frequent gas bubbles (black arrows), warranting for adaptive radiotherapy (i.e. replanning including gas).

In patients E and B the presence of gas bubbles was highly reproducible, with gas present in more than half of the fractions imaged (Figure 6-2, Figure 6-3), resulting in a cumulative dose

difference effect (Figure 6-4, Pat.E,B). In the other 4 patients, gas bubbles were detected sporadically.

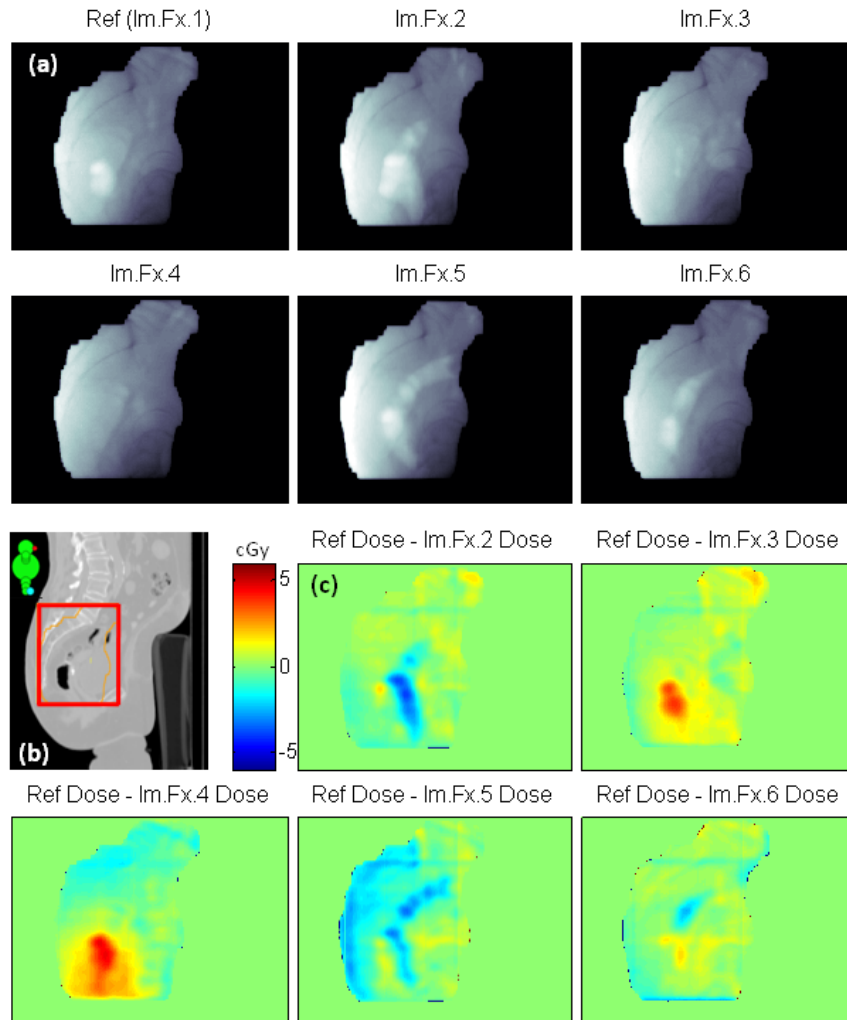


Figure 6-3: Patient B, RL field ($GA=90^\circ$). (a) EPID images show frequent gas bubbles, but provide no information on their impact on dose. (b) Lateral view from the TPS showing the imaging plane (red). (c) Dose difference maps between the first imaged fraction (Im.Fx.) and five later treatment days. Dose maps confirm correct setup, but display large variations due to gas bubbles, warranting for adaptive radiotherapy.

6.1.4 Discussion

In this study we provide proof of concept of an automated *in vivo* EPID dosimetry and its added value with respect to standard imaging protocols. Although here we present data from one site only, conclusions may apply in general

Clinical imaging protocols are used to determine appropriate couch shifts to position the patient correctly. However, if setup involves accessories such as the belly board, this shift may place the accessory differently at every fraction, affecting the dose for those fields that cross the accessory upstream of the patient. Recording *in vivo* images periodically and calculating the cumulative dose (or dose difference) map is a valuable indicator of the total effect of this uncertainty.

Similarly, at the planning stage any gas bubbles are usually contoured out and overridden by setting their HU value to that of water. This method has two flaws: it ‘adds’ tissue to the CT scan, making the patient thicker, and it assumes that gas bubbles will not be present during treatment. The impact of these approximations on delivered dose is generally not known. In two patients we found differences of approximately 10 cGy on one of the fields of 4-field treatments. Assuming each field delivers 10 Gy, this is a difference of 1%. While this difference is generally not clinically significant, there may be exceptional anatomies which produce larger differences. The method we propose would automatically monitor the cumulative effect and if necessary prompt re-planning taking into account the presence of gas (i.e. adaptive radiotherapy).

Another uncertainty in RT in which our method can find use is reproducibility of patient contour. As the patient becomes more comfortable with the treatment, his or her position on the belly board may progressively be more relaxed and alter the abdomen displacement in the board’s opening (e.g. Figure 6-1.b vs. Figure 6-2.b). Again, the cumulative effect may be

monitored in time. Similar effects may take place also with other setup methods and with weight changes.

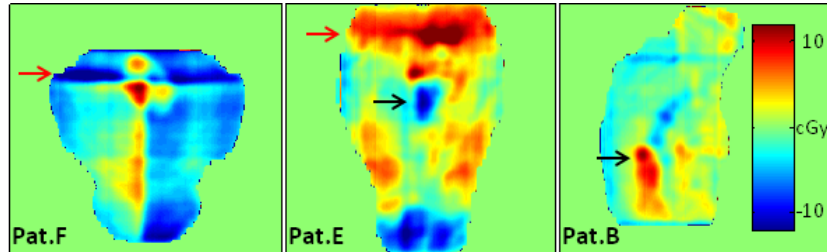


Figure 6-4: Cumulative dose difference maps, summed over all imaged fractions. Belly board-couch interface setup errors sum in Patients F and E, indicating a systematic error which warrants intervention (red arrows). In Patients E and B dose differences due to presence/absence of gas bubbles accumulate (black arrows). In Patient B setup appears to be reliable.

The *in vivo* EPID dosimetry we propose may, in principle, be completely automated. The images acquired with the treatment beam (no added dose or time) may be sent automatically to a workstation which, making use of calibration data and the patient's CT, will calculate dose maps. These maps can be compared to a reference map (ideally from the TPS) to calculate dose difference maps. Tolerances to specific organs can be set in accordance to clinical tolerances, and the system may raise a warning flag to the user when these are reached. The user can then investigate the issue and if necessary adapt the treatment (e.g. replanning, modifying setup procedure, introduce more image guidance).

This proof of principle in 3D-conformal RT may in principle be extended to IMRT without large modifications. To be applicable to VMAT, on the other hand, it would be necessary to perform all dose calculations in 3D. This can be achieved by multiplying by many TMR ratios to calculate dose in 3D for every gantry angle, but with the current system this would require excessive computational time.

6.1.5 Conclusion

In vivo dosimetry can bring much benefit to the clinic, especially for: monitoring dose delivery in treatment, triggering adaptive radiotherapy, and guiding IGRT. The automated EPID *in vivo* dosimetry we are developing does not increase delivered dose or treatment time, and provides information not apparent in current imaging protocols.

In this paper we give proof of principle of our method in relative dosimetry mode to monitor inter-fractional variability. In rectal cancer patients treated on the belly board, we were able to identify relevant dose delivery differences, which may serve to guide intervention and adaptive RT.

The EPID-based *in vivo* dosimetry we are implementing is open source and simple to commission and use. It may be of particular use in centres with limited resources, such as in developing countries. All the MATLAB code is freely available to anyone who will request it by contacting the authors.

6.2 *In vivo* portal imaging dosimetry identifies delivery errors in rectal cancer radiotherapy on the belly board device

S. Peca, R. Sinha, D. Brown, and W.L. Smith

Abstract

INTRODUCTION: We recently developed a novel, open source *in vivo* dosimetry which uses the electronic portal imaging device (EPID) to detect dose delivery discrepancies. We applied our method on rectal cancer patients treated prone on a belly board device.

METHODS: EPID *in vivo* dosimetry was performed on ten rectal cancer patients treated prone on the belly board with a four field box arrangement. EPID images were acquired approximately once per week from each treatment beam. Our dosimetry method used these images along with CT data to reconstruct patient planar dose at isocentre depth.

RESULTS: Our algorithm proved sensitive to dose discrepancies, and detected discordances in seven patients. The majority of these were due to soft tissue differences between planning and treatment, present despite matching to bony anatomy. As a result of this work, quality assurance procedures have been implemented for our immobilization devices.

CONCLUSION: *In vivo* dosimetry is a powerful quality assurance tool that can to detect delivery discrepancies, including changes in patient set up and position. The added information on actual dose delivery may be used to evaluate equipment and process quality, and as a guide for adaptive radiotherapy.

6.2.1 Introduction

In vivo dosimetry by transit electronic portal imaging device (EPID) images is a growing field in radiotherapy^{91, 141, 156} which may be useful in treatment quality assurance.¹⁵⁷ We have recently developed a low-resource EPID *in vivo* dosimetry method which is very simple to implement and develop further.¹⁰⁴ In a preliminary study, we found evidence of higher than expected interfractional variability in rectal cancer patients treated prone on the belly board.¹³⁰ The purpose of this paper is to demonstrate the utility of our dosimetry method by detecting, for the first time, dose discrepancies *in vivo* in rectal cancer treatment on the belly board. This study illustrates the power of EPID *in vivo* dosimetry to review new and existing treatment delivery techniques by: detecting potential delivery errors, identifying the cause of error, and estimating its dosimetric impact. No additional equipment is required, and it may be applied as a QA study or for every treatment fraction to monitor machine performance and patient setup accuracy.

The standard of care for stage II and III rectal cancer is radiation therapy with concurrent chemotherapy followed by surgery.^{158, 159} Given typical pelvic anatomy, the small bowel often falls into the upper region of the treated volume and is the primary dose limiting organ at risk. Acute grade III small bowel toxicity develops 2-3 weeks into treatment and can include diarrhea, abdominal pain, and nausea with reported incidence of 7-28%.¹⁵⁹⁻¹⁶² Late effects, such as perforation or obstruction, may develop after months/years. A review of multiple studies found that partial small bowel irradiation of ~50 Gy resulted in late obstruction or perforation rates in 2-9% of patients.¹⁶³ This rate rose to 30% in patients treated with a larger field that extended superiorly to the level of the lumbar vertebrae.¹⁶⁴ The volume of the small bowel that receives a relatively low dose is a good predictor of acute toxicity. In two studies, the greatest sensitivity for predicting early toxicity was associated with the small bowel volume receiving 15-25 Gy.^{165,}

¹⁶⁶ Late toxicities, on the other hand, are better predicted by the small bowel volume receiving higher doses.¹⁶³

To spare the small bowel during rectal radiotherapy, the “belly board” is often used as an immobilization device. It is composed of cushions attached to a hard base on which the patient lies prone. An opening allows the abdomen to be displaced downwards. It is inexpensive, customizable, increases patient comfort, and can reduce the volume of small bowel in the treatment volume by 13-167 cc.¹⁶⁷ The major challenge in using the belly board is patient position reproducibility. First, the prone position suffers from larger random and systematic setup errors in with respect to supine.¹⁶⁷ In addition, prone with belly board has larger mean positioning errors compared to prone without, with the greatest difference in the AP direction (4.4 vs 2.3 mm).^{152, 167} Belly board setup is also susceptible to differences in rotation of the pelvis: a study¹⁵³ found that the sacrum-to-S1-vertebra angle varies by approximately $\pm 10^\circ$ over multiple fractions, and may drift over the course of treatment.

Based on our center’s experience we hypothesized that even after appropriate bony anatomy alignment, inter-fractional soft tissue discrepancies persist. These may be due to: setup procedure, belly board position with respect to patient, belly board wear, or persistent bowel gas. As we show herein, *in vivo* dosimetry provides an assessment of dose delivery accuracy, which may inform adjustment of setup and delivery processes in subsequent fractions.

6.2.2 Methods

Ten consecutive rectal cancer patients (2 females, 8 males, treated in 2014-2015), who were prescribed 45 Gy in 25 fractions with 3D conformal radiotherapy (3D-CRT) in a four-field box arrangement, were enrolled. Collection of extra images was approved by the local Ethics

Board and patients gave written consent. All patients were treated in a prone position with a full bladder on an in-house belly board device: a frame of rectangular cushions which left a 37x42 cm² (lateral by longitudinal) opening in the center, 8 cm deep. Patients were positioned with the iliac crest aligned to the lower end of the belly board aperture. This setup allows close alignment with the lumbosacral joint, allowing optimal small bowel displacement.¹⁶⁸

Patients 1, 2, 7, 8 were treated on a Clinac 21EX and patients 3-6, 9-10 on a Trilogy (Varian Medical Systems, Palo Alto California, USA). Portal images were acquired with Varian aSi-1000 EPIDs in *cine* mode (*i.e.* continuous acquisition) placed 50 cm downstream of isocentre, with the following parameters: patients 1-2: 15 frames/sec (f/s), 4 frames/image (f/i); patients 7-8: 7.825 f/s, 4 f/i; patients 3-6, 9-10: 7.825 f/s, 8 f/i. Each field produced 4-20 *cine* images, depending on MU and imaging parameters. Of the 40 fields, 38 were 15 MV and two were 6 MV. EPID dosimetry was performed approximately once per week and resulted in 2-8 imaged fractions per patient. The fraction numbers indicated in the manuscript correspond to the chronological order in which they were acquired, not with the physical fraction number of the treatment course. Eight fields with enhanced dynamic wedges were excluded because *cine* imaging is susceptible to dose rate modulation artifacts.¹⁶⁹

Every *cine* set was processed in MATLAB (The MathWorks, Inc., Natick, MA) with our in-house algorithm¹³⁰ summarised below. Each *cine* image was inverted, a flood field correction through 20 cm of water applied, beam-on artifacts removed, beam-off frame loss corrected for. All *cines* of the field were summed into a single image. EPID backscatter was accounted for following the method proposed by Berry *et al.*¹⁴⁶ The resolution was reduced to 512x384 to reduce computational load. From this image, dose was calculated inside the EPID-measured field (50% line) at isocentre depth. This calculation makes use of the patient's planning CT and of

correlation ratios¹⁰² between EPID signal and isocentre dose. EPID-calculated dose was compared (pixel-by-pixel and gamma analysis) to that of the Treatment Planning System (TPS; Varian Eclipse 11.0.31, AAA, 2.5mm dose calculation grid). Each dose difference map was visually inspected; features of interest and regions of dose difference of approximately $\pm 10\%$ or more were investigated by referring to the planning CT. Gamma analysis was performed with 5%, 3 mm criteria as proposed previously.¹¹⁹⁻¹²¹ These thresholds were chosen taking into account the limited accuracy of our *in vivo* dose reconstruction^{118, 120, 130} and the variability of internal organs.¹⁷⁰

6.2.3 Results and discussion

164 *cine* sets corresponding to multiple fractions of 32 fields from the 10 patients were analyzed. Figure 6-5 shows results for a patient whose measured dose closely matched planned dose in the isocentre plane. Relevant dose differences were detected in seven patients. These were grouped into five sources of error: (1) soft tissue filling of the belly board opening; (2) belly board positioning (with respect to patient bony anatomy); (3) persistent gas; (4) patient bony anatomy setup; (5) other. Observations are summarised in

Table 6-1. Discordances in delivery were identified by our EPID *in vivo* dosimetry, while the explanations result from a more in-depth analysis of MV, kV, and CT images.

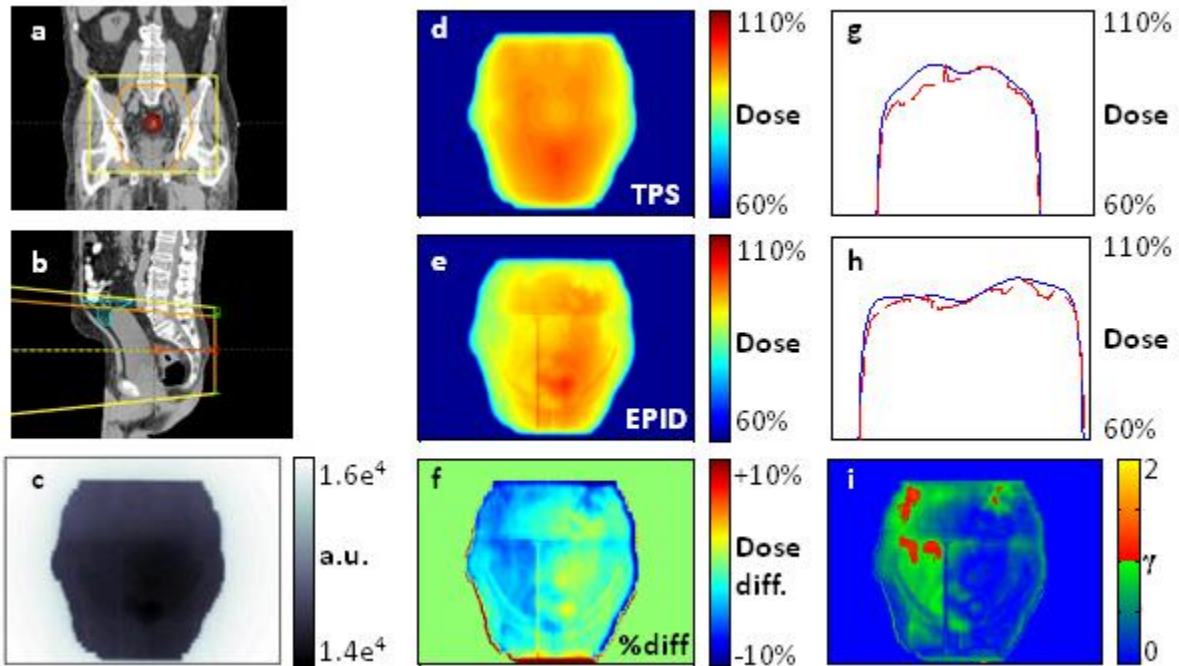


Figure 6-5: Example of *in vivo* EPID dose calculation showing good agreement with planned dose at isocentre depth (patient 1, PA field, fraction 2). (a,b) Frontal, sagittal views of CT and field with the small bowel contoured in cyan. (c) Single *cine* frame. (d) Planned dose map. (e) EPID-reconstructed dose at isocentre depth. (f) Point-to-point dose difference map. (g,h) Cross-plane and in-plane dose profiles (blue: TPS; dashed red: EPID dose). (i) 5%, 3 mm gamma evaluation, showing good agreement.

Table 6-1: Quality assurance summary from *in vivo* EPID dosimetry on 10 rectal cancer patients. In brackets are the imaged fields and fractions in which the dose discrepancy was visible. S-I: superior-inferior, L-R: left-right, AP:antero-posterior, PA:postero-anterior, LAT:lateral, fx:fraction(s).

<i>Patient</i>	N.imaged fields (Tot. 164)	Soft tissue changes in belly board opening	Belly board positioning errors ≥ 1.5 cm	Bowel gas	Patient setup errors ≥ 1 cm (bony anatomy)	Other
1	8 (4 fields, 2 fx)					
2	17 (3 fields, 6* fx)		Board misaligned by 2cm S-I [AP field, fx 5]	Persistent gas [LAT fields, fx 2, 5, 6] (Figure 6-8)	1 cm S-I setup error [AP field, fx 4]	
3	12 (2 fields, 6 fx)	Stretched soft tissue caused +8% AP field dose [both fields, all fx] (Figure 6-6)	Board misaligned by 2cm S-I [both fields, fx 2, 5]			
4	20 (4 fields, 5 fx)	Stretched soft tissue caused +4% AP field dose [AP field, all fx]				Tissue reduction in post. region (LAT fields, all fx) (Figure 6-9). Unexplained +10-15% dose areas [PA field, all fx]
5	12 (2 fields, 6 fx)		Board misaligned by 2cm S-I [both fields, fx 1]			
6	16 (4 fields, 4 fx)		Board misaligned by 2cm S-I [AP, PA fields, fx 3] (Figure 6-7)		1.5 cm L-R setup error [AP field, fx 2], probable VRT setup error [LAT fields, fx 2]	
7	21 (3 fields, 7 fx)	Stretched soft tissue caused +3% AP field dose [AP field, all fx]				
8	16 (4 fields, 4 fx)					
9	18 (3 fields, 6 fx)					
10	24 (3 fields, 8 fx)					Genitals placed differently (AP field, all fx)

* AP field fx 6 not usable due to imager mis-placement.

6.2.3.1 Soft tissue filling of belly board opening

In three patients (3, 4, 7) the EPID-measured dose was consistently higher in the superior region of the AP field. The region of increased signal coincides with the belly board opening (Figure 6-6.d). This effect appears in almost all imaged fractions (not shown), so it is likely not due to random setup errors. Since a local signal increase is attributable to decreased attenuation, the most likely explanation is soft tissue displacement from the beam path, *i.e.* reduced filling of the patients' abdomen into the belly board opening. This may be a result of setup procedure, patient cooperation, or belly board differences between simulation and treatment units. This difference in abdomen drop was confirmed by inspection of the lateral kV setup images (not shown). As a result, the superior region of the AP field received 8%, 4%, 3% more dose than planned for patients 3 (Figure 6-6), 4, 7 respectively. If the AP field contributes to approximately a quarter of the total dose, the maximum dose discrepancy of 8% accounts to approximately 2% of the total dose. This could result in increased dose to small bowel and resulting acute toxicity. Although it is probable that the small bowel contour of the planning CT is not an accurate representation of its location at treatment, judging by the large volume of the contour in the field (Figure 6-6.d, e) it is likely that at least some small bowel received extra dose. Two patients presented grade 2 acute toxicity and the third grade 0-1; the sample size being too small to detect a specific result of increased toxicity.¹⁷¹

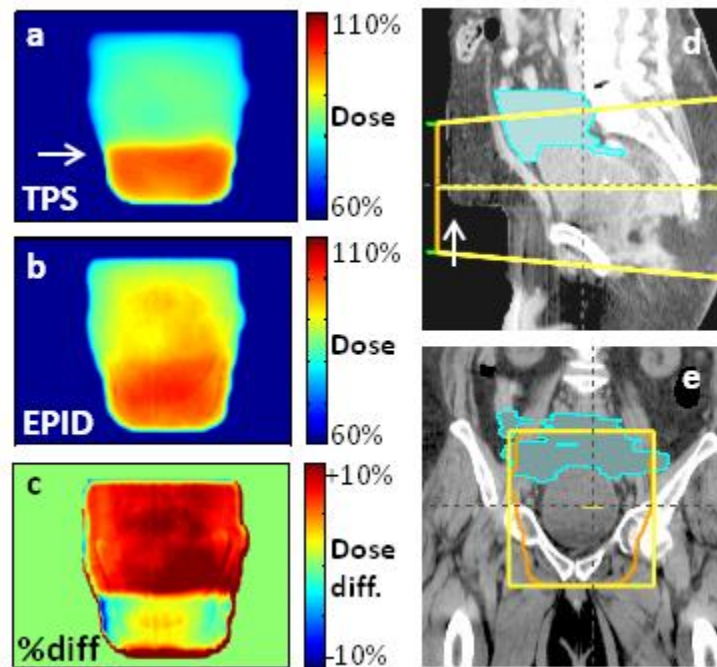


Figure 6-6: Variability in the amount of abdomen that fills the belly board opening affects dose in patient 3, AP field. The filling of the opening is ‘sharp’ at planning (a, d: white arrow). The EPID-calculated dose map at isocentre depth, averaged over 6 fractions, displays a more gradual dose gradient (b). This is due to both different patient positioning and to the softer belly board cushion at the treatment unit (due to greater wear and tear), which in effect makes the hole in the board shallower. The dose discrepancy is especially clear in a point-to-point dose difference map (c). As a result, some of the small bowel (d, e: cyan) was likely overdosed by ~8%. (Dose percentages with respect to AP field.)

We used *in vivo* dosimetry results to guide a single *ad hoc* dose-volume histogram analysis. For patient 3 only, we simulated the observed effect by increasing the MUs of the AP field by 8%. The volume of small bowel receiving 25 Gy increased by 155 cc. Banerjee *et al.* reported the volume of small bowel receiving 25 Gy is a good predictor of grade III acute GI toxicity.¹⁶⁵ Modest increases in dose may thus have a relevant effect on the dose-volume

histogram and potentially increase toxicity. This is a good example of how EPID *in vivo* dosimetry can guide analysis to discern clinically significant differences in delivered dose.

In light of these *in vivo* dosimetry results, we tested the stiffness of the cushions of three boards (simulator and two treatment units) by applying various weights and measuring compression. The simulator belly board (with least wear) was the stiffest, that used for patients 1, 2, 7, 8 was softer (2 mm extra compression), and that for patients 3-6, 9, 10 was drastically softer (8 mm extra). As well, stiffness was uneven between left and right cushions of the same board due to room set up (door on the left of board in one treatment unit, on the right in simulator and other unit). These differences cause variations in soft tissue contours and in anatomy rotation. As a result of this study, we are updating our center's belly boards. These results demonstrate the need for regular quality assurance on immobilization devices.

6.2.3.2 Belly board positioning with respect to patient

EPID *in vivo* dosimetry was able to detect four cases in which the belly board placement was sub-optimal with respect to bony anatomy: patients 2, 3, 5 (not shown), and 6 (Figure 6-7). Typically, after the patient is set up and imaged, the treatment couch is shifted to line up bony anatomy. Depending on the initial setup, this may result in the belly board being in a different location. For all cases, the variability in board placement was ~2 cm, while the allowed variability in our centre is ± 1 cm. This incident was seen in only one of the imaged fractions for each patient, so it was likely a random event of limited clinical consequence.

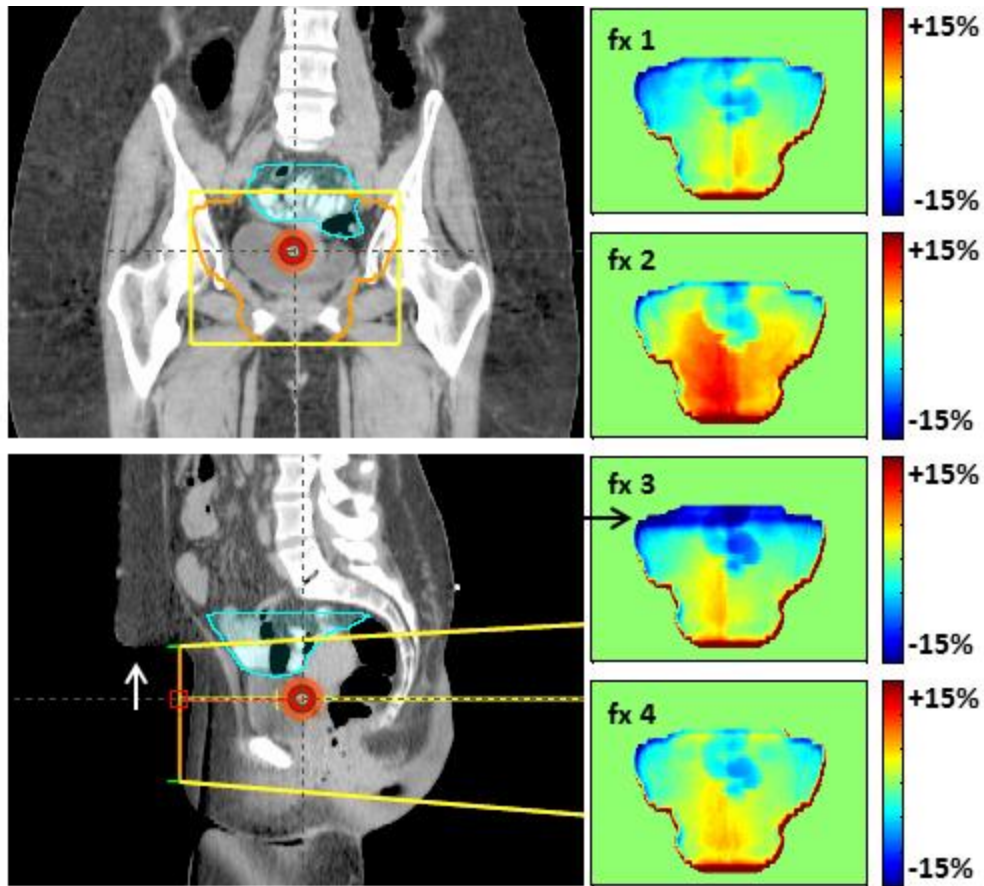


Figure 6-7: Belly board positioning error (patient 8). Dose difference maps for four non-consecutive fractions show that on fx 3, the belly board was placed about 1.5 cm inferior with respect to planning CT (arrows). As a result, an extra ~6 cm of attenuator are in the superior region of the field, causing dose reduction to the target and more small bowel to be in the field.¹⁶⁸

6.2.3.3 Persistent bowel gas

In numerous instances, we found inter-fractional deviations in dose due to the presence of bowel gas. In particular, in patient 2 we found persistent bowel gas, with variations in quantity and location. While soft tissue changes at the belly board opening would affect dose delivery from the AP field only, the presence of gas will mainly affect the dose deposited by the PA field.

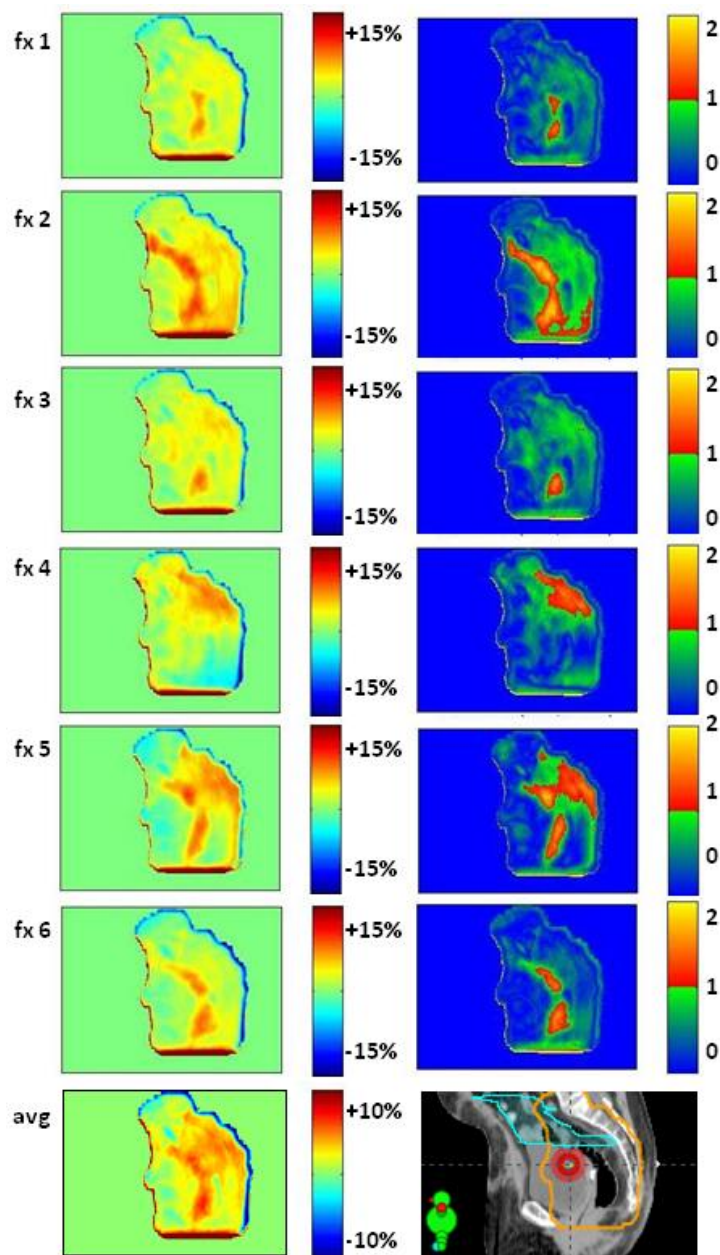


Figure 6-8: Persistent bowel gas affects dose (patient 2). Dose difference maps (left) and 5%, 3mm gamma analysis (right) over six non-consecutive treatment fractions for the left lateral field. The average dose difference map (bottom) indicates consistently more gas at treatment than simulation. There was likely some overdose to the small bowel (cyan contour on the planning CT). For patients like this, *in vivo* dosimetry may warrant adaptive treatment by repeating CT to account for consistent gas. (Percentages with respect to the lateral field's dose.)

From the lateral images (Figure 6-8) we approximated the amount of tissue displaced by the gas and estimated that the dose to a small volume (<10 cc) of the small bowel increased by ~5% of the PA field's dose. This result suggests that, for this patient, the practice of contouring out gas and assigning it density of 1 g/cc (*i.e.* assuming it is not present at treatment) does not accurately represent the treatment conditions. An example of using *in vivo* dosimetry for adaptive radiotherapy would be to identify patients in which gas is reproducible, and replan without contouring it out (or, as a compromise, assign an intermediate density). Further study is needed to warrant clinical practice changes; this result is given to exemplify the power of EPID *in vivo* dosimetry for personalized, adaptive treatments.

6.2.3.4 Bony anatomy setup error

The *in vivo* dosimetry detected two cases of bony anatomy setup error (patients 2 and 6, not shown). In both cases, a dose difference map for one fraction presented a region of underdosage at the location of the belly board opening similar to Figure 6-7, fx 3. Further inspection showed that the entire bony anatomy was ~1-1.5cm inferior with respect to the planned location. On those treatment days there was no kV imaging. This is a good example of how *in vivo* EPID dosimetry allows evaluation of imaging protocols.

6.2.3.5 Other

We found two further cases of consistent dose differences, related to the prone treatment position. The dose maps obtained from the lateral fields of patient 4 (Figure 6-9) may be explained by a different patient position (e.g. contracting the gluteus muscles or rotation of pelvis, due to uneven belly board stiffness) at treatment with respect to planning. In patient 10,

different orientation of the genitals caused increased EPID signal in the inferior region of the field (not shown). These types of errors are only detectable by routine *in vivo* dosimetry.

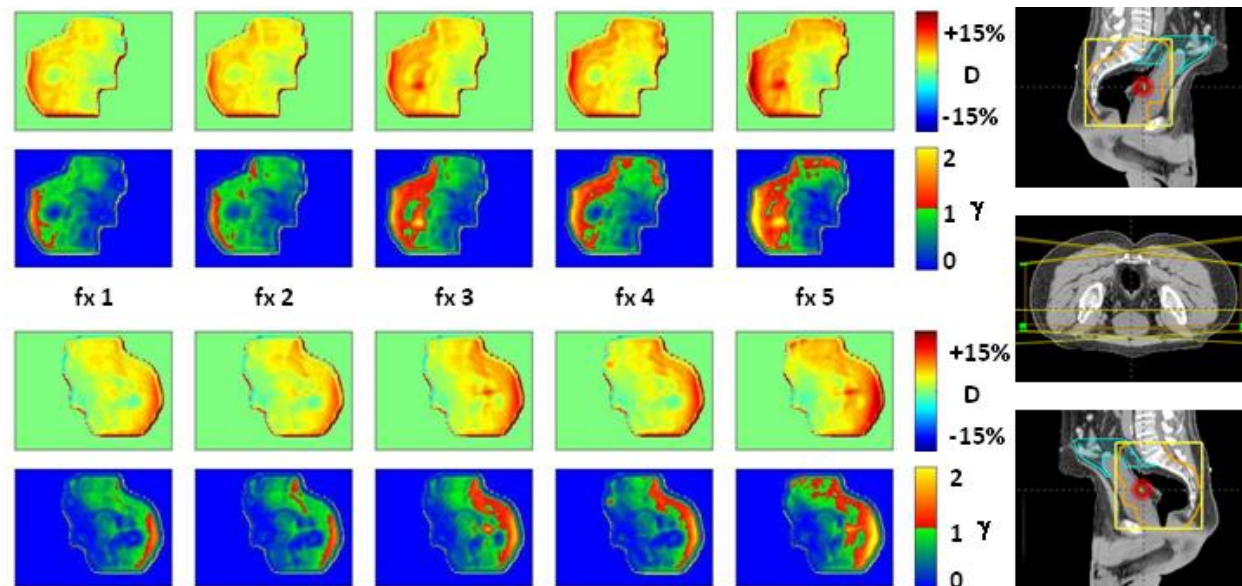


Figure 6-9: Systematic dose discrepancy indicative of muscle relaxation and/or anatomy rotation at treatment with respect to planning (patient 4). Dose difference maps (first row) and 5%, 3 mm gamma evaluation (second row).

6.2.3.6 Limitations

As this study is demonstration of the power and utility of *in vivo* dosimetry to QA delivery techniques, the small sample size and qualitative nature of the analysis limit to our institution the applicability of specific improvements. Also, further development is needed to extend our dosimetry technique to dynamic treatments (*i.e.* IMRT, VMAT). Extension to IMRT may be achieved by summation of all *cine* images into an integrated image. Extension to VMAT would be more laborious, as it would require dose estimation for multiple angles of the treatment arc and 3D summation of the resulting 2D dose maps. In either case, dose accuracy may suffer from the smaller, irregularly shaped subfields present in many dynamic treatments.

A characteristic limitation of using the planning CT to reconstruct dose via EPID images is that the CT may not reflect accurately the patient's setup or anatomy at treatment, producing a dose calculation error.⁴⁰ As a result, dose differences should mainly be interpreted as flags warranting further investigation.

The routine use of the EPID for *in vivo* dosimetry may raise the question of potential radiation damage to the imager, shortening its life span. Studies have found that amorphous Silicon diodes are remarkably resistant to radiation,^{56, 172} with the only probable effect an increase in the necessary dark field correction.^{124, 139, 173} The electronics linked to the imaging panel are known to be more radiosensitive,¹⁷⁴ so care must be taken to ensure only the panel itself is irradiated. For some large fields this may not be possible, so transit dosimetry may not be possible for all fields. As well, some fields with large couch angles may not allow extension of the imager arm due to possible collisions.

6.2.4 Conclusions

We applied a novel, simple, open-source EPID *in vivo* dosimetry method to verify dose delivery in rectal cancer patients treated on the belly board device. The selected patient group was one where we still use 3D-CRT and had significant concerns regarding set up consistency. This tool allowed us to quantify the impact of these concerns to the multidisciplinary tumour group. As a result of this process, we are making improvements to our belly boards by testing cushion stiffness and replacing foam regularly. As well, these results emphasize the need for a more detailed setup procedure (e.g. climb onto belly board from specific side, shift posteriorly to fill board opening), and a lighter weighting of the AP field, most susceptible to soft tissue differences. These results have encouraged our groups to consider more VMAT supine

treatments for eligible rectum patients. EPID *in vivo* dosimetry is a powerful tool to detect errors and evaluate the quality of treatment, and ought to be more widely implemented in the clinic.

General Conclusion

Application of our 2D EPID dosimetry by correlation ratios *in vivo* proved successful. Data acquisition did not interfere with the working of the clinic, and dose maps were successfully calculated. It was in part a surprise to detect actual dose delivery differences across fractions and with respect to planning, and it added useful information to evaluate the quality of our treatment for rectal cancer on the belly board. These differences were related to patient anatomy variations and setup, and produced large dose differences. Evidently, this work shows the potential for EPID dosimetry to detect errors and guide adaptive treatment.

We also found that running our dosimetry in relative mode (i.e. rescaling all dose maps to the same global value and comparing the first fraction to subsequent ones) allowed to focus on subtle changes in small regions of the field. As well, this mode allowed more reliable comparison of dose maps coming from different equipment when patient treatments were rescheduled on other machines.

The major limitation of this study is that results cannot be easily generalized to other sites, where there may be larger inhomogeneities, field shape irregularities, and other confounding factors. To this aim, the following chapter attempts to evaluate the method more generally, and to propose new site-specific metrics for the identification of relevant dose differences.

Chapter Seven: Morphological dose difference analysis for a novel *in vivo* portal dosimetry

General Introduction

In 2008 the British Institute of Radiology recommended that “*in vivo* dosimetry should be used at the beginning of treatment for most patients.”¹⁴ In the previous chapter we gave proof of principle of the clinical feasibility of our in-house IVD method. In this chapter, we present results on 20 patients, in a variety of body sites (rectum, lung, liver, brain, cervix), to investigate the applicability of our method. As well, in this chapter we begin address the question: how should *in vivo* data be used? This is currently an open question in IVD research. Traditionally, dose maps have been compared by means of gamma analysis⁹⁶ and more recently by chi analysis.^{133, 175, 176} These analyses result in a map which highlights regions of discrepancy, but have limitations and caution is necessary when interpreting results.^{177–181} In this chapter we also propose a morphological image analysis approach to automatically determine whether dose difference maps should be flagged as relevant to the user.

At the time of writing, this chapter is ready for submission to peer review. I coordinated patient recruitment and analyzed the data, and designed the morphological analysis, for which Leigh Conroy provided useful assistance. Dr. Wendy Smith and Dr. Derek Brown provided guidance. Dr. Smith was also directly involved in directing analysis and revising the manuscript.

Morphological dose difference analysis for a novel *in vivo* portal dosimetry

S. Peca, D. Brown, and W.L. Smith

Abstract

INTRODUCTION: In radiotherapy, *in vivo* dosimetry (IVD) is desirable for patient safety and for quality assurance of treatment. Recently, we have developed a simple IVD method which makes use of the portal imager. Here we describe our results on 16 patients, in which dose differences are analyzed with a novel morphological connected component (CC) approach.

METHODS: Transit portal images that make use of the treatment beams were acquired approximately once per week for 16 patients, treated in multiple body sites. Dose difference (DD) maps were processed with gamma and CC analysis. For a subset of 10 rectal cancer patients, ROC curves were drawn to compare discriminatory power of DD, gamma, and CC metrics.

RESULTS: 262 fields were verified. EPID IVD and planned dose disagreement was $1.5 \pm 6.6\%$ at isocentre. For a liver treatment with lung in the field our EPID IVD detected diaphragm movement of about 5 mm. The ROC analysis suggests that CC analysis has more discriminatory power than gamma (area under the curve: 0.794 vs 0.765).

CONCLUSION: Our EPID IVD may be applied to clinical treatments, and provides additional information on dose delivery. CC analysis is a valid alternative to gamma, and may be more sensitive to inter-fractional soft tissue changes.

7.1 Introduction

Electronic Portal Imaging Device (EPID) *in vivo* dosimetry (IVD) is dose delivery verification by images produced using the treatment fields.^{29, 82} EPID IVD has the potential to identify treatment delivery errors including: dose calculation, data transfer, patient setup and motion, and mechanical inaccuracies and miscalibrations. IVD may also guide or trigger adaptive radiotherapy.¹⁰⁵ Recent critical errors which led to major injury or death^{19, 28, 31} may have been avoided or reduced by EPID IVD. Although not a new field, challenges related to the use of EPIDs for IVD have greatly limited its routine clinical implementation.¹²⁰

One of the challenges to clinical EPID IVD is that available methods for dose calculation from EPID images are either complex and laborious to implement,^{88, 89, 91, 99, 107} or proprietary^{117, 145, 182}. To address this, our group has developed a simple open-source method for 2D EPID IVD that is easy to implement and improve (see^{104, 130} and Chapters 4, 5, 6.2). It is based on a single-point dose estimation by correlation ratios, initially proposed by Piermattei *et al.*¹⁰² Preliminary results in rectal cancer patients have shown potential in treatment technique review and as a treatment quality review.¹³⁰

A further obstacle to the use of routine EPID IVD is the choice of a metric for automated identification of relevant dose differences,⁹⁷ as the widely adopted gamma analysis has limitations.¹⁸⁰ Bojchko *et al.*¹⁸³ introduced known errors into *in vivo* images and showed that 3% / 3 mm gamma analysis had good detection power for errors in overall dose, field shaping, and anatomical changes, but not for patient positioning. Unfortunately, the application of tighter gamma tolerances *in vivo* is likely to be unpractical, as it would greatly increase the number of false positives. Rather, it is reasonable that for *in vivo* measurements, compared to pre-treatment QA, the dose difference criterion should be loosened to account for acceptable anatomical and

setup uncertainty, to 5% / 3 mm.^{118–120} This suggests that an alternative metric to gamma analysis for EPID IVD is needed. As well, gamma analysis results are normally summarised as the percentage of pixels which pass a pre-specified criteria, independently of whether the failing pixels are spread out or clumped together (which may occur, for example, in proximity to an organ at risk). For this reason, a morphological approach which considers the spatial distribution of the failing points, and the physical area affected (rather than the percentage of the field), may be more suitable.

We have investigated the use of connected component (CC) analysis for evaluation of dose difference (DD) maps. CC analysis is a simple morphological evaluation of a binary image, which quantifies the number and size of isolated ‘islands’ in the image. Figure 7-1 illustrates the analysis which we propose for dose difference maps.

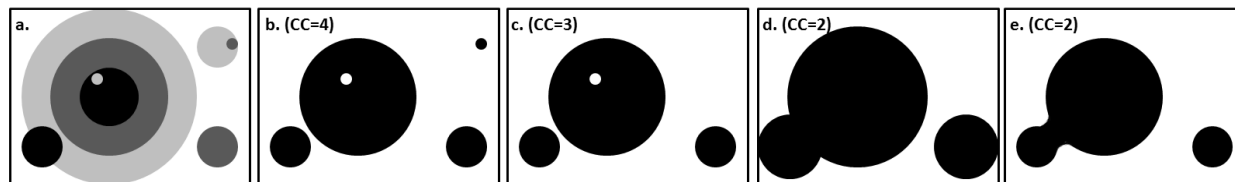


Figure 7-1: Illustration of the morphological approach proposed to evaluate dose difference maps. (a) Initial dose difference with multiple pixel values. (b) Thresholding produces a binary image, with 4 connected components (CC). (c) Small components are ignored. (d) Dilation and (e) erosion by the same radius produce final image, with 2 CCs. The area of the largest CC was chosen as metric for dose difference detection.

In this paper we report *in vivo* results of our EPID IVD method in multiple body sites. In addition, we use receiver operating characteristic (ROC) curves to compare three image analysis metrics techniques which can be used as triggers for error detection. These are: (1) pixel-by-pixel dose difference, (2) gamma analysis and (3) CC analysis.

7.2 Methods

7.2.1 Patients and in vivo imaging

Sixteen cancer patients treated by 3D-conformal radiotherapy were enrolled in this study, which was approved by the local ethics board. Sites were: rectum (patients 1-10, prone on the belly board device), liver (two patients), whole brain (two patients) cervix (two patients). Of the liver patients, one was treated with an SBRT (stereotactic body RT) protocol of 30 Gy in 5 fractions. Patients were treated on a Clinac 21EX (accelerator A) or a Trilogy (accelerator B) (Varian Medical Systems, Palo Alto California, USA). Portal images were acquired with two Varian aSi-1000 EPIDs in *cine* mode (i.e. continuous acquisition). The imaging parameters for *cine* mode are the numbers of frames acquired per second (f/s) and the number of frames averaged into one *cine* image (f/i), and these are characteristic of each accelerator and energy. In addition, the EPID on accelerator A received a license upgrade during the study, increasing the resolution from 512×384 (half) to 1024×768 (full), while the EPID on accelerator B was always run in full resolution. The resulting imaging parameters for accelerator (A, B) and energy (6 MV, 15 MV) were: A-6 MV-half: 12.86 f/s, 8 f/i; A-6 MV-full: 7.50 f/s, 8 f/i; A-15 MV-half: 15 f/s, 4 f/i; A-15 MV-full: 7.83 f/s, 4 f/i; B-6 MV: 7.83 f/s, 8 f/i; B-15 MV: 7.83 f/s, 8 f/i. Each field, at each fraction, produced a set of 4-20 *cine* images, depending on MU and imaging parameters. Imaging was performed approximately once per week per patient.

Each *cine* set was processed with our in house *in vivo* dosimetry MATLAB (The MathWorks, Inc., Natick, MA) routine, which is described elsewhere (^{104, 130} and chapters 4, 5, 6.2). The steps are: (1) the *cine* images are pre-processed and summed; (2) the resulting image is converted to dose at isocentre depth by means of correlation ratios and of the patient's CT data;

(3) this dose map is corrected by 2D multi-Gaussian convolution. Planned dose calculation was performed using Varian Eclipse AAA with a 2.5mm grid.

7.2.2 EPID vs planned dose evaluation

The EPID-calculated dose maps were compared to those predicted by the TPS with three techniques: dose difference, gamma, and connected components. For each technique, multiple metrics were tested, as described below. These comparisons were performed in the high dose region (>80% of maximum dose) to disregard expected inaccuracies at the field edge.

1. Dose difference (pixel-by-pixel) with respect to maximum dose. The tested metrics were the fraction of the field with dose difference less than: 5%, 10%, 15%, 20%, 25%, 30%.
2. Gamma evaluation, with criteria: 5% / 3mm and 10% / 3mm. The metric was the fraction of the field with $\gamma < 1$.
3. CC analysis of dose difference, with respect to maximum dose. The metric was the area of the largest CC, at thresholding levels of 5% and 10%, as described below.

The CC analysis of dose difference maps follows the steps outlined in Figure 7-1. The first step of the CC analysis consists in thresholding the dose difference map with a certain threshold level. The tested thresholds were 5% to 12% in steps of 1%. From each binary mask, CCs smaller than 1 cm² were discarded, to ignore small inaccuracies in the dose reconstruction. Subsequently, CCs were smoothed by image dilation and erosion.¹⁸⁴ Various dilation and erosion radii were tested (0.5 cm to 3 cm) and it was found that results were virtually unaffected by this choice, as long as the images were dilated and eroded by the same radius. Finally, the size (in cm²) of the largest CC was taken as a metric to detect relevant dose differences.

7.2.3 ROC analysis

The pixel-by-pixel dose difference, gamma, and CC analyses were utilized to draw receiver operating characteristic (ROC) curves, as recently outlined by Bojchko and Ford,¹⁸³ making use of Analyse-it Standard Edition (Leeds, UK). To this aim, the 164 DD maps from the 10 rectal cancer patients were investigated making use of available MV and kV images, and of the planning CT. The relevant findings are described in Chapter 6.2.

This analysis led us to label 78 fields as ‘positive’ of dose discrepancies, mainly due to soft tissue differences between simulation and treatment.¹³⁰ Although the great majority of these differences were within clinical tolerance (i.e. no harmful errors), they were of interest in quantifying the reproducibility and accuracy of the setup procedure.

For a delivery to be classified as ‘positive’ either ~20% or more of the field had dose discrepancies of more than 10%, or there had to be distinct regions of DD which were due to suboptimal treatment. Example of the latter are thin (~1 cm) regions of +3-8% dose extending L-R across the field, which, after comparing kV setup images to planning CT, were found to be due to differences in soft tissue and belly board location. Positive events were further classified into: bony alignment errors, belly board positioning errors, soft tissue changes (i.e. not due to board misalignments), and bowel gas changes (see Chapter 6.2).

For each ROC curve, the area under the curve (AUC) was calculated to quantify the performance of the chosen metric as a marker for dose differences. Differences between AUCs were judged significant based on a 95% confidence interval as proposed by Delong *et al.*¹⁸⁵

7.3 Results and Discussion

A total of 262 fields delivered to 16 patients were verified. An example of the EPID *in vivo* dosimetry graphical output is provided in Figure 7-2.

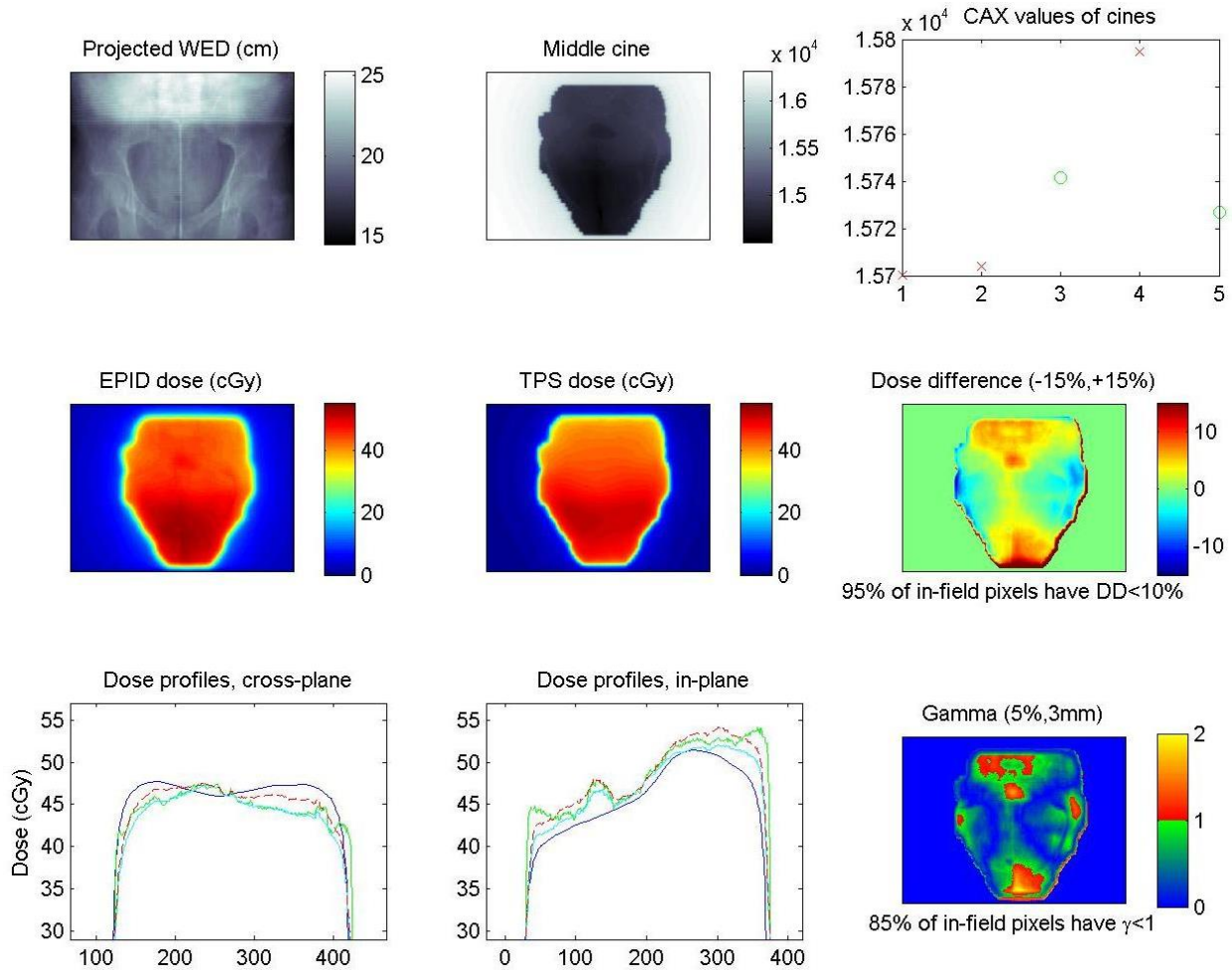


Figure 7-2: Example output of our EPID *in vivo* dosimetry; prone cervix patient, AP field. (a) Projection of water equivalent depth (WED) along ray lines from source to each EPID pixel, from planning CT. (b) One of the *cine* EPID images (a.u.). (c) Value of the central 5×5 pixels for each of the 5 *cines* (*x* axis). The first two *cines* are discarded as they suffer from beam-on artifacts.⁸⁰ (d) Planar dose at isocentre depth, reconstructed from EPID and WEDs. (e) Planned dose. (f) In-field pixel-by-pixel dose difference map. (g,h) Cross-plane and in-plane central profiles of: planned dose (blue), dose reconstruction steps (green, cyan), and final EPID dose (dashed red). (i) Gamma evaluation (5% / 3mm).

7.3.1 SBRT case study: lung-liver border

The fields of the SBRT liver patient included the inferior portion of the right lung. The marked difference in attenuation produced increased contrast and thus increased dose difference detection power, as illustrated in Figure 7-3. This treatment consisted in large doses of 6 Gy per fraction, increasing the requirements of dosimetric accuracy and precision. To account for breathing motion, beam gating was triggered by the Varian RPM (real-time position management) system. Notwithstanding this precaution, our *in vivo* dosimetry detected noticeable differences between the two imaged fractions. As breathing motion may be patient- and fraction-specific, *in vivo* data is valuable in providing guidance on the width of field margins to ensure target coverage, and for quality assurance of the treatment delivery technique.

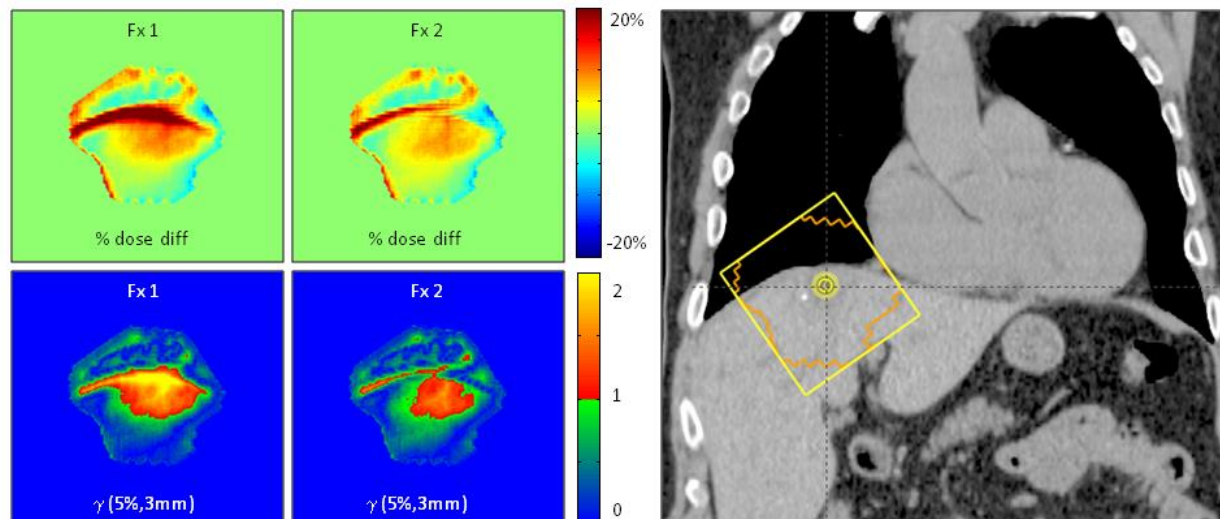


Figure 7-3: Left: Results from EPID IVD from the liver SBRT case treated with exhale breath hold monitored by RPM. Percent difference (top) and gamma analysis (bottom) maps between EPID-measured and TPS dose display a region of disagreement across the centre of the field, more so in fraction 1 (left). Inspection of the breath-held planning CT (right) showed that the region of discrepancy is in the lung-liver border. IVD indicates that at time of treatment the liver was 4-7 mm inferior with respect to planning.

In the presence of lung, our dose calculation algorithm loses accuracy.¹⁰⁴ This is due to scatter dose differences which are currently not accounted for during the calibration measurements performed in homogeneous phantoms. For this reason, the data from the SBRT patient is excluded from further analysis.

7.3.2 Dose difference and gamma analyses

Across the 15 patients (249 fields) in which lung was not in the field, the CAX dose difference between TPS and EPID was $1.5 \pm 6.6\%$ (mean \pm SD), and the median percentage of in-field pixels passing gamma analysis were 72% and 96% for 5% / 3mm and 10% / 3mm criteria respectively (Table 7-1). The large variability is due in part to the limited accuracy of the algorithm, and in part to true dose discrepancies.

Table 7-1: Dose difference statistics (pixel-by-pixel and gamma) for 15 patient treatments.

Site	N. of patients	N. of imaged fields	Mean CAX DD* (% \pm SD)	Median % of field** with $\gamma < 1$ (5%/3mm)	Median % of field** with $\gamma < 1$ (10%/3mm)	Median % of field** with DD < 10%	Median % of field** with DD < 15%	Median % of field** with DD < 20%
Rectum	10	164	1.4 \pm 6.2 %	73.2 %	96.1 %	95.8 %	99.9 %	100 %
Other	6	85	1.9 \pm 7.3 %	69.7 %	96.2 %	93.3 %	98.7 %	99.9 %
All	15	249	1.5\pm6.6 %	72.1 %	96.1 %	94.9 %	99.7 %	100 %

*Dose difference, with respect to TPS maximum dose
 **Region of >80% of TPS dose

7.3.3 ROC analysis of dose difference, gamma, and CC metrics

We ran our in-house morphological CC analysis on the 164 rectal dose difference maps. An example is provided in Figure 7-4.

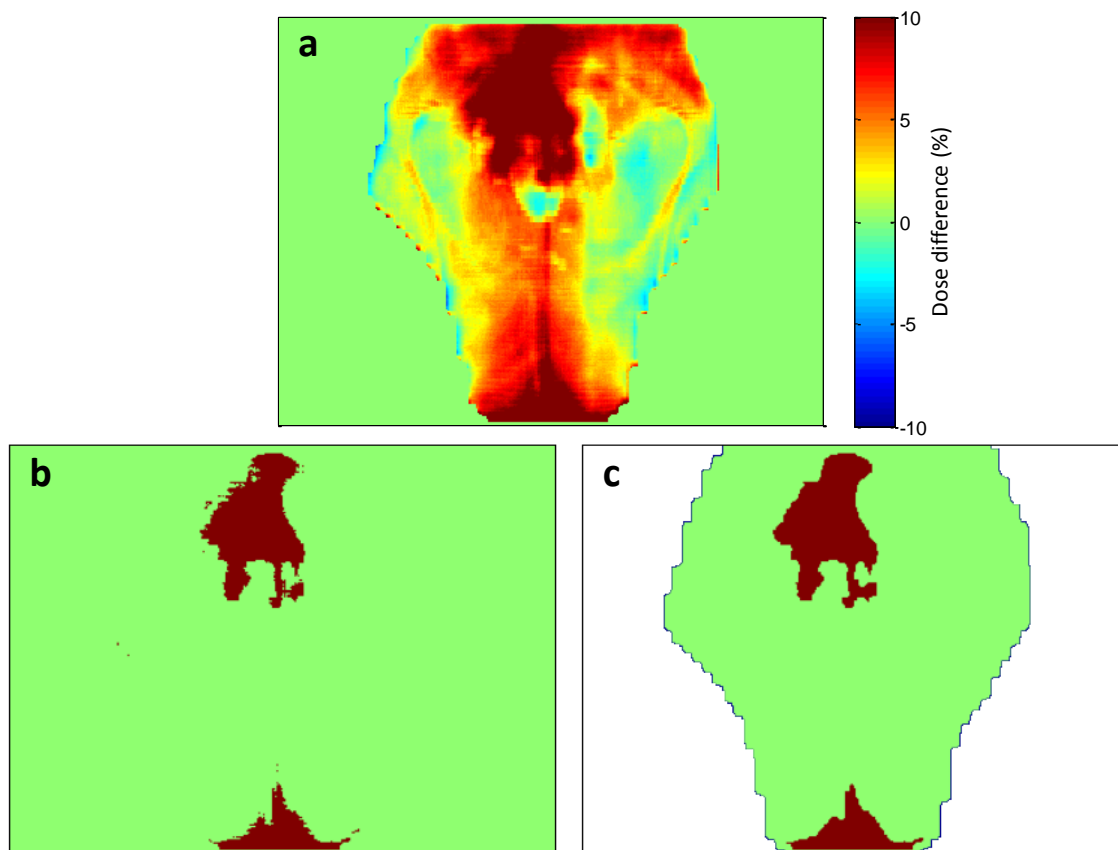


Figure 7-4: Illustration of the connected component (CC) analysis. (a) Planned vs EPID-calculated dose difference map. (b) Binary dose difference map, thresholded at 10%. (c) Binary map after removal of small CCs, dilation, erosion, overlaid on field mask. Two CCs result, the largest having area 21 cm². (Data: single fraction of an Ant-Post field.)

In Figure 7-5 we report the ROC curves from of the tested metrics. The CC analysis curves gave the largest AUC, suggesting it may be the best discriminator, although for the 10% dose difference threshold, it is not significantly different from gamma. For all three metrics (dose difference, gamma, area of largest CC), the AUC values (and therefore the discriminatory power of the tests) are comparable to previously reported simulations of body contour changes of 0.5-1.0 cm in which 3% / 3mm gamma analysis resulted in ROC curves of area 0.67-0.88.¹⁸³

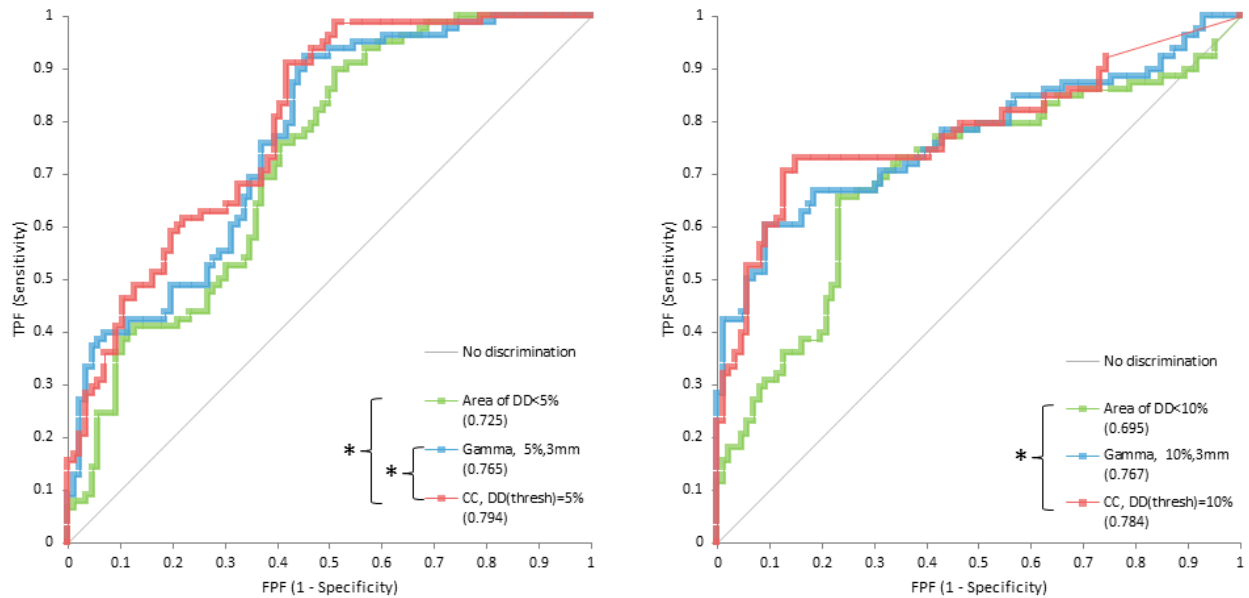


Figure 7-5: ROC curves for various metrics suggest that connected component (CC) analysis performs best in detection of specific dose discrepancies. The larger the area under the curve (AUC, in parenthesis in the legend), the greater the ability of the metric to discriminate relevant dose differences between plan and delivery. At multiple dose difference (DD) levels, including 5% (a) and 10% (b), the largest AUC comes from CC analysis. (TPF: true positive fraction; FPF: false positive fraction; *:p<0.05).

To better illustrate the discriminatory power of CC analysis, compared to gamma and DD, Figure 7-6 reports values for the three metrics for all 164 tested fields. The 78 true positives (those fields which a more in-depth analysis of MV, kV, and CT images revealed of interest in regards to QA of treatment delivery) are represented by crosses (x), while the 86 true negatives are circles (o). For each plot, the horizontal line is a compromise between sensitivity and specificity. Crosses below such line are false negatives, circles above are false positives.

Connected component analysis performs better in discriminating fields 94-96 (AP field, patient 7, region (a) of Figure 7-6), where delivery was affected by reduced displacement of soft tissue in the belly board opening. This was likely due to differences in patient setup procedure,

and in belly board devices between simulator and treatment units (see Chapter 6.2). CC analysis is also best in identifying fields 149-164 as positive, labelled as region (b). These are the AP and LAT fields of patient 10, in which the soft tissue of the male genitals were positioned differently at treatment with respect to simulation.

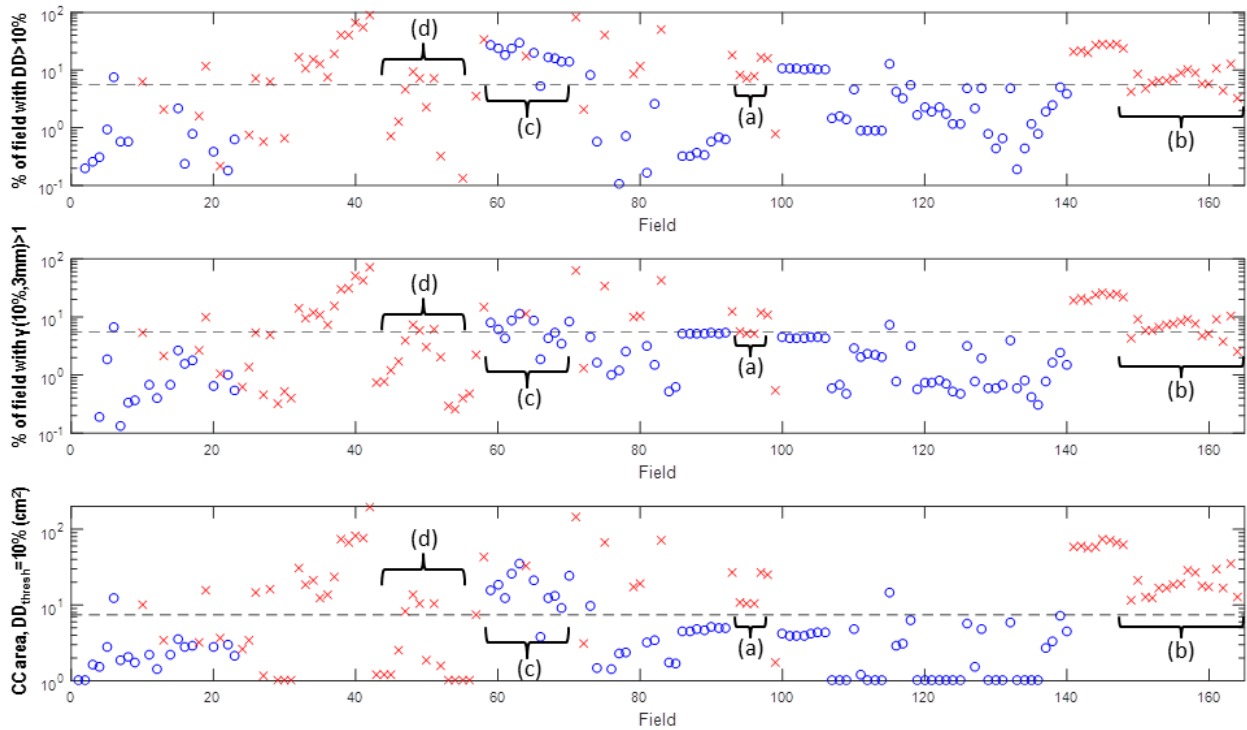


Figure 7-6: Connected component (CC) analysis (bottom) performs equal or better than gamma analysis (middle) and dose difference (DD) alone (top). Crosses: fields manually flagged for relevant dose discrepancy (positives); circles: other fields (negatives). CC better discriminates positive dose deviations due to soft tissue variations caused the belly board immobilization device (a) and setup differences (b). CC also produced some false positives (c). The dashed lines represent choices between sensitivity and specificity.

For fields 61-69 (region (c), AP and PA fields of patient 5), gamma analysis showed slightly better specificity than both CC and DD, who mislabeled four negative fields as (false) positives. These fields were labelled as negative because analysis of available MV, kV, and CT

images for this patient was not able to determine the reason for the dose difference from plan. There may be other underlying causes for this discrepancy, meaning they should actually have been labelled as positive. In that case, gamma would actually have mislabeled four fields as (false) negatives, displaying worse sensitivity than DD and CC.

Lastly, for fields 43-57 (region (d), AP and LAT fields of patient 4) all three metrics output some false negatives. Further analysis suggested that at CT simulation this patient may have contracted muscles. Gluteus contraction would explain the systematic dose difference in the posterior rim of the lateral fields, and abdominal contraction would account for the different attenuation in the region of the belly board opening, as seen in the AP field. These were small effects which neither of the metrics had the sensitivity to detect.

Based on the relative differences between each metric's score for the fields described above (regions a, b, c, of Figure 7-6), a qualitative ranking of the metrics' sensitivity may be determined. Along with previous observations (^{104, 130} and Chapters 5 and 6.2), this allows us to summarize the sensitivity of our EPID IVD to various types of errors, in Table 7-2.

Table 7-2: Qualitative sensitivity, to various types of errors, of our EPID in vivo dosimetry (IVD), evaluating results by dose difference (DD) only, by gamma analysis, and by morphological connected component (CC) analysis. (References: ^{104, 130} and Chapter 6.2)

	TPS dose calculation errors	Data transfer errors	Output calibration errors	Field shape collimation errors	Bony alignment errors	Belly board positioning errors	Other soft tissue changes	Bowel gas changes
EPID IVD, DD only	Good	Good	V. good	V. good	Med	Med	Low	Low
EPID IVD, Gamma	Good	Good	Good	V. good	Med	Med	Med	Med
EPID IVD, CC	Good	Good	Good	V. good	Good	Good	Good	Good

7.3.3.1 Limitations

The distinction between positive and negative events for ROC analysis is partly subjective, based upon the dose difference maps, and the kV (not always available), MV, and CT images. This is unlike the work by Bojchko and Ford¹⁸³ who introduced known errors and had an objective classification between modified and unmodified deliveries. While the present method suffers of an inevitable bias, it also illustrates the power to determine the metric which is most appropriate to answer a specific question, by ‘teaching’ the system the type of dose difference to detect. For example, if the user wants to detect anatomical and setup differences for the purpose of QA of the treatment process, he/she can classify a subset of dose maps accordingly, determine the best metric by ROC analysis, and use that metric to test other dose maps.

In this study we present results for 3D conformal RT only. In principle, the method is extendable to IMRT without modifications. Extension to VMAT, on the other hand, would require projection through the CT data and dose reconstruction at every gantry angle. While this is possible thanks to *cine* imaging, it would greatly increase computational requirements. In addition, the signal-to-dose correlation ratios measured with simple square fields of $5 \times 5 \text{cm}^2$ and up may not be adequate to estimate dose from small and irregularly shaped VMAT subfields.

As with all CT-based reconstruction, there is a dose calculation error associated with differences in patient setup and anatomy between time of CT and that of treatment.⁴⁰ As a result, such dose differences ought to be treated primarily as flags warranting further investigation. Also, as the patient population is small and heterogeneous, no generalizations can be made. Rather, the purpose of this work was to give proof of principle of a novel, simple EPID IVD method, and of a morphological analysis of dose difference images.

7.4 Conclusion

We give proof of concept of a novel, open-source, clinical EPID *in vivo* dosimetry, and propose a new morphological analysis of 2D dose difference maps. For an arbitrary task of identifying dose discrepancies due to soft tissue and setup differences, connected component analysis performs equal to or better than gamma analysis. In future work, the location of connected components of dose differences may be overlaid to contoured organs at risk, providing further clinically useful information.

7.5 Appendix: Further results in lung

In this chapter, results from 16 patients treated in multiple sites were presented. In addition, another four patients were enrolled in the study. For these the treatment volume was in the lung, where our EPID-based dose calculation accuracy is limited (see Ch.3, Results). Their data was excluded from this chapter for publication purposes, and is presented in this appendix for completeness.

The total number of patients enrolled in the study was 20, and the number of courses was 21 (one patient was treated in two sites). Of these courses, 15 were in relatively homogeneous body sites (rectum: 10, cervix: 2, whole brain: 2, liver: 1) and six in regions of high inhomogeneity (lung: 5, liver with lung in field: 1). Table 7-3 presents the results for all courses.

Table 7-3: Dose difference statistics (pixel-by-pixel and gamma) for all fields.

Site, technique	N. of courses	N. of fields verified (multiple fx)	Mean CAX dose difference* (%±SD)	Gamma: Median % of field** w/ $\gamma < 1$ (5% / 3mm)	Gamma: Median % of field** w/ $\gamma < 1$ (10%/3mm)	Median % of field** with dose difference <10%	Median % of field** with dose difference <15%	Median % of field** with dose difference <20%
Rectum, prone on belly board	10	164	1.4±6.2 %	73.2 %	96.1 %	95.8 %	99.9 %	100 %
Other non-lung treatments	5	85	1.9±7.3 %	69.7 %	96.2 %	93.3 %	98.7 %	99.9 %
All, no lung	15	249	1.5±6.6 %	72.1 %	96.1 %	94.9 %	99.7 %	100 %
Lung	6	85	7.1±11.9 %	52.0 %	72.5 %	54.7 %	85.5 %	98.6 %
All	21	334	2.7±8.3 %	67.9 %	94.8 %	91.9 %	99.3 %	100 %

*With respect to TPS maximum dose
 **Region of >80% of TPS dose

In the presence of lung, our EPID-based calculation overestimates dose by approximately 7%, in agreement with the preliminary results of Chapter 3, with a very large variability across patients. This large variability is displayed in Figure 7-7 and is related to the amount of lung tissue in the field. Of the six patients with lung in the field, one had dose difference maps of the same order of agreement as the homogeneous group, three had somewhat larger dose difference, and two had drastically larger differences.

Acknowledgment

We are grateful to *Analyse-it* (Leeds, UK) for providing a free license which enabled graphing of the ROC curves.

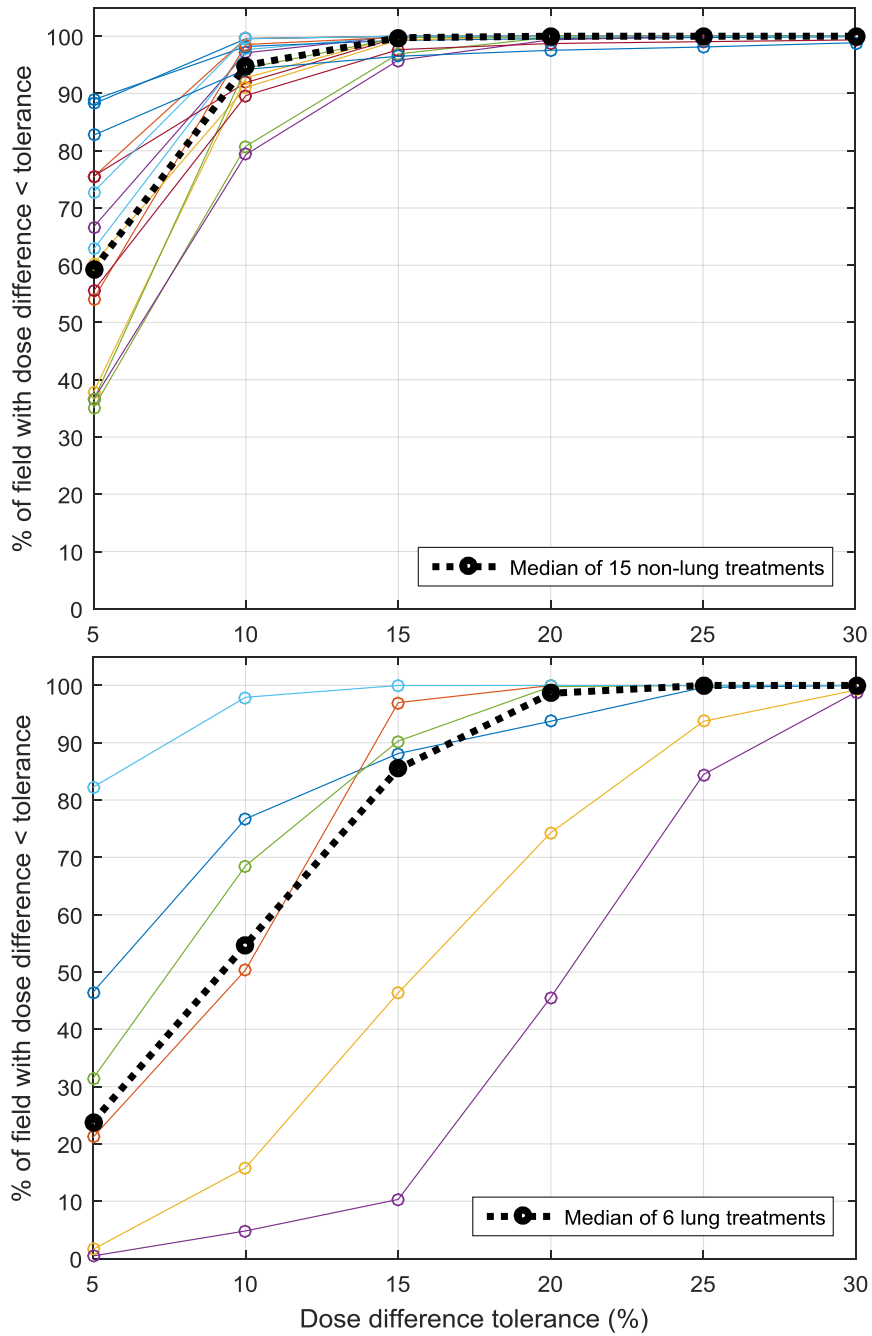


Figure 7-7: Pixel-by-pixel dose difference between dose calculations from EPID images and TPS, 21 treatments. Solid coloured points are median values for a single patient; dashed black is median over all patients. For fields which do not go through lung (top), a median value of 96.1% of the field has dose difference less or equal to 10%. For fields through lung (bottom) there is more variability across patients and worse agreement with TPS.

General Conclusion

In this chapter, we applied our in-house EPID IVD to twenty patients treated in multiple body sites in our centre. We found that routine implementation is clinically feasible, but also that accuracy and precision depend the homogeneity of the treated region. As a result, it is important to set adequate tolerances for dose difference and distance-to-agreement to maximize sensitivity and specificity. We also found that morphological connected component analysis of dose difference maps is as effective or better than gamma analysis in identifying relevant dose discrepancies. More work is needed to determine the ideal tolerances for the purposes of error detection and adaptive treatment.

Chapter Eight: **Conclusions and future work**

In vivo dosimetry is a growing field.²⁹ Although governing bodies have been recommending the use of routine IVD for most patients,¹⁴ very few centres have implemented it. Among the reasons for this lag in clinical implementation are the requirements of most IVD systems in terms of resources and time. The advantage of using the EPID for IVD is that it is already mounted on the great majority of linear accelerators, requires no additional setup time, and can be deployed for the majority of treatment fields, for the majority of patients. Although a great number of research papers have been published in the field of EPID IVD, currently a small number of centres make use of it. This is likely due to the complexities associated with some proposed methods. Nonetheless, multiple papers support the enormous potential of EPID IVD to: prevent critical errors, assess patient setup and anatomical changes, and guide adaptive radiotherapy. Routine EPID IVD may allow safer, better treatments, with minimal resources.

In this thesis, I described our in-house EPID IVD method, which builds on the model proposed by Piermattei *et al.*,¹⁰² namely, correlation ratios. These ratios (between EPID signal and dose at mid-depth, and between dose at mid-depth and dose at isocentre depth) allow an intuitive and simple reconstruction of dose from images. The major challenge we had to face was that of using correlation ratios measured on the CAX to determine dose in the whole plane. A first empirical approach gave adequate results in central regions of regularly shaped fields, but not elsewhere (Ch. 3). To improve this, we developed a model-based approach which relies on 2D convolution of the EPID image by a multi-Gaussian kernel which, in turn, was derived also from empirical data (Ch. 4).

Application of our novel EPID IVD in the clinic proved successful and provided useful insight into the strengths and limitations of the method. Image acquisition during treatment does not impact clinical workflow, and thus may be performed for the majority of patients. We found very high sensitivity *in vivo* to small variations in dose, primarily to variability in anatomy and setup. This high sensitivity is due in part to the dose error amplification which comes from differences at treatment with respect to the planning CT (Ch.5, Figure 5-10). Results suggest that the widely adopted 3% / 3mm gamma analysis is probably ill-suited to *in vivo* dose evaluation, and that looser tolerances are needed. As well, analysis of the largest connected component of dose difference maps suggest that, for the detection of some types of errors, a morphological image analysis approach may be of greater value than gamma. Whatever the method used in analysis, this enhanced sensitivity can provide useful information on the general quality of dose delivery. In rectal cancer patients treated prone on the belly board we found, among other results, noticeable inter-fractional soft tissue variations in at least three of 10 patients. This result helps guide the choice of margin size for this type of treatment, and prompted us to replace some cushions of our clinic's belly boards. For the other body sites, it is difficult to draw specific conclusions, due to the small number of patients. Nonetheless, results suggest that dose calculation is reliable except in the presence of lung, where a systematic error was detected, likely due to increased scattering.

In conclusion, the EPID IVD method that I propose in this thesis has good potential to be developed into a clinical tool. It is simple and open source, and thus can be further developed and improved. It requires no additional hardware or software, other than the readily available MATLAB environment. It is sensitive to gross errors (field shaping, output, etc.) and thus can detect most harmful errors. As well, it is sensitive to more subtle differences due to patient

position, motion, anatomy, and setup. The user can use this additional information to help assess quality of the treatment delivery. This same information can be used to guide adaptive treatments or identify those patients which may benefit from increased imaging. Finally, the computational environment in which the dose difference maps are analyzed make it possible to apply multiple and novel image analysis tools to flag relevant dose differences, such as gamma and morphological analyses.

Future work

In the hope that this research work will continue, the following are suggestions to address current limitations of the dose calculation method and to further develop it.

It was found that the beam-end image loss correction was suboptimal, with increasing error at low MUs (Ch.5, Figure 5-8). This can be improved by increasing the number of data points that produce the correction of Figure 5-3. Alternatively, a further MU correction factor may be introduced based on the trend of dose difference with MU visible in Figure 5-8. This limitation may be also circumvented entirely by eliminating frame averaging, to the expense of increasing 8-fold the number of *cines* and thus requiring more digital storage, or by switching from *cine* to integrated mode, losing the possibility of real-time intervention.

Tests were performed with square fields on homogeneous slab phantoms, but further measurements are needed to quantify the dose calculation error associated with irregular fields and inhomogeneities. For the latter, it would be sufficient to repeat some measurements described in Ch. 5, substituting varying amounts of solid water with slabs of lung- and bone-mimicking materials. Keeping total water equivalent thickness constant, dose differences between the two cases would be due to not considering scatter differences. This study may lead

to inhomogeneity correction factors to improve dose calculation in the presence of lung (Ch.7, Table 7-1). Regarding field shapes, measurements in Ch.5 could be repeated with varying degrees of irregularity in the fields, up to the amount typical of IMRT sub-fields.

As all the work presented in this thesis is with 3D-conformal radiotherapy, a natural extension would be to other treatment techniques such as IMRT or VMAT (volumetric arc therapy). The small and irregular IMRT sub-fields may require dedicated correlation ratios, as mentioned above. For VMAT, the current limitation would be in the script that calculates the water equivalent thickness along every ray line from the source to each EPID pixel, which runs in approximately 2 hours on a standard PC. For static gantry deliveries (3D-CRT, IMRT) this is not a difficulty, as this can be made to run before delivery, as it makes use of the planning CT only. For VMAT, on the other hand, the large number of projections at multiple gantry angles would require optimization of said script. The images (acquired in *cine* mode) can be resolved by gantry angle based on header information.

A second possibility of extension of the current method is to make it work in real-time. This would require hardware modifications for most linear accelerators (e.g. installation of a ‘frame-grabber’ board for non-TrueBeam Varian units⁹⁰) and some improvements in the dose calculation script which currently requires about 10 s. As well, each treatment unit would need a dedicated computer to perform the MATLAB processing. This possibility is of particular interest in IMRT, to ensure accurate motion of the MLC leaves, and in SRS and SBRT, where large doses per fraction increase the likelihood of harmful errors. At the onset of this research project, we made the choice of recording images in *cine* rather than *integrated* mode purposely to allow for future implementation in real-time. One main advantage of real-time measurement is the

possibility of detecting errors and interrupting treatment while the beam is on. Recently, Woodruff *et al.* have reported on the first, functional, real-time EPID IVD.¹⁴¹

Finally, two important goals must be attained before clinical implementation of this EPID IVD: automation of image export and analysis, and determination of optimal dose difference evaluation metrics. Regarding the former, a script can be made to run in the record and verify (R&V) system that would send all images to a computer which could be programmed to read identifier information from the headers and process them as they come. Secondly, it is essential that only the dose discrepancies that are of interest be flagged to the user. For this, more work is required to determine the optimal alert criteria (dose difference and distance-to-agreement tolerances for gamma analysis, size of connected components for morphological analysis, etc.). These criteria will depend on body site (accuracy may likely differ across sites), technique (e.g. standard fractionation vs. hypofractionated), and intent (i.e. curative vs. palliative). As well, different metrics will be more or less sensitive to different types of error (output, MLC position, anatomical variations, setup changes, etc), so a combination of different metrics will provide the most useful sensitivity, as in the seminal work by McDermott *et al.*⁹² For the purpose of adaptive radiotherapy, the accumulation of dose difference over consecutive fractions will likely prove to be most useful.

References

- ¹ Canadian Cancer Society, “Canadian Cancer Statistics 2015: Special topic: Predictions of the future burden of cancer in Canada,” (2015).
- ² L.E. Antonuk *et al.*, “Thin-film, flat-panel, composite imagers for projection and tomographic imaging,” *IEEE Trans. Med. Imaging* **13**(3), 482–90 (1994).
- ³ G.J. Kutcher *et al.*, “Comprehensive QA for radiation oncology: Report of AAPM Radiation Therapy Committee Task Group 40,” *Med Phys* **21**(4), (1994).
- ⁴ B. Fraass *et al.*, “Quality assurance for clinical radiotherapy treatment planning: Report of AAPM Radiation Therapy Committee Task Group 53,” *Med. Phys.* **25**(10), 1773–1829 (1998).
- ⁵ E.E. Klein *et al.*, “AAPM TG 142 report: quality assurance of medical accelerators.,” *Med. Phys.* **36**(9), 4197–4212 (2009).
- ⁶ J.F. Williamson, P.B. Dunscombe, M.B. Sharpe, B.R. Thomadsen, J. a. Purdy, and J. a. Deye, “Quality Assurance Needs for Modern Image-Based Radiotherapy: Recommendations From 2007 Interorganizational Symposium on ‘Quality Assurance of Radiation Therapy: Challenges of Advanced Technology,’” *Int. J. Radiat. Oncol. Biol. Phys.* **71**(1 SUPPL.), 2–12 (2008).
- ⁷ ASTRO, *Safety is No Accident: A Framework for Quality Radiation Oncology and Care* (2012).
- ⁸ M.G. Herman *et al.*, “Clinical use of electronic portal imaging: Report of AAPM Radiation Therapy Committee Task Group 58,” *Med Phys* **28**(5), 712 (2001).
- ⁹ M. Van Herk, P. Remeijer, C. Rasch, and J. V. Lebesque, “The probability of correct target dosage: Dose-population histograms for deriving treatment margins in radiotherapy,” *Int. J. Radiat. Oncol. Biol. Phys.* **47**(4), 1121–1135 (2000).
- ¹⁰ D. Yan, F. Vicini, J. Wong, and A. Martinez, “Adaptive radiation therapy,” *Phys. Med. Biol.* **42**(1), 123 (1997).
- ¹¹ C.L. Brouwer, R.J.H.M. Steenbakkers, J.A. Langendijk, and N.M. Sijtsema, “Identifying patients who may benefit from adaptive radiotherapy: Does the literature on anatomic and dosimetric changes in head and neck organs at risk during radiotherapy provide information to help?,” *Radiother. Oncol.* **115**(3), 285–94 (2015).
- ¹² S.J. Frank *et al.*, “Quantification of prostate and seminal vesicle interfraction variation during IMRT.,” *Int. J. Radiat. Oncol. Biol. Phys.* **71**(3), 813–20 (2008).
- ¹³ J. Nijkamp *et al.*, “Adaptive radiotherapy for prostate cancer using kilovoltage cone-beam computed tomography: first clinical results.,” *Int. J. Radiat. Oncol. Biol. Phys.* **70**(1), 75–82 (2008).

- 14 British Institute of Radiology, *Towards Safer Radiotherapy* (2008).
- 15 D.A. Jaffray *et al.*, “Assuring Safety and Quality in Image Guided Delivery Of Radiation
Therapy,” *Pract. Radiat. Oncol.* (2013).
- 16 T.D. Solberg *et al.*, “Quality and safety considerations in stereotactic radiosurgery and
stereotactic body radiation therapy: Executive summary,” *Pract. Radiat. Oncol.* **2**(1), 2–9
(2012).
- 17 WHO, *Radiotherapy risk profile* (2008).
- 18 W. Bogdanich and R.R. Ruiz, “Radiation Errors Reported in Missouri,” *New York Times*
(February 24, 2010), 2–5 (2010).
- 19 W. Bogdanich, “As Technology Surges, Radiation Safeguards Lag,” *New York Times* 1–
13 (2010).
- 20 IAEA (International Atomic Energy Agency), *Lessons learned from accidental exposures
in radiotherapy* (Vienna, 2000).
- 21 W. Bogdanich, *A Pinpoint Beam Strays Invisibly, Harming Instead of Healing*, *New York
Times* (December 29, 2010), (2010).
- 22 G. Huang *et al.*, “Error in the delivery of radiation therapy: Results of a quality assurance
review,” *Int. J. Radiat. Oncol. Biol. Phys.* **61**(5), 1590–1595 (2005).
- 23 J.M. Moran *et al.*, “Safety Considerations for IMRT,” *Pract. Radiat. Oncol.* **1**(1), 190–195
(2011).
- 24 WHO, *World Health Organization. Report on the Results of the Web-Based Modified
Delphi Survey of the International Classification for Patient Safety* (Geneva, 2007).
- 25 J. Shafiq, M. Barton, D. Noble, C. Lemer, and L.J. Donaldson, “An international review
of patient safety measures in radiotherapy practice.,” *Radiother. Oncol.* **92**(1), 15–21
(2009).
- 26 B.G. Clark, R.J. Brown, J. Ploquin, and P. Dunscombe, “Patient safety improvements in
radiation treatment through 5 years of incident learning,” *Pract. Radiat. Oncol.* **3**(3), 157–
163 (2013).
- 27 J.A. Purdy *et al.*, “Medical accelerator safety considerations: report of AAPM Radiation
Therapy Committee Task Group No. 35.,” *Med. Phys.* **20**(4), 1261–1275 (n.d.).
- 28 S. Derreumaux *et al.*, “Lessons from recent accidents in radiation therapy in France,”
Radiat. Prot. Dosimetry **131**(1), 130–135 (2008).
- 29 B. Mijneer, S. Beddar, J. Izewska, and C. Reft, “In vivo dosimetry in external beam
radiotherapy.,” *Med. Phys.* **40**(7), 70903 (2013).
- 30 ICRP, “ICRP 86: Prevention of accidental exposures to patients undergoing radiation
therapy.,” *Ann ICRP* **30**(3), 7–70 (2000).
- 31 M. V Williams, “Radiotherapy near misses, incidents and errors: radiotherapy incident at

- Glasgow.,” *Clin. Oncol. (R. Coll. Radiol)*. **19**(1), 1–3 (2007).
- 32 W.P.M. Mayles, “The Glasgow incident--a physicist’s reflections.,” *Clin. Oncol. (R. Coll. Radiol)*. **19**(1), 4–7 (2007).
- 33 J. Krishnamoorthy, A. Salame-Alfie, and J. O’Connell, “An analysis of radiation therapy medical events in New York State: the role of the state radiation programs in patient safety.,” *Health Phys.* **106**(5 Suppl 2), S71-7 (2014).
- 34 E. Yorke, D. Gelblum, and E. Ford, “Patient safety in external beam radiation therapy,” *Am. J. Roentgenol.* **196**(4), 768–772 (2011).
- 35 M. Baeza, “Accident prevention in day-to-day clinical radiation therapy practice,” *Ann. ICRP* **41**(3–4), 179–187 (2012).
- 36 ICRP, “ICRP publication 112: Preventing accidental exposures from new external beam radiation therapy technologies.,” *Ann. ICRP* **39**(4), 3–5 (2009).
- 37 J. Cunningham, M. Coffey, T. Knöös, and O. Holmberg, “Radiation Oncology Safety Information System (ROSIS) - Profiles of participants and the first 1074 incident reports,” *Radiother. Oncol.* **97**(3), 601–607 (2010).
- 38 www.cancer.org, *Cancer Facts & Figures 2005*, (n.d.).
- 39 www.cancer.org, *Cancer Facts & Figures 2015*, (n.d.).
- 40 R.A. Rozendaal, B.J. Mijnheer, O. Hamming-Vrieze, A. Mans, and M. van Herk, “Impact of daily anatomical changes on EPID-based in vivo dosimetry of VMAT treatments of head-and-neck cancer,” *Radiother. Oncol.* (2015).
- 41 S. Cilla *et al.*, “An in-vivo dosimetry procedure for Elekta step and shoot IMRT,” *Phys. Medica* **30**(4), 419–426 (2014).
- 42 D.N. Margalit *et al.*, “Technological advancements and error rates in radiation therapy delivery,” *Int. J. Radiat. Oncol. Biol. Phys.* **81**(4), (2011).
- 43 J.A. Kalapurakal *et al.*, “A comprehensive quality assurance program for personnel and procedures in radiation oncology: Value of voluntary error reporting and checklists,” *Int. J. Radiat. Oncol. Biol. Phys.* **86**(2), 241–248 (2013).
- 44 A. Mans *et al.*, “Catching errors with in vivo EPID dosimetry.,” *Med. Phys.* **37**(6), 2638–2644 (2010).
- 45 E. Yorke *et al.*, “Diode in vivo dosimetry for patients receiving external beam radiation therapy. Report of Task Group 62 of the AAPM Radiation Therapy Committee,” (87), 57 (2005).
- 46 A.S. Pradhan, J.I. Lee, and J.L. Kim, “Recent developments of optically stimulated luminescence materials and techniques for radiation dosimetry and clinical applications.,” *J. Med. Phys.* **33**(3), 85–99 (2008).
- 47 J.A. Kalef-Ezra, A. Boziari, J. Litsas, P. Tsekeris, and T. Koligliatis, “Thermoluminescence dosimetry for quality assurance in radiation therapy.,” *Radiat. Prot.*

- Dosimetry **101**(1–4), 403–5 (2002).
- 48 T. Kron, “Thermoluminescence dosimetry and its applications in medicine--Part 2: History and applications.,” *Australas. Phys. Eng. Sci. Med.* **18**(1), 1–25 (1995).
- 49 M. Soubra, J. Cygler, and G. Mackay, “Evaluation of a dual bias dual metal oxide-silicon semiconductor field effect transistor detector as radiation dosimeter.,” *Med. Phys.* **21**(4), 567–72 (1994).
- 50 R. Ramani, S. Russell, and P. O’Brien, “Clinical dosimetry using MOSFETs.,” *Int. J. Radiat. Oncol. Biol. Phys.* **37**(4), 959–64 (1997).
- 51 N. Jornet, P. Carrasco, D. Jurado, A. Ruiz, T. Eudaldo, and M. Ribas, “Comparison study of MOSFET detectors and diodes for entrance in vivo dosimetry in 18 MV x-ray beams.,” *Med. Phys.* **31**(9), 2534–42 (2004).
- 52 ESTRO, *Practical guidelines for the implementation of in vivo dosimetry with diodes in external beam radiation therapy with photon beams (entrance dose)* (2001).
- 53 R.C. Granke, K.A. Wright, W.W. Evans, J.E. Nelson, and J.G. Trump, “The film method of tissue dose studies with 2.0 mev. roentgen rays.,” *Am. J. Roentgenol. Radium Ther. Nucl. Med.* **72**(2), 302–7 (1954).
- 54 K.B. Pulliam *et al.*, “A six-year review of more than 13,000 patient-specific IMRT QA results from 13 different treatment sites.,” *J. Appl. Clin. Med. Phys.* **15**(5), 4935 (2014).
- 55 P. Mayles, A.E. Nahum, and J.-C. Rosenwald, *Handbook of radiotherapy physics: theory and practice* (Taylor & Francis, Boca Raton, FL, 2007).
- 56 L.E. Antonuk, “Electronic portal imaging devices: a review and historical perspective of contemporary technologies and research.,” *Phys. Med. Biol.* **47**(6), R31–R65 (2002).
- 57 S. Devic, “Radiochromic film dosimetry: past, present, and future.,” *Phys. Med.* **27**(3), 122–134 (2011).
- 58 J. Thoelking, Y. Sekar, J. Fleckenstein, F. Lohr, F. Wenz, and H. Wertz, “Characterization of a new transmission detector for patient individualized online plan verification and its influence on 6MV x-ray beam characteristics.,” *Z. Med. Phys.* (2015).
- 59 M.K. Islam *et al.*, “An integral quality monitoring system for real-time verification of intensity modulated radiation therapy.,” *Med. Phys.* **36**(12), 5420–8 (2009).
- 60 B. Perrin, A. Garner, J. Beck, R. Speakman, O. J, and G. Budgell, “Initial evaluation of the integral quality monitor,” in *United Kingdom Radiat. Oncol.* (Birmingham UK, n.d.).
- 61 D. Hoffman, E. Chung, C. Hess, R. Stern, and S. Benedict, “SU-E-T-571: Newly Emerging Integrated Transmission Detector Systems Provide Online Quality Assurance of External Beam Radiation Therapy,” *Med. Phys.* **42**(6), 3467–3467 (2015).
- 62 L.E. Reinstein *et al.*, *Radiotherapy portal imaging quality: Report 24 of AAPM Task Group 28* (1987).
- 63 J. Marks, A. Haus, H. Sutton, and M. Griem, “The value of frequent verification films in

- reducing localization error in the irradiation of complex fields,” *Cancer* **37**, 2755–2761 (1976).
- 64 S. Taborsky, W. Lam, R. Sterner, and G. Skarda, “Digital imaging for radiation therapy verification,” *Proc. SPIE* **314**, 164–171 (1981).
- 65 H. Meertens, M. van Herk, and J. Weeda, “A liquid ionisation detector for digital radiography of therapeutic megavoltage photon beams.,” *Phys. Med. Biol.* **30**(4), 313–21 (1985).
- 66 F.H. Attix, *Introduction to Radiological Physics and Radiation Dosimetry* (1986).
- 67 P. Greer and P. Vial, “Epid Dosimetry,” *Concepts Trends Med. Radiat. Dosim.* 129–144 (2011).
- 68 J. Yorkston, “Recent developments in digital radiography detectors,” *Nucl. Instruments Methods A* **580**, 974–985 (2007).
- 69 B.M. McCurdy, K. Luchka, and S. Pistorius, “Dosimetric investigation and portal dose image prediction using an amorphous silicon electronic portal imaging device.,” *Med. Phys.* **28**(6), 911–924 (2001).
- 70 A. Oppelt, *Imaging Systems for Medical Diagnostics: Fundamentals, Technical Solutions and Applications for Systems Applying Ionizing Radiation, Nuclear Magnetic Resonance and Ultrasound, 2nd Edition* (2006).
- 71 P.B. Greer and C.C. Popescu, “Dosimetric properties of an amorphous silicon electronic portal imaging device for verification of dynamic intensity modulated radiation therapy.,” *Med. Phys.* **30**(7), 1618–1627 (2003).
- 72 C. Kirkby and R. Sloboda, “Consequences of the spectral response of an a-Si EPID and implications for dosimetric calibration.,” *Med. Phys.* **32**(8), 2649–2658 (2005).
- 73 D.A. Jaffray, J.J. Battista, A. Fenster, and P. Munro, “X-ray scatter in megavoltage transmission radiography: physical characteristics and influence on image quality.,” *Med. Phys.* **21**(1), 45–60 (1994).
- 74 B.M.C. McCurdy and P.B. Greer, “Dosimetric properties of an amorphous-silicon EPID used in continuous acquisition mode for application to dynamic and arc IMRT.,” *Med. Phys.* **36**(7), 3028–3039 (2009).
- 75 R.D. Evans, *The Atomic Nucleus* (McGraw-Hill, 1955).
- 76 N.C. Yang, P.K. Lechner, and W.G. Hawkins, “Effective atomic numbers for low-energy total photon interactions in human tissues.,” *Med. Phys.* **14**(5), 759–66.
- 77 F. Khan, *The Physics of Radiation Therapy* (2003).
- 78 V.W. Huang, J. Seuntjens, S. Devic, and F. Verhaegen, “Experimental determination of electron source parameters for accurate Monte Carlo calculation of large field electron therapy.,” *Phys. Med. Biol.* **50**(5), 779–86 (2005).
- 79 T. Kron *et al.*, “Small field segments surrounded by large areas only shielded by a

- multileaf collimator: comparison of experiments and dose calculation.,” *Med. Phys.* **39**(12), 7480–9 (2012).
- 80 L.N. McDermott, S.M.J.J.G. Nijsten, J.-J. Sonke, M. Partridge, M. van Herk, and B.J. Mijnheer, “Comparison of ghosting effects for three commercial a-Si EPIDs.,” *Med. Phys.* **33**(7), 2448–2451 (2006).
- 81 L.N. McDermott, R.J.W. Louwe, J.J. Sonke, M.B. van Herk, and B.J. Mijnheer, “Dose-response and ghosting effects of an amorphous silicon electronic portal imaging device.,” *Med. Phys.* **31**(2), 285–295 (2004).
- 82 W. Van Elmpt, L. McDermott, S. Nijsten, M. Wendling, P. Lambin, and B. Mijnheer, “A literature review of electronic portal imaging for radiotherapy dosimetry,” *Radiother. Oncol.* **88**(3), 289–309 (2008).
- 83 V.N. Hansen, P.M. Evans, and W. Swindell, “The application of transit dosimetry to precision radiotherapy.,” *Med. Phys.* **23**(5), 713–21 (1996).
- 84 T.R. McNutt, T.R. Mackie, and B.R. Paliwal, “Analysis and convergence of the iterative convolution/superposition dose reconstruction technique for multiple treatment beams and tomotherapy.,” *Med. Phys.* **24**(9), 1465–76 (1997).
- 85 G. Jarry and F. Verhaegen, “Patient-specific dosimetry of conventional and intensity modulated radiation therapy using a novel full Monte Carlo phase space reconstruction method from electronic portal images.,” *Phys. Med. Biol.* **52**(8), 2277–99 (2007).
- 86 M. Partridge, M. Ebert, and B.M. Hesse, “IMRT verification by three-dimensional dose reconstruction from portal beam measurements.,” *Med. Phys.* **29**(8), 1847–58 (2002).
- 87 A. Kavuma, M. Glegg, M. Metwaly, G. Currie, and A. Elliott, “A novel method for patient exit and entrance dose prediction based on water equivalent path length measured with an amorphous silicon electronic portal imaging device.,” *Phys. Med. Biol.* **55**(2), 435–452 (2010).
- 88 A. Kavuma, M. Glegg, M. Metwaly, G. Currie, and A. Elliott, “Calculation of exit dose for conformal and dynamically-wedged fields, based on water-equivalent path length measured with an amorphous silicon electronic portal imaging device.,” *J. Appl. Clin. Med. Phys.* **12**(3), 3439 (2011).
- 89 K. Chytyk-Praznik, E. VanUytven, T. a vanBeek, P.B. Greer, and B.M.C. McCurdy, “Model-based prediction of portal dose images during patient treatment.,” *Med. Phys.* **40**(3), 31713 (2013).
- 90 T. Fuangrod *et al.*, “A system for EPID-based real-time treatment delivery verification during dynamic IMRT treatment.,” *Med. Phys.* **40**(9), 91907 (2013).
- 91 E. Van Uytven, T. Van Beek, P.M. McCowan, K. Chytyk-Praznik, P.B. Greer, and B.M.C. McCurdy, “Validation of a method for in vivo 3D dose reconstruction for IMRT and VMAT treatments using on-treatment EPID images and a model-based forward-calculation algorithm,” *Med. Phys.* **42**(12), 6945–6954 (2015).

- 92 L.N. McDermott, M. Wendling, J.J. Sonke, M. van Herk, and B.J. Mijnheer, “Replacing Pretreatment Verification With In Vivo EPID Dosimetry for Prostate IMRT,” *Int. J. Radiat. Oncol. Biol. Phys.* **67**(5), 1568–1577 (2007).
- 93 R. Boellaard, M. Essers, M. Van Herk, and B.J. Mijnheer, “New method to obtain the midplane dose using portal in vivo dosimetry,” *Int. J. Radiat. Oncol. Biol. Phys.* **41**(2), 465–474 (1998).
- 94 R. Boellaard, M. van Herk, and B.J. Mijnheer, “A convolution model to convert transmission dose images to exit dose distributions.,” *Med. Phys.* **24**(2), 189–99 (1997).
- 95 R. Boellaard, M. van Herk, H. Uiterwaal, and B. Mijnheer, “Two-dimensional exit dosimetry using a liquid-filled electronic portal imaging device and a convolution model.,” *Radiother. Oncol.* **44**(2), 149–57 (1997).
- 96 D. a Low, W.B. Harms, S. Mutic, and J. a Purdy, “A technique for the quantitative evaluation of dose distributions.,” *Med. Phys.* **25**(5), 656–661 (1998).
- 97 I. Olaciregui-Ruiz, R.A. Rozendaal, B. Mijnheer, M. van Herk, and A. Mans, “Automatic in vivo portal dosimetry of all treatments.,” *Phys. Med. Biol.* **58**(22), 8253–64 (2013).
- 98 H. Spreeuw *et al.*, “Portal dosimetry in wedged beams,” **16**(3), 244–257 (2015).
- 99 A. Mans *et al.*, “3D Dosimetric verification of volumetric-modulated arc therapy by portal dosimetry,” *Radiother. Oncol.* **94**(2), 181–187 (2010).
- 100 R. Pecharromán-Gallego *et al.*, “Simplifying EPID dosimetry for IMRT treatment verification.,” *Med. Phys.* **38**(2), 983–992 (2011).
- 101 M. Wendling *et al.*, “In aqua vivo EPID dosimetry,” *Med. Phys.* **39**(1), 367 (2012).
- 102 A. Piermattei *et al.*, “In vivo dosimetry by an aSi-based EPID.,” *Med. Phys.* **33**(11), 4414–4422 (2006).
- 103 “Central axis depth dose data for use in radiotherapy,” *Br. J. Radiol.* (Supplement 25), (1996).
- 104 S. Peca and D.W. Brown, “Two-dimensional in vivo dose verification using portal imaging and correlation ratios,” *J. Appl. Clin. Med. Phys.* **15**(4), 117–128 (2014).
- 105 L.C.G.G. Persoon *et al.*, “Interfractional trend analysis of dose differences based on 2D transit portal dosimetry,” *Phys. Med. Biol.* **57**(20), 6445–6458 (2012).
- 106 W. Bogdanich, “Radiation Offers New Cures, and Ways to Do Harm,” *New York Times* 1–18 (2010).
- 107 M. Wendling, R.J.W. Louwe, L.N. McDermott, J.-J. Sonke, M. van Herk, and B.J. Mijnheer, “Accurate two-dimensional IMRT verification using a back-projection EPID dosimetry method.,” *Med. Phys.* **33**(2), 259–273 (2006).
- 108 S.J. Blake *et al.*, “Characterization of a novel EPID designed for simultaneous imaging and dose verification in radiotherapy.,” *Med. Phys.* **40**(9), 91902-1-11 (2013).

- 109 J.W. Jung, J.O. Kim, I.J. Yeo, Y.-B. Cho, S.M. Kim, and S. DiBiase, “Fast transit portal dosimetry using density-scaled layer modeling of aSi-based electronic portal imaging device and Monte Carlo method.,” *Med. Phys.* **39**(12), 7593–602 (2012).
- 110 K. Chytyk and B.M.C. McCurdy, “Comprehensive fluence model for absolute portal dose image prediction.,” *Med. Phys.* **36**(4), 1389–1398 (2009).
- 111 G. Asuni, T.A. van Beek, S. Venkataraman, I.A. Popescu, and B.M.C. McCurdy, “A Monte Carlo tool for evaluating VMAT and DIMRT treatment deliveries including planar detectors.,” *Phys. Med. Biol.* **58**(11), 3535–50 (2013).
- 112 M. Sabet, P. Rowshanfarzad, P. Vial, F.W. Menk, and P.B. Greer, “Transit dosimetry in IMRT with an a-Si EPID in direct detection configuration,” *Phys. Med. Biol.* **57**(7), N295–N306 (2012).
- 113 P. Rowshanfarzad, M. Sabet, D.J. O’Connor, P.M. McCowan, B.M.C. McCurdy, and P.B. Greer, “Detection and correction for EPID and gantry sag during arc delivery using cine EPID imaging,” *Med. Phys.* **39**(2), 623 (2012).
- 114 P. Rowshanfarzad, M. Sabet, D.J. O’Connor, P.M. McCowan, B.M.C. McCurdy, and P.B. Greer, “Gantry angle determination during arc IMRT: evaluation of a simple EPID-based technique and two commercial inclinometers.,” *J. Appl. Clin. Med. Phys.* **13**(6), 3981 (2012).
- 115 H.C. Woodruff, T. Fuangrod, P. Rowshanfarzad, B.M.C. McCurdy, and P.B. Greer, “Gantry-angle resolved VMAT pretreatment verification using EPID image prediction.,” *Med. Phys.* **40**(8), 81715 (2013).
- 116 W.D. Renner, K. Norton, and T. Holmes, “A method for deconvolution of integrated electronic portal images to obtain incident fluence for dose reconstruction.,” *J. Appl. Clin. Med. Phys.* **6**(4), 22–39 (2005).
- 117 W.D. Renner, M. Sarfaraz, M. a Earl, and C.X. Yu, “A dose delivery verification method for conventional and intensity-modulated radiation therapy using measured field fluence distributions.,” *Med. Phys.* **30**(11), 2996–3005 (2003).
- 118 A. Piermattei *et al.*, “A National project for in vivo dosimetry procedures in radiotherapy: First results,” *Nucl. Instruments Methods Phys. Res. Sect. B Beam Interact. with Mater. Atoms* **274**, 42–50 (2012).
- 119 A. Fidanzio *et al.*, “Breast in vivo dosimetry by EPID.,” *J. Appl. Clin. Med. Phys.* **11**(4), 3275 (2010).
- 120 S. Cilla *et al.*, “Correlation functions for Elekta aSi EPIDs used as transit dosimeter for open fields.,” *J. Appl. Clin. Med. Phys.* **12**(1), 3279 (2011).
- 121 A. Piermattei *et al.*, “Real-time dose reconstruction for wedged photon beams: a generalized procedure.,” *J. Appl. Clin. Med. Phys.* **12**(4), 3538 (2011).
- 122 F. Greco *et al.*, “ASi-EPID transit signal calibration for dynamic beams: A needful step for the IMRT in vivo dosimetry,” *Med. Biol. Eng. Comput.* **51**(10), 1137–1145 (2013).

- 123 C. Lee, F. Menk, P. Cadman, and P.B. Greer, “A simple approach to using an amorphous silicon EPID to verify IMRT planar dose maps.,” *Med. Phys.* **36**(3), 984–992 (2009).
- 124 S.M.J.J.G. Nijsten *et al.*, “A global calibration model for a-Si EPIDs used for transit dosimetry.,” *Med. Phys.* **34**(10), 3872–3884 (2007).
- 125 C. Yeboah and S. Pistorius, “Monte Carlo studies of the exit photon spectra and dose to a metal/phosphor portal imaging screen.,” *Med. Phys.* **27**(2), 330–339 (2000).
- 126 K. Pulliam, J. Kerns, R. Howell, D. Followill, J. O’Daniel, and S. Kry, “MO-G-BRE-02: A Survey of IMRT QA Practices for More Than 800 Institutions,” *Med. Phys.* **41**(6), 432–432 (2014).
- 127 P. Rowshanfarzad, B.M.C. McCurdy, M. Sabet, C. Lee, D.J. O’Connor, and P.B. Greer, “Measurement and modeling of the effect of support arm backscatter on dosimetry with a varian EPID.,” *Med. Phys.* **37**(5), 2269–2278 (2010).
- 128 J. Camilleri, J. Mazurier, D. Franck, P. Dudouet, I. Latorzeff, and X. Franceries, “2D EPID dose calibration for pretreatment quality control of conformal and IMRT fields: A simple and fast convolution approach.,” *Phys. Med.* **32**(1), 133–40 (2016).
- 129 M.G. Witte, J. van der Geer, C. Schneider, J. V Lebesque, and M. van Herk, “The effects of target size and tissue density on the minimum margin required for random errors.,” *Med. Phys.* **31**(11), 3068–3079 (2004).
- 130 S. Peca, D. Brown, and W.L. Smith, “In Vivo EPID Dosimetry Detects Interfraction Errors in 3D-CRT of Rectal Cancer,” *IFMBE Proc.* **51**, 531–534 (2015).
- 131 C.W. Coffey, J.L. Beach, D.J. Thompson, and M. Mendiondo, “X-ray beam characteristics of the Varian Clinac 6-100 linear accelerator.,” *Med. Phys.* **7**(6), 716–22 (1980).
- 132 G. Narayanasamy, D. Saenz, W. Cruz, C.S. Ha, N. Papanikolaou, and S. Stathakis, “Commissioning an Elekta Versa HD linear accelerator,” *J. Appl. Clin. Med. Phys.* **17**(1), 179–191 (2016).
- 133 W. Ansbacher, “Three-dimensional portal image-based dose reconstruction in a virtual phantom for rapid evaluation of IMRT plans.,” *Med. Phys.* **33**(9), 3369–3382 (2006).
- 134 H. Akaike, “A new look at the statistical model identification,” *IEEE Trans. Automat. Contr.* **19**, 716–723 (1974).
- 135 K. Yamaoka, T. Nakagawa, and T. Uno, “Application of Akaike’s information criterion (AIC) in the evaluation of linear pharmacokinetic equations,” *J. Pharmacokinet. Pharmacodyn.* **6**(2), 165–175 (1978).
- 136 S. Quirk, N. Becker, and W. Smith, “External respiratory motion: Shape analysis and custom realistic respiratory trace generation,” *Med. Phys.* **39**(8), 4999 (2012).
- 137 S.A. Naqvi, M.A. Earl, and D.M. Shepard, “Convolution/superposition using the Monte Carlo method,” *Phys. Med. Biol.* **48**, 2101–2121 (2003).

- 138 P.B. Greer, “Correction of pixel sensitivity variation and off-axis response for amorphous silicon EPID dosimetry.” *Med. Phys.* **32**(12), 3558–3568 (2005).
- 139 R.J.W. Louwe *et al.*, “The long-term stability of amorphous silicon flat panel imaging devices for dosimetry purposes.” *Med. Phys.* **31**(11), 2989–2995 (2004).
- 140 M. Wendling, L.N. McDermott, A. Mans, J.-J. Sonke, M. van Herk, and B.J. Mijnheer, “A simple backprojection algorithm for 3D in vivo EPID dosimetry of IMRT treatments.” *Med. Phys.* **36**(7), 3310–3321 (2009).
- 141 H.C. Woodruff *et al.*, “First Experience With Real-Time EPID-Based Delivery Verification During IMRT and VMAT Sessions,” *Int. J. Radiat. Oncol.* **93**(3), 516–522 (2015).
- 142 S. Cilla *et al.*, “Calibration of Elekta aSi EPIDs Used as Transit Dosimeter,” *Technol. Cancer Res. Treat.* **10**(1), 39–48 (2011).
- 143 M. Russo *et al.*, “Step-and-Shoot IMRT by Siemens Beams: An EPID Dosimetry Verification During Treatment,” *Technol. Cancer Res. Treat.* 1–11 (2015).
- 144 J. Gimeno *et al.*, “Commissioning and initial experience with a commercial software for in vivo volumetric dosimetry,” *Phys. Medica* **30**(8), 954–959 (2014).
- 145 S. Celi, E. Costa, C. Wessels, A. Mazal, A. Fourquet, and P. Francois, “EPID based in vivo dosimetry system : clinical experience and results,” **17**(3), 262–276 (2016).
- 146 S.L. Berry, C.S. Polvorosa, and C.-S. Wu, “A field size specific backscatter correction algorithm for accurate EPID dosimetry.” *Med. Phys.* **37**(6), 2425–2434 (2010).
- 147 K. Pulliam, J. Kerns, R. Howell, D. Followill, J. O’Daniel, and S. Kry, “MO-G-BRE-02: A Survey of IMRT QA Practices for More Than 800 Institutions,” *Med. Phys.* **41**(6), 432–432 (2014).
- 148 L.C.G.G. Persoon, M. Podesta, S.M.J.J.G. Nijsten, E.G.C. Troost, and F. Verhaegen, “Time-Resolved Versus Integrated Transit Planar Dosimetry for Volumetric Modulated Arc Therapy: Patient-Specific Dose Differences During Treatment, a Proof of Principle.” *Technol. Cancer Res. Treat.* **15**(6), 1533034615617668 (2015).
- 149 A. Van Esch *et al.*, “Testing of the analytical anisotropic algorithm for photon dose calculation,” *Med. Phys.* **33**(11), 4130 (2006).
- 150 T.G. Shanahan *et al.*, “Minimization of small bowel volume within treatment fields utilizing customized ‘belly boards,’” *Int. J. Radiat. Oncol. Biol. Phys.* **19**(2), 469–476 (1990).
- 151 J.Y. Kim *et al.*, “Intensity-modulated radiotherapy with a belly board for rectal cancer,” *Int. J. Colorectal Dis.* **22**, 373–379 (2007).
- 152 A.S. Allal, S. Bischof, and P. Nouet, “Impact of the ‘Belly Board’ Device on Treatment Reproducibility in Preoperative Radiotherapy for Rectal Cancer,” *Strahlentherapie und Onkol.* **178**(5), 259–262 (2002).

- 153 M. Kasabasic, D. Faj, A. Ivkovic, S. Jurkovic, and N. Belaj, "Rotation of the sacrum during bellyboard pelvic radiotherapy," *Med. Dosim.* **35**(1873–4022; 1873–4022; 1), 28–30 (2010).
- 154 C. Kirkby and R. Sloboda, "Comprehensive Monte Carlo calculation of the point spread function for a commercial a-Si EPID.," *Med. Phys.* **32**(4), 1115–1127 (2005).
- 155 M.G. Witte, J. van der Geer, C. Schneider, J. V Lebesque, M. Alber, and M. van Herk, "IMRT optimization including random and systematic geometric errors based on the expectation of TCP and NTCP.," *Med. Phys.* **34**(9), 3544–3555 (2007).
- 156 B.J. Mijnheer, P. González, I. Olaciregui-ruiz, R.A. Rozendaal, M. Van Herk, and A. Mans, "Overview of 3-year experience with large-scale electronic portal imaging device – based 3-dimensional transit dosimetry," *PRRO* **5**(6), e679–e687 (2015).
- 157 P.J.A.M. Brouwers *et al.*, "Set-up verification and 2-dimensional electronic portal imaging device dosimetry during breath hold compared with free breathing in breast cancer radiation therapy," *Pract. Radiat. Oncol.* **5**(3), e135–e141 (2015).
- 158 R. Sauer *et al.*, "Adjuvant vs. neoadjuvant radiochemotherapy for locally advanced rectal cancer: The German trial CAO/ARO/AIO-94," *Color. Dis.* **5**, 406–415 (2003).
- 159 R. Sauer *et al.*, "Preoperative versus postoperative chemoradiotherapy for rectal cancer.," *N. Engl. J. Med.* **351**(17), 1731–1740 (2004).
- 160 J.F. Bosset *et al.*, "Chemotherapy with preoperative radiotherapy in rectal cancer," *N Engl J Med* **355**(11), 1114–1123 (2006).
- 161 L.P. Morten Brændengen, Kjell M. Tveit, Åke Berglund, Elke Birkemeyer, Gunilla Frykholm and A.B.G. Johan N. Wiig, Per Bystrom, Krzysztof Bujko, "Randomized Phase III Study Comparing Preoperative Radiotherapy With Chemoradiotherapy in Nonresectable Rectal Cancer," *J. Clin. Oncol.* **26**(22), 3687–3694 (2008).
- 162 J.M. Robertson, M. Söhn, and D. Yan, "Predicting Grade 3 Acute Diarrhea During Radiation Therapy for Rectal Cancer Using a Cutoff-Dose Logistic Regression Normal Tissue Complication Probability Model," *Int. J. Radiat. Oncol. Biol. Phys.* **77**(1), 66–72 (2010).
- 163 B.D. Kavanagh *et al.*, "Radiation Dose-Volume Effects in the Stomach and Small Bowel," *Int. J. Radiat. Oncol. Biol. Phys.* **76**(3 SUPPL.), 101–107 (2010).
- 164 A.C. Mak, T.A. Rich, T.E. Schultheiss, B. Kavanagh, D.M. Ota, and M.M. Romsdahl, "Late complications of postoperative radiation therapy for cancer of the rectum and rectosigmoid," *Int. J. Radiat. Oncol. Biol. Phys.* **28**(3), 597–603 (1994).
- 165 R. Banerjee, S. Chakraborty, I. Nygren, and R. Sinha, "Small Bowel Dose Parameters Predicting Grade ≥ 3 Acute Toxicity in Rectal Cancer Patients Treated With Neoadjuvant Chemoradiation: An Independent Validation Study Comparing Peritoneal Space Versus Small Bowel Loop Contouring Techniques," *Int. J. Radiat. Oncol.* **85**(5), 1225–1231 (2013).

- 166 K.L. Baglan, R.C. Frazier, D. Yan, R.R. Huang, A. a Martinez, and J.M. Robertson, “The dose-volume relationship of acute small bowel toxicity from concurrent 5-FU-based chemotherapy and radiation therapy for rectal cancer.,” *Int. J. Radiat. Oncol. Biol. Phys.* **52**(1), 176–83 (2002).
- 167 E.M. Wiesendanger-Wittmer, N.M. Sijtsema, C.T. Muijs, and J.C. Beukema, “Systematic review of the role of a belly board device in radiotherapy delivery in patients with pelvic malignancies,” *Radiother. Oncol.* **102**(3), 325–334 (2012).
- 168 O. Koelbl, D. Vordermark, and M. Flentje, “The relationship between belly board position and patient anatomy and its influence on dose–volume histogram of small bowel for postoperative radiotherapy of rectal cancer,” *Radiother. Oncol.* **67**(3), 345–349 (2003).
- 169 P.B. Greer, “3D EPID based dosimetry for pre-treatment verification of VMAT – methods and challenges,” *J. Phys. Conf. Ser.* **444**(1), 12010 (2013).
- 170 J.J. Nuytens, J.M. Robertson, D. Yan, and a Martinez, “The position and volume of the small bowel during adjuvant radiation therapy for rectal cancer.,” *Int. J. Radiat. Oncol. Biol. Phys.* **51**(5), 1271–1280 (2001).
- 171 J.F. Bosset *et al.*, “Preoperative chemoradiotherapy versus preoperative radiotherapy in rectal cancer patients: Assessment of acute toxicity and treatment compliance: Report of the 22921 randomised trial conducted by the EORTC Radiotherapy Group,” *Eur. J. Cancer* **40**(2), 219–224 (2004).
- 172 P. Munro and D.C. Bouius, “X-ray quantum limited portal imaging using amorphous silicon flat-panel arrays.,” *Med. Phys.* **25**(5), 689–702 (1998).
- 173 S.M.J.J.G. Nijsten, B.J. Mijnheer, A.L. a J. Dekker, P. Lambin, and A.W.H. Minken, “Routine individualised patient dosimetry using electronic portal imaging devices.,” *Radiother. Oncol.* **83**(1), 65–75 (2007).
- 174 P. Winkler and D. Georg, “An intercomparison of 11 amorphous silicon EPIDs of the same type: implications for portal dosimetry.,” *Phys. Med. Biol.* **51**(17), 4189–4200 (2006).
- 175 A. Bakai, M. Alber, and N. Fridtjof, “A revision of the γ -evaluation concept for the comparison of dose distributions,” *Phys. Med. Biol.* **48**(21), 3543 (2003).
- 176 P.M. McCowan, D.W. Rickey, P. Rowshanfarzad, P.B. Greer, W. Ansbacher, and B.M. McCurdy, “An investigation of gantry angle data accuracy for cine-mode EPID images acquired during arc IMRT,” *J. Appl. Clin. Med. Phys.* **15**(1), 187–201 (2014).
- 177 J.J. Kruse, “On the insensitivity of single field planar dosimetry to IMRT inaccuracies.,” *Med. Phys.* **37**(6), 2516–2524 (2010).
- 178 G. Budgell, “Comment on ‘On the insensitivity of single field planar dosimetry to IMRT inaccuracies’ [Med. Phys. 37, 2516-2524 (2010)].,” *Med. Phys.* **37**(12), 6497–6498; author reply 6499 (2010).
- 179 B.E. Nelms, H. Zhen, and W.A. Tomé, “Per-beam, planar IMRT QA passing rates do not

- predict clinically relevant patient dose errors,” *Med. Phys.* **38**(2), 1037 (2011).
- 180 B.E. Nelms *et al.*, “Evaluating IMRT and VMAT dose accuracy: Practical examples of failure to detect systematic errors when applying a commonly used metric and action levels,” *Med. Phys.* **40**(11), 111722 (2013).
- 181 T. Moodie, J. Sykes, and R. Gajewski, “A revision of the γ -evaluation concept for the comparison of dose distributions,” *Phys. Med. Biol.* **59**(23), 7557–7561 (2014).
- 182 A. Pinkerton, M. Hannon, J. Kwag, and W.D. Renner, “Experience Using DosimetryCheck software for IMRT and RapidArc Patient Pre-treatment QA and a New Feature for QA during Treatment,” *J. Phys. Conf. Ser.* **250**, 12101 (2010).
- 183 C. Bojchko and E.C. Ford, “Quantifying the performance of in vivo portal dosimetry in detecting four types of treatment parameter variations,” *Med. Phys.* **42**(12), 6912–6918 (2015).
- 184 R.M. Haralick, S.R. Sternberg, and X. Zhuang, “Image analysis using mathematical morphology,” *IEEE Trans. Pattern Anal. Mach. Intell.* **9**(4), 532–50 (1987).
- 185 E.R. DeLong, D.M. DeLong, and D.L. Clarke-Pearson, “Comparing the areas under two or more correlated receiver operating characteristic curves: a nonparametric approach,” *Biometrics* **44**(3), 837–45 (1988).
- 186 The International Commission on Radiation Units and Measurements, “Prescribing, Recording, and Reporting Intensity-Modulated Photon-Beam Therapy (IMRT). ICRU Report 83,” *J ICRU* **10**, (2010).

Appendix: Copyright permissions

Permission to reproduce Figure 1-3

19/09/2015

RightsLink Printable License

ELSEVIER LICENSE TERMS AND CONDITIONS

Sep 19, 2015

This is a License Agreement between Stefano Peca ("You") and Elsevier ("Elsevier") provided by Copyright Clearance Center ("CCC"). The license consists of your order details, the terms and conditions provided by Elsevier, and the payment terms and conditions.

All payments must be made in full to CCC. For payment instructions, please see information listed at the bottom of this form.

Supplier	Elsevier Limited The Boulevard, Langford Lane Kidlington, Oxford, OX5 1GB, UK
Registered Company Number	1982084
Customer name	Stefano Peca
Customer address	
License number	3712600098223
License date	Sep 19, 2015
Licensed content publisher	Elsevier
Licensed content publication	Practical Radiation Oncology
Licensed content title	Patient safety improvements in radiation treatment through 5 years of incident learning
Licensed content author	Brenda G. Clark, Robert J. Brown, Jodi Ploquin, Peter Dunscombe
Licensed content date	July–September 2013
Licensed content volume number	3
Licensed content issue number	3
Number of pages	7
Start Page	157
End Page	163
Type of Use	reuse in a thesis/dissertation
Portion	figures/tables/illustrations
Number of figures/tables/illustrations	1
Format	both print and electronic
Are you the author of this Elsevier article?	No
Will you be translating?	No
Original figure numbers	Figure 1

<https://s100.copyright.com/App/PrintableLicenseFrame.jsp?publisherID=70&publisherName=ELS&publication=1879-8500&publicationID=37788&rightID=1&tp...> 1/8

Title of your thesis/dissertation	In vivo dosimetry by portal imaging
Expected completion date	Dec 2015
Estimated size (number of pages)	200
Elsevier VAT number	GB 494 6272 12
Permissions price	0.00 CAD
VAT/Local Sales Tax	0.00 CAD / 0.00 GBP
Total	0.00 CAD

Terms and Conditions

INTRODUCTION

1. The publisher for this copyrighted material is Elsevier. By clicking "accept" in connection with completing this licensing transaction, you agree that the following terms and conditions apply to this transaction (along with the Billing and Payment terms and conditions established by Copyright Clearance Center, Inc. ("CCC"), at the time that you opened your Rightslink account and that are available at any time at <http://myaccount.copyright.com>).

GENERAL TERMS

- Elsevier hereby grants you permission to reproduce the aforementioned material subject to the terms and conditions indicated.
- Acknowledgement:** If any part of the material to be used (for example, figures) has appeared in our publication with credit or acknowledgement to another source, permission must also be sought from that source. If such permission is not obtained then that material may not be included in your publication/copies. Suitable acknowledgement to the source must be made, either as a footnote or in a reference list at the end of your publication, as follows:
"Reprinted from Publication title, Vol /edition number, Author(s), Title of article / title of chapter, Pages No., Copyright (Year), with permission from Elsevier [OR APPLICABLE SOCIETY COPYRIGHT OWNER]." Also Lancet special credit - "Reprinted from The Lancet, Vol number, Author(s), Title of article, Pages No., Copyright (Year), with permission from Elsevier."
- Reproduction of this material is confined to the purpose and/or media for which permission is hereby given.
- Altering/Modifying Material:** Not Permitted. However figures and illustrations may be altered/adapted minimally to serve your work. Any other abbreviations, additions, deletions and/or any other alterations shall be made only with prior written authorization of Elsevier Ltd. (Please contact Elsevier at permissions@elsevier.com)
- If the permission fee for the requested use of our material is waived in this instance, please be advised that your future requests for Elsevier materials may attract a fee.
- Reservation of Rights:** Publisher reserves all rights not specifically granted in the combination of (i) the license details provided by you and accepted in the course of this licensing transaction, (ii) these terms and conditions and (iii) CCC's Billing and Payment terms and conditions.
- License Contingent Upon Payment:** While you may exercise the rights licensed immediately upon issuance of the license at the end of the licensing process for the transaction, provided that you have disclosed complete and accurate details of your proposed use, no license is finally effective unless and until full payment is received from you (either by publisher or by CCC) as provided in CCC's Billing and Payment terms and conditions. If full payment is not received on a timely basis, then any license preliminarily granted shall be deemed automatically revoked and shall be void as if never

complies with the terms and conditions determined by the rights holder.

Additional Terms & Conditions applicable to each Creative Commons user license:

CC BY: The CC-BY license allows users to copy, to create extracts, abstracts and new works from the Article, to alter and revise the Article and to make commercial use of the Article (including reuse and/or resale of the Article by commercial entities), provided the user gives appropriate credit (with a link to the formal publication through the relevant DOI), provides a link to the license, indicates if changes were made and the licensor is not represented as endorsing the use made of the work. The full details of the license are available at <http://creativecommons.org/licenses/by/4.0>.

CC BY NC SA: The CC BY-NC-SA license allows users to copy, to create extracts, abstracts and new works from the Article, to alter and revise the Article, provided this is not done for commercial purposes, and that the user gives appropriate credit (with a link to the formal publication through the relevant DOI), provides a link to the license, indicates if changes were made and the licensor is not represented as endorsing the use made of the work. Further, any new works must be made available on the same conditions. The full details of the license are available at <http://creativecommons.org/licenses/by-nc-sa/4.0>.

CC BY NC ND: The CC BY-NC-ND license allows users to copy and distribute the Article, provided this is not done for commercial purposes and further does not permit distribution of the Article if it is changed or edited in any way, and provided the user gives appropriate credit (with a link to the formal publication through the relevant DOI), provides a link to the license, and that the licensor is not represented as endorsing the use made of the work. The full details of the license are available at <http://creativecommons.org/licenses/by-nc-nd/4.0>. Any commercial reuse of Open Access articles published with a CC BY NC SA or CC BY NC ND license requires permission from Elsevier and will be subject to a fee.

Commercial reuse includes:

- Associating advertising with the full text of the Article
- Charging fees for document delivery or access
- Article aggregation
- Systematic distribution via e-mail lists or share buttons

Posting or linking by commercial companies for use by customers of those companies.

20. Other Conditions:

v1.8

Questions? customercare@copyright.com or +1-855-239-3415 (toll free in the US) or +1-978-646-2777.

Permission to reproduce Chapter 6.1

01_03



PERMISSION LETTER

September 8, 2015

Springer reference

World Congress on Medical Physics and Biomedical Engineering, June 7-12, 2015, Toronto, Canada

Volume 51 of the series IFMBE Proceedings pp. 531-534

In Vivo EPID Dosimetry Detects Interfraction Errors in 3D-CRT of Rectal Cancer

Authors: S. Peca, D. Brown, W. L. Smith

© Springer International Publishing Switzerland 2015

DOI 10.1007/978-3-319-19387-8_130

Print ISBN 978-3-319-19386-1

Online ISBN 978-3-319-19387-8

Your project

Requestor: Stefano Peca

PhD Candidate

University of Calgary

Medical Physics

University: University of Calgary

Purpose: Dissertation/Thesis

With reference to your request to reuse material in which Springer Science+Business Media controls the copyright, our permission is granted free of charge under the following conditions:

Springer material

- represents original material which does not carry references to other sources (if material in question refers with a credit to another source, authorization from that source is required as well);
- requires full credit (Springer and the original publisher, book/journal title, chapter/article title, volume, year of publication, page, name(s) of author(s), original copyright notice) to the publication in which the material was originally published by adding: "With permission of Springer Science+Business Media";
- may not be altered in any manner. Abbreviations, additions, deletions and/or any other alterations shall be made only with prior written authorization of the author and/or Springer Science+Business Media;
- Springer does not supply original artwork or content.

This permission

- is non-exclusive;
- is valid for one-time use only for the purpose of defending your thesis and with a maximum of 100 extra copies in paper. If the thesis is going to be published, permission needs to be reobtained.
- includes use in an electronic form, provided it is an author-created version of the thesis on his/her own website and his/her university's repository, including UMI (according to the definition on the Sherpa website: <http://www.sherpa.ac.uk/romeo/>);
- is subject to courtesy information to the co-author or corresponding author;
- is personal to you and may not be sublicensed, assigned, or transferred by you to any other person without Springer's written permission;
- is only valid if no personal rights, trademarks, or competitive products are infringed.

This license is valid only when the conditions noted above are met.

PERMISSION LETTER

Permission free of charge does not prejudice any rights we might have to charge for reproduction of our copyrighted material in the future.

Rights and Permissions
Springer Science+Business Media
Tiergartenstr. 17
69121 Heidelberg
Germany